

## ABSTRACT

Title of dissertation: ABOVE THE CLOUDS:  
1-D MODELING OF OBSERVATIONS OF  
TIDALLY LOCKED EXTRASOLAR WORLDS

Mahmuda Afrin Badhan  
Doctor of Philosophy, 2019

Dissertation directed by: Professor L. Drake Deming  
Department of Astronomy  
University of Maryland College Park

Doctor Shawn Domagal-Goldman  
Planetary Systems Laboratory  
NASA Goddard Space Flight Center

Unique and exotic planetary environments give us an opportunity to understand how planetary systems form and evolve over their lifetime, by placing our planetary system in the context of vastly different extrasolar systems. With orbital separations a fraction of the Mercury-Sun distance, these close-in planets provide us with valuable insights regarding interactions between the stellar and planetary atmospheres. Further, observational biases actually allow such planets to be the first to be observed via transit spectroscopy.

Observed spectrophotometric signatures from transit measurements can reveal spectrally active species in a planet's atmosphere. Present observational technologies can also shed light on the atmosphere's structure and dynamics. Future missions will allow us to constrain these properties with unprecedented accuracy, and are also being designed to observe increasingly smaller, cooler and less extreme planets. The eventual goal, after all, is to identify a world like our own. To interpret the

observations with any certainty, however, we must build robust atmospheric models that sufficiently factor both physical and chemical processes expected in those atmospheres.

3-D climate modeling has shown that tidally-locked Earth-like planets, at the inner edge of M dwarf habitable zones, may retain water-vapor-rich stratospheres. However, flaring M dwarfs have strong UV activity, which may photodissociate  $\text{H}_2\text{O}$ . Using synthetic stellar UV within a 1-D photochemical model, I assess whether water vapor loss driven by high stellar UV would affect its detectability in *JWST*/MIRI transmission spectroscopy. I pseudo-couple a 3-D climate model to our 1-D model to achieve this. In a follow-up study, I also compute 125 additional atmospheric states by varying the Earth-like planet's orbital distance (thus moistness) and methane production rates. I check for and quantify the simultaneous presence of detectable ozone and methane in an otherwise abiotic anoxic atmosphere.

I have also implemented techniques to robustly quantify atmospheric properties of hot Jupiters from data-driven retrievals, and built a versatile template for hot Jupiter atmospheres within our 1-D photochemical modeling tool, which was previously only valid for cool rocky worlds. I sketch out a plan for using this work towards mapping non-equilibrated (non-LTE) emissions from methane in the upper atmospheres of observable giants.

ABOVE THE CLOUDS: 1-D MODELING OF OBSERVATIONS  
OF TIDALLY LOCKED EXTRASOLAR WORLDS

by

Mahmuda Afrin Badhan

Dissertation submitted to the Faculty of the Graduate School of the  
University of Maryland, College Park in partial fulfillment  
of the requirements for the degree of  
Doctor of Philosophy  
2019

Advisory Committee:

Professor L. Drake Deming, Chair/Advisor  
Doctor Shawn Domagal-Goldman, Co-Advisor  
Doctor Ravi Kumar Kopparapu, Co-Advisor  
Professor Douglas P. Hamilton  
Professor Eliza M.-R. Kempton  
Professor Ricardo Arevalo Jr., Dean's Rep

© Copyright by  
Mahmuda Afrin Badhan  
2019



## Preface

I am grateful for the existence of the CRESST program, a cooperative agreement between NASA GSFC and UMD (and other member institutes), for providing means for UMD scientists to conduct research activities at GSFC. I am also grateful for the research and financial support of the Virtual Planetary Laboratory, and the fairly newly formed Sellers Exoplanet Environment Collaboration (SEEC) for fostering intra-GSFC collaborations.

This dissertation is comprised of science from two related but separate studies on tidally-locked habitable planets, which form Chapters 4 and 5, and a chapter dedicated to tools and techniques I have developed for future analyses of hot Jupiter atmospheres (Chapter 3). Chapter 6, the future work chapter, connects directly to Chapter 3 in the sense that the efforts described in Chapter 3 can be used for the hot Jupiter portion of the study proposed in Chapter 6. Chapter 3 is focused on creation and validation efforts and is not a standalone publication. However, I have presented the content of Chapter 3 at various domestic meetings between 2015 and 2017, including the 2017 Astrobiology Science Conference, followed by the Gordon Research Conference on the Origin of the Solar System the same year. I was awarded travel grants to attend both conferences from the respective organizing committees.

Most of Chapter 4 is from a recent manuscript with the same title, i.e. "Stellar Activity Effects on Moist Habitable Terrestrial Atmospheres Around M dwarfs". The manuscript has been accepted and is in press with the *the Astrophysical Journal* (*ApJ*). The latest version is presently available on arxiv (Afrin Badhan et al. 2019b).

I have expanded the chapter beyond the original paper with content from my ADASS conference proceedings paper, which is focused on the methodology (e.g. Figure 4.1 is directly from the inproceedings paper). The inproceedings paper is *in press* (Afrin Badhan et al. 2019a). Chapter 4 also includes selected content from responses to the reviewer. I have presented the study at three conferences: poster presentation at the 2018 Division of Planetary Science meeting in Knoxville, TN; oral presentations at the local American Geophysical Union Fall meeting in December, and then the American Astronomical Society winter meeting, two weeks later, in Seattle, WA.

Chapter 5, entitled "Robust Quantification of Abiotic CH<sub>4</sub> and O<sub>3</sub> in Moist Habitable Anoxic Terrestrial Atmospheres Orbiting a 3300 K M Dwarf Host", is a follow-up study to Chapter 4 and is motivated by the ozone results of Chapter 4. While Chapter 4 focuses on the habitability of the atmospheres and detectability of major greenhouse gases with the upcoming *James Webb Space Telescope*, (*JWST*) mission, Chapter 5 is meant to be a biosignature false positive case study to inform observational efforts of the *Origin Space Telescope (OST)* mission. The paper is currently in preparation for submission to the aforementioned journal (*ApJ*).

Chapter 1 and 2 both serve as background chapters. Chapter 1 introduces exoplanet characterization efforts, providing some motivational background for hot Jupiter work, as well as an overview of global circulation model studies of tidally-locked Earths, and a brief introduction to biosignature false positive studies. Chapter 2 gives motivational and mathematical background on atmospheric processes and atmospheric modeling tools; it can be thought of as an expanded Methods chapter. This dissertation thus follows a traditional layout.

## Dedication

*To my late dada (birthdate unknown - February 11 of my college senior year), my grandmother on my dad's side, who raised me from birth till I moved to the US. You were my best friend, and you had told me that had you been allowed to remain in school, you would have written a book. You told me you wanted to fulfill your bucket list through me, so here it is. I am pretty sure heaven has universal translation.*

## Acknowledgments

Given how the past several years have been for me, writing this particular document is definitely stirring some emotions here, but I will try my best not to come off too sappy. Having said so, I feel like I will never truly be ever satisfied with what I write here as I have so much to say, but only so much time and space. But here I go anyway. Those who have known me and been with me throughout my quest to get a PhD know I have not had the smoothest journey through graduate school, largely, due to circumstances beyond my control, but I kept pushing as I have a very specific future career goal in mind. I have been through three different research projects spanning two different fields, and have been here longer than my classmates had, most of whom got their PhDs in the last couple of years, although a couple have left the program as well. It is hard to imagine the journey is about to end soon for me as well, that all of that is about to pay off for me soon.

I could talk about how my resilience and unwilling to quit this path has gotten me here, but in all honesty, I would not have made it to this stage if it was not for the support of the few who helped me get here, and my friends, colleagues and support staff in this department. I will forever be grateful for the things they have done for me, the way some of them have been there for me during emotionally and mentally challenging periods, and in general—for their seemingly eternal and unconditional kindness and faith in my ability to succeed. I have some friends who got through graduate programs without much support at all, so I feel extremely grateful to have meet some wonderfully supportive people throughout the years at the UMD

Astronomy Department and NASA Goddard Space Flight Center. I would like to thank these people individually in the following paragraphs, in no specific order.

I would like to begin by thanking my aunts, uncles and cousins in New York, and my parents back home in Bangladesh. While I do not share details of my life here with them, I am grateful for their unconditional love, and for I have not been too great about keeping in touch. I am particularly grateful to my aunts, uncles and cousins for providing me with food and shelter and love while I was in between semesters in undergrad. To my parents—thank you for letting me, your only child, spend 10+ years away from you half way across the world so that I can pursue a fruitful life pursuing a unique degree and career path in a pollution-free environment. Clean air has no price tag. I have not gone back home since 2015 due to health concerns, and I am thankful that I have parents who were strong enough to put up with that, clearly putting my needs and health ahead of their need to see me.

I am thankful for the support of my peers here at UMD Astronomy throughout the years. They include former classmate, Dr. Krista Smith, and junior peers such as Dana Louie, Pradip Gatkine, Amy Steele, Teal, Sara Frederick, Thomas Rimlinger, Corbin Taylor, Laura Lenkic and Yvette Thackarey. They each served some positive role in my life here. Yvette joined our department merely two years ago, and back then I had no idea she'd become my person in the department. I would simply not have gotten through some new challenges I faced few months back if it was not for her. Yvette has been a friend as well as a mom figure to me here, she and her family have been godsend for me. I hope we stay friends forever! I would also like to thank former undergraduates Lucy Lu, Jennifer Liang and Emily Garhart, for letting me

be a mentor and role model to them in the past, as their nonstop support for me, their own success and personal growth have enriched my own experience.

Amongst GSFC folks, I am grateful to group co-lead, Dr. Giada Arney, for her kindness, patience, generally a high level of emotional intelligence that an impulsive person like me has found incredibly useful, and last but not least, scientific consultations. Dr. Ravi Kopparapu, my co-advisor and esteemed committee member, has also been incredibly patient with me, answering my questions, pointing me to resources for my papers and learning, and being incredibly prompt with comments related to my manuscripts. I often think about how I would not have any science without Ravi, who is known for his numerous habitable zones defining papers, seeing that all of my work since 2016 have been motivated by prior and current Kopparapu et al. work. I am incredibly grateful for the research paths I have had due to Ravi's science and always feel honored to be associated with him, especially at meetings.

I am also grateful to GSFC postdocs Der-You Kao and Sandra Bastelberger for lending me their virtual ear over Slack from time to time, and to Sherry Hawkins (IT admin), Jay Friedlander (poster printing guy) and Brittany Griffiths (fairly recently hired administrative superstar) for various kinds of auxiliary support in recent years. I would also like to thank the CRESST faculty, Ginny Peles, Prof. Prof. Lee Mundy, Dr. Tracy Huard, Dr. David Holdridge and Vivi Varada for managing my GSFC-UMD logistics. I would also like to thank some of my GSFC peers, especially Amber Britt (fellow astronomy student), Xandra Brosius and Elle Lavender (atmospheric science students), for their empowering friendship and perceptive insights, and for stimulating discussions as scientists. Seriously, I can go on...please find me in person!

I would also like to thank the incredibly wonderful administrative and business managing folks of our department. I have been known to be singing praises of them. I will be eternally grateful for the kindness, diligence and prompt and tireless support of Susan Lehr, Barbara Hansborough, Mary Ann Phillips, Eric McKenzie, Dorinda Kimbrell, Adrienne Newman (we miss you!), Alyssa Pagan and Olivia Dent. I am also grateful for various types of support over the years from Elizabeth Warner, Dr. Peter Teuben, Dr. Marc Pound and Dr. Mark Wolfire. You all are like family to me by now, I cannot imagine being in a department without you. On that note, I'd also like to thank my undergrad advisors, Prof. Darby Dyar (Mount Holyoke College) and Prof. Janice Hudgings (now at Pomona College), for continuing to "think the world of me" (their own words) post college years and for cheering me on from far.

I would like to thank Prof. Ricardo Arevalo Jr. of the Geology Department for agreeing to serve as the esteemed Dean's Representative in my committee. I also thank Professors Cole Miller and Andy Harris for their diligence and communication regarding department expectations. I would also like to give a big thank you to Professors Richard Mushotzky (second year department advisor) and Douglas Hamilton (also esteemed committee member), who have both been part of my UMD life since the beginning. Richard and Doug have always been there for me, shown concern for my well-being, help me brainstorm ideas to solve problems, and often even reached out from their end when they had not seen me in a while. Richard and Doug—I absolutely love any opportunity to talk to both of you. You have both been wonderful sounding boards. I am particularly thankful to Doug for being there for me in 2015, which was a very tough year for me professionally and personally.

I also feel incredibly blessed to have been part of this department while Prof. Eliza Kempton—another esteemed member of my dissertation committee—was hired. Seeing that we both do theoretical atmospheric modeling work, I have been fortunate enough to be able to learn and even use tools she developed, not to mention get her thoughts on my science and my papers. I am also grateful to Eliza for serving as a letter writer for my job applications, despite knowing me for such a short length of time, and for starting the weekly exoplanet meetings at our department!

It goes without saying that I would not have gotten to this stage if it was not for my department advisor and thesis Chair, Prof. Drake Deming. I think it is hard to find a senior scientist as accomplished as Drake who also has such a strong human side. I think the most an advisor can do for a student in a precarious stage is to not judge them, not be petty, be supportive and encouraging and Drake has the formula down pretty well, despite having spent most of his career years as a chief scientist at GSFC. Drake is incredibly kind, patient, encouraging, non-threatening and relentlessly optimistic towards his students, and he has extended those qualities to me, more so than ever when I needed the most support. Drake and Dr. Shawn Domagal-Goldman, my two advisors, mutually share the above qualities, which make both of them be the type to not give up on their students. Needless to say, I am grateful for these traits in them and aspire to be that way myself.

Speaking of Shawn, I do not know what I did to deserve the chance to work with him, all I can say is I got incredibly lucky to have such an incredible supervisor in my life. I was between projects when I reached out to Shawn end of 2015, and Shawn saw something in me and was kind enough to take me on as a student.

Shawn did not receive the best version of me, as I have not been the most cheerful person to work with, but somehow he always seems to know how to keep a positive climate. Shawn has gotten to see brutally honest sides of me most, and no other faculty-type knows about my inhibitions and struggles as much as Shawn does; I trust his judgement and discretion that much. I am thankful to Shawn for putting up with me, although for sure, I do not always show it. He had no obligation to help me get a PhD but yet he did. As Shawn's first graduate student, I can only hope I will make him very proud in the future and I hope to have the opportunity to do what he did for me for someone else. Such legacies are worth spreading.

Finally, I would like to thank the very special faculty who has been my one consistent advocate throughout the years. This would be Professor Stuart Vogel. I would not be here right now in any form or fashion without Stuart, who has stepped up for me on countless occasions by advocating for me, even after his role as Department Chair ended. I have no idea where I would be now without Stuart's uniquely powerful support and department initiatives. I only hope that I am worth it, and that I will have the opportunity to extend the same kindness and advocacy support to a future student. After all, I did decide to seek a PhD as I aspire to be a faculty at a small liberal arts school someday, similar to my beloved undergrad.

Sincerely,

Mahmuda Afrin Badhan

# Table of Contents

Preface	ii
Dedication	iv
Acknowledgements	v
Table of Contents	xi
List of Tables	xiii
List of Figures	xiv
List of Abbreviations	xvi
Chapter 1: Introduction	1
1.1 Exoplanets 101	1
1.2 The Transit Method for Exoplanet Atmosphere Characterization	4
1.3 Why We Study Tidally-Locked Jupiter-sized and Earth-like Planets	7
1.3.1 Hot Jupiters	8
1.3.2 Tidally-locked Earths	12
1.3.2.1 A Brief Overview of Global Circulation Model (GCM) Studies of Habitable Zone Exoplanets around M dwarfs	14
1.3.2.2 A Brief Overview of Biosignature False Positives and Negatives	17
1.4 Current Status and Outlook for Exoplanet Characterization: Summary of Expectations from Future Missions and Dissertation Deliverables	19
Chapter 2: 1-D Atmospheric Modeling: An Overview of Atmospheric Dynamics, Photochemical Models, Radiative Transfer and Retrievals	27
2.1 Atmospheric Dynamics and 1-D Photochemical Models	28
2.1.1 Atmos – Our Coupled 1-D Photochemical and Climate Model	31
2.1.2 The Numerical Recipe	35
2.1.2.1 The Equations for Modeling Chemical Evolution in an Atmosphere	35
2.1.2.2 Finite Differencing the Equations and Going from PDEs to ODEs	40
2.1.2.3 Boundary Conditions	41
2.1.2.4 The ODEs to Solve to Obtain Steady-state Mixing Ratios	43
2.1.2.5 Rainout, Lightning, Photolysis and Redox Balance	45
2.2 Spectral Models – Radiative Transfer and Retrieval Computation	48
2.2.1 Tools for Radiative Transfer and Retrieval Modeling	49
2.2.1.1 Exo-Transmit	49
2.2.1.2 SMART	50
2.2.1.3 NEMESIS	51
2.2.2 The Numerical Recipe for Retrieval Computations	54
2.2.3 The Forward Model	57
2.2.3.1 Spectroscopic Information Content	57
2.2.3.2 Analytical Thermal Structure (P-T profile) for Irradiated Planets	59

Chapter 3: Irradiated Gas Giants: Forward Modeling & Retrieval Efforts .....	62
3.1 Irradiated Exoplanet Retrieval Efforts with NEMESIS .....	62
3.2 Irradiated Exoplanet Photochemical Modeling: Hot Jupiters.....	72
3.2.1 Hot Jupiter Photochemical Modeling: Community Motivation.....	72
3.2.2 Hot Jupiter Photochemical Modeling with Atmos PHOTOCHEM.....	79
3.2.2.1 Preliminary Efforts: Validation with Published WASP12b Model...	80
3.2.2.2 Modifying WASP12b Template to HD189733b Template .....	81
Chapter 4: The Impact of Stellar UV Activity on Moist Habitable Terrestrial Planetary Atmospheres Around M dwarfs.....	83
4.1 Introduction.....	84
4.2 Methods.....	88
4.2.1 Planet Parameters: Moist Atmosphere Simulations.....	90
4.2.2 Stellar Parameters: Variable UV Activity.....	93
4.2.3 Photochemistry in the Atmosphere via Atmos.....	96
4.2.4 Radiative Transfer Spectra via Exo-Transmit.....	101
4.3 Results.....	103
4.3.1 Atmospheric Constituent Mixing Ratio Profiles.....	103
4.3.2 Transmission Spectra.....	106
4.4 Discussion.....	109
4.5 Conclusions.....	114
Chapter 5: Robust Quantification of Abiotic CH <sub>4</sub> and O <sub>3</sub> in Moist Habitable Anoxic Terrestrial Atmospheres Orbiting a 3300 K M Dwarf Host.....	117
5.1 Introduction.....	118
5.1.1 Future Biosignature Study with the Origin Space Telescope.....	119
5.1.2 This Study: Motivation and Structure .....	121
5.2 Methods.....	125
5.2.1 Summary of the Methods Section from Chapter 4.....	125
5.2.2 Varying the Methane Surface Boundary Condition flux(CH <sub>4</sub> ) .....	128
5.2.3 Lowering Instellation from 1.213So to 0.8, 1.029, 1.103 & 1.176So .....	130
5.3 Results.....	136
5.3.1 Case I: Instellation Unchanged, Methane Production Increased .....	136
5.3.2 Case II: Instellation Varied with updated H <sub>2</sub> O, Methane Also Varied .	148
5.3.2.1 Instellation Cases with S > So .....	149
5.3.2.2 Instellation Case with S < So .....	158
5.4 Discussion and Summary .....	161
Chapter 6: Outlook .....	167
6.1 Future Work: Mapping 3.3 μm non-LTE Emissions from Methane (CH <sub>4</sub> ) from Exoplanets for a Range of Temperatures and Host Stars.....	167
6.1.1 Spectral Modeling and Addition of non-LTE fluorescence effects .....	171
6.2 Dissertation Takeaway.....	175
Bibliography .....	177

## List of Tables

Table 1.1 <i>JWST</i> Instrument Details for Exoplanet Observations.....	19
Table 3.1 Line-list Sources for correlated $k$ -distribution tables in NEMESIS <sup>L</sup> .....	61
Table 4.1 1-D Model Parameters from GCM: Planet and Star Properties.....	80
Table 4.2 PHOTOCHEM Key Species with Lower Boundary Conditions.....	89
Table 5.1 Planet Parameters from GCM for the Four New Installations.....	124
Table 5.2 Species boundary conditions and $K_{zz}$ profiles in PHOTOCHEM <sup>FT</sup> .....	124
Table 5.3 Summary of Findings for O <sub>3</sub> and CH <sub>4</sub> Detectability at 5 ppm Level.....	154

<sup>L</sup>Figure/Table from other people's work AND I left graphics completely unmodified

<sup>LM</sup>Figure/Table from other people's work AND modified by me

<sup>FT</sup>This is a figure-table combo (indicated as I do not cross-list these in both lists)

## List of Figures

Figure 1.1 Transit Method Schematic <sup>LM</sup> .....	5
Figure 1.2 Protoplanetary Disk C/O Ratio around a Solar-type star <sup>L</sup> .....	9
Figure 1.3 Clouds Masking Spectral Features in Transmission <sup>LM</sup> .....	10
Figure 1.4 Cloud Schematic Based on Equilibrium Chemistry and Condensation <sup>L</sup> ...	11
Figure 1.5 TRAPPIST-1e As Seen by <i>Spitzer</i> <sup>L</sup> .....	12
Figure 1.6 GCM/3-D Climate Model Surface Properties of TRAPPIST 1-d,e,f <sup>L</sup> .....	15
Figure 1.7 False Positive Scenarios for Earth-Like Planets Around M dwarfs <sup>L</sup> .....	17
Figure 1.8 Future Mission Simulated Emission Spectra for TRAPPIST-1-e <sup>LM</sup> .....	21
Figure 2.1 Degeneracy in Retrieval Results Demonstrative Example: WASP12b <sup>LM</sup> ..	50
Figure 2.2 Example profiles using the Line et al. Semi-Analytic P-T Formula <sup>FT</sup> .....	58
Figure 3.1 Validation: HD189733b Real Data Retrievals with NEMESIS MCMC....	65
Figure 3.2 Validation: HD209458b Real Data Retrievals with NEMESIS MCMC....	66
Figure 3.3 HD189733b Simulated Data Retrievals with NEMESIS MCMC.....	67
Figure 3.4 HD189733b Real Data Retrievals with NEMESIS MCMC (2).....	67
Figure 3.5 WASP12b Atmos vs Kopparapu et al. (2012) WASP12b (Solar C/O)....	68
Figure 3.6 WASP12b template modified to Solar C/O HD189733b template.....	69
Figure 4.1 3-D to 1-D "pseudo" coupling + PHOTOCHEM inner workings.....	79
Figure 4.2 Spectral Data + Photolysis Cross-Section Curves of Key Species.....	84
Figure 4.3 Mixing Ratio Profiles of Key Species + Relative Humidity Profile.....	94
Figure 4.4 Transmission Spectra Results using Exo-Transmit.....	97
Figure 4.5 Spectral Comparison: Exo-Transmit vs SMART Results .....	101
Figure 5.1 Spectra from Figure 4.4 over Wavelength Range 8.5-10.5 $\mu\text{m}$ .....	112
Figure 5.2 Mean terminator profiles of $\text{H}_2\text{O}(P)$ and $T(P)$ from GCM.....	122
Figure 5.3 Spectral Contributions from $\text{CH}_4$ and $\text{O}_3$ : Medium UV 2 star.....	129-130
Figure 5.4 Spectral Contributions from $\text{CH}_4$ and $\text{O}_3$ : low UV/inactive star.....	131
Figure 5.5 Spectral Contributions from $\text{CH}_4$ and $\text{O}_3$ : Medium UV 1 star.....	132
Figure 5.6 Spectral Contributions from $\text{CH}_4$ and $\text{O}_3$ : High UV star.....	135
Figure 5.7 Spectral Contributions from $\text{CH}_4$ and $\text{O}_3$ : Very High UV 2 star.....	137
Figure 5.8 $\text{CH}_4$ and $\text{O}_3$ Spectral Contributions: All Stars, $S = 1600 \text{ W/m}^2$ .....	142
Figure 5.9 Mixing Ratio Profiles: All $flux(\text{CH}_4)$ , All Stars, $S = 1600 \text{ W/m}^2$ .....	143
Figure 5.10 $\text{CH}_4$ and $\text{O}_3$ Spectral Contributions: All Stars, $S = 1500 \text{ W/m}^2$ .....	144
Figure 5.11 Mixing Ratio Profiles: All $flux(\text{CH}_4)$ , All Stars, $S = 1500 \text{ W/m}^2$ .....	145

Figure 5.12 CH <sub>4</sub> and O <sub>3</sub> Spectral Contributions: All Stars, $S = 1400 \text{ W/m}^2$ .....	146
Figure 5.13 Mixing Ratio Profiles: All $flux(\text{CH}_4)$ , All Stars, $S = 1400 \text{ W/m}^2$ .....	147
Figure 5.14 CH <sub>4</sub> and O <sub>3</sub> Spectral Contributions: All Stars, $S = 1088 \text{ W/m}^2$ .....	150
Figure 5.15 Mixing Ratio Profiles: All $flux(\text{CH}_4)$ , All Stars, $S = 1088 \text{ W/m}^2$ .....	151
Figure 6.1 non-LTE processes and planet examples <sup>LM</sup> .....	158
Figure 6.2 Table + Flow Chart Showing the Tasks and Tools in Grand Scheme <sup>LM</sup> ..	161
Figure 6.3 Condensation Curves and Exoplanet Classification Bins <sup>LM</sup> .....	163
Figure 6.4 Methane non-LTE 3.3 micron emissions in GJ1214b <sup>L</sup> .....	164

<sup>L</sup>Figure/Table from other people's work AND I left graphics completely unmodified

<sup>LM</sup>Figure/Table from other people's work AND modified by me

<sup>FT</sup>This is a figure-table combo (indicated as I do not cross-list these in both lists)

## List of Abbreviations

### **Missions/Telescope (Arrays)/Surveys/Instruments/Techniques:**

CIRS	Composite Infrared Spectrometer (on <i>Cassini</i> )
<i>CoRoT</i>	Convection, Rotation and planetary Transits space observatory
VIMS	Visible and Infrared Mapping Spectrometer (on <i>Cassini</i> )
<i>HabEx</i>	Habitable Exoplanet Imaging Mission
<i>HST</i>	Hubble Space Telescope
WFC3	Wide Field Camera 3 (on <i>HST</i> )
NICMOS	Near Infrared Camera and Mult-Object Spectrometer (on <i>HST</i> )
<i>JWST</i>	James Webb Space Telescope
NIRISS	Near-Infrared Imager and Slitless Spectrograph (on <i>JWST</i> )
NIRSPEC	Near-Infrared Spectrograph (on <i>JWST</i> )
NIRCam	Near-Infrared Camera (on <i>JWST</i> )
MIRI	Mid-Infrared Instrument (on <i>JWST</i> )
<i>K2</i>	Kepler 2, Kepler's second mission phase
(K)ELT	(Kilodegree) Extremely Little Telescope
ELT	Extremely Large Telescope (note: the telescope class)
(E-)ELT	The Extremely Large Telescope (note: named telescope)
<i>LUVOIR</i>	Large Ultra-Violet/Optical/Infrared Surveyor
MUSCLES	Measurements of the UV Spectral Characteristics of Low-mass Exoplanetary Systems
<i>OST</i>	Origin Space Telescope
MISC	Mid-Infrared Imager, Spectrometer, Coronagraph (on <i>OST</i> )
<i>TESS</i>	Transiting Exoplanet Survey Satellite
<i>WASP</i>	Wide Angle Search for Planets (a series of survey telescopes...)
IRAC	The Infrared Array Camera (on <i>Spitzer Space Telescope</i> )
MIPS	The Multiband Imaging Photometer (on <i>Spitzer Space Telescope</i> )
VLT	Very Large Telescope
SPHERE	Spectro-Polarimetric High-contrast Exoplanet REsearch (on <i>VLT</i> )
RV/R-V	Radial Velocity
TMT	Thirty Meter Telescope
GMT	Giant Magellan Telescope

### **Institutions, organizations, journals, programs and other entities:**

AAS	American Astronomical Society
AGU	American Geophysical Union
ApJ	Astrophysical Journal
CRESST (II)	Center for Research & Exploration in Space Sciences & Technology (II)
DPS	Division of Planetary Sciences
ESO	European Southern Observatory
GSFC	Goddard Space Flight Center
JPL	Jet Propulsion Laboratory
NASA	National Aeronautics and Space Administration

NAI	NASA Astrobiology Institute
NCAR	National Center for Atmospheric Research
NexSS	Nexus for Exoplanet System Science
NIST	National Institute of Standards and Technology
NPP	NASA Postdoctoral Program
SEEC	Sellers Exoplanet Environments Collaboration
STScI	Space Telescope Science Institute
UMD/UMCP	University of Maryland, College Park
UW	University of Washington
VPL	Virtual Planetary Laboratory

**Spectroscopy, code databases and other science abbreviations:**

CAM(4/5)	Community Atmospheric Model (version 4/version 5)
IR	Infra-red
(I/O)WA	(Inner/Outer) Working Angle
LBL	Line-by-Line
(N/M/F)UV	(Near/Mid/Far) Ultra-violet
(N/M/F)IR	(Near/Mid/Far) Infra-red
VUV	Vacuum Ultra-violet
EUV/XUV	Extreme Ultraviolet
k-tables	opacity (“k”) distribution tables
KIDA	KInetic Database for Astrochemistry
GCM	Global Circulation Model
PRATE(S)	Photolysis Reaction Rate(s)
QY	Quantum Yield
RXN	Reaction
SED	Spectral Energy Distribution
XSEC	Cross-Section
SNR or S/N	Signal to Noise Ratio
TOA	top-of-atmosphere
LTE	Local thermal equilibrium
HC(AER)	Hydrocarbon (Aerosol)
pp(m/b)	Parts Per (Million/Billion)
PSG	Planetary Spectrum Generator
(I/O)HZ	(Inner/Outer) Habitable Zone
(S/L)L	(Short-/Long-)Lived
REDOX	Reduction & Oxidation
VMR	volume mixing ratio/mixing ratio
high- <i>T/P</i>	high-temperature/pressure
<i>T(P)</i> or <i>P-T</i>	Pressure-Temperature profile/Thermal Structure

**Symbols and Units:**

Ab	Bond Albedo
Ag	Geometric Albedo
$M_{\odot}$	Solar Mass
$M_{\oplus}$	Mass of Earth

$SZA/z$	Solar Zenith Angle
$L_{\odot}$	Solar Luminosity
$S_0$	Solar Constant
$T_{eff}$	Effective temperature
$T_{eq}$	Equilibrium temperature
$T_{surf}$	Surface temperature
$P_{surf}$	Surface Pressure
$\mu$	Mean Molecular Weight
$n$	number density
$R_{\oplus}$	Earth's radius
$M_p$	Planet mass
$R_p$	Planet radius
$M_j$	Jupiter mass
$R_j$	Jupiter radius
$M^*$	Stellar mass
$R^*$	Stellar radius
$R_{\odot}$	Solar radius
$Ly-\alpha$	Lyman- $\alpha$
$C$	Speed of light
$k_B$	Boltzmann's constant
$k_{zz}$	Eddy diffusion coefficient
$K_{eq}$	equilibrium rate constant
$H$	Planck's constant
$R_{GAS}$	Gas Constant
$flux$	Molecular flux of species in molecules/cm <sup>2</sup> /s or Teramoles/yr
$N_A$	Avogadro's Constant

### Chemical Species:

O	atomic/odd oxygen
O <sub>2</sub>	molecular oxygen
O <sub>3</sub>	ozone
OH	the hydroxyl radical
H <sub>2</sub> O	water
H	atomic hydrogen
H <sub>2</sub> O <sub>2</sub>	hydrogen peroxide
H <sub>2</sub>	molecular hydrogen
CH <sub>3</sub>	the methyl radical
CH <sub>4</sub>	methane
CHNO(S)	carbon, hydrogen, nitrogen, oxygen(, sulphur)
C <sub>2</sub> H <sub>4</sub>	ethylene
C <sub>2</sub> H <sub>6</sub>	ethane
CO	carbon monoxide
CO <sub>2</sub>	carbon dioxide
He	Helium
Ar	Argon
Na	sodium (alkali metal)

K	potassium (alkali metal)
TiO	titanium oxide
VO	vanadium oxide
H <sub>2</sub> CO	formaldehyde
H <sub>2</sub> S	hydrogen sulphide
HS	the hydrosulfide radical
S	atomic sulphur
SO	sulphur oxide
SO <sub>2</sub>	sulphur dioxide
H <sub>2</sub> SO <sub>4</sub>	sulphuric acid
S <sub>2</sub> , S <sub>3</sub> , S <sub>4</sub> , S <sub>8</sub>	disulphur, trisulphur, tetrasulphur, octasulphur molecules
SO <sub>3</sub>	sulphur trioxide
HNO <sub>3</sub>	nitric acid
N	atomic/odd nitrogen
NO <sub>(2)</sub>	nitrogen/nitric (di)oxide
N <sub>2</sub> O	nitrous oxide
NO <sub>3</sub>	nitrate ion
N <sub>2</sub>	molecular nitrogen

## Chapter 1: Introduction

### 1.1 Exoplanets 101

In the past 25 years, the space science community has managed to transcend barriers and develop new frontiers in the quest for finding new planets. We have gone from detecting the first extrasolar planet (exoplanet) to building tools and missions that will allow us to quantify the occurrence of potentially habitable planets, and even detect chemical signatures of a potential biosphere from them. The first ever exoplanet was detected around a neutron star, not a regular main sequence (hydrogen-burning) star like ours, in the early 90s, from timing of radio pulses (Wolszczan & Frail 1992; Wolszczan 1994). In 1995, the first exoplanet orbiting a Sun-like star, 51 Pegasi, was discovered using the radial velocity method (Mayor & Queloz 1995). The radial velocity method is the oldest and popular method by which planets around other Sun-like stars have been detected historically. Also known as the Doppler technique, this method involves tracking wobbles in the periodic Doppler shift in the spectral lines of a star as a planet and the host star orbit their mutual center of mass.

This radial velocity (RV) technique gives us a lower limit for the mass of the planet and orbital period. If the planet also intercepts the light from the star in our line of sight while orbiting, known as transiting, we can obtain an estimate of the radius and other orbital properties, by observing the light curve from the planet over several consecutive orbits and then averaging those light curves. We can also learn about the composition of the atmosphere from features revealed in its absorption, emission and reflection spectrum as the planet passes in front of the star (known as

a primary transit) and then disappears behind it (secondary eclipse). Inferring these properties from the light curve will only be possible if the spectrophotometric measurements are sufficiently precise and well-sampled in time.

This method, known as the transit method, which gives us the light curve of a planet as it transits the host, is the second most utilized method for exoplanet detection. It is also the primary method by which we have characterized exoplanet atmospheres to learn about their makeup and thermal structure. Both ground and space-based missions with spectrophotometric instruments are able to measure light curves. The first successful exoplanetary transit measurement was obtained almost exactly two decades ago, when transits were discovered in high-precision photometric light curves of the Sun-like star HD209458 (Charbonneau et al. 2000). Surface gravity, escape velocity and average bulk density of the planetary companion were inferred for the first time. This star was chosen for this pioneering transit follow-up study as radial velocity measurements in the mid-90s (Vogt et al. 1994 and Baranne et al. 1996) indicated the presence of a planetary mass companion in a close orbit.

The above study demonstrated the reliability of this technology in the detection and first order characterization of close-in giant planets. Exoplanet characterization has been enabled by observations made by the *Hubble Space Telescope (HST)* and the *Spitzer Space Telescope*. Discoveries of previously unknown transiting exoplanets have continued since, thanks to the now-retired *Kepler Space Telescope* (Borucki et al. 2009, 2011), as well as other ground and space-based searches. The *Kepler* mission, in particular, has revolutionized exoplanet science by observing over 530,000 stars with precision photometry and discovering close to 2700 planets over its nine+ year

lifetime that ended in October 2018. From the radius measurements obtained via transit discoveries by *Kepler*, known exoplanets had been divided into the following size bins as of May 2016 (by the *Kepler* team): Mars-sized ( $0.5\text{-}0.7 R_{\oplus}$ ), Earth-sized ( $0.7\text{-}1.2 R_{\oplus}$ ), super-Earth-sized ( $1.2\text{-}1.9 R_{\oplus}$ ), mini or sub-Neptune sized ( $1.9\text{-}3.1 R_{\oplus}$ ), Neptune-sized ( $3.1\text{-}5.1 R_{\oplus}$ ), sub-Jupiter-sized ( $5.1\text{-}8.3$ ), Jupiter-sized ( $8.3\text{-}13.7 R_{\oplus}$ ) and super-Jupiter-sized ( $13.7\text{-}22.0 R_{\oplus}$ ). Due to gravity arguments, planets above  $6 R_{\oplus}$  are generally categorized as gas giants. Super-Earths are planets larger than Earth but smaller than Neptune. They may or may not have an atmosphere. Super Earths and mini Neptunes have the largest occurrence rate amongst the detected population.

Chen & Kipping et al. (2016) proposed the following classification scheme instead based on mass-size relationship informed by data: Terran (rocky worlds like in our system with ocean and atmospheres possible, but with no  $\text{H}_2/\text{He}$  envelope,  $M_p = 0.5\text{-}2M_{\oplus}$  and  $R_p \sim M_p^{0.28}$ ), Neptunian (rocky interiors with volatile envelope, gas giants less dense than Jupiter,  $M_p = 2.1M_{\oplus}\text{-}0.4M_J$ ,  $R_p \sim M_p^{0.59}$ ), and Jovian worlds (large gas giants subjected to gravitational self-compression like Jupiter,  $M_p = 0.5M_J\text{-}0.08 M_{\odot}$  and  $R_p \sim M_p^{-0.04}$ ). While this classification system certainly makes exoplanets more akin to Earth and our neighbors, the categories are separated by the mass-radius relationship and spans a wider mass and radius range. Finally, terran or not, these planets tend to be incredibly close to their host—close enough to be tidally-locked—so their atmospheres can be fried. Future missions with coronagraphic and microlensing abilities will help us mitigate the close-in planet bias by enabling searches farther out<sup>1</sup> (e.g. Bennett 2008; Bennett & Gaudi 2007, Noecker et al. 2016; Lee et al. 2018).

---

<sup>1</sup>Relevant 2019 Sagan Workshop presentations can be found at <http://nexsci.caltech.edu/workshop/2019/agenda.shtml>.

The goal of my dissertation has been to develop and use atmospheric modeling tools and planet templates to predict spectral signatures from gas molecules found in such tidally-locked planets. This is enabled by exoplanet observations that provide us with spectrophotometric light curves of these planets. This allows us to build a foundation for reverse engineering future observations into constituent planet properties. Characterizing a diversity of planets is of utmost priority for the exoplanet science community, as this is the only way we can eventually stumble upon a habitable one in the absence of extraterrestrial communications. As such, future transit spectroscopy exclusively motivates this work and the rest of this chapter will be dedicated to talking about transiting planets we can characterize now and in coming decades.

## 1.2 The Transit Method for Exoplanet Atmosphere Characterization

A primary transit occurs when a planet passes in front of its host star in the observer's line of sight. The stellar light is blocked by the lower part of the atmosphere, where optical depth is large. Higher up, some of the light is reprocessed by the molecules in the atmosphere, and transmits through the planet's limb to the observer. This causes a dip in the stellar light with an amplitude that is proportional to the square of the ratio of the radius of the planet to the radius of the star at that wavelength. So, we obtain wavelength-dependent radius of the planet, as the planet appears to have slightly different sizes at different wavelengths, depending on whether any constituent is absorbing at that wavelength or not and how much. The greater the absorption by molecules, the less transmitted, and thus the bigger the planet appears. Since reprocessed stellar light reveals the identity of those molecules and the planet's

size, we can also get an idea of the compositions possible in the sampled atmosphere as well as densities and planet type. This method can even detect trace species present, but is not particularly sensitive to the thermal gradient, and thus only the approximate local temperature needs to be known.

A secondary eclipse occurs when a planet passes behind the host star. We can obtain the reflection (visible wavelengths) and emission spectra (in IR) of the planet this way. Thermal IR emission from the side facing the host star (dayside) decreases temporarily while the planet is blocked by the star. The dip in the IR emission intensity at a given wavelength is proportional to the planet-to-star integrated flux contrast at that wavelength, and can be attributed to be coming from the planet. Thermal emission data is sensitive to the temperature gradient of the sampled pressure range.

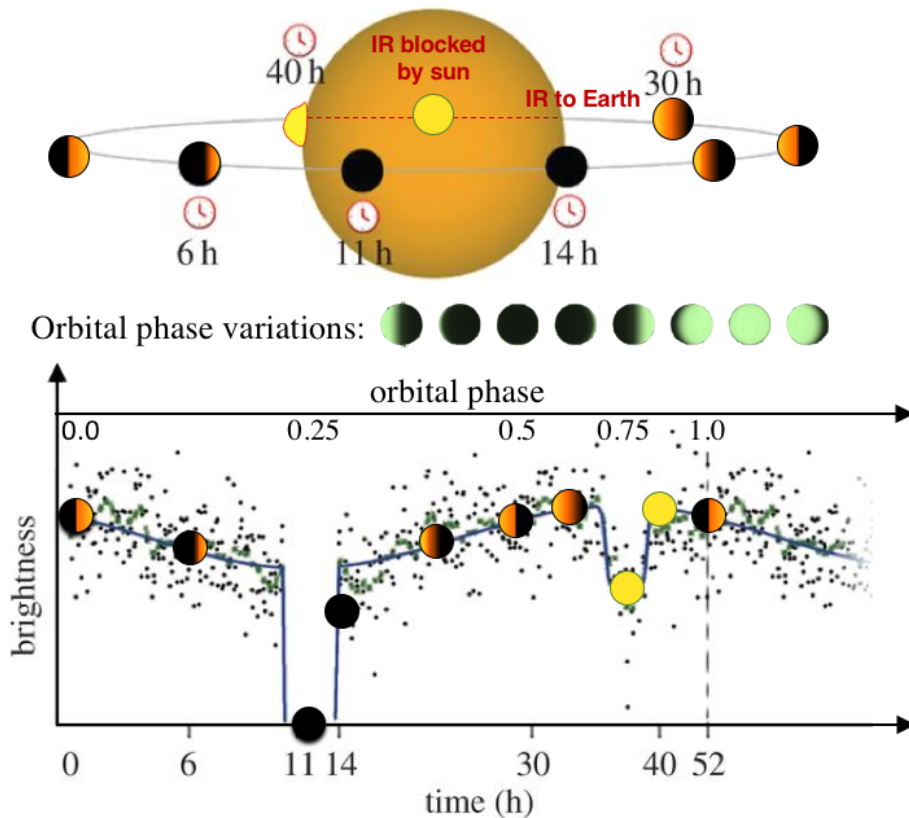


**Figure 1.1:** A schematic representation of the transit method for a planet with an orbital period of 52-hr, with items relevant to phase geometry overlaid on a background showing attributes of the transit method. (Said background is Figure 5 from Tinetti et al. 2012.) This figure assumes both the primary transit (the big dip) and secondary eclipse (the shallow dip) happen in our line of sight. Relation between time lapsed and orbital phase is shown via the two x-scales.

While reflection spectra peaks in the visible, the planet's thermal emission peaks in the IR. The contrast between the blackbody emission from the planet versus the star is also higher in IR. *Kepler* relied on the former attribute, while *Spitzer* relies on the latter for measuring the thermal emission at secondary eclipse from planets with large enough contrast. Since mid-infrared (MIR) measures the amount of heat, this method allows us to constrain the thermal structure of the sampled portion of the atmosphere, and is another way to quantify the most abundant species in the dayside of the atmosphere. For the high planet-to-star contrast cases for which we can track multiple consecutive orbits, we can also track the orbital phase variations in reflected light and thermal emission. The cyclic variations in the brightness during ingress and egress of the planet (in the course of a planet's orbit) shed light on properties that vary due to rotation such as inclination, eccentricity and 3-D variations in atmospheric properties (more in Section 1.3.2.1).

It should be noted that presently, the degeneracies in planetary properties inferred from transit light curve measurements this way can be significant<sup>2</sup>. This has stunted our ability to make definite conclusions regarding the planets. This limitation

---

<sup>2</sup> Degeneracy amongst the parameters means different combination of the parameters can give the same spectrum (see Ch. 2).

comes from both the quality of the presently available data from space instruments, and high particulates that prevent light from reaching the lower altitudes that would otherwise contribute the most to the reprocessing of stellar light, topics I will address further later on in this chapter, and also in the descriptions about the motivations for atmospheric retrievals in Chapter 2 and 3. This necessitates the need for the conception, development and successful deployment of both ground-based and space-borne future instruments with higher sensitivity to the atmosphere's structure and composition, multi-wavelength coverage to allow us to obtain molecular transition features from the same species at different wavelengths, and superior spectral resolution.

### 1.3 Why We Study Tidally-Locked Jupiter-sized and Earth-like Planets

Both the radial velocity and transit methods favor detection of planets that are massive with large atmospheres, and extremely close to their host stars, close enough to be tidally-locked. The geometric probability of transit is much higher for close-in planets. The idea behind maximizing transit signal is to maximize the contrast between the planet and star radii and their respective thermal IR radiation levels. For a given planet, both ratios would be higher if the stellar host is a smaller and less massive star; a planet orbiting an M star is more favorable for characterization than one around a G star like our sun. Accordingly, the first exoplanets we found were nothing like anything we see in our own Solar System. Such exotic planets continue to dominate our detections with present technology, allowing us to build and robustly test the theoretical models for characterizing these planets.

51 Pegasi b is a Jupiter-sized planet but has an orbital period of only few days, placing it a fraction of the Mercury-sun distance. As I mentioned earlier, planets so close to their host stars are tidally-locked. This particular class of planets are known as hot Jupiters. They were the first to be detected via both methods. While they are far from habitable, attributes such as proximity to the host star, their existence being unique to extrasolar systems, and their over-representation in data due to observational bias have made them compelling targets for characterization studies.

### 1.3.1 Hot Jupiters

Hot Jupiters are the most readily detected exoplanet class by present technology, due to proximity to their host stars ( $a \ll 1$  AU) and Jupiter-scale sizes. These tidally-locked planets are fascinating: they have scorching temperatures, resemble stellar atmospheres rather than planetary ones, have no clear analog within our Solar System, and should not have formed where we find them (but see Batygin et al. [2015](#)). While we believe they likely formed further out and migrated in that close (Lin et al. [1996](#) and references therein), there is still no consensus on what could have driven this dramatic move (for a recent review, see Dawson et al. [2018](#)).

Hot Jupiters hold keys to advancing our understanding of formation history and subsequent evolution of planetary systems. Determining the elemental composition in the envelopes of gas giants is crucial for this. It is easier to unveil the elemental composition of these close-in giant planets than our gas giants. In our solar system giants, where the temperatures are very low, low altitude condensation cold traps

remove carriers of some of the most important elements (e.g. oxygen), from the regions our space probes can observe. There are more kinds of clouds due to the cold temperatures. This makes the accurate determination of elemental composition difficult, leaving an accounting of their net bulk composition incomplete. The high temperatures do not allow for such cold traps to form in hot Jupiters, so we have a “cleaner window” into their bulk composition.

Chemical disequilibrium processes (e.g. eddy mixing, photochemistry, zonal winds, etc.) can be diagnosed in planetary atmospheres by studying the observed trends in the abundances of detected species (Line & Yung 2013). At the deepest levels of the atmosphere, where pressures and temperatures are high, reaction time-scales are short. So, constituents tend to stay at equilibrium. Pressure and temperature decrease with increasing height in planets without thermal inversion (i.e. no stratosphere), slowing the reaction rates to a point where vertical transport starts dominating, causing species to be quenched. Vertical mixing increases here, meaning the lower unobserved regions can communicate with the upper regions probed by our IR instruments. In the uppermost regions, UV insolation levels increase, disassociating certain species. Since the high temperatures ensure thermochemical equilibrium in the lower altitudes here, planets with equilibrium temperatures below 1200K have been noted to have the obvious signs of disequilibrium (Liang et al. 2003, 2004; Zahnle et al. 2009a, 2009b; Line et al. 2010, 2011, 2013; Moses et al. 2011, 2013; Visscher & Moses 2011; Kopparapu et al. 2012; Venot et al. 2012). In hot Jupiters, we are able to infer the presence of such processes via photochemical modeling.

In irradiated planets, disequilibrium mechanisms prevail in the upper atmosphere (Parmentier et al. 2015b; Morley et al. 2016, Madhusudhan 2016), playing a noticeable role in depleting certain constituents while enhancing others. In addition, clouds and hazes appear to dominate both transmission and reflection spectra of such planets over a range of equilibrium temperatures and planetary sizes. Their presence can significantly alter both the thermal structure and composition in the higher altitudes, masking spectral features by obscuring the upper atmosphere (see Figure 1.2).

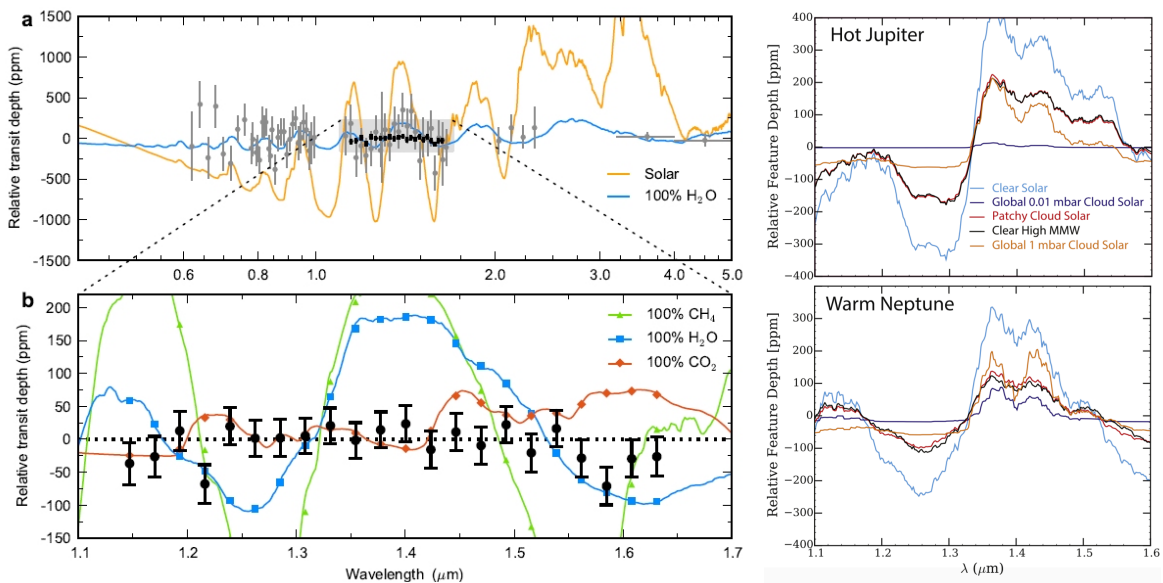


**Figure 1.2:** *Left panel:* Kreidberg et al. 2014 results from the 60-orbit *HST*/WFC3 primary transit campaign of GJ 1214b. High altitude clouds appear to be masking spectral features in the wavelength range shown. *Right panel:* Impact of non-uniform cloud cover on transmission from a typical representative hot Jupiter and a warm-Neptune (Line & Parmentier 2016).

The species and processes responsible for such high-altitude effects vary by planet type, as well as the atmosphere's [C]/[O] ratio (e.g. in Kopparapu et al. 2012). The

[C]/O] ratio of a planet is a key diagnostic parameter for core-accretion. It tells us where the planet should have formed within its proto-planetary disk (e.g. Atreya et al. 2016). Planets that have more carbon relative to oxygen may have formed beyond the snow line (see Figure 1.3), and thus would exhibit shortage of oxygen bearing species. Recent work (e.g. Madhusudhan 2014; 2016) suggest that the chemical depletions observed in hot Jupiter atmospheres could help us constrain their migration mechanisms, with low O abundances indicating disk-free migration mechanisms.

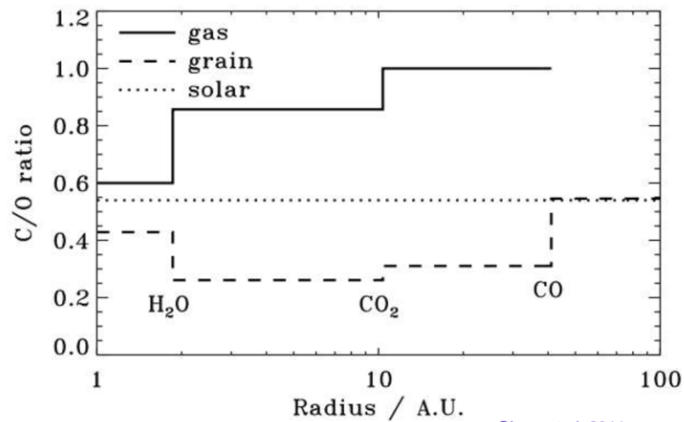
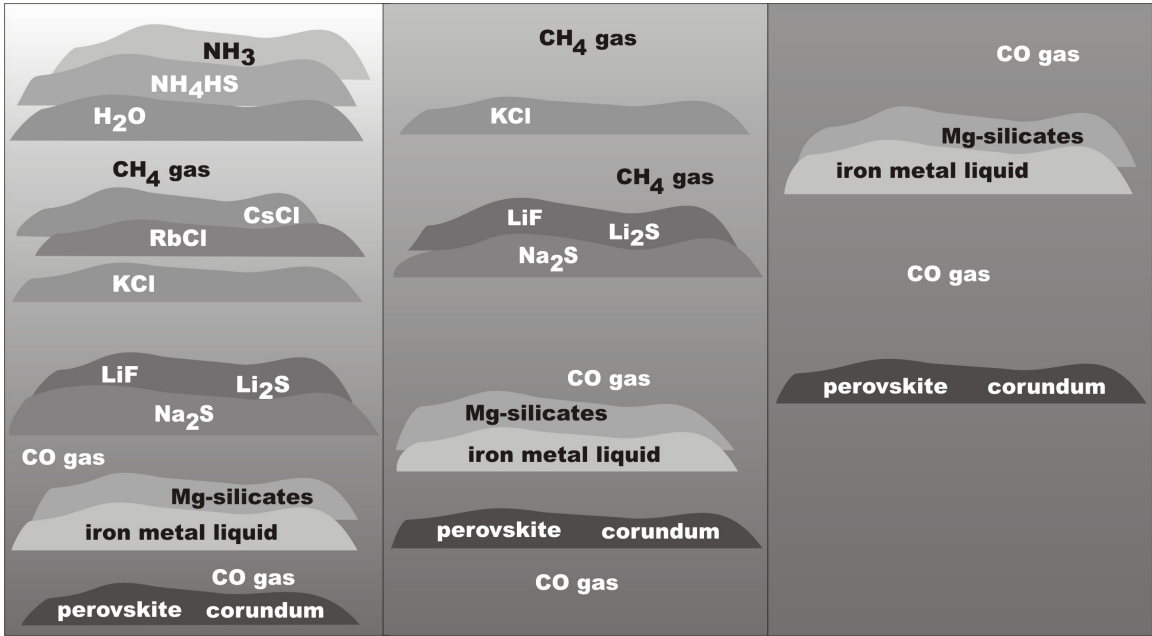


**Figure 1.3:** The C/O ratio in gas and grains in a typical proto-planetary disk around a solar-type star. The CO<sub>2</sub>, H<sub>2</sub>O and CO snow lines are marked for reference (Oberg et al. 2011).

**Figure 1.4:** From Marley et al. 2013 (modified originally from Lodders 2003), a schematic illustration of cloud layers based on equilibrium chemistry and precipitation considerations. From left to right, the panels correspond to T<sub>surf</sub> of ~120 K (Jupiter-like), ~600 K (a bit hotter than Venus) and 1300K (cooler hot Jupiters). Refractory clouds are more likely closer to the surface as temperature falls, volatiles move progressively to the top. Only metal clouds can form on really hot planets.



We must model the impact of metallicity variations to composition on hot Jupiter observations. To be able to map the depletion patterns carefully, we also want to know the effect of high-altitude aerosols on the observed spectral features. High-temperature exoclouds continue to remain a modeling challenge, as their makeup and distributions are a mystery. Past and ongoing efforts by various research groups have helped us identify some of the possible species (e.g. see Figure 1.4 appearing on the preceding page). However, continued progress in this area is highly anticipated by the community in advance of next generation missions.

### 1.3.2 Tidally-locked Earths

The only temperate planets (i.e. residing within the habitable zone of host star) we have any hope of characterizing in the near future are ones orbiting the

smallest and least massive stars, namely M dwarfs. We have already found such planets with current technology such as LHS 1140b (Dittman et al. 2017) and the TRAPPIST-1 system (Gillon et al. 2017, see Figure 1.5) with its seven resident planets. The Earth-like planet discovered to date nearest to us also orbits an M star, Proxima Centauri (Anglada-Escude et al 2016). Besides M stars being the most abundant and longest living stars in our universe, both planet-to-star contrast and size ratios are maximized for detections around them, resulting in easier and more frequent detections (Figure 1.8). In the last section, I will cover planned future characterization efforts.

Short orbital periods are observationally advantageous due to allowing for more full transits over a fixed amount of time. The smaller the scale height of the planet, the smaller the signals would be, so the greater the number of orbits we want

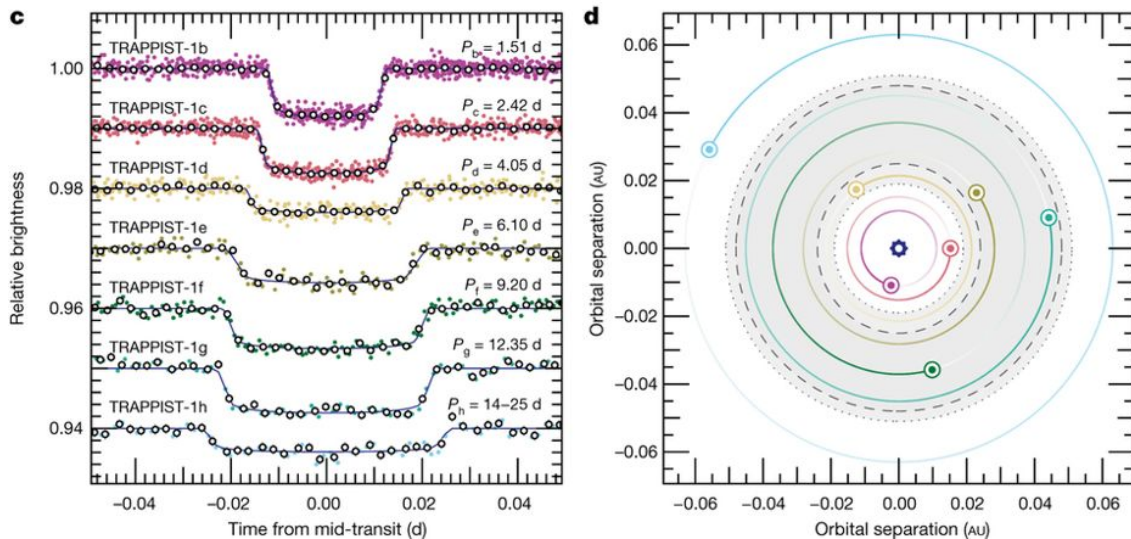


**Figure 1.5:** *Left:* The TRAPPIST-1 system with its seven temperate rocky planets (from TRAPPIST-1b through TRAPPIST-1e as seen by *Spitzer* (observed September – October 2016). These are photometric measurements that were stacked together to increase signal to noise ratio. Best fit light curve is overplotted. *Right:* The seven orbits with same color code as left panel. The grey zone marks the habitable zone (zone over which liquid ocean can exist).

to be averaging to maximize the signal-to-noise ratio. M dwarf habitable zones are close enough to the central host star that they overlap with the tidally-locked orbital distance region. Feasibility studies regarding the habitability of these planets have been conducted with 1-D models recently by collaborators (Barnes et al. 2015 and references therein, 2016; Tilley et al. 2017, 2019; Lincowski et al. 2018, 2019; Lustig-Yaeger et al. 2019; Meadows et al. 2018), with varying assumptions for composition. While 1-D models are good enough to tell us the distances over which liquid water may be maintained given a certain composition, the compositions need to be informed by 3-D models. Climate systems are inherently 3-D and affect the composition in surprising ways that are not always intuitive (see Section 1.3.2.1). My investigations of such planets are laid out over Chapters 4 and 5. These studies were enabled by the recent influx of theoretical work on these planets via 3-D climate models (Figure 1.6).

### 1.3.2.1 A Brief Overview of Global Circulation Model (GCM) Studies of Habitable Zone Exoplanets around M dwarfs

3-D general circulation models (GCMs) capture the climates in the planets and signals that vary spatially and temporally. The climate is a function of many factors including incoming light, rotation rates, primary composition of the atmosphere, volatile inventory, surface properties and the presence of aerosols. 3-D climate modeling of habitable zone planets around M dwarfs has become a popular means of studying these planets over the present decade (please refer to Introduction section of Chapter 4 for relevant citations), engaging the earth science community in extrasolar science.

Besides allowing for measurements of latitudinal and longitudinal variation in

temperature and major species compositions, 3-D modeling also informs our understanding of vertical mixing in the atmospheres via modulation of zonal winds and how that varies with the orbital properties. It was necessary to use 3-D model outputs for the studies in Chapters 4 and 5 as 3-D modeling treats the water reservoir in these planets more accurately, by modeling the water in all three phases globally. The phases of water do play a huge role in temperature regulation (thus habitability); sea-ice phase will be more reflective of sunlight, and act as a greenhouse gas in vapor phase by modulating the humidity.

The phases could regulate temperature in ways unfamiliar to us due to widely differing orbital-rotational factors on these M dwarf HZ planets. Cloud fraction and coverage can also only be properly captured through 3-D modeling. Since Earth-like planets orbiting low mass stellar hosts are tidally-locked into slow-synchronous rotation speeds (orbital-rotational period longer than 5 Earth-days), the Coriolis force – which increases with rotation and size of rotating body – is weak in these planets like it is on Venus. This plays a major role in atmospheric circulation (Joshi 2003; Merlis & Schneider 2011). Large differences in atmospheric circulation and the permanent nature of the sun-facing side together create scenarios not found on earth, such as enhanced mixing both laterally and vertically driven by a single large circulation pattern spanning from the day to the nightside. The increased convection also causes increased cloud coverage on the permanent dayside (Yang et al. 2013), causing the albedo to spike cooling the planet despite the permanent Sun-facing geometry.

This effect goes away for terrestrial rotators far enough out to have periods above 5 days, e.g. TRAPPIST-1e. This shows that inner habitable zone planets are the

most promising candidates for finding water, even from the perspective of atmospheric dynamics, and not just more amendable to better quality measurements. Chen et al. (2018) have found that day/night chemical gradients would be driven on these kinds of planets with assumed like  $N_2$ - $O_2$  compositions. Recent studies have shown

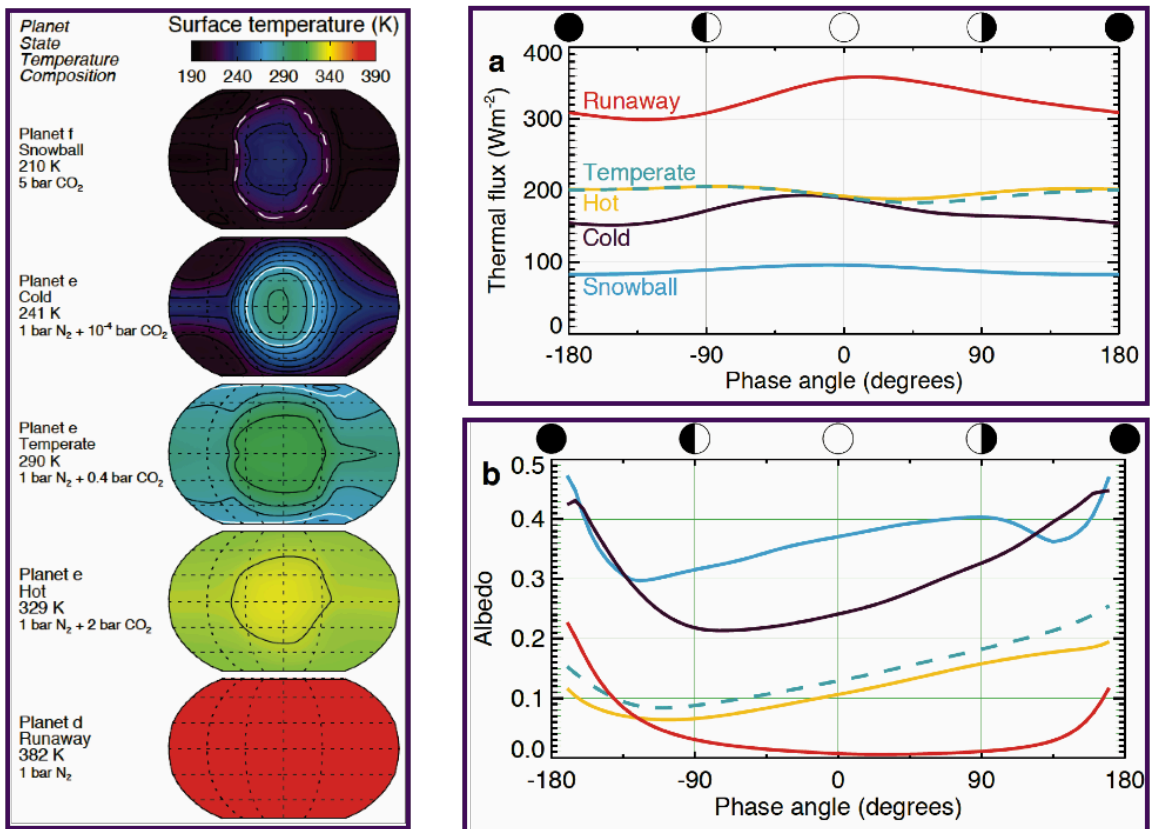


**Figure 1.6:** (From Wolf 2017) *Left:* 3-D maps of surface temperatures of TRAPPIST-1 d, e, and f (which cover the inner and outer habitable zone according to Figure 1.5) revealed by GCM studies. *Right:* The MIR thermal phase-curve observations that were used towards the GCM findings. Going from top to bottom, these show climate states designated as runaway greenhouse (i.e inner edge of habitable zone) → temperature (suitable) → hot → cold to snowball Earth across the phases. Albedo can be computed and increases till glaciation. These atmospheres would have high albedo due to thick persistent cloud decks.

that both emission and reflection spectra vary widely with land/water fraction and phase (Yang et al. 2014; Haqq-Misra et al. 2018), and factoring ocean heat dynamics may be important (Hu & Yang, 2014; Del Genio et al. 2019; Way et al. 2018; Yang et al. 2019). The 1-D study I detail in Chapter 4 pursues an important consequence of the increased circulation that is favorable to habitability—the enhanced water vapor content that results in the GCM computations over measurable altitudes (Kopparapu et al. 2017; Fujii et al. 2017).

### 1.3.2.2 A Brief Overview of Biosignature False Positives and Negatives

The tidally-locked M dwarf planets discussed above can have varying compositions from planet to planet just like any other planet. They can be N<sub>2</sub> dominated, they can be CO<sub>2</sub> dominated, or they can have large quantities of both gases. A false positive scenario for a biosignature happens when gases that are typically over-produced on Earth due to biological sources is seen to be present at large quantities with solely abiotic origin in those planets. A false negative scenario is where some abiotic process within the planet depletes species that may otherwise be produced in large quantities via biological means. If we were to look at Earth as an exoplanet from another system, we would find both scenarios as we have a plethora of both biological sources, sinks and geochemical sources and sinks for at least the C-based species.

Figure 1.7 from Meadows (2017) is a now a widely-circulated figure showing the different false positive scenarios that may arise for each shown case of atmospheric makeup. For each of the five cases, the kind of short-wavelength spectra/wavelength combo needed to help us check for the presence or absence of the indicated

species are provided. (Long wavelength advantage is discussed in the last section.)

On the left we have a photosynthetic biosphere just like Earth. Here, simultaneous presence of  $O_2 + O_3 + CH_4$  and absence of  $CO$  indicates a biotic origin. The other four cases are false positive scenarios, where the presence of circled species along with the absence of cross-circled species together indicates a false positive detection scenario. This discussion will be relevant to Chapter 5.

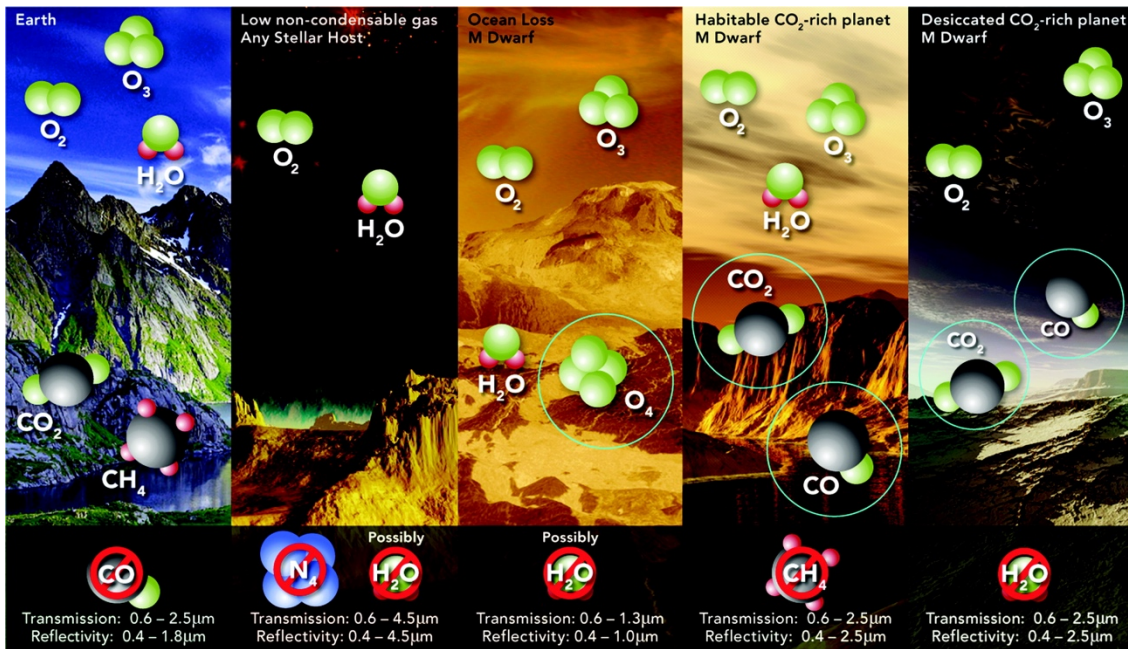


**Figure 1.7:** From Meadows, 2017 (Credits: Hasler, Meadows, Domagal-Goldman): False positives for the different environments predicted for Earth-like planets orbiting M dwarf hosts.

## 1.4 Current Status and Outlook for Exoplanet Characterization: Summary of Expectations from Future Missions and Dissertation Deliverables

To find the composition and temperature of a planet, we must "retrieve" the abundances of the responsible molecular species from observed spectroscopic signatures in their transmission (from primary transit) and also reflection and emission spectra (from secondary eclipse), the reverse engineering process I mentioned earlier. Our community approaches this task via programs combining a radiative transfer "forward" model for the theoretical spectra, with Bayesian numerical convergence schemes, to retrieve the input parameters from the observed spectra (more on this in Chapter 2). The parameters are updated simultaneously via sequential iterations, until reasonable agreement between modeled and observed spectra is achieved. The variable (retrievable) parameters are those that can be constrained from light curves and spectra, i.e. properties such as abundances of atmospheric gases and aerosols, thermal structure, planetary radii, surface gravity, density, orbital properties.

Determining the atmospheric constituents requires high-precision spectrophotometric measurements and robust models to match the data that only depend minimally on prior assumptions but are instead informed by the data. NASA's future astrophysics missions will meet the former requirement. This will begin with the *James Webb Space Telescope (JWST)*, which should launch soon. Space missions currently in concept study phases for the 2030s will help us reach much farther: these missions include the *Origin Space Telescope (OST)*, the *Large UV/Optical/IR Surveyor (LUVOIR)*, and the *Habitable Exoplanet Imaging Mission (HabEX)*.

These three missions are being reviewed as part of the Astro2010 Decadal Survey and all three of them have direct imaging capabilities via coronagraphy. However, we should already be obtaining better exoplanet data within the next few years due to *JWST*; we do not need to wait decade(s). With *JWST*, high-fidelity spectroscopy of samples of exoplanets will become a possibility for the first time; *JWST*'s highest resolving modes even have the potential to detect relatively trace gases (see Table 1.1).

<i>JWST</i> instrument specifications for transit/eclipse spectroscopy of exoplanets				
Instrument	Spectroscopic mode(s) and mode details	Resolving power	$\lambda$ range ( $\mu\text{m}$ )	Major molecules present in band
<b>NIRISS</b>	Grism, cross-dispersed, slit-less	700	0.6 - 2.5	H <sub>2</sub> O, CO <sub>2</sub> , CO, CH <sub>4</sub>
<b>NIRSpec</b>	Prism, wide slit (1.6")	100	0.6 - 5.0	CH <sub>4</sub> , H <sub>2</sub> O, HDO
	Grating, wide slit (1.6")	~500-1300 or ~1500-3500 ~700-1300 or ~2000-3500	0.6 - 1.8 (above) 1.7 - 3.0 2.9 - 5.0	O <sub>2</sub> , O <sub>3</sub> , H <sub>2</sub> O, CO <sub>2</sub>  H <sub>2</sub> O, NH <sub>3</sub> , HCN, C <sub>2</sub> H <sub>2</sub> HDO, CH <sub>4</sub> , NH <sub>3</sub> , PH <sub>3</sub> , CO, CO <sub>2</sub> , HCN, C <sub>2</sub> H <sub>2</sub> , C <sub>2</sub> H <sub>6</sub> , CH <sub>3</sub> D
<b>NIRCam</b>	Grism, slit-less	1700	2.4 - 5.0	H <sub>2</sub> O, HDO, CH <sub>4</sub> , PH <sub>3</sub> , CO, CO <sub>2</sub> , HCN
<b>MIRI</b>	Prism, 0.6" slit or slit-less	100	5.0-10.0	H <sub>2</sub> O, HDO, NH <sub>3</sub> , PH <sub>3</sub>
	IFU (0.2" - 0.27"/pixel), MRS	2400 - 3600	5.0-7.7 7.7-11.9 (above) 11.9-18.3 (above) 18.3-28.3	H <sub>2</sub> O, HDO, CH <sub>4</sub> H <sub>2</sub> O, CH <sub>4</sub> , CH <sub>3</sub> D, NH <sub>3</sub> , PH <sub>3</sub> , O <sub>3</sub> CO <sub>2</sub> , H <sub>2</sub> O, NH <sub>3</sub> , HCN, C <sub>2</sub> H <sub>2</sub> , C <sub>2</sub> H <sub>6</sub> H <sub>2</sub> O

**Table 1.1:** The four *JWST* spectroscopy instruments, their wavelength coverage for each observation mode, and the resolving power  $R$  achieved in those modes. Rightmost column shows molecular bands (from Tinetti et al. 2013) we can expect to resolve in each mode.

There is a key difference between atmospheric characterization efforts enabled by *JWST* versus the future coronagraphic missions; *JWST* will primarily observe transiting planets, including rocky planets orbiting M stars, whereas the coronagraphic missions are targeting Earth-analog planets orbiting F/G/K stars. If selected

and successfully launched, *LUVOIR* (*LUVOIR* team interim report, 2018) and *HabEX* (interim report: Gaudi et al. 2018) will extend *JWST*'s efforts with shorter wavelength coverage and direct imaging capabilities, while *OST* will complement their efforts towards unraveling the existence of other potential biospheres via long-wavelength IR observations. The short wavelength range accessed by *LUVOIR* is important for constraining mass losses from the upper atmosphere of planets as well as aerosol scattering. Most importantly, these complementary bandpasses will provide access to measurements of non-overlapping transitions from the biosignature combination of molecular oxygen ( $O_2$ ), ozone ( $O_3$ ) and methane ( $CH_4$ ).

*OST*'s role in the exoplanet hunt will be to characterize potentially habitable planets for the presence of these trace biosignatures, enabled by its novel transit spectro-meter (known as MISC—more info in Chapter 5), state of the art cooling (down to 4K) technologies (Matsuo et al. 2016) and wide 5-26  $\mu\text{m}$  thermal IR coverage (hence the cooling needs). *OST* is particularly relevant to my dissertation work as it motivates the work of Chapter 5. *OST* should also be informative to the work in Chapter 4; the spectral resolution of MISC at long wavelengths (and concurrent ground-based monitoring) may help mitigate any impact from inhomogeneous stellar photospheres on observations of  $H_2O$  features in transmission spectroscopy (Rackham et al. 2018). Further, the long IR wavelengths may see through the clouds, depending on particle sizes, and help constrain clouds as a result. Since the planet-to-star fluxes would be the most favorable over the *OST* bandpass for Earth-like planets transiting low mass host stars (see top panel of Figure 1.8 below), *OST* should also help us constrain the thermal structure.

Planet selection criteria for *JWST*, *OST* and related future missions will be largely informed by missions and surveys preceding them. A variety of techniques have already discovered Earth-sized ( $R_p < 1.5 R_\oplus$ ) planets, e.g. follow-up of known RV planets via the M<sub>Earth</sub> and TRAPPIST ground-based telescopic surveys. The *Transiting Exoplanet Satellite Survey (TESS)* launched by NASA last year, for example, will keep finding small cool planets around early-to-mid (i.e. warmer/larger) M stars—following *Kepler*'s legacy—for future missions to characterize. Late-type M stars – as in the coolest and smallest main sequence stars, will be targets of SPECULOOS (Search for habitable Planets Eclipsing ULtra-cOOl Stars), an ESO project that will look for planets transiting cool stars per namesake. Still, *OST* may need a larger aperture to achieve clear transformative advance(s) over *JWST* for habitable planet studies. The exact performance of *JWST* will, of-course depend on the time-series systematics, which can only be ascertained once the mission has launched and is fully operational.

Follow-up characterization efforts will need to harness the power of upcoming Extremely Large Telescopes (ELTs). An ELT<sup>3</sup> is a class of ground-based telescope employing segmented mirrors. ELTs have extremely large primary mirror apertures, ranging in size from 20 meters to 100 meters across (Snellen et al. 2010, 2013), giving them the largest collection area amongst all classes of telescope built to date and thus maximum sensitivity (as exposure time required to achieve a given a given signal-to-noise ratio, S/N, goes as the fourth power of the diameter). ELTs are located in various places around the world, have wavelength coverage spanning radio to UVOIR (ultra-

---

<sup>3</sup>Note: The European Extremely Large Telescope is also abbreviated as “ELT” (sometimes “E-ELT”).

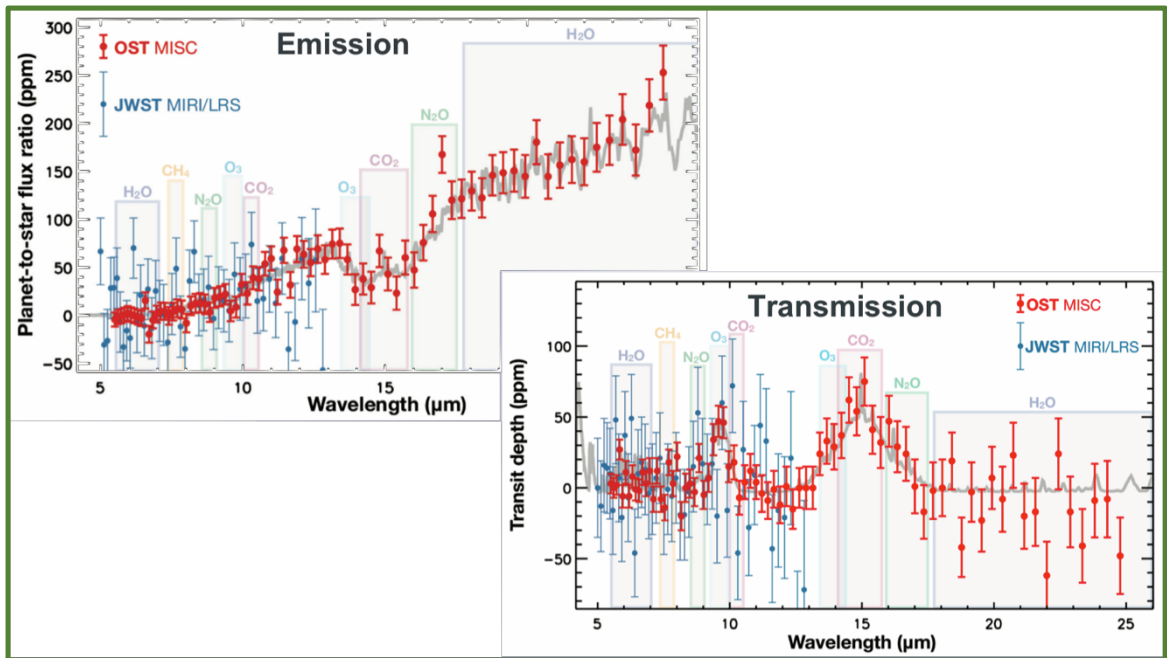
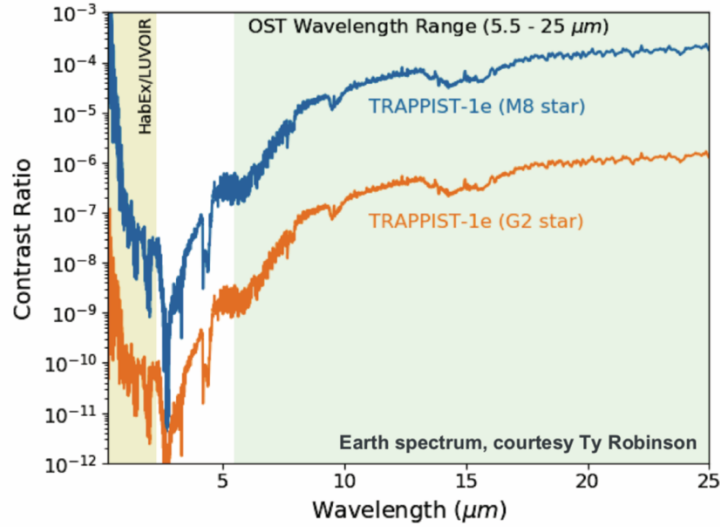


**Figure 1.8:** *Top panel:* Courtesy of Tyler Robinson (NAU), simulated emission spectrum for the Trappist-1e orbiting an M8 star (blue) is compared with the planet’s contrast when orbiting a G2 star like our Sun instead (orange). Contrast is also shown for *HabEx* and *LUVOIR* wavelengths for comparison. Note: The bandpass gap in between would be covered by *JWST*’s *NIRISS* and *NIRSPEC* instruments as noted in Table 1.1. *Bottom panel:* Models of TRAPPIST-1e-like emission/transmission spectra with uncertainties simulated (for 30 orbits) for OST MISC and *JWST*/MIRI in LRS mode (which does not extend till the full bandpass). Note this assumes the same noise floor for MIRI as is predicted for *NIRISS* and *NIRSPEC* (30 ppm), which is highly optimistic for MIRI and less than quoted in literature (50 ppm, Green et al. 2016, also see Chapter 4). Still, it is clear that the MISC uncertainties are much lower over the bandpass it has in common with MIRI.

violet, optical and infra-red), and benefit a wide range of astronomical science requiring data resolutions higher than achievable by space-based observations (Hippler 2019). Several future ELTs are being planned and built right now by various international consortiums. Instruments include spectrographs for transit and RV measurements, imagers for photometric characterization as well as coronagraphs for high contrast direct imaging (e.g. Soummer et al. 2009, Mello et al. 2018). Upcoming ELTs will benefit exoplanet science goals of the next two decades (GMT<sup>4</sup>: Szentgyorgyi et al. 2012, ELT<sup>3</sup>: Udry et al. 2014, TMT<sup>4</sup>: Crampton et al. 2008) by increasing our chances of finding an Earth-like habitable planet around other stars (e.g. Parmentier 2014, Rodler et al. 2014 and references therein).

While this is all great, the community still needs robust and detailed models to simulate spectra for different atmospheric states. A thorough exploration of the parameter space is really important for exoplanet scenarios, where different sets of properties can result in the same spectrum—the case of degenerate retrieval solutions I mention earlier. We also need to understand how much detail at the chemistry level retrieval codes can handle for data from such future missions.

Upon establishing a parameter space for degenerate variables, the physical plausibility of each scenario can be explored only through improved models and better data. Since it is yet not possible for us to understand such processes in planets with no solar system analogs, this is a long-standing problem the community is tackling slowly. Thankfully, we are able to make advancements by harnessing the collec-

---

<sup>4</sup>GMT: Giant Magellan Telescope (Chile; first light: 2025), TMT: Thirty Meter Telescope (Hawaii, USA; first light: 2027)

tive power of tools developed by stellar astronomers, planetary astronomers and atmospheric scientists. This requires that we engage in collaborative interdisciplinary modeling that leverages our intuition from Solar System atmospheres, knowledge of atmospheric chemistry spanning a wide pressure and temperature range, archived observations, and future mission simulations of exoplanet transits.

My dissertation research seeks to advance three key components in current exoplanetary atmosphere characterization efforts: 1) development of 1-D photochemical models that best reproduce atmospheric processes in tidally-locked Jupiter-sized giant planets and tidally-locked Earth-like rocky planets, 2) some quantification of detectable biosignatures from potentially habitable tidally-locked Earth-like planets orbiting M dwarfs; 3) putting these findings in the context of interpreting high-resolution spectra from future technologies. The primary deliverables of my research are models that predict the atmospheric composition of tidally-locked Earths orbiting M dwarf stellar hosts, and hot Jupiters orbiting FGKM stars, in preparation for the multi-wavelength observations we are expecting from the various *JWST* instruments, and eventually the *LUVOIR*, *HabEX* and *OST* missions in the future.

My work has helped build a foundation for extending the utility of well-respected planetary science tools—to extract planetary science—from future astrophysics missions. Going into the future, visible and UV observation capabilities are of increasing interest to the exoplanet community as they will enable measurement of atmospheric properties currently inaccessible to us, such as the thermal structure of the uppermost atmosphere and oxygen abundance determination. These benchmarking efforts from my team at GSFC and our collaborators will allow us to influence the

design parameters and target selections for the aforementioned future flagship exoplanet missions. Future missions are being designed to observe increasingly cooler planets (to eventually find habitable ones) orbiting Sun-like stars as well, thus treatment of disequilibrium effects will carry more weight in the accuracy of retrievals.

## Chapter 2: 1-D Atmospheric Modeling: An Overview of Atmospheric Dynamics, Photochemical Models, Radiative Transfer and Retrievals

In this chapter, I will cover the numerical methodology behind the techniques I have used in my scientific investigations in exoplanetary studies thus far. While the presently publishable materials that appear in the forthcoming chapters only deal with 1-D photochemical and spectral modeling, I spent the first year and half of my graduate career as an exoplanet scientist doing radiative transfer and atmospheric retrievals, using the same tool for both. In practice, however, developing atmospheric models incorporating the physics and chemistry in a planetary atmosphere is the first step to being able to effectively characterize a planet's atmosphere.

Climate models compute the thermal structure of an atmosphere, while photochemical models provide us with the chemical profiles of the various species comprising the atmosphere. Establishing self-consistent profiles of these atmospheric properties (“forward model” of the atmosphere) is necessary prior to use in radiative transfer work. Retrieval modeling, which is essentially inverse modeling, involves finding the combination of these properties (and others e.g. radius, cloud top pressure) that—when fed into a radiative transfer routine—computes a spectrum that best matches our observed spectrum. For example, Kopparapu et al. ([2012](#)), a paper about the photochemical modeling of the hot Jupiter WASP-12b, compares the spectrum for the planet with photochemistry included with one that only has equilibrium chemistry included. The spectrum generated with the photochemical gas abundances is shown to be a clear better match to observed photometric data points of the planet.

Besides the fact that both composition and thermal structure impact host star light filtering through a planetary atmosphere, there is also degeneracy amongst the two parameters when being retrieved from the analysis of observed data. We ideally need our priors to be as much informed as our present scientific capabilities allow. Thus, while the retrieval tools I used assumed compositions to be constant throughout the atmosphere for exoplanets, retrieval work these days tend to factor varying compositions into account. Thus, while my atmospheric retrieval endeavors took place earlier in my exoplanet research career, I cover this topic later on in this chapter and in less detail. The material will be relevant to the next chapter.

Finally, I will only be reviewing the numerical methods and processes as they pertain to the particular tools and templates I have used in my research work. The description includes features I have added to as part of my work with the Atmos 1-D atmospheric modeling tool (see Section 2.1.1). While I will not divert into a discussion about the state of the art in the field, the mathematics described below apply to all tools used in the field for the given type of computation. In the following chapters, however—where I report scientific findings as well as cover tool development efforts—I may compare our tools with other similar tools available in the community (and used in relevant literature) as appropriate.

## 2.1 Atmospheric Dynamics and 1-D Photochemical Models

To understand how 1-D photochemical models are relevant to the study of planetary atmospheres, we must first consider how air is transported horizontally and vertically. Atmospheric dynamics is controlled by gradients in several key

parameters: temperature, pressure, the Coriolis parameter, gravity, density, friction, moisture, and radiation (Holton and Hakim 2013). The relative importance of each term can be determined by using a technique called scale analysis. The choice of horizontal length scale and time period of interest dictate the relative importance of vertical and horizontal motion. Without considering the effects of radiation, planetary-scale transport stratifies an atmosphere in the north-south (or meridional) direction. In contrast, the east-west direction becomes well-mixed by zonal jets. The motion of mid-latitude jets can be approximated with a geostrophic flow, with the horizontal pressure gradient balancing the Coriolis force (Holton and Hakim 2013). Vertical stratification in density, pressure, and temperature can be approximated with hydrostatic balance. Convective motion becomes important near the equator, and air masses have an approximate North-South symmetry called a Hadley cell. The mid-latitude jets mentioned above result from the cooling of descending airmasses.

In a planetary atmosphere, temperature and compositional variation with altitude is more pronounced and persistent over the course of a year than lateral variations. Vertical transport is a much slower process than horizontal transport, and it is dictated by ambient conditions such as the local temperature gradient, which sets the lapse rate and thus the stability of the atmosphere against vertical mixing. On the other hand, the Coriolis force plays a much bigger role in horizontal transport, and circulation patterns tend to homogenize the atmospheres laterally. Both vertical mixing and the susceptibility of any region of the atmospheric column to compositional changes depends on how the region reacts to the Sun. While solar heating of surface and radiative cooling of air affects the strength of vertical mixing, the extent of

photochemical enhancement of depletion of a species at a given altitude depends on the penetration depth of the UV photons, which is determined by the amount of material present above that altitude. While it may seem like photochemistry would primarily affect the middle atmosphere (i.e. region from tropopause to  $\sim 100$  km), the troposphere and the region above are linked through the radiative and dynamical processes we have described. In fact, on Earth, they exchange trace constituents that are important to the photochemistry of the ozone layer (Holton and Hakim 2013). Thus 1-D photochemical models are extremely useful for studying the evolution of a diverse set of planetary atmospheres.

With tidally-locked planets, there is the whole issue of dichotomy in atmospheric structure and composition between the permanently irradiated dayside and the always dark night side. However, recent studies on tidally-locked HZ planets (discussed in Chapter 1) have found that stronger zonal jets and thermal tides should compensate these temperature gradients to provide lateral homogeneity, as well as enhance the vertical mixing of water vapor below large persistent cloud decks. Furthermore, tidally-locked planets, by the nature of their close-in location to the host star, are more susceptible to photochemical disequilibrium. The photochemistry is driven by stellar flux over the dayside of the planet; closest to the substellar point the photons are the most numerous and the photolysis rates the fastest. Due to the large circulations, the resulting compositional changes should propagate throughout the planet. Thus 1-D photochemical models can still help us understand tidally-locked planets, especially the smaller and cooler ones we are now finding and will continue to find as a result of advancement in detection technology.

Of-course, photochemical models require the pressure-temperature ( $P$ - $T$ ) profile as one of the fixed input parameters, so we must have some means of computing the planet's thermal structure. This can be computed from climate models. The atmospheric modeling community have had access to sophisticated climate models for Earth-like temperatures for a while as they had to be developed for our own planet. Over the past decade, the community began developing these models further for use in exoplanet studies. Although great strides have been made in constraining the thermal structure of the cooler planets in our own Solar System from observations via missions such as *Cassini* for the outer Solar System, sophisticated climate models are clearly yet to be available for the exotic temperature regimes of most of the exoplanets we have discovered to date. However, recent literature gives us ways of calculate them semi-analytically for irradiated giant planets, a topic I will cover later.

### 2.1.1 Atmos – Our Coupled 1-D Photochemical and Climate Model

In our group at NASA GSFC, we develop the “Atmos” tool. Atmos is a coupled 1-D photochemical & radiative-convective climate model (Arney et al. [2016](#), [2017](#)). Atmos—an effort originally started within the groups of Dr. Kevin Zahnle (NASA Ames) and Professor Jim Kasting (PSU Geosciences)—has been extensively used in the 1-D photochemical (via the “PHOTOCHEM” module) and climate modeling (via the “CLIMA” module) of well-studied terrestrial environments such as early Mars (based on the Mars template in Smith et al. [2014](#), which used chemistry from Zahnle et al. [2008](#) and Catling et al. [2010](#) studies), the Archean and Modern Earth phases of Earth's biosphere history, as well as high- $O_2$  temperate rocky planet atmospheres,

and the templates for these validated simulations are part of our public version<sup>1</sup>. The two modules can be used standalone, and are also being developed independently by us, and by our remote collaborators with research roots in Vikki Meadow's UW group and Jim Kasting's PSU group. PHOTOCHEM computes steady-state abundances of all specified long-lived non-background atmospheric gases and hazes, by factoring equilibrium chemistry, photochemistry, and transport by eddy vertical mixing and molecular diffusion, given boundary conditions for the species. Short-lived species are those that do not build up enough to diffuse, but partake in reactions with longer-lived constituents, so they included in the species input list for the sole purpose of the reaction list and mass tracking. Background gases are typically assumed to be constant throughout the atmosphere. Details on specific inputs and boundary conditions are part of forthcoming chapters. As climate state studies are not part of my dissertation research, I have personally only employed the PHOTOCHEM module for my work. Henceforth, I will only talk about PHOTOCHEM going forward.

Our PHOTOCHEM module can be scaled up for larger planets and to a wider range of densities, pressures and temperatures—I may have been the first person to attempt such modifications to the current version of Atmos. I began developing a hot Jupiter template within Atmos upon joining our group. This template is largely based on the WASP12b photochemical model in Kopparapu et al. (2012)—the original attempt from scratch. Dr. Kopparapu subsequently went onto developing a template for GJ1214b, which was modified for mini-Neptune photochemical modeling studies such as that of the planet GJ436b in Miguel et al. (2014). We have been working

---

<sup>1</sup>Public Atmos: <https://github.com/VirtualPlanetaryLaboratory/atmos/>

towards adding a mini-Neptune model template. While I have only added a hot Jupiter template within the Atmos framework thus far, I modified the WASP12b template to create a template for the cooler hot Jupiter HD189733b. The development of these templates and its use by collaborating scientists will be a major focus of Chapter 3.

We are in the process of extending the validity of PHOTOCHEM to other small worlds found within our solar system (e.g. Venus, Titan), for both solar and extrasolar applications. A large part of improving Atmos involves generalizing many routines by replacing hardcoded portions with statements that will work for planets beyond Earth. The Venus work is primarily being done by collaborators at other institutions. The Virtual Planetary Laboratory (VPL) is a large team with international participants, and our remote collaborators with their own validated photochemical models have been great resources for these other planets. In relation to such efforts, we have been updating various constituents of our model. We have updated the model's database of reaction pathways and vacuum UV (VUV) photo-absorption cross-section coefficients using data from KIDA: KInetic Database for Astrochemistry<sup>2</sup> (efforts of former undergraduate student W. Sluder—now at Northrop Grumman, with KIDA data from former postdoc E. Hebrard—now faculty at U. Exeter). Fellow graduate student R. Felton also coupled Atmos to “Geo”—a geophysical-geochemical modeling tool (see Neveu et al. 2015), to better understand carbon cycles on lifeless planets. R. Felton has also been working with group co-lead Dr. G. Arney and new NPP, Dr. S. Bastelberger, on getting Atmos to compute optical depths for any given species to help streamline the mechanism for handling hydrocarbon aerosol and haze production.

---

<sup>2</sup>KIDA (KInetic Database for Astrochemistry): <http://kida.obs.u-bordeaux1.fr/>

My colleague A. Britt—formerly a postbac in our group and about to start her PhD at NAU under Professor Tyler Robinson—recently used *Atmos* to reconcile *Curiosity* mission data with *Atmos* models showing the production and destruction of methane in the Martian atmosphere. This study has become a part of her Master’s thesis (defended June 2019) at the Fisk-Vanderbilt Bridge program, and the journal article is under review. Upon the request of GSFC scientist A. Mandell, A. Britt also attempted a quick study of possible interest to the *TESS* mission (prior to its launch), that involved coupled runs between the two modules to discern the dependencies (if any) on planet observability relative to planetary radius & solar Insolation for Super-Earths. D. Tillon—now a fellow graduate student at UMD Astronomy supervised by Professor Eliza M.-R. Kempton—spent their postbac year with us taking steps to make *Atmos* accessible via Python libraries and executables utilizing menu display packages to allow for use of code without requiring Fortran or prior familiarity. A secondary library, *pyUI*, manages functions and a class necessary for running, analyzing, and interpreting the I/O results of *Atmos*, using machine-native scripts to manage, edit, and execute all necessary files. As a team, we have also been updating radiative transfer coefficients and adding more stellar data—including synthetic UV data modeled after real stars (e.g. Chapter 4)—our stellar database. Lastly, we are always open to incorporating community feedback: What would YOU like to see in our next release?

Photochemical models should help us prepare for both future transit geometry and direct imaging observations. Future exoplanet space missions are being designed to observe increasingly cooler planets (to eventually find habitable ones), thus adequate treatment of disequilibrium chemistry will be especially important for in-

interpreting their findings. While Chapter 4 and Chapter 5 provide a very brief overview of the numerical principle behind the convergence scheme employed by our photochemical model, I will cover the governing equations in the next section, focusing on features relevant to my templates. For example, my templates are free of haze particles, so I will not talk about how particles are prescribed. For further details, please refer to Appendix B of the book Catling & Kasting (2017) and references therein.

## 2.1.2 The Numerical Recipe

### 2.1.2.1 The Equations for Modeling Chemical Evolution in an Atmosphere

Using the reverse Euler method, PHOTOCHEM solves a set of nonlinear, coupled ordinary differential equations (derived from partial differential equations) for the mixing ratios of all quantifiable constituents diffusing through a background gas (e.g. N<sub>2</sub> for rocky planets, H<sub>2</sub> for gas giants), over the modeled atmospheric column. A photochemical model has to solve these two key equations:

$$\underline{Continuity} : \frac{\partial n_i}{\partial t} = P_i - l_i n_i - \frac{\partial \Phi_i}{\partial z}, \quad (2.1)$$

$$\underline{Flux} : \Phi_i = -K_{zz} n \frac{\partial f_i}{\partial z} - D_i n_i \left[ \frac{1}{n_i} \frac{\partial n_i}{\partial z} + \frac{1}{H_i} + \frac{1 + \alpha_{Ti}}{T} \frac{\partial T}{\partial z} \right], \quad (2.2)$$

where,  $t$  = time,  $z$  = altitude, and for species  $i$ ,  $n_i$  = number density (molecules/cm<sup>3</sup>),  $P_i$  = chemical production rate (molecules/cm<sup>3</sup>/s),  $l_i$  = chemical loss frequency (s<sup>-1</sup>),  $\Phi_i$  = flux,  $f_i = n_i/n$  = mixing ratio ( $n = \sum n_i$ ).  $K_{zz} = K$  (notation used in equations below) eddy diffusion coefficient (cm<sup>2</sup> s<sup>-1</sup>),  $D_i$  and  $\alpha_{Ti}$  = molecular diffusion and thermal

diffusion coefficients, respectively, of species  $i$  with respect to the background.  $H_i = k_B T / m_i g$  give scale heights of species  $i$ , where  $k_B$  = Boltzmann's constant,  $m_i$  is its molecular mass, and  $\mu$  is the mean molecular mass of the atmosphere. All quantities are in cgs units. The derivation of eq. (2.2) can be found in Banks and Kockarts (1973, Chapter 15). The molecular diffusion between two gases with indices  $i = 1$  and  $i = 2$  is:

$$D_{12} = \frac{b_{12}}{n_1 + n_2} \quad (2.3)$$

where  $b_{12}$  is the binary diffusion parameter between the gas pair. In our model, hard-coded diffusion values for a water-rich Earth is included. For other rocky bodies and/or dry atmospheres, these values are scaled by the species and quantity of the background gas (i.e. N<sub>2</sub> or CO<sub>2</sub>) within the model. In a multi-component mixture, or when we specify diffusion for a non-rocky planet template, where we do not readily have versions of  $D_{12}$  scaled by non-N<sub>2</sub> background gas, we specify molecular diffusion with the original formulation from Banks and Kockarts (1973, eq. 15.23):

$$D_i = 1.52 \times 10^{18} \left[ \frac{1}{M_i} + \frac{1}{M} \right] \frac{T^{1/2}}{n} \quad (2.4)$$

where  $M_i$  = molecular weight of species  $i$ ,  $M$  = mean molecular weight of the atmosphere, and  $n$  = total number density. As thermal diffusion is important in the upper atmosphere, where molecular diffusion dominates, and the lower atmosphere is dominated by eddy,  $\alpha_{Ti}$  (in eq. 2.2) can be set to 0 in the lower portion. The second term in eq. (2.2)—which shows how the mixing ratio depends  $D_i$ —can be recast using:

$$\frac{\partial f_i}{\partial z} = \frac{1}{n} \frac{\partial n_i}{\partial z} - \frac{n_i}{n^2} \frac{\partial n}{\partial z} \quad (2.5)$$

and using the ideal gas law  $p = nk_B T$ , the second term in eq. (2.5) can be recast with  $p$ :

$$\frac{1}{p} \frac{\partial p}{\partial z} = \frac{1}{n} \frac{\partial n}{\partial z} - \frac{1}{T} \frac{\partial T}{\partial z} \quad (2.6)$$

But  $\frac{1}{p} \frac{\partial p}{\partial z} = -\frac{1}{H_a} = -\frac{K_B T}{mg}$  is the pressure scale height. Substituting this relation back to eq. (2.6), allows us to recast eq. (2.5) as:

$$\frac{\partial f_i}{\partial z} = \frac{1}{n} \frac{\partial n_i}{\partial z} + \frac{n_i}{n} \left[ \frac{1}{T} \frac{\partial T}{\partial z} + \frac{1}{H_a} \right] \quad (2.7)$$

Assuming no particulate species (otherwise we would need to account for fall velocities of such species) and noting that in steady-state  $\partial n / \partial t = 0$  and differentiating eq. (2.2) with respect to the altitude, we can recast eq. (2.1) to eq. (2.8) below:

$$\frac{\partial f_i}{\partial t} = \frac{P_i}{n} - \ell_i f_i + \frac{1}{n} \frac{\partial}{\partial z} \left[ (K + D_i) n \frac{\partial f_i}{\partial z} + n D_i f_i \left( \frac{1}{H_i} - \frac{1}{H_a} + \frac{\alpha_{T_i}}{T} \frac{\partial T}{\partial z} \right) \right] \quad (2.8)$$

Note that the terms in the square bracket are left entirely undifferentiated to keep the equation in its conservative form, as this allows explicit number density conservation when the equation is cast in the finite difference form, as we will see later in this section (specifically, eq. 2.16). For now, we can see that for steady-state solutions, the LHS would be equal to zero, and multiplying the RHS by  $n$ , we get eq. (2.8) as (2.9) below:

$$-\frac{\partial}{\partial z} [\Phi_i] + P_i - \ell_i n_i = 0 \quad (2.9)$$

Now substituting  $L_i = \ell_i n_i$  where  $L_i$  is the chemical loss rate of species  $i$  in molecules/cm<sup>3</sup> (just like the production rate units), and summing over all levels  $delz$  from level  $N^{low}$  to level  $N^{up}$  (the total number of discrete levels in the atmospheric vertical grid of equal height  $delz$  each) from the lower to upper boundary of the model yields

$$\sum_{N_{low}=1}^{nz=N_{up}} (P_i(nz) - L_i(nz))dz + \Phi^{low} - \Phi^{up} = 0 \quad (2.10)$$

The fluxes are computed within the model and included in output files. The column-integrated production and loss rates for each species are stored in vectors TP(I) and TL(I) in the model, where I is the index for species number, so max(I) = the number of long-lived species in the model that diffuse through a background gas.

It is also worth noting that since the molecular diffusion term  $D_i$  is only implemented for atomic and molecular hydrogen, for other non-background gas species, eq. (2.8) would take the simplified form below:

$$\frac{\partial f_i}{\partial t} = \frac{P_i}{n} - \ell_i f_i + \frac{1}{n} \frac{\partial}{\partial z} \left( K n \frac{\partial f_i}{\partial z} \right) \quad (2.11)$$

where  $i$  is any other species in the model besides H, H<sub>2</sub> and any background gas(es).

The corresponding simplified expression for the flux  $\Phi_i$  of such species is then:

$$\Phi_i = -K n \frac{\partial f_i}{\partial z} \quad (2.12)$$

The Eddy diffusion  $K$  ( $= K_{zz}$  as well) profile varies with altitude and does not depend on species in our models. It is meant to be a single parameter for 1-D representation of the combined 3-D effects of atmospheric turbulence and mixing. As we will see in the following chapters, we do not have a thorough knowledge of how these profiles would behave in tidally-locked atmospheres or in extreme temperature regimes. While Eddy profiles discrepancies have negligible effect on the redox state of an atmosphere (Kasting, 1979), their values do depend on both the temperature gradient and ambient wind velocities. Prof. Kasting's dissertation quantifies the impact of Eddy diffusion uncertainty on the photochemistry for Earth, but how the shape va-

ries with planet type has not been clearly established. With that in mind, we have to get creative for exoplanet applications. Sometimes, we are able to adopt profiles from recent literature we can find (e.g. for hot Jupiters, there is Moses et al. 2011 and a few Showman group studies). Vertical chemical quenching timescales for hot Jupiters have been studied (Visscher et al. 2006; Line et al. 2010; Bilger et al. 2013). For Earth-like planets, we can use eq. 2 (originally from Gierasch & Conrath 1985, pp. 121) from Gao et al. (2015), if free convection can be assumed, or use the profiles in Atmos' current templates (Kasting, 1979; Kasting, 1990). These profiles can then be scaled to match some boundary condition, if needed, like in Gao et al. (2015). However, Gao et al. (2015) does not account for the planet being tidally-locked, which enhances vertical mixing as mentioned earlier. This will be highlighted again in Chapters 4 and 5.

In our photochemical models, we assume a single Eddy diffusion coefficient profile for all species. The studies in Zhang & Showman (2018a, b) attempt to quantify Eddy diffusion coefficient for a few hot Jupiter cases for the tidally-locked examples shown, and also show cases of different Eddy diffusion profiles for cooler solar system planetary objects, and as a function of varying composition. They compute these Eddy profiles from strength of mixing parameters from global circulation models (GCMs) of these exoplanetary atmospheres. In other words, they emphasize the need for different Eddy profiles for variable compositions of different species. Thus, unless we have an independent way of knowing the mixing ratios at certain altitudes along the pressure grid of modeled species, the dependency of the steady-state mixing ratios to the assumed  $K_{zz}$  profile is a caveat for result interpretation. Indeed, obtaining the coefficients from theoretical 3-D models such as GCMs (e.g. Parmentier et al. 2013) is

the only reliable way to acquire the Eddy profile for 1-D exoplanet models. However, GCMs also do not easily extend to low pressure regions, a topic that motivates the studies in Chapter 4 and 5. While this is mitigated by the fact that molecular diffusion dominates the upper atmosphere, gravity waves can also cause an increase in mixing in the uppermost atmosphere (Zhang & Showman 2018a). Ongoing and future developments in photochemical models of exoplanetary atmospheres should attempt to keep Eddy diffusion details updated with new literature coming out on this topic as they pertain to templates for existing planet types.

### 2.1.2.2 Finite Differencing the Equations and Going from PDEs to ODEs

Eqs. 2.8 and 2.11 give us a set of partial differential equations (PDEs) for the mixing ratios of each trackable species  $i$  that varies as a function of altitude. For the long-lived species, which are specified in the model with both lower and upper boundary conditions, the model uses a finite differencing method to compute the mixing ratio at each grid point along the vertical grid.

For simplicity's sake, if we continue to work with eqs. (2.11) and (2.12) to demonstrate the finite differencing process in the simplest possible way—using the form that ignores molecular diffusion and advection terms but is valid for most species in the model anyway<sup>3</sup>—with species mixing ratios defined at the midpoints of each vertical grid level and the fluxes defined at the grid boundaries, the spatial derivatives are approximated by centered, second-ordered finite difference equations:

---

<sup>3</sup>The simplification comes from Jim Kasting's handwritten notes, a piece of legacy passed down from generation to generation.

$$\underline{Continuity} : \frac{\partial f_i^{j+1/2}}{\partial z} = \frac{f_i^{j+1} - f_i^j}{\Delta z} \quad (2.13)$$

$$\underline{Flux} : \frac{\partial \Phi_i^j}{\partial z} = \frac{\Phi_i^{j+1/2} - \Phi_i^{j-1/2}}{\Delta z} \quad (2.14)$$

where the superscript  $j$  indicates the vertical grid boundaries and thus  $j \pm 1/2$  indicates the grid mid-points. Using eq. (2.12), the fluxes evaluated at half-grid points can be evaluated the following way:

$$\Phi_i^{j\pm 1/2} = K^{j\pm 1/2} n^{j\pm 1/2} \frac{f_i^{j(+1)} - f_i^{j(-1)}}{\Delta z} \quad (2.15)$$

Similar to eq. (2.12), eq. (2.11) can be cast into the following finite differencing form:

$$\frac{\partial f_i^j}{\partial t} = \frac{P_i^j}{n^j} - \ell_i^j f_i^j + \frac{1}{n^j (\Delta z^2)} \left[ (Kn)^{j+1/2} (f_i^{j+1} - f_i^j) - (Kn)^{j-1/2} (f_i^j - f_i^{j-1}) \right] \quad (2.16)$$

This is only valid at the interior points  $j = 2$  through  $NZ-1$  because  $f_j^0$  and  $f_j^{NZ+1}$  are not defined. Substituting eq. (2.15) into eq (2.16) above and rearranging gives:

$$\frac{\partial f_i^j}{\partial t} = \frac{P_i^j}{n^j} - \ell_i^j f_i^j - \frac{1}{n^j \Delta z} \left[ \Phi_i^{j+1/2} - \Phi_i^{j-1/2} \right] \quad (2.17)$$

The expression above is evaluated within the model at every point along the vertical grid for every long-lived species, assuming the surface/ground and top-of-atmosphere (TOA) boundary fluxes have been specified, or can be calculated at those boundaries from other types of boundary conditions input by us.

### 2.1.2.3 Boundary Conditions

The boundary conditions (lower:  $\Phi^{low}$  and upper:  $\Phi^{up}$ )—which must be supplied for every species that contributes to the atmospheric makeup—take the finite differencing forms when we substitute the  $j$ 's and assumptions into eq. (2.16):

Surface/Ground/Lower Boundary:

$$\frac{\partial f_i^1}{\partial t} = \frac{P_i^1}{n^1} - \ell_i^1 f_i^1 + \frac{1}{n^1 \Delta z} \left[ \Phi_i^{low} + (Kn)^{1+1/2} \left( \frac{f_i^2 - f_i^1}{\Delta z} \right) \right] \quad (2.18)$$

TOA/Upper Boundary:

$$\frac{\partial f_i^j}{\partial t} = \frac{P_i^{NZ}}{n^{NZ}} - \ell_i^{NZ} f_i^{NZ} - \frac{1}{n^{NZ} \Delta z} \left[ \Phi_i^{up} + (Kn)^{NZ-1/2} \left( \frac{f_i^{NZ} - f_i^{NZ-1}}{\Delta z} \right) \right] \quad (2.19)$$

where  $j = 1$  at the ground, and  $j = NZ =$  total no. of layers at the uppermost boundary. Eq. (2.18) recognizes that the flux at  $j - 1/2$  level is just the flux at ground  $j = 1$  level itself. Since  $NZ + 1/2$  is just above our grid, eq. (2.19) just assumes  $\Phi^{up} = \Phi^{NZ+1/2}$ .

By default,  $\Phi^{up}$  is 0 for all species in the model for which molecular diffusion is not included (so namely species apart from H and H<sub>2</sub>). Within the template, this can be overridden for other species if we supply upper boundary conditions in the form of a non-zero (i.e. both downward and upward)  $\Phi^{up}$ , a fixed mixing ratio, or an effusion velocity,  $v_{eff}$ , which is equal to  $D_i/H_a$  for H and H<sub>2</sub>. This can be set to  $J_i H_a$ , where  $J_i$  is the photolysis rate, for major species that photo-dissociate above the model grid (e.g. O<sub>2</sub> in Modern Earth template). If the latter option is used, the main product of photolysis must be given a downward flux as those species then fall into the atmosphere below. In our Earth templates, we do this for atomic N since N<sub>2</sub> photolysis does occur above the upper boundary. The resulting N concentrations, however, are not

high enough to affect photochemistry. I do not use this option for H<sub>2</sub> in the hot Jupiter template; the only reactive background gas. With irradiation levels being so high, upper atmosphere H<sub>2</sub> begins breaking down within the modeled column.

When we assume a fixed mixing ratio at the lower boundary, then  $\partial f^i / \partial t$  is just set to 0 for that species, and the  $\Phi^{low}$  is computed within the model with that assumption. When gases included as part of the “inert” list, like background gases are in the templates in our public version, it means they are forced to maintain this lower boundary mixing ratio throughout the atmosphere. It does not mean the gas is always actually inert, it just means the gas is so well-mixed throughout the column that the model instantaneously balances any loss with a flux across the lower boundary to maintain the same mixing ratio at all heights. For species that are removed chemically at the surface or dissolve into oceans, i.e. have a negative flux at the lower boundary, a deposit velocity (“ $v_{dep}$ ”), is specified instead. This is meant to be a catch-all non-precipitation term representing all main forms of interactions of the species with the surface, with diffusion through ocean dominating.  $v_{dep}$  relates to the flux through  $\Phi^{low} = -v_{dep}n_i^1 = -v_{dep}n^1 f_i^1$ , and can only take values in the range:  $0 < v_{dep} < 1$  (in cm s<sup>-1</sup>), with highest values indicating reaction/destruction upon hitting the surface.

#### 2.1.2.4 The ODEs to Solve to Obtain Steady-state Mixing Ratios

Eqs. 2.16 or 2.17 can be recast into the following form to give eq. (2.20) below:

$$\frac{\partial f_i^j}{\partial t} = A f_i^{j+1} + B f_i^j + C f_i^{j-1} + E_i^j \quad \text{with:} \quad (2.20)$$

$$A = \frac{K^{j+1/2}}{n^j (\Delta z^2)}$$

$$B = -\frac{K^{j+1/2}}{n^j(\Delta z^2)} - \frac{K^{j-1/2}}{n^j(\Delta z^2)} - \ell_i^j$$

$$C = \frac{K^{j-1/2}}{n^j(\Delta z^2)}$$

$$E_i^j = \frac{P_i^j}{n^j}$$

Re-writing eq. 2.20 with  $x_k = f_i^j$  and  $E_k = E_i^j = P_i^j/n^j$ , where  $k = i + (j-1)(NQ)$  and  $i = 1$  to  $NQ$ ,  $j = 1$  to  $NZ$ , where  $NQ$  and  $NZ$  are the total number of species and total no. of equal height layers, respectively, we obtain (2.21) below, ready to be solved:

$$\frac{dx_k}{dt} = Ax_{k+1} + Bx_k + Cx_{k-1} + E_k \quad (2.21)$$

We use  $E_k = E_i^j$  instead of  $D_k = D_i^j$  to show the fourth part to avoid confusion with the diffusion term  $D_{12}$  or  $D_i$ , which is specified in the model for only H and H<sub>2</sub><sup>4</sup> anyway.

We now have the system of ordinary differential equations (ODEs)<sup>4</sup> above as replacing the spatial derivatives with the above approximations has allowed us to reduce the PDEs. A total of  $NZ$  times  $NQ$  ODEs will need to be solved for a template with  $NQ$  (i.e.  $\max(i)$ ) long-lived species distributed over  $NZ$  layers (i.e.  $\max(j)$ , this is typically 100 or 200). Eq. (2.21) is cast in vector form with the LHS  $\frac{d\mathbf{x}}{dt}$  equal to  $\mathbf{F}(\mathbf{x})$ . The time-derivative is approximated by simple forward differencing, and values of  $\mathbf{x}$  at the  $n^{\text{th}}$  time step evaluated by Taylor expanding around  $\mathbf{F}(\mathbf{x}^n)$ . We obtain the Jacobian matrix  $\mathbf{J}$  that way.  $\mathbf{J}$  can be substituted back to obtain the next timestep and so on.

It is worth noting here that short-lived species such as the singlet D oxygen

---

<sup>4</sup>It is worth reminding here that Eq. (2.20) is more complicated for H & H<sub>2</sub>, as they factor molecular diffusion and advection.

atom ( $O^1D$ )—for which we indicate a fixed quantity in the model as their abundance is not tracked—do not contribute to  $f_i$  in these equations. Transport is not important for short-lived species and photochemical equilibrium can be assumed for such species, so they do not have to be part of the solution matrix, which may get ill-conditioned (i.e. nearly singular) for species so minor their abundance goes to near zero. In the case of an ill-conditioned matrix, the model fails to converge as the run “gets lost”. This can even happen for a long-lived species, especially if the density of a short-lived species depends on a long-lived species which has become a minor constituent over a certain altitude range. This also implies that species that react with themselves can never be left as short-lived in the template. A workaround we often use is ignoring the errors in mixing ratios of problem species over problematic certain range of altitude—information the model prints real-time while running—thus not letting such species influence the time step. This is a particularly useful way to converge high- $T$  templates such as the hot Jupiter templates, which do not converge without imposing these kinds of certain conditions, and even species-by-species level ignoring is sometimes required. Species that are part of the inert list tend to be very long-lived and not part of  $NQ$ , and thus are excluded automatically. In a weakly reducing atmosphere where  $CO_2$  abundance is high,  $CO_2$  can be part of this list.

### 2.1.2.5 Rainout, Lightning, Photolysis and Redox Balance

The time-dependent diurnally averaged photolysis rate of a species  $i$  at grid point  $j$  at a given wavelength depends on the wavelength-dependent stellar flux, wavelength-dependent photolysis cross-section (XSEC), and the source function.

Since the diurnal factor is twice as much for a tidally-locked planets as it is for a rapidly rotating one, with only the dayside hemisphere being irradiated, this means a tidally-locked planet is irradiated by twice the flux at a given orbital distance from the host star. The source function uses a two-stream radiative transfer approximation of Toon et al. (1989) (using multiple scattering technique of Yung et al. 1976) with effects of absorption and Rayleigh scattering included<sup>5</sup>. Some aspects of radiative transfer computations in general are briefly discussed in the next section. As far as Rayleigh scattering is concerned, PHOTOCHEM originally computed the cross-section for air, CO<sub>2</sub>, N<sub>2</sub> and O<sub>2</sub> only. Upon joining the team, I added data for H<sub>2</sub>O (per von Paris 2013 suggestion), H<sub>2</sub> and He (from Kopparapu et al. 2012 WASP12b model). For exoplanet and our solar system application, we should also consider adding the data for methane, ammonia and carbon monoxide as for atmospheres where they are present in quantities greater than 1%, the code defaults to using the air value.

For species that have multiple photolysis paths, we have the quantum yield, QY, available for each photolysis reaction path, so the rate of each path is given by XSEC\*QY, and the sum of QYs = 1. To get the integrated rate of a reaction, the cross-sections are read in and interpolated into a user-specified grid, which has remained same across all our templates so far (fixed to a 1983 JPL recommended grid spanning 1216 to 8500 Å). The rates are looped over wavelength and stored in a matrix.

The regular temperature-driven two and three body equilibrium chemistry reactions use temperature and pressure dependent rates, by using data for the reaction rate, temperature coefficient, and activation energy user-supplied for each reaction

---

<sup>5</sup> The climate model actually uses the same model to ensure self-consistency for coupled runs.

in the reaction list. For three body reactions, we have two sets of the three parameters as we factor low- and high- pressure limit values. The column integrated rate of a reaction is obtained by summing over the layers.

Rainout, aqueous chemistry and lightning are additional physical processes included for the temperate planets. As they are prescribed for Earth-like  $P/T$  conditions, the current low- and high- $T$  templates we have (i.e. Titan, Venus, Mars, hot Jupiter) skip those subroutines when the model is run for them. The solubilities are implemented from Henry's law, and modified for some species (e.g.  $\text{CO}_2$ ,  $\text{SO}_2$ ,  $\text{H}_2\text{CO}$ ,  $\text{H}_2\text{SO}_4$ ) according to pH values to account for aqueous phase reactions that are strictly the most accurate for a thermal profile very close to Earth's. In the absence of lower boundary or troposphere conditions fixed by us for the water vapor, the troposphere  $\text{H}_2\text{O}$  mixing ratio is fixed to a relative humidity profile from Manabe & Wetherald (1967), and not computed from a complete cycle of condensation and evaporation.

Lightning is the main non-anthropogenic source of odd nitrogen species and oxygen in Earth's atmosphere. The lighting routine does not compute the effects of ion chemistry. Including ion chemistry as an atmospheric process is a priority for future upgrades of the model. Lightning production of NO and CO are included from Kasting (1979, 1990), with other species being informed by the model in Chameides et al. (1977). CO recombines to  $\text{CO}_2$  following equilibration, but NO production goes down with decreasing  $\text{O}_2$  concentration till  $f(\text{O}_2)$  of  $10^{-3}$ , when it stabilizes to 5%. Adequate inclusion of lightning by-products is important for the total redox conservation in atmospheres, which is important for gauging numerical self-consistency within the model. We aim to achieve the lowest value we can for redox conservation;

redox conservation is a measure of the balance between the amount of reducing and oxidizing species at model boundaries. Redox conservation value at a given boundary comes from the balancing total flux of oxidants there with the total flux of reductants. When a key oxidant/reductant is missed or its abundance grossly miscomputed due missing production and/or loss source(s), this value can end up being directly proportional to the flux of species that is primarily driving the redox imbalance.

## 2.2 Spectral Models – Radiative Transfer and Retrieval Computation

To assess the composition of a transiting exoplanet, we must "retrieve" the abundances of the responsible molecular species from observed spectroscopic signatures in their transmission (from primary transit, i.e. limb) and emission spectra (secondary eclipse, i.e. planet's dayside). A radiative transfer model of the planet is computed via supplying a user-specified initial "*a priori*" profile. Upon generating this "forward model", Bayesian numerical schemes are employed to update the parameter values through successive attempts till a final fit (or a series of fits) to the measured spectra is obtained. The retrieved parameter ranges are used to make conclusions about the atmospheric composition and stored for future atmospheric retrieval work.

Over this past decade, studies on well-known giant exoplanet candidates such as HD209458b, HD209458b, GJ1214b, and a few *WASP* (ground-based) and *CoRoT* (space mission) candidates, have employed retrieval codes. This effort has been extended to smaller cooler planets recently (Feng et al. 2018). The deployment of new high-precision ELTs and exoplanet-relevant space missions (*JWST*, *OST*, *LUVVOIR*, *Hab-EX*, etc.) will not only increase the diversity of planets we end up studying with retriee-

val codes, but should allow for tighter constraints to be drawn on their properties.

Below I first give a short overview of the spectral modeling tools relevant to past and ongoing work described in this dissertation. Tool(s) relevant to only new work will be briefly described in the final chapter of this dissertation. In order to keep the descriptions concise, I provide some of the theory behind these calculations.

## 2.2.1 Tools for Radiative Transfer and Retrieval Modeling

### 2.2.1.1 Exo-Transmit

Exo-Transmit (Kempton et al. [2017](#)) is an extremely user-friendly open source software that calculates a transiting exoplanet's transmission spectrum for an atmosphere resulting from species for which spectral contribution has been established in IR, including trace species, for which opacity data are available in the package.

Exo-Transmit comes preloaded with templates with different compositions of the gases included as a function of  $P/T$ , known as the equation-of-state files (EOS files). The varying compositions come from different metallicity considerations or solar metallicity with different  $[C]/[O]$  ratio. Please see Table 1 of Kempton et al. ([2017](#)) for the list of atomic and molecular opacities and collision-induced absorption (CIA) sources. Exo-Transmit is extremely fast at computing the spectrum as the as the opacity data it uses is already available at the native wavelength resolution of the calculation points ( $R \sim 1000$ ) and the pressure ( $P = 10^n$  Pascal, where  $-4 < n < 8$  and  $\Sigma(n) = 44$ ) and temperature grid points ( $T$  goes from 100 to 3000K in 100K steps) of the mixing ratio/EOS files. It can handle user-supplied custom  $P-T$  and composition (which is then interpolated to the coarser pressure and temperature grid of the

opacity data), surface gravity, host star and planet sizes. I use Exo-Transmit for the spectral modeling portion of the studies covered in Chapters 4 and 5. Section 4.2.4 of Chapter 4 describes some features of the tool applicable to our work in further detail.

### 2.2.1.2 SMART

VPL’s foundational spectral modeling tool, **SMART** (**S**pectral **M**apping and **R**adiative **T**ransfer, Meadows & Crisp 1996), is a 1-D, plane parallel, multi-stream, multiple-scattering radiative transfer model that interfaces with both HITRAN (Rothman & Gordon 2014) and HITEMP spectroscopic databases (see Section 2.2.3.1 below for more on these databases). The number of streams can be tuned. SMART can thus be used to generate high-resolution synthetic spectra for a wide temperature range, and takes user supplied 1-D profiles of  $P$ - $T$ , mixing ratios and aerosol optical depths to compute monochromatic optical properties of each layer. SMART has been used in most terrestrial exoplanet work coming out of VPL (Misra & Meadows & Crisp 2014, Lustig-Yaeger et al. 2015; Tovar et al. 2015), and was also used for the WASP12b spectra in Kopparapu et al. (2012; computed by Amit Misra).

SMART uses gaseous absorption coefficients at reference  $P$ - $T$ -wavenumber values, computed within the model by a companion line-by-line (see Section 2.2.3.1 for what that means) model (LBLABC). It also saves computational time by not using the line-by-line directly, as it instead employs some type of mapping algorithm. It also accommodates temperature-dependent CIA coefficients, which is particularly relevant for  $N_2$  and  $O_2$  dominated atmospheres like Earth. A Mie scattering model is used to compute the optical properties of liquid water clouds, while crystal geometry op-

tics is employed for ice (cirrus) cloud parametrization. Vibrational-rotational absorption is computed in the visible and infrared wavelengths for all spectrally active gases at those wavelengths, meaning SMART can also be used for generating reflection spectra of planets. The total extinction at a point is computed by combining gas extinction optical depths with depths from Rayleigh scattering and aerosol absorption.

Having said all that, I do not use SMART directly for any portion of this dissertation due to government restrictions. In Chapter 4, I just compare my Exo-Transmit-computed spectra with the spectrum computed via the SMART transit (SMART-T) module for Kopparapu et al. (2017). This module computes transmission along limb-traversing paths (Misra et al. 2014 a,b; Misra 2014) by incorporating path length difference between atmospheric layers, refraction effects and a limb-darkening model. When the transit module is used, two additional inputs are required: 1) the index of refraction of the surface for rocky bodies, and 2) the host star radius for all cases.

### 2.2.1.3 NEMESIS

The Oxford Planetary Group's **Non-Linear Optimal Estimator for Multivariate Spectral Analysis**), or NEMESIS, is a closed-source atmospheric retrieval software suite that can compute IR planetary spectrum for giant planets, as well retrieve the best fit input parameters from user-supplied observed IR spectrum data for a planet. NEMESIS was created by Prof. Pat Irwin of Oxford University's Atmospheric Physics group (Irwin et al. 2008) to conduct retrievals on *Cassini/CIRS* studies of the outer solar system, particularly Saturn and Jupiter. NEMESIS has been extensively validated over a decade of retrieval work on *Cassini/CIRS* (Hesman et al. 2012; Nixon et al.

2012, 2013, 2014b, 2016; Fletcher et al. 2014, 2015; Irwin et al. 2016; Barstow et al. 2016) returns of our outer planetary atmospheres, in addition to exoplanet atmospheres in recent years (Nixon et al. 2014a, Lee et al. 2012, 2014; Barstow et al. 2012, 2013, 2014, 2015). By default, NEMESIS uses absorption opacities from correlated- $k$  tables (available for CO, CO<sub>2</sub>, CH<sub>4</sub>, and H<sub>2</sub>O), but can also compute a spectrum via line by line (LBL) data directly. Please see Section 2.2.3.1 for more on this. Now it also allows users to use NH<sub>3</sub>, CH<sub>4</sub> and H<sub>2</sub>O cross-sections provided by ExoMol (Barber et al. 2006; Yurchenko et al. 2011; Yurchenko & Tennyson 2014), an effort detailed in the dissertation paper Garland & Irwin (2019). The original algorithm only employs the optimal estimation (OE) convergence scheme to update the parameter values. While OE is sufficient for the high quality CIRS datasets, we need more robust methods for the low resolution and low SNR exoplanet data. The parameters retrieved from present observations exhibit high levels of degeneracy as mentioned in Chapter 1 (see Figure 2.1), meaning several different combinations of input parameters can fit the same spectra. This means we cannot constrain the parameters in the best possible way with OE, as OE does not allow full marginalization over the available parameter space, introducing dependency on the model parameters/the priors. In order to fully sample the parameter space, the results need to be data driven.

Over this past decade, graduate students and research scientists within the Oxford local group have updated high- $T$  data for brown dwarf applications (Garland & Irwin 2019) and additional exoplanet work. These include future mission simulations for *JWST* transmission spectroscopy (see Barstow et al. papers). NEMESIS has also been used to fit ground-based data; Baudino et al. (2018) used it on VLT/SPHERE

data, which also entailed coupling to the Exo-REM radiative-convective equilibrium model (Baudino et al. 2015, 2017). Other efforts include inter-comparison with retrieval models from other groups (e.g. CHIMERA, see Line et al. 2013, 2016; Barstow et al. 2017; Kreidberg et al. 2015; Rocchetto, 2017), new absorption data for CH<sub>4</sub>, NH<sub>3</sub>, etc. species (from ExoMol), and improvement to other high-*T* relevant data such as partition functions (Garlard & Irwin 2019), update of the CIA data and alkali metal faraway wing profile (Baudino et al. 2017), and updates to convergence scheme.

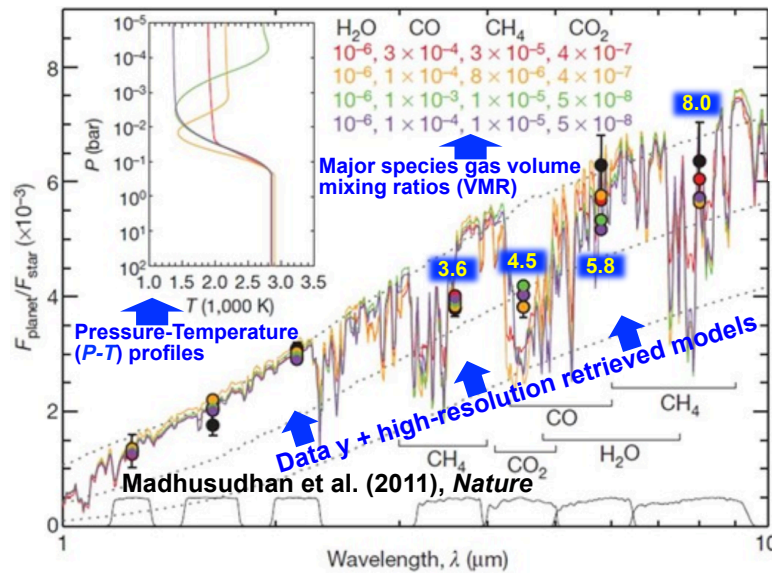


**Figure 2.1:** An example of degeneracy observed in the hot Jupiter WASP12b retrieval results from 6-channel (i.e. IRAC + MIPS photometric channels) *Spitzer* data (Madhusudhan et al. 2011). Several combinations of the atmospheric parameters fit this sparse dataset equally well. The temperature profiles used here employ an old, purely mathematical parameterization scheme. The purple profile was used as the thermal structure model for the Kopparapu et al. 2012 WASP12b work, and I use the same profile for the template reproduction in Chapter 3.

While NEMESIS can adequately model lower altitudes, where pressures and temperatures are high enough for equilibrium chemistry to prevail, it does not have any chemical evolution abilities or a multi-scattering scheme in secondary eclipse modes. It must use data fed in from a standalone chemical model (e.g. our Atmos PHO-

TOCHEM module) directly to achieve this. Present exoplanet data for a diverse range of planets amenable to characterization efforts come from IR wavelengths, which samples mostly lower middle to high altitudes, where the various disequilibrium processes and particle scattering are important enough to introduce structural variety. It is possible to verify the extent of validity of retrievals with NEMESIS and similar tools, by comparing and contrasting them with both real and synthetic observations of hot Jupiter templates for which we have photochemical models for (e.g. *JWST* synthetic observations generated with noise profiles), and then comparing them with spectrum generated with mixing ratios computed without photochemistry factored.

## 2.2.2 The Numerical Recipe for Retrieval Computations

A combo radiative transfer and retrieval tool like NEMESIS typically employ a standalone radiative transfer spectral generator using user-defined “*a priori*” initial parameter estimates  $\mathbf{x}_a$ , and a separate statistical tool that iterates these parameters  $\mathbf{x}$  till some convergence criterion is met to minimize the difference between the model  $\mathbf{F}(\mathbf{x})$  and the data  $\mathbf{y}$ . So, an “inverse problem” is solved by  $\chi^2$  (cost function) minimization, where we obtain the atmospheric parameters  $\mathbf{x}$  by inverting observations  $\mathbf{y}$ :  $\mathbf{y}$  [data] =  $\mathbf{F}(\mathbf{x})$  [theoretical model computed at  $\mathbf{x}$  from physics + chemistry] +  $\mathbf{e}$  [noise in  $\mathbf{y}$ ].  $\chi^2$  takes a non-standard form here with two separate expressions, where the first portion is “data driven”, and the second part compares the trial  $\mathbf{x}$  and  $\mathbf{x}_a$ :

$$\chi^2(\mathbf{x}) = (\mathbf{y} - \mathbf{F}(\mathbf{x}))^T \mathbf{S}_e^{-1} (\mathbf{y} - \mathbf{F}(\mathbf{x})) + (\mathbf{x} - \mathbf{x}_a)^T \mathbf{S}_a^{-1} (\mathbf{x} - \mathbf{x}_a), \quad (2.22)$$

where  $\mathbf{S}_e$  and  $\mathbf{S}_a$  are the error and a priori covariance matrices, respectively.

In my retrieval work, I used two different statistical approaches to solve the inverse problem: the Optimal Estimation (OE) and the more robust Markov Chain Monte Carlo (MCMC) approaches. The OE technique, native to NEMESIS, has seen extensive use in both Earth and solar system atmospheric remote sensing, with applications extended to exoplanets in the past eight years.

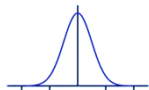
The OE scheme does  $\chi^2$  minimization via the Levenberg-Marquardt principle: a braking parameter  $\lambda$  is adjusted automatically within the code each time in response to the goodness-of-fit of  $\mathbf{F}(\mathbf{x})$  (computed with current  $\mathbf{x}_n$ ), to compute the next trial state  $\mathbf{x}'_{n+1}$ . If the current solution is a better fit than the previous trial, the braking parameter is reduced to compute the next  $\mathbf{x}$ , if it is worse,  $\lambda$  is increased, and so on (eq. 2.23). So, the parameters are updated linearly till a single final solution is obtained upon satisfying some user-specified convergence criterion on  $\lambda$  and  $\chi^2$ :

$$\mathbf{x}'_{n+1} = \mathbf{x}_n + \frac{\mathbf{x}_{n+1} - \mathbf{x}_n}{1 + \lambda} \quad (2.23)$$

The OE scheme, while very fast and efficient for updating parameter values sequentially, is only good for high quality datasets where the errors are expected to be linear or Gaussian in nature. Thus, for exoplanet datasets—which are both ill-conditioned and ill-constrained due to the simultaneous use of multiple instrument observations (in a single retrieval effort), low SNR, and insufficient spectral resolution—OE can only converge to the closest solution, aka the “local” minimum closest to the *a priori* profiles  $\mathbf{x}_a$ . Since a linear convergence method cannot fully sample the wide unknown exoplanet parameter space, we need to use convergence schemes that can jump around the parameter space efficiently, giving us an estimate of probable

solutions that do not depend strongly on the a priori (which are just wild starting guesses for exoplanets and brown dwarfs anyway). The datasets we have from present space missions cannot properly resolve spectral features, so we expect a range of parameter combination fits that may not be in anyway related to each other.

The MCMC method (Ford 2005) is now the most widely used approach by the exoplanet community for that very reason. The “Monte Carlo” method allows randomness in each subsequent guess since trial states are drawn from a Gaussian distribution (eq. 2.24). The “Markov Chain” process ensures that the current solution depends on the previous but not solutions prior to that:

$$\mathbf{x}'_{n+1} = \mathbf{x}_n + \text{Gaussian} \quad (2.24)$$


The step size of this parameter exploration walk—the  $1\sigma$  width of the Gaussian—is adjusted to allow a certain percentage of the proposed solutions to be accepted. This continues till the  $\chi^2$  stops jumping up and down over a large number of steps (this is periodically evaluated). This method is much slower; depending on the number of parameters, we need anywhere from 10,000 to a few tens of million model runs to achieve relaxation. In this way, MCMC allows us to recover the global minimum solution by producing a posterior distribution of possible solutions, thus allowing quantification of uncertainty estimates for each  $\mathbf{x}$ . In my retrieval work, I use both OE and MCMC. When we do not know a suitable starting point, it makes sense to get a local minimum with OE and use it as the initial starting profile values.

## 2.2.3 The Forward Model

### 2.2.3.1 Spectroscopic Information Content

The most accurate but extremely computationally expensive way of calculating the radiative transfer through a synthetic user-specified atmosphere is to use a line-by-line (LBL) method. Lists of spectroscopic feature strength (as a function of wavelength) are available for each species, but their validity for a particular model application depends on the temperature and pressure ranges required by the atmosphere. The number of spectral features increases rapidly with increasing temperature for most molecules. So, while the HITRAN database computed at 296K is good for most solar system applications, the HITEMP and CDS1000/4000 (for CO<sub>2</sub>) databases exist to enable the modeling of irradiated exo-planets and brown dwarfs. The databases give the line strengths at the standard temperature; opacities can be calculated only after computing the strengths  $S$  at the desired temperatures  $T$  (eq. 2.25):

$$S = \frac{S_0 Q(T_0) \exp(-c_2 E_1/T) [1 - \exp(-c_2 \nu_0/T)]}{Q(T) \exp(-c_2 E_1/T_0) [1 - \exp(-c_2 \nu_0/T_0)]} \quad (2.25)$$

where  $T_0$  is the temperature at which the strengths are quoted (296K),  $S_0$  is the line intensity at that temperature,  $\nu_0$  = vacuum wavenumber,  $E_1$  is the lower-state energy, and  $c_2$ , the second radiation constant, is  $hc/k_B$  ( $c$  = light speed,  $h$  = Planck constant,  $k_B$  = Boltzmann constant).  $Q(T)$  is the partition function at the temperature.

In the LBL method, the absorption of each individual spectral line (in the region of interest) is computed and the resulting spectrum is convolved with the necessary instrument function. The lines are read real-time from the large databases, which may even contain a few million entries. Thus, computing them for each pressure, tem-

perature and wavelength can take anywhere from hours to months per single model run. As a result, a direct line-by-line method is not well-suited for retrieval algorithms unless there are only a few lines in the spectral region concerned and/or the spectral range is very small, or the number of models is low (i.e. suitable for OE but not MCMC). The correlated  $k$ -distribution method, which utilizes the behavior of absorption coefficients to be correlated from layer to layer to compute storable opacity data over frequency bins, was introduced to speed up this process. This allowed a model run that would usually take six hours to be done in a less than a minute. The NEMESIS software has tools to allow users to compute these tables directly from the databases, and store them for direct use in spectra generation work. NEMESIS now also uses cross-sections for some of the species for which previous data are poor (e.g. CH<sub>4</sub>) and for species that are new to the database (e.g. NH<sub>3</sub>). The cross-sections are simply line-by-line calculations over a  $P$ - $T$  grid that is then integrated preserving an area, (typically  $\Delta\nu = 1\text{cm}^{-1}$ ). In terms of speed, this is intermediate between using  $k$ -tables and LBL, but can overestimate the amount of absorption present (Garland & Irwin 2019).

The atmosphere is divided into  $N_{lev}$  discrete layers prior to radiative transfer computation, just like how we do it for the photochemical modeling. Within each of these user-defined layers, the optical depth is computed for use in the radiative transfer equations. The optical depth for the  $k_{th}$  gas in the  $z^{th}$  layer at wavelength  $\lambda$  is:

$$\Delta\tau_{k,z,\lambda} = f_{k,z}\sigma_{k,z,\lambda}\frac{\Delta P_z}{\mu_{atm}g} \quad (2.26)$$

where  $f_{k,z}$  is the gas VMR of the  $k_{th}$  gas in the  $z^{th}$  layer,  $\sigma_{k,z,\lambda}$  is the absorption cross section per molecule,  $\Delta P_z$  is the pressure thickness in the  $z^{th}$  layer,  $\mu_{atm}$  is the mean

molecular weight of the atmosphere being modeled and  $g$  is the planet's gravity. Upon computing the optical depths for each of these layers, we are able to solve for the upwelling irradiance as eq. (2.27) below:

$$I_\lambda = \sum_{z=0}^{N_{lev}} B_\lambda(T_z) e^{-\sum_{j=z}^{N_{lev}} \Delta\tau_{j,\lambda} \Delta\tau_{z,\lambda}} \quad (2.27)$$

where  $N_{lev}$  is the number of atmospheric layers and  $B_\lambda$  is the Planck function at wavelength  $\lambda$  at the temperature  $T_z$  in the  $z^{th}$  layer. The total state vector  $\mathbf{x}$ —given in eq. 2.28 below--representing the information in  $f_{k,z}$  and  $T_z$  we are retrieving, can be represented for the major gases  $\text{CO}_2$ ,  $\text{CO}$ ,  $\text{H}_2\text{O}$  and  $\text{CH}_4$  by:

$$\mathbf{x} = [\log(f_{\text{H}_2\text{O}}), \log(f_{\text{CH}_4}), \log(f_{\text{CO}}), \log(f_{\text{CO}_2}), T]^T \quad (2.28)$$

or, if using the physics-informed T formulation from Section 2.2.3.2 below, then:

$$\mathbf{x} = [\log(f_{\text{H}_2\text{O}}), \log(f_{\text{CH}_4}), \log(f_{\text{CO}}), \log(f_{\text{CO}_2}), \log(\kappa_{IR}), \log(\gamma_{v_1}), \log(\gamma_{v_2}), \beta, \alpha]^T \quad (2.29)$$

### 2.2.3.2 Analytical Thermal Structure (P-T profile) for Irradiated Planets

The parameterized thermal structure for highly irradiated atmospheres in the (Line et al. 2012, 2013) work was the first formulation used in atmospheric retrieval work to be derived from semi-analytic physical principles (Guillot et al. 2010). Temperature, described as a function of pressure-dependent optical depth, is given by:

$$T^4(\tau) = \frac{3T_{int}^4}{4} \left(\frac{2}{3} + \tau\right) + \frac{3T_{irr}^4}{4} (1 - \alpha) \xi_{\gamma_1}(\tau) + \frac{3T_{irr}^4}{4} \alpha \xi_{\gamma_2}(\tau)$$

with

$$\xi_{\gamma_i} = \frac{2}{3} + \frac{2}{3\gamma_i} \left[1 + \left(\frac{\gamma_i \tau}{2} - 1\right) e^{-\gamma_i \tau}\right] + \frac{2\gamma_i}{3} \left(1 - \frac{\tau^2}{2}\right) E_2(\gamma_i \tau) \quad (2.30)$$

where  $E_2(\gamma T)$  is the 2<sup>nd</sup> order exponential integral, which is typically already computed within a full radiative transfer tool, and  $T_{irr}$  is the incoming stellar input. The five parameters making up the functional form of  $T-\kappa_{IR}$  (grey/gray altitude-variant IR opacity),  $Y_{v1}$  (visible opacity stream 1/ $\kappa_{IR}$ ),  $Y_{v2}$  (visible opacity stream 2/ $\kappa_{IR}$ ),  $\beta$  (albedo + emission + redistribution), and  $\alpha$  (stream allocation)—are described in further detail inside the table included in Figure 2.2 below. I used this function form to parametrize the thermal structure in NEMESIS as continuously retrieving each layer of the atmosphere produces physically improbable results for the  $P$ - $T$  profile. While  $P$ - $T$  can be informed by secondary eclipse measurements of a planet’s dayside, this only helps constrain the structure over the altitudes thermally contributing to the spectrum (Feng et al. 2016). For the other regions in the grid with  $N_{lev}$  layers, the retrieval model just guesses a profile made out of individual layer values that helps match the spectrum the best, without considering the thermal structure in its entirety.

The ideal retrieval scenario has fewer retrievable parameters—which add to the degrees of freedom—than total data points. This is only possible for high-resolution data. Individually retrieving the temperature of some 50, 100 or even 200 discrete vertical grid points does not make sense unless the dataset helps constrain multiple regions of the atmosphere. For present exoplanet datasets from space, it is thus important to find a way to reduce degrees of freedom in the model, so a physics-motivated thermal structure that uses five parameters like the one here to construct a  $P$ - $T$  profile, is much preferred both from computational time and accuracy perspectives.

$T(P) = (T_{int}, \gamma_1, \gamma_2, \tau_{IR}, \alpha, T_{irr})$ , where $\tau_{IR} \rightarrow \tau_{IR}(\kappa_{IR}, g_p, P)$ , $T_{irr} \rightarrow T_{irr}(\beta, R_*, T_*, a)$ Profile assumes 1 upwelling IR stream + 2 independent visible downwelling streams.	
$T_{int}$	Internal heat flux from outgoing IR stream (held constant in Mike Line's retrievals)
$\kappa_{IR}$	Grey ( $P$ -independent) thermal/IR opacity, controls tropopause altitude (retrieved)
$\alpha$	Partitions solar flux (visible only) between the two incoming streams (retrieved)
$\gamma_1, \gamma_2$	Ratios of Planck mean opacities of each visible stream to $\kappa_{IR}$ (retrieved)
$\beta$	"Catch-all" scaling term for albedo + emissivity + day-night redistribution; controls net stellar irradiation, so determines equilibrium temperature of planet (retrieved)

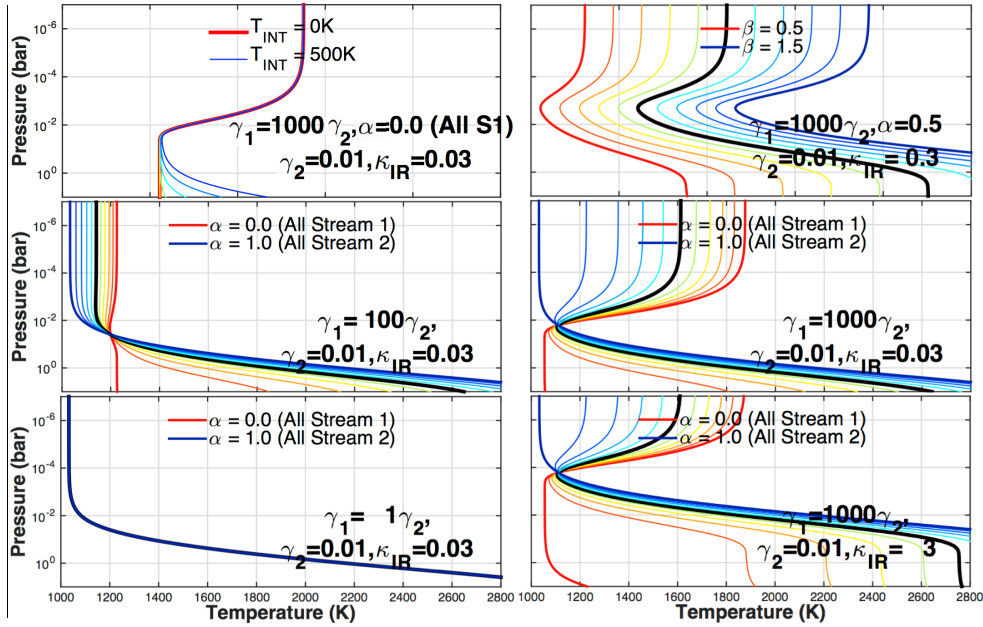


**Figure 2.2:** My plots of the radiative equilibrium  $P$ - $T$  parameterization from Line & Yung 2013 (from the analytical derivations in Guillot 2010; Hansen 2008; Heng 2012; Robinson & Catling 2012). The effect of varying each parameter is shown. If one of the downwelling opacities ( $\gamma_1$  or  $\gamma_2$ ) is much higher than the other, thermal inversion is possible. Under such dichotomy, the troposphere temperature also goes up upon raising the internal flux (which I investigated). The degree of inversion depends on how much of the total flux is present in the higher  $\gamma_1$  stream. When  $\gamma_1 = \gamma_2$ , the same structure is computed, regardless of how the flux is distributed. This parameterization forces the uppermost regions to conform to isothermal shapes and is thus only valid for equilibrium models. The Parmentier model (used to generate the  $P$ - $T$  figure from Koppurapu et al. 2018 in Chapter 6) includes additional opacity streams, accounting for more processes.

## Chapter 3: Irradiated Gas Giants: Forward Modeling & Retrieval Efforts

In this chapter, I summarize the model development and validation work I have done on a few well-studied hot Jupiters in two different GSFC exoplanet groups. I present a narrative of the techniques and features I built and/or improved within the NEMESIS spectral analysis and the Atmos photochemistry modeling tools introduced in Chapter 2, and then tested and officially validated via reproducing hot Jupiter literature results from 2010-2015. While I have made numerous general upgrades to the codes I helped develop that have benefited the entire userbase of both NEMESIS and Atmos, I will only focus on activities I conducted with hot Jupiters in mind. Potentially publishable science from these developments are part of the last chapter, entitled “Future Work”. I begin chronologically here. I first summarize the work I did with NEMESIS from 2014 to mid-2015. The second part of this write-up is dedicated to the details of my hot Jupiter photochemical model template development efforts from 2016 to early 2017, which I mentioned briefly in the preceding chapter.

### 3.1 Irradiated Exoplanet Retrieval Efforts with NEMESIS

The NEMESIS radiative transfer and atmospheric retrieval package, described briefly in Chapter 2, was heavily updated post 2010 for application to hot Jupiter and brown dwarf data. Initial extensions included the addition of primary transit, secondary eclipse and direct imaging modules. I got involved with NEMESIS in early 2014, was eventually granted developer access to the NEMESIS repository later that year, and became the only external investigator to be involved in its development for exoplanet applications from April 2014 through summer 2015.

Towards the end of 2014, I began building a framework for a MCMC-based retrieval algorithm within the code to enable data-driven retrievals. During my preceding months of involvement in NEMESIS development, I had made several technical discoveries, such as “death spiral” scenarios that either break the algorithm or result in the creation of infinitely large log files, the dependence of the retrieved profile height recalculations on user-modified temperature profiles, and a few other major codebase bugs that I shared in meetings. These were critical towards improving exoplanet results published by the NEMESIS community. This experience gave me insight that proved to be invaluable for the development of the new MCMC platform.

I used the NEMESIS team’s high- $T$  opacity-distribution tables, aka  $k$ -tables (i.e. tables of correlated- $k$  values), available at the time with modified setup files to reproduce the early Lee et al. and Barstow et al. work for the mini-Neptune GJ1214b observed in primary transit (Barstow et al. 2013) and the hot Jupiter HD189733b observed in secondary eclipse (Lee et al. 2012). High- $T$   $k$ -tables are only available for H<sub>2</sub>O, CO, CH<sub>4</sub> and CO<sub>2</sub> within the NEMESIS codebase, the four major non-background species inferred to be present in irradiated giant atmospheres. The database also contains atomic absorption from alkali metals Na and K. See Table 3.1 for the line list sources, taken from Barstow et al. (2017), which details the retrieval analysis of 10 hot Jupiters observed in transmission (from Sing et al. 2016). Parameters for He and H<sub>2</sub>, the two background gases in giant planet atmospheres, do not require opacity data but have their presence factored into the Rayleigh scattering routine in NEMESIS. H<sub>2</sub>-H<sub>2</sub> and H<sub>2</sub>-He CIA opacities are included, latter being a new addition.

The reproduction of Barstow et al. results allowed me identify and diagnose

**Table 3.1** Sources for the Gas Absorption Line Data used for computed  $k$ -tables

Gas	Source
H <sub>2</sub> O	HITEMP2010 (Rothman et al. 2010)
CO <sub>2</sub>	CDS-1000 (Tashkun et al. 2003)
CO	HITRAN1995 (Rothman et al. 1995)
CH <sub>4</sub>	STDS (Wenger & Champion 1998)
Na	VALD (Heiter et al. 2008)
K	VALD (Heiter et al. 2008)

any changes in retrievals due to i) updates I made in the Nemesis algorithm and ii) updated line parameter databases since those results were published. Line databases important for deciphering extrasolar atmospheres and outer Solar System objects are continually being improved via laboratory or ab initio investigations as these atmospheres are not only far hotter or far cooler than our own but can also have very different surface pressures (Chamberlain et al. 1990, Fortney et al. 2016). Since calculation of the forward model utilizes correlated  $k$ -distribution amongst atmospheric layers, high- $T$  updates to these line parameters, which usually involve additional lines being factored and updated broadening coefficients, could impact the retrievals quite significantly, especially for bodies that are poorly constrained from observations.

In Barstow et al. (2011), a series of “bracketed retrievals” were conducted on GJ1214b transmission spectrum to see how varying the *a priori* value of one parameter at a time affects the retrieved value of all six parameters (number density of two hypothetical clouds, the mixing ratio of three species, and the radius). I also explored the effect of including newer photometric points with greater S/N ratio on those results. Finding non-trivial discrepancies between my attempts and the study results, I

sought to trace the issues back to updates in the retrieval algorithm and  $k$ -tables for individual species. I found that the CH<sub>4</sub>  $k$ -table had been modified from its original version and has erroneous values above 2.0  $\mu\text{m}$ . The spectral fitting inconsistencies are fixed with a different table. My then GSFC supervisor (A. Mandell) suggested that I apply  $k$ -distribution theory to create my own  $k$ -tables of H<sub>2</sub>O, CO<sub>2</sub>, CO and CH<sub>4</sub>.

Some of the bracketed retrievals failed to converge within the specified number of iterations. I observed an oscillating behavior in the convergence parameters in these non-converging scenarios. For ill-constrained problems, NEMESIS often fails to meet all of convergence criteria simultaneously. These retrievals thus stop only after they have reached the maximum number of iterations. I proposed a solution that involved tweaking the algorithm to enable any retrieval to converge under an alternate set of criteria, invoking NEMESIS to force-converge before we approached oscillating behavior. The amendments were pushed to the main version.

When I began using NEMESIS, it only had the OE convergence scheme for retrievals. I was encouraged by NEMESIS author to complete the MCMC wrapper within NEMESIS—an effort he began in 2014 that I completed. Since the MCMC method generates a posterior distribution of the parameters through a random walk process, it relies less on the quality of measurement data than a purely OE-based method. An MCMC method samples the solutions over a grid of values and thus finds a range of possible solutions, which includes local minima as well as the global minima. Given the quality of our current datasets, this method has proven to be a worthy approach.

With a properly working MCMC algorithm, we expect a range of values for each parameter that roughly fall in a normal distribution. The computation time is linearly

dependent on the number of spectral points, in addition to the number of retrieval parameters, making it very expensive. Retrieval runs go faster, especially for photometric data points (e.g. when fitting *Spitzer* IRAC and MIPS data), if the  $k$ -tables are binned to the data resolution and used directly in retrievals. We refer to these tables as “channel-integrated”  $k$ -tables. This does mean we need to compute  $k$ -tables for each dataset resolution and then combine across the desired wavelength range, which is time consuming.

We can save time in thermal structure retrieval by casting  $T(P)$  profile in the equation form (last section of Chapter 2) and retrieving the equation parameters instead of trying to (unphysically) retrieve the temperature at each pressure point. Henceforth, I coded the equation and the Jacobians for each of the five parameters from the Line et al. (2013) paper into NEMESIS. Such parametrization schemes drastically reduce the retrieval cost, while also increasing the physical plausibility of retrieved results as the schemes are informed by physics. It is worth noting that the analytical radiative equilibrium thermal structure from Line et al. (2013) requires aerosol-free atmosphere assumption. While both Line and Parmentier models were developed from the same theoretical groundwork (Guillot et al. 2010), Parmentier’s form factors more atmospheric processes (see Parmentier et al. 2015a for details).

I also computed some new high-resolution and *Spitzer* channel-integrated  $k$ -distribution tables from the high-temperature spectroscopic databases brought up in Chapter 2 (HITEMP, CDS-4000, BT2) to improve the speed, versatility, portability and reliability of retrieval models, while allowing for more transition lines. I used the hybrid version of NEMESIS to get a distribution of likely values for the five-parameter

*pressure-temperature (P-T)* profile, and altitude-invariant major species volume-mixing ratios of the daysides of two popular hot Jupiters HD189733b and HD209458b. I used both OE and MCMC as OE can be used to acquire priors for the MCMC run and is typically used for that anyway in a multi-platform retrieval routine.

I used the Oxford group's prior work and Mike Line's PhD work results for validation (Lee et al. 2011, Barstow et al. 2014; Line et al. 2011, 2012, 2013; Diamond-Lowe et al. 2014). Data in those papers came from *HST*/WFC3 and *Spitzer*/(IRAC + MIPS). I compared them with retrievals on *JWST*/NIRSPEC simulated spectra of those atmospheres. I retrieved the *P-T* profiles and altitude-invariant H<sub>2</sub>O, CO<sub>2</sub>, CH<sub>4</sub> and CO VMRs from the simulated emission spectra. HD209458b is particularly intriguing as the first photometric observations with the *Spitzer* telescope indicated the presence of stratospheric thermal inversion in this planet (Knutson et al. 2008, see Figure 3.2). This was disproven recently in light of new *Spitzer* data that lacked the (previously observed) emission features in the 3.6 and 4.5 μm bands. In the published retrievals for the dataset, it was noted that an unnaturally high CO abundance had to be used (with respect to CO<sub>2</sub>) within their models to fit the emission features—that is, high enough to be unphysical. Initially, I was initially not able to fit those emission features fully with the MCMC runs, despite pumping up the CO abundance and using OE to identify a good starting point (i.e. local minimum), which is necessary for MCMC initialization on ill-constrained datasets like this one. When I took a retrieved *P-T* profile (i.e. an already converged/best case scenario profile) and generated a forward model with it, I was able to produce the emission, as shown in Figure 3.2. Upon consulting M. Line (private communication; September 2015), and allowing the two Planck

mean opacity terms comprising the  $P$ - $T$  profile (Figure 2.2 in Chapter 2) to take lower values than the range they published, I was able to fit the data with NEMESIS MCMC.

In addition, I consistently retrieved lower temperatures for the low altitudes in both HD189733b (Figure 3.1) and HD209458b (Figure 3.2). This happened because I imposed a temperature upper limit of 3000K over the pressure levels we are sensitive to over the IR bandpass. CHIMERA group’s work did not impose an upper limit and assumed the 3000K radiative transfer value for temperatures  $> 3000$ K.

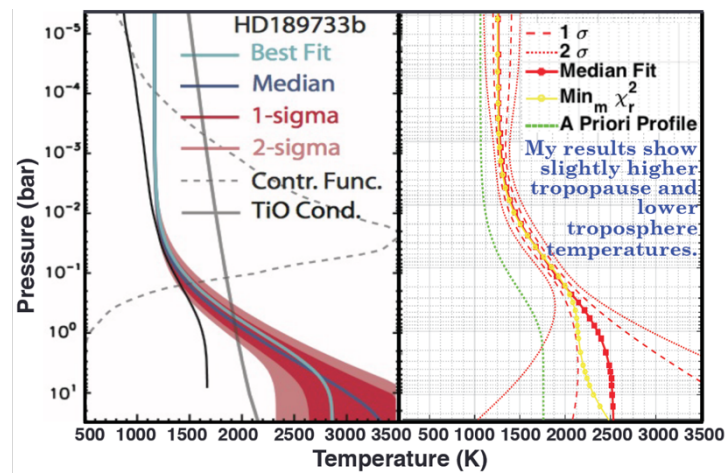


**Figure 3.1:** Left: Retrieved  $P$ - $T$  profiles shown from Line et al. (2012) HD189733b results (uses old HST/NICMOS data from Swain et al. 2009), with the planet’s thermal contribution function overlaid. Right: My attempt at replication, which found a slightly higher tropopause location in addition to lower overall troposphere temperatures.

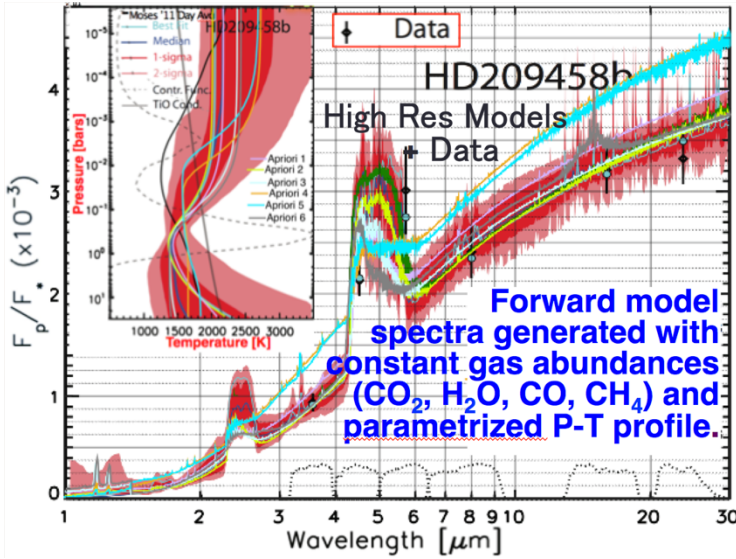


**Figure 3.2:** Forward models generated with six different input parameter profiles (see temperature inset) to obtain a priori solutions to initialize the MCMC runs on Knutson et al. (2008) HD209458b Spitzer data. Here I have overlaid my work on a plot from Line et al 2013.)

Retrievals on the *JWST*/NIRSpec simulated spectra of HD189733b and HD209458b are also shown (Figure 3.3 and 3.4) and are new work. The project, however, abruptly ended there, so these are the first new and last results I got with my efforts. The NIRSPEC simulator, developed by then fellow GSFC-resident PhD student, Natasha Batalha (Batalha et al. 2015), is now part of the publicly available community tool called PandExo (Batalha et al. 2017). PandExo relies on STScI’s exposure time calculator Pandeia described in Pontoppidan et al. (2016). Identical results between the combined 1.7-5  $\mu\text{m}$  and NIRSPEC1/G235M isolated cases may be telling us that the most reliability constrained species here is  $\text{H}_2\text{O}$  (since  $\text{H}_2\text{O}$  has a feature in the NIRSPEC1 band but not NIRSPEC2). Suppose we encounter a planet lacking appreciable amount of water vapor (perhaps a planetary atmosphere with high  $[\text{C}]/[\text{O}]$  ratio, e.g. see the super-solar  $[\text{C}]/[\text{O}]$  WASP12b results in Kopparapu et al. 2012), we may not need to use the NIRSPEC 1.7-3  $\mu\text{m}$  observation mode at all!  $\text{CO}_2$  and  $\text{CO}$  VMR

distributions are obtained as well, but they would be degenerate with respect to each other, since  $R \sim 100\text{-}200$  is not high enough for distinguishing between the two molecules, per Table 1.1 in Chapter 1. Also, we are finally able to constrain  $\text{CH}_4$  abundance from the  $3.31 \mu\text{m}$   $\text{CH}_4$  feature (resolved for  $R \sim 100\text{-}200$ ), whereas present datasets have only managed to give us a  $\text{CH}_4$  upper limit for HD189733b (see Figure 3.4).

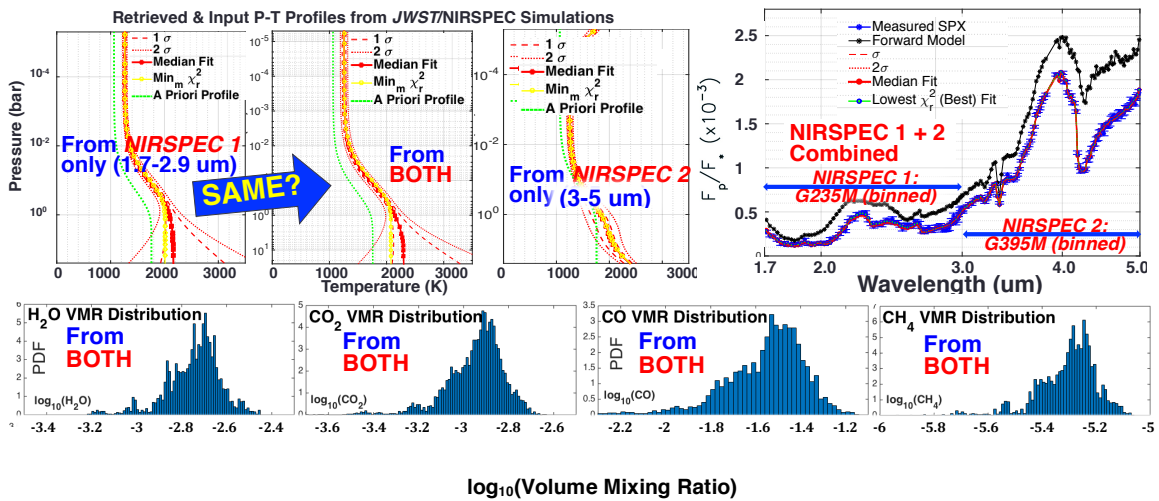


**Figure 3.3:** NIRSPEC simulations of HD189733b dayside emission in two different instrument modes. Since NEMESIS cannot presently handle datasets larger than 1024 points, the simulations shown have been binned to a variable resolution of  $R \sim 100$  to 200 for both G235 and G395 gratings—mimicking NIRSPEC’s LRS/prism capability when combined (full 1.7–5  $\mu\text{m}$ ). Forward model spectra (top right, in black), simulations created from that model (top right, in blue), and best-fit retrieved spectra (in red) are shown for the combined case. The constant volume mixing ratio values retrieved with NEMESIS MCMC are also shown (bottom panel). Retrieved  $P$ - $T$  profile statistics are also shown in red (top left), but for the separate instruments as well as the combined 1.7–5  $\mu\text{m}$  case. The  $P$ - $T$  plots show that the 1.7–2.9  $\mu\text{m}$  mode alone retrieves the same profile as combined (LRS) case. Such behavior may help us devise strategies for follow-up observations by indicating the dominant species.

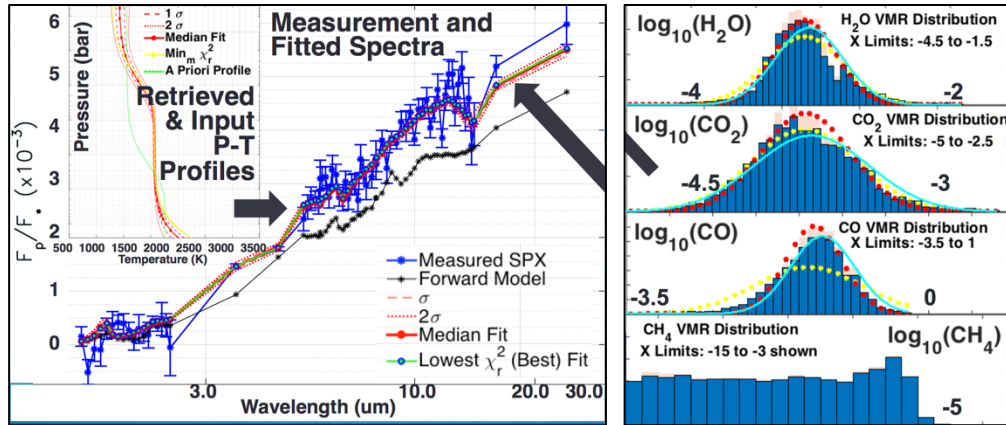


**Figure 3.4:** Results from my NEMESIS retrievals on the HD189733b Barstow et al. (2013) data (data sources: *Spitzer* IRS & MIPS, and the Swain et al. (2009) *HST*/NICMOS data re-analyzed). I did this to test my new MCMC and  $P$ - $T$  parameterization additions to NEMESIS. My retrieved volume mixing ratios matched the ranges given in recent literature using this dataset with similar methods. We could only get an upper limit on  $\text{CH}_4$  abundance, which was in line with the efforts in literature.

The anticipated capabilities of *JWST* should help us get answers to many lingering questions we have regarding hot Jupiter atmospheres. Rochetto et al. (2016) explores biases in future (*JWST*-simulated) atmospheric retrievals of hot Jupiters, using hypothetical cloud-free hot Jupiter atmospheric states generated by 1-D photochemical models for a range of  $[\text{C}]/[\text{O}]$  values. The retrievals from using an isothermal  $P$ - $T$  profiles were compared with those that allowed the  $P$ - $T$  to take a parameterized form instead—something I also investigated in 2015 as part of my similar hot Jupiter retrieval efforts with NEMESIS MCMC. As expected from my own efforts, Rochetto et al. (2016) found biases in the retrieved altitude-invariant mixing ratio values with the isothermal  $P$ - $T$  prescription, and was able to draw tighter constraints on the composition as well as the thermal structure with the parameterized assumption.

## 3.2 Irradiated Exoplanet Photochemical Modeling: Hot Jupiters

In Chapter 1, I briefly described why accurate interpretation of irradiated exoplanet observations require that we consider photochemistry in our atmospheric models of these planets. Recent literature (e.g. Line et al. [2010](#) for HD189733b, Kopparapu et al. [2012](#) for WASP12b) has shown that chemical disequilibrium may prevail in regions of irradiated planetary atmospheres sampled by space probes, thus possibly responsible for non-intuitive chemical trends inferred from fitting chemical models to observations. For example, Swain et al. ([2008](#)) found methane rather than carbon monoxide (latter being thermodynamically favored) from analyzing their transmission spectrum of HD189733b. This can be in part due to the photochemical breakdown of weakly bond species in its atmosphere, which may enhance CH<sub>4</sub> from the recombination of short-lived free C-based radicals (Liang et al. [2004](#)). Photochemistry-induced variations are also greater for species not usually abundant in equilibrium at the sampled altitudes, which also affects spectral interpretation.

Below, I provide a brief overview of recent noteworthy literature on hot Jupiter properties inferred via photochemical models, and then summarize my own hot Jupiter photochemical model efforts to date with the Atmos PHOTOCHEM module. A thorough description of the chemical and dynamical processes in hot Jupiters can be found in Part III of Liang ([2006](#); PhD thesis).

### 3.2.1 Hot Jupiter Photochemical Modeling: Community Motivation

Hot Jupiters have been studied by various exoplanet atmospheric modeling groups with both equilibrium and disequilibrium effects considered. Other groups

have also developed 1-D photochemical models to explain presently available hot Jupiter observations, and here I will review efforts not highlighted within the context of the preceding chapters. These efforts date back to the previous decade; Liang et al. (2004) modeled photochemically-generated hydrocarbon aerosols expected in these planets before they were even called “hot Jupiters”, finding the presence of such aerosols to be insignificant compared to Jupiter and Saturn. Zahnle et al. (2009, 2011) developed a 1-D photochemical kinetics code to capture the stratosphere heating and chemistry in hot Jupiters orbiting a solar-twin host, focusing the detection of carbon dioxide and photochemically altered S-containing species for atmospheres with  $T_{eq}$  in the 1200-2000 K range—such species can provide additional stratospheric heating. They found that while  $S_2$  and HS (latter more abundant under hot Jupiter conditions) heat the stratosphere, the total heating is insensitive to metallicity. They also found the  $CO_2$  abundance to be a measurable function of metallicity, but not dependent on insolation, mixing, temperature and gravity, confirming that  $CO_2$  may be useful in probing metallicity (suggested by Lodders & Feggle 2002).

The work above was motivated by the need to map stratospheric heating sources to understand the source of thermal inversions in hot Jupiter middle atmospheres (first seen by Richardson et al. 2007; Harrington et al. 2007, soon confirmed by *Spitzer* observations, e.g. Knutson et al. 2008a, 2009; Machalek et al. 2008). These inversions may have been triggered by evaporation of TiO and VO (Hubeny et al. 2003; Burrows et al. 2007, 2008; Fortney et al. 2008), but irradiation levels alone may not provide enough heating for this (Torres et al. 2008, Knutson et al. 2010), necessitating investigations into other heat sources. In the Solar System, thermal inversions

are often caused by photochemically generated new species and depletion of responsible absorber(s); photochemistry may also need to be invoked to explain this additional middle atmosphere heating leading to thermal inversions in hot Jupiters. It is worth noting here that the spectral models used in these studies typically assume local thermodynamic equilibrium (LTE), an assumption that tends to overestimate radiative cooling (i.e. underestimate the temperature). Non-LTE models can improve the agreement by factoring vibrational heating in the upper atmospheres. This is one of the motivations behind pursuing the non-LTE modeling work laid out in Chapter 6.

More recently, Moses et al. (2011) used KINETICS—the 1-D photochemical, thermochemical and diffusion model from Caltech/JPL (Allen et al. 1981 and references therein)—to investigate coupled chemistry of CHNO species on both HD189733b and HD209458b. They found that the mixing ratios of the species are significantly affected by vertical quenching, particularly for the cooler HD189733b. Equilibrium is maintained for a wider altitude range for HD209458b due to its hotter atmosphere ensuring more efficient mixing (Chapter 1). For both planets studied in Moses et al. (2011), CH<sub>4</sub> and NH<sub>3</sub> are found to be enhanced at lower altitudes due to quenching, while depleted at higher altitudes due to photochemistry, which lead to enhancements of nitriles (e.g. HCN) and complex hydrocarbons instead (Liang et al. 2004; Zahnle et al. 2009, 2011; Line et al. 2010), along with the hydroxyl (OH) and methyl (CH<sub>3</sub>) fast-reacting radicals. However, the species CO, H<sub>2</sub>O, N<sub>2</sub> and CO<sub>2</sub> closely follow their equilibrium profiles for  $P \gtrsim 1 \mu\text{bar}$ . These species remain relatively unaffected due to their strong bonds and/or efficient recombination. In addition, large quantities of atomic H are produced from photochemistry due to H<sub>2</sub>O-initiated

catalytic feedbacks (Liang et al. 2003; Yelle 2004; Garcia Munoz 2007), and H exceeds H<sub>2</sub> abundance in the uppermost atmosphere.

The explanations above are also responsible for the differences from transport-induced quenching between Figures 3.5 (photochemistry + equilibrium chemistry in WASP12b with Atmos) and 3.6 (photochemistry + equilibrium chemistry in the much cooler HD189733b with Atmos). Since the depleted and enhanced species could affect the thermal structure and spectral signatures dramatically, they studied the sensitivity of their results to the  $P$ - $T$  and  $K_{zz}$  profiles to infer observational consequences. As emphasized in the preceding chapters, the results are highly sensitive to these factors and the metallicity—parameters that are not well-constrained by current observations. Constraining metallicity and the CH<sub>4</sub> abundance from future hot Jupiter observations would allow us to pinpoint the CH<sub>4</sub>→CO quench point. Also, a relatively low  $K_{zz}$  ( $< 10^8 \text{ cm}^2 \text{ s}^{-1}$ ) would deem transport-induced quenching to less important, although  $K_{zz}$  values of tidally-locked planets tend to be on the higher (refer to relevant discussion in Chapter 2) end generally. Furthermore, even if prevailing  $K_{zz}$  is low, heavy species in the atmosphere can still be dragged up into the uppermost atmosphere due to vertical hydrodynamical wind.

One key recommendation to come from this study is the consideration of N-bearing species (instead of just the typical CO, CO<sub>2</sub>, H<sub>2</sub>O, CH<sub>4</sub>) when analyzing transit and eclipse data. This recommendation would be more important for high [C]/[O] planets due to greater photochemical production of N-based species (Kopparapu et al. 2012). Recent *HST*/WFC3 transmission spectra of hot Jupiters showed a feature at 1.55  $\mu\text{m}$ , which can be attributed to NH<sub>3</sub> or HCN—both strong indicators of chemical

disequilibrium as have learned. Constraining the atmospheric N abundance from these observations may help us identify likely planet formation pathways. MacDonald & Madhusudhan (2017) explored the detectability of N-based chemistry in hot Jupiters over NIR wavelengths 1-5  $\mu\text{m}$ . In their retrievals, they found weak detections of  $\text{NH}_3$  in WASP-31b ( $2.2\sigma$ ), HCN in WASP-63b ( $2.3\sigma$ ), and excess absorption in HD 209458b likely from  $\text{NH}_3$ . These features should soon be detectable with *JWST*.

The Moses et al. (2011) study also suggests that photochemically-formed soot in cooler hot Jupiters was overemphasized in Zahnle et al. (2011). Soot should be prevalent on hotter Jupiters as complex hydrocarbons may not survive long in those atmospheres due to higher- $T$  kinetics and the higher abundance of atomic H. Neutral C-N-O cannot explain the differences in inferred  $P$ - $T$  profiles of the two planets studied here. In hot Jupiters, soot and other organic solid condensates (and destruction of relevant absorbers) can also come from ion chemistry initiated by energetic UV radiation such as EUV and Ly- $\alpha$  radiation. See Lavvas & Koskinen (2017) for a recent study on the impact of aerosol properties on the spectra of both of planets ( $P$ - $T$  profile source: Moses et al. 2011, Line et al. 2014).

Photochemical hazes can still form in hotter Jupiter atmospheres with super-Solar  $[\text{C}]/[\text{O}]$  (Fleury et al. 2019). In reduced atmospheres, high-altitude hazes and new condensible products can result from EUV-induced upper atmosphere processes, which can obscure important observers as mentioned in Chapter 1. Clouds and hazes all kinds of exoplanetary and brown dwarf atmospheres (Morley 2016) can originate from condensation chemistry as well as photochemistry. Wakeford et al. (2014) examined expected cloud condensate species for hot Jupiters and the impact

of varying their properties on the resulting broadband (visible + IR) transmission spectra. The Different vibrational modes could be discerned from the longwave spectra. Vibrations bonds should allow for distinctions between the two cloud forming mechanisms. Using Wakeford et al. (2014) and follow-up studies as a diagnostic tool, future IR observations of hot Jupiters (e.g. with *JWST*/MIRI) may allow us to identify the clouds and constrain their location and distribution.

Since photochemistry dominates in the upper altitudes, there can be large variations in the abundance of impacted species with longitude as well. By comparing the difference in abundances of quenched species in the limb (from primary transit observations) with the dayside (from secondary eclipse observations), the rate of horizontal transport in the lower stratosphere may be roughly inferred (also Moses et al. 2011). The study also finds CO rather than CH<sub>4</sub> to be the dominant C-bearing species in the upper atmosphere, despite factoring photochemistry, contradicting the aforementioned conclusions from Swain et al. (2008) and also Zahnle et al. (2009; 2011). It should be noted that photochemically-generated nitriles and hydrocarbons from the dayside can possibly convert back to CH<sub>4</sub> on the nightside. This can potentially flow back to the dayside and be a strong absorber of stellar irradiation, which can lead to strong non-LTE emission (Swain et al. 2010).

Other groups have also developed models to conduct photochemical studies focused on both HD189733b and HD209458b and compared their findings with Moses et al. (2011). Venot et al. (2012) describes the development and attributes of (e.g. associated chemical reaction rate coefficients) their own chemical network to study these two planets, a network supposedly valid for atmospheres with simple C- and N-

based species and for temperatures within the range 300-2500 K and pressures from 10 mbar up to a few 100 bars. Their chemical scheme is based on applied combustion models previously validated over a range of temperatures and pressures typical to hot Jupiters. They compare their results with the Moses et al. (2011) calculations (see Figures 4 through 8 of Venot et al. 2012) and other models, also finding disequilibrium to be more prevalent in the cooler planet of the two planets, but compute different steady-state mixing ratio profiles. They find the abundance of ammonia and nitriles to be heavily chemical network dependent, and cite the necessity of observational verification (e.g.  $\text{NH}_3$  has a spectral feature at 10.5  $\mu\text{m}$ ). Agundez et al. (2014) developed a pseudo 2-D atmospheric model to study longitudinal chemical transport in these hot Jupiter atmospheres. In addition to the usual chemical kinetics, vertical and horizontal transport were both modeled. The horizontal transport was modeled as a uniform zonal wind and the Eddy diffusion coefficients were obtained from GCMs. The composition on the nightside was quenched to the dayside composition. Such longitudinal homogeneity of chemical composition was achieved due to the zonal wind being strong, particularly for HD189733b for lacking thermal inversion. This means changes in the emission spectra with phase barely depend on the composition, and is instead dictated by the changing thermal structure as the planet orbits.

A follow-up study (Moses et al. 2013) with the KINETICS 1-D chemical kinetics model explored the impact of  $[\text{C}]/[\text{O}]$  ratio on the chemical composition and resulting spectra for hot Jupiter atmospheres. Equilibrium chemistry—which provide the deep atmospheric abundances for major species—is highly sensitive to  $[\text{C}]/[\text{O}]$  ratios. The results from the study also support other findings in Kopparapu et al. (2012); they

found that for  $[C]/[O] < 1$ , O-bearing molecules like  $H_2O$  and  $CO_2$  were preferred over  $CO$ , and whereas  $CH_4$ ,  $HCN$ , and  $C_2H_2$  became significant for  $[C]/[O] > 1$ , indicating a greater degree of impact from disequilibrium processes. N-bearing species without C or O remained relatively unaffected by the  $[C]/[O]$ . Upon comparing spectral results from their models with *Spitzer* photometric data, they concluded the following: (1) disequilibrium models with  $C/O \sim 1$  matched WASP-12b, XO-1b, and CoRoT-2b, confirming these planets' likelihood for being C-rich; (2) HD 189733b data are consistent with  $C/O < 1$ ; (3)  $HCN$  can potentially provide more opacity at 3.6 and 8.0  $\mu m$  channels than  $CH_4$  for  $C/O > 1$ ; (4) low derived  $H_2O$  is likely indicative of an atmosphere with a  $[C]/[O]$  ratio greater than solar value (e.g Kopparapu et al. [2012](#); Madhusudhan et al [2011a](#), [2012](#)); and (5) chemical kinetics alone cannot explain the high  $CO_2$  they inferred from the HD189733b NIR data. The study concluded by providing possible formation scenarios for C-rich planets: 1) accretion of CO-rich but  $H_2O$ -poor gas envelope; b) accretion of C-rich solids when migrating inward from beyond snow line.

### 3.2.2 Hot Jupiter Photochemical Modeling with Atmos PHOTOCHEM

Unlike Earth-like planets, we do not have any observationally-verified knowledge regarding lower boundary conditions in these planets. We thus need to use equilibrium chemistry profiles as the input mixing ratios (i.e. the dotted profiles in the two figures below), and for major species, we hold the lower boundary fixed to the lowest atmospheric level abundance value given by the equilibrium profiles. We also need to use the generalized binary diffusion equation to compute molecular diffusion—versus the  $T$  and  $N_2$  abundance dependent simplified formulations used for

N<sub>2</sub>-dominated terrestrial atmospheres—as these atmospheres have H<sub>2</sub> as background gas, not N<sub>2</sub>. We also use extremely low albedos compared to our values for Earth templates in Atmos (0.01 versus 0.25 for Earth) for the hot Jupiter templates, as hot Jupiters lack reflective clouds. We also properly calculate thermochemical reaction rates within the model for each reaction by using the temperature info and reaction rate constant supplied in the reaction list input file. The Earth templates use custom hardcoded expressions for majority of the reactions, obtained over the year from various legacy sources. We can also use new UV cross-section data from KIDA.

### 3.2.2.1 Preliminary Efforts: Validation with Published WASP12b Model

The sources for the spectral data, photolysis cross-section info, and rate coefficient data are consistent with those used in Kopparapu et al (2012). The stellar spectra of the G0V star, Beta Comae, is binned to 50 Å with Ly-α from Landsman & Simon (1993). The reaction list uses reactions published in Zahnle et al. (2011) and Kopparapu et al. (2012), and involves 179 reactions with 21 species. The *P-T* profile was taken from Madhusudhan (2011) and the Eddy diffusion from Line et al. (2010).

I was able to obtain almost identical steady-state mixing ratio values to those computed in Kopparapu et al. (2012), as we see in Figure 3.5 below. Minor discrepancies arose from incremental updates to the model, the most notable of these updates being corrected Rayleigh scattering, which was off by 16 orders of magnitude in Kopparapu et al. (2012) due to incorrect units for the wavelength.

Due to the super high equilibrium temperature, the WASP12b model requires several thousands of steps for convergence, and requires the convergence criterion

to be tweaked for species with profiles that fall rapidly with altitude, as this likely causes numerical stability. The photochemistry is also less noticeably impacted by UV data accuracy than the cooler HD189733b, as the G0V star irradiating this planet is way less active than the K2V planet irradiating HD189733b.

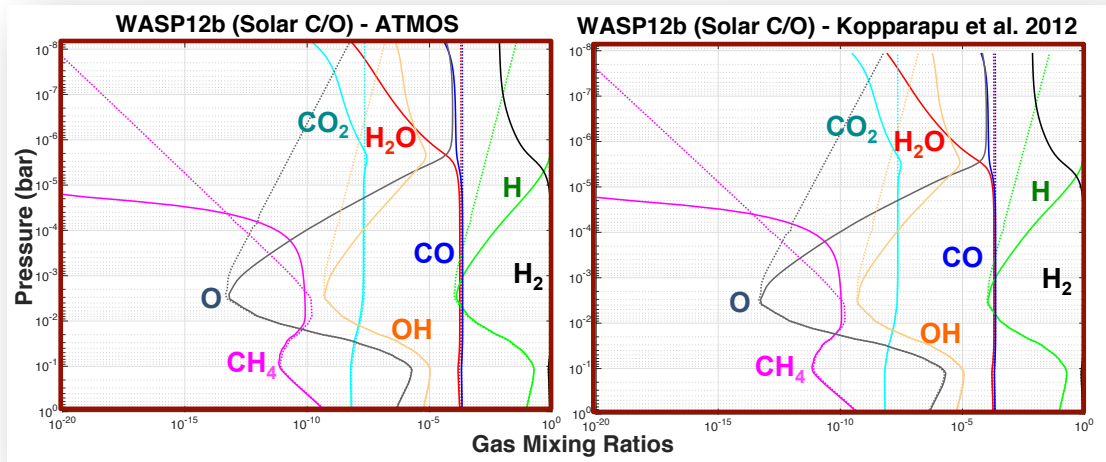


**Figure 3.5:** My attempted replication of the WASP12b model from Kopparapu et al. (2012) within Atmos for solar  $[C]/[O]$ . Each panel shows the equilibrium chemistry profiles (dotted curves)—used as the initiating (input) mixing ratio profiles within Atmos—and the steady-state profiles computed by the photochemical model (solid curves). To generate the equilibrium chemistry profiles, I used a generalized version of the script that was used to generate them for Kopparapu et al. (2012). The script uses the equilibrium chemistry principles from White et al. (1958) and convergence testing from Eriksson (1971), given user-supplied  $P$ - $T$ .

### 3.2.2.2 Modifying WASP12b Template to HD189733b Template

For the stellar data, I used the high-resolution stellar spectra of the K2V Star: Epsilon Eridani from Domagal-Goldman et al. (2014). Reaction list and temperature

profile sources are identical to those used for WASP12b. This template converged without much tweaking as HD189733b is a much cooler planet. Unlike WASP12b, I did not find much atomic oxygen or hydroxyl in this planet. The star is cooler (K2V vs G0V) but more active in FUV, meaning less irradiation with stronger photolysis effects implied at given planetary distance. HD189733b also further away than WASP12b is to its star (355x solar irradiation vs x1900). As such, diversion from chemical equilibrium starts at a lower altitude. Effects of photochemical disequilibrium is once again clearly more relevant for cooler hot Jupiters, consistent with literature.

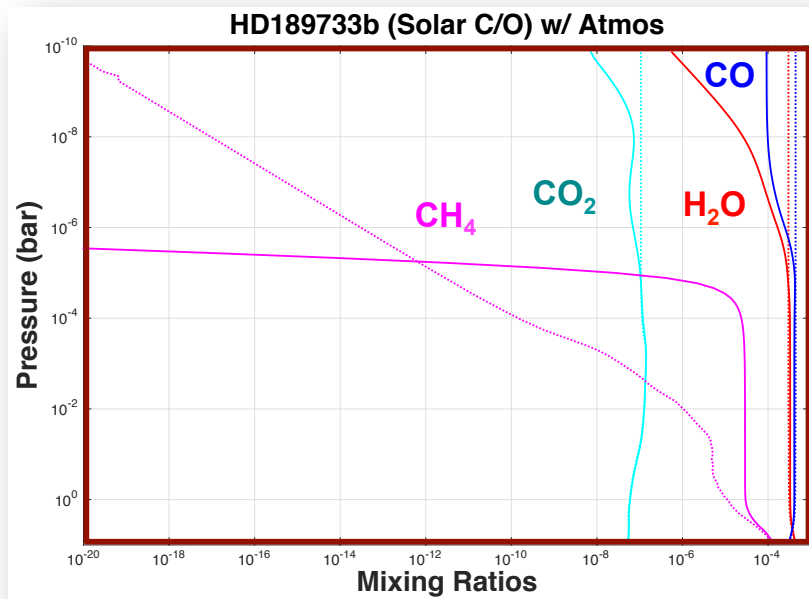


**Figure 3.6:** Steady-state mixing ratios computed by Atmos PHOTOCHEM for the HD189733b template, assuming solar  $[C]/[O]$  (for the equilibrium chemistry calculation). While this template has the same number of species as the WASP12b template above, only retrievable non-background gases are shown in this figure.

## Chapter 4: The Impact of Stellar UV Activity on Moist Habitable Terrestrial Planetary Atmospheres Around M dwarfs

### Abstract

Transit spectroscopy of terrestrial planets around nearby M dwarfs is a primary goal of space missions in coming decades. 3-D climate modeling has shown that slow-synchronous rotating terrestrial planets may develop thick clouds at the substellar point, increasing the albedo. For M dwarfs with  $T_{\text{eff}} > 3000$  K, such planets at the inner habitable zone (IHZ) have been shown to retain moist greenhouse conditions, with enhanced stratospheric water vapor ( $f_{\text{H}_2\text{O}} > 10^{-3}$ ) and low Earth-like surface temperatures. However, M dwarfs also possess strong UV activity, which may effectively photolyze stratospheric  $\text{H}_2\text{O}$ . Prior modeling efforts have not included the impact of high stellar UV activity on the  $\text{H}_2\text{O}$ . Here, we employ a 1-D photochemical model with varied stellar UV, to assess whether  $\text{H}_2\text{O}$  destruction driven by high stellar UV would affect its detectability in transmission spectroscopy. Temperature and water vapor profiles are taken from published 3-D climate model simulations for an IHZ Earth-sized planet around a 3300 K M dwarf with an  $\text{N}_2\text{-H}_2\text{O}$  atmosphere; they serve as self-consistent input profiles for the 1-D model. We explore additional chemical complexity within the 1-D model by introducing other species into the atmosphere. We find that as long as the atmosphere is well-mixed up to 1 mbar, UV activity appears to not impact detectability of  $\text{H}_2\text{O}$  in the transmission spectrum. The strongest  $\text{H}_2\text{O}$  features occur in the *JWST* MIRI instrument wavelength range and are comparable to the estimated systematic noise floor of  $\sim 50$  ppm.

## 4.1 Introduction

Planets orbiting close enough to their host M dwarf stars to be tidally-locked have their day-sides continuously subjected to the enormous UV stellar irradiation. The first habitable zone (HZ) exoplanets to have their atmospheres characterized will likely be such tidally-locked planets orbiting nearby M dwarf stars. Thus, there is a need to understand the behavior of such planetary atmospheres. Observed spectroscopic signatures from transit measurements can reveal spectrally active species in a planet's atmosphere. Present observational technologies not only inform us about the observed atmosphere's composition, but can also shed light on the planet's physical properties and atmospheric dynamics. NASA's upcoming space missions, such as the *James Webb Space Telescope (JWST)*, will meet the sensitivity and broad wavelength coverage requirements to constrain extrasolar planetary atmospheric composition with unprecedented accuracy.

Chemical disequilibrium processes (e.g. photolysis, vertical convection, life, etc.) can be diagnosed in planetary atmospheres by studying the observed trends in the abundances of detected species (e.g. Line & Yung 2013). In the deep atmosphere, where pressures and temperatures are high, reaction timescales are short. So, species tend to stay in chemical equilibrium. Temperatures tend to decrease with increasing altitude in planetary atmospheres without thermal inversions, slowing the reaction rates to a point where vertical transport starts dominating, causing species to spread out. For slowly rotating Earth-like planets, changes to the large-scale circulation lead to an increased efficiency of vertical mixing (Yang et al. 2013). This means the lower unobserved region—the troposphere—is able to communicate with the upper

regions probed by our space infra-red (IR) instruments. In the uppermost regions, the high ultra-violet (UV) instellation (i.e. stellar insolation from stars other than the Sun) can lead to photolysis and increasing depletion in the abundances of some molecular species. Planets with equilibrium temperatures below 1200K (i.e. they receive < 340-400 times the Earth-equivalent instellation  $S_0$ , using geometric albedo range of 0.01-0.15 from Heng & Demory (2013)), have been shown to have the most obvious signs of disequilibrium via chemical kinetics modeling (Liang et al. 2003, 2004; Zahnle et al. 2009b,a; Line & Yung 2013; Moses et al. 2011, 2013; Visscher & Moses 2011; Kopparapu et al. 2012; Hu et al. 2012; Miller-Ricci Kempton et al. 2012).

Disequilibrium mechanisms play a noticeable role in altering atmospheric composition at altitudes probed by remote sensing techniques. Disequilibrium sources within the solar system include Venus's sulfuric acid hazes (e.g. Yung & Demore 1982; Krasnopolsky & Pollack 1994), Titan's hydrocarbon hazes (e.g. Allen et al. 1980; Yung et al. 1984), and even Earth's ozone—a product of  $O_2$  photolysis (e.g. Chapman 1930a,b, 1942). Observational (Knutson et al. 2014; Kreidberg et al. 2014, 2018; Greene et al. 2016; Wakeford et al. 2015, 2017) and theoretical (Benneke & Seager 2013; Mbarek & Kempton 2016; Arney et al. 2017; Heng & Demory 2013; Morley et al. 2017) studies have shown that clouds and hazes dominate both transmission and reflection spectra of all kinds of planets. They can alter the thermal structure and composition in the higher altitudes, in addition to masking spectral features from the lower atmosphere. 3-D climate simulations have shown that for synchronously rotating planets, persistent substellar clouds may act in favor of habitability by increasing planetary albedo and decreasing the surface temperature, allowing

planets to remain habitable at higher stellar fluxes than that of Earth's (e.g. Yang et al. 2013; Way et al. 2016; Kopparapu et al. 2016, 2017; Bin et al. 2018). A synchronous orbit (i.e. planet spin = planet orbit) around the host star is a valid assumption for planets in the HZs of such low-mass stars (Leconte et al. 2015).

Planet rotation rate, and thus the Coriolis effect, plays a key role in modulating atmospheric circulation and climate (e.g. Merlis & Schneider 2010; Yang et al. 2014a; Noda et al. 2017; Fujii et al. 2018). For slowly rotating planets, the Coriolis effect is weak, and planets maintain large-scale day-night thermal circulation patterns. Such worlds are characterized by strong convection and upwelling air around their substellar point, and downwelling air on the antistellar side. These effects combine to yield strong vertical mixing of H<sub>2</sub>O, which creates the ubiquitous substellar cloud deck for slow rotators (e.g. Yang et al. 2013), and significantly enhances stratospheric H<sub>2</sub>O planet-wide (Kopparapu et al. 2017, Fujii et al. 2017). Planetary stratospheres are more readily sensed by transit observations than tropospheres due to refraction effects (e.g. Misra et al. 2014, B  tr  mieux & Kaltenegger 2014), and cloud opacity can prohibit observations of the relatively wet lower layers. The exact range of pressures accessible to and sensed by IR observations depends on the star-planet distance as well as the star and planet type, because the location of condensates varies with those parameters. Kopparapu et al. (2017) found that slow rotators around M dwarfs maintain moist greenhouse conditions (stratospheric H<sub>2</sub>O content >10<sup>-3</sup>, Kasting et al. 1993), despite relatively mild surface temperatures (~280 K). Therefore, we may expect to observe stronger H<sub>2</sub>O features in the transmission spectra of habitable slow rotators around M dwarfs compared to a true Earth-twin; Earth has a relatively dry

stratosphere ( $f_{H_2O} \sim 10^{-6}$ ). At 1 mbar (the model top of the 3-D climate model), vertical mixing should remain strong enough to compete with the photochemical  $H_2O$  loss (Yang et al. 2014a; Kopparapu et al. 2016; Fujii et al. 2017). The question then becomes, is the  $H_2O$  loss above 1 mbar from photodissociation significant enough to affect our ability to detect it with *JWST*? If so, can we quantify this effect?

To answer this, we study the composition of such planets with a 1-D atmospheric model that includes chemical kinetics (including photolysis) and vertical mixing. We explore the influence of UV irradiation on the composition of the atmosphere at the planet's terminator (simulated by a 3-D climate model), which is probed by transit transmission observations. We consider a 1-D model column extending above the stratosphere to explore chemical complexity from photochemical disequilibrium and its impact on observing. We look for any discernible impact on the spectra of a selected planet-star pair within the moist greenhouse regime of Kopparapu et al. (2017). Here we report our findings for an  $N_2$ - $H_2O$ -dominated moist terrestrial inner HZ planet modeled around a 3300 K M dwarf with synthetically varied stellar UV emissions from 1216-4000 Å. We compare our spectra with Kopparapu et al. (2017) and discuss implications for future observations of moist habitable atmospheres with *JWST*.

The rest of this paper is laid out as follows: in Section 4.2, we give an overview of the analysis method and describe the various modeling tools employed in this study. In Section 4.3, we present our findings for each stellar profile scenario, for a total of five scenarios. In Section 4.4, we discuss the implications of the results on molecular detection via future observations with *JWST*, and we conclude in Section 4.5.

## 4.2 Methods

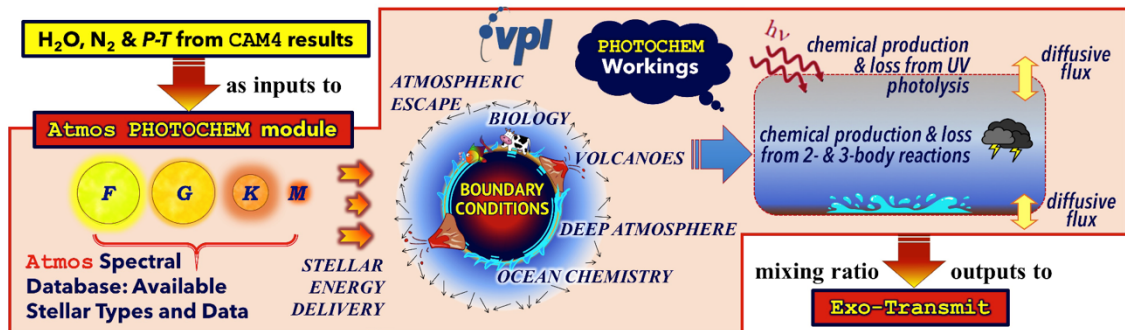
We use 3-D global climate model (GCM) results of a specific H<sub>2</sub>O-rich atmosphere case from Kopparapu et al. (2017) as the input for our 1-D models in this study (see Table 4.1, more details in Section 4.2.1). Specifically, we use terminator mean vertical profiles of P, T, N<sub>2</sub>, and H<sub>2</sub>O from the GCM as inputs for a 1-D photochemistry model (Figure 4.1). We augment our 1-D atmospheres with other species (see Section 4.2.3), including a "modern Earth" constant CO<sub>2</sub> mixing ratio of 360 ppm. We let the atmosphere evolve for five different UV cases (see Section 4.2.2), including the original UV-quiet model star used in the Kopparapu et al. (2017) study. We determine steady-state abundances for all modeled species for each simulated atmosphere. We then generate transmission spectra to determine the spectral observables of these habitable moist greenhouse atmospheres with self-consistent photochemistry.

The 3-D and 1-D models are not coupled—the GCM is run first and the output fed to the photochemical model, but the output from the latter does not provide feedback into the GCM. Currently, there is no 3-D model available with full chemical mapping capabilities for planets around M dwarfs that can simulate anoxic atmospheres (but see Chen et al. 2018, which assumes an Earth-like N<sub>2</sub>-O<sub>2</sub> biosphere). Current GCMs also do not extend to very low pressures, and thus cannot fully capture dynamics affecting upper atmosphere composition. While there are ongoing efforts to increase this range, this comes at a much higher computational cost as well.

The GCM is the Community Atmosphere Model (CAM), developed by the National Center for Atmospheric Research (NCAR) to simulate the climate of Earth (Neale et al. 2010). For the Kopparapu et al. (2017) work, Version 4 (CAM4) was

adapted to simulate Earth-like aquaplanets (i.e. an ocean planet with no land) around M dwarf stars. For our 1-D chemical modeling, we use the Atmos 1-D photochemical modeling tool, most recently developed by the Virtual Planetary Laboratory (VPL). Atmos comes with stellar flux data from the VPL spectral database. We use this data and stellar spectra from the MUSCLES Treasury Survey (Youngblood et al. 2016) to provide a range of UV fluxes for the UV-active simulations. This way we are able to realistically portray time-averaged low, medium, and high UV activity. We run a single 1-D model per UV case, for a total of five UV cases (Inactive/Low UV, Medium UV 1, Medium UV 2, High UV, Very High UV). We thus run five photochemical models for the same planet (see Table 4.1), each initiated with the same physical properties and mixing ratio profiles. We use the Exo-Transmit spectral tool to compute the transmission spectrum for each UV model (Kempton et al. 2017).

**Figure 4.1:** Our 3-D to 1-D "pseudo" coupling method shown above with the inner workings of the Atmos 1-D photochemistry indicated. Within the 1-D model, steady state mixing ratios are computed for species included in the template from user-supplied a) boundary (surface + TOA) conditions for those species, b) relevant chemical reactions involving them, and c) Eddy vertical diffusion profile  $K_{zz}$ .



## 4.2.1 Planet Parameters: Moist Atmosphere Simulations

CAM has been widely used for studies of habitable exoplanets (Yang et al. 2013, 2014a, 2016; Shields et al. 2013; Yang et al. 2014b; Wolf & Toon 2014, 2015; Kopparapu et al. 2016, 2017; Wolf 2017; Haqq-Misra et al. 2018; Wang et al. 2014,

**Table 4.1:** 1-D Model Parameters: Planet and Star Properties

Parameter	Value
Planet Mass	$1M_{\oplus}$
Planet Radius	$1R_{\oplus}$
Planet Surface Gravity <sup>1</sup>	$1g$
Planet Surface Pressure <sup>1</sup>	1.008 bar
Planet Surface Temperature	266 K
Planet Surface Albedo	0.00
Star Mass	$0.249M_{\odot}$
Star Radius	$0.137R_{\odot}$
Star Temperature $T_{\text{eff}}$	3300 K (Spectral Type M3)
Star Insolation Flux $S$	$1650 \text{ W/m}^2$ ( $1.213S_{\odot}$ )
Solar Zenith Angle <sup>2</sup>	50 degrees (substellar value)
Period	19.6 days
Semi-major Axis	0.0895 AU

<sup>1</sup>Surface values are terminator mean values, not global mean.

<sup>2</sup>We use this value in all runs to reproduce Earth's chemistry.

2016; Bin et al. 2018). CAM4 has been updated to include a flexible correlated- $k$  radiative transfer module (Wolf & Toon 2013), and updated water vapor absorption coefficients from HITRAN2012. The moist habitable atmospheres computed by CAM4 Kopparapu et al. (2017) assumed an Earth mass aquaplanet, with a 50m thick "slab" ocean. The slab ocean acts as a thermodynamic layer, where energy fluxes (radiant, latent, and sensible) are calculated between atmosphere and ocean. There is no ocean

heat transport, thus the temperature of the ocean is set by surface energy exchange process only. All simulations assumed an atmosphere composed of 1 bar of  $N_2$  and variable  $H_2O$ . Further details on the numerical scheme can be found in Neale et al. (2010) and Section 2.1 of Kopparapu et al. (2017).

We use the terminator mean surface values and vertical profiles from a single GCM run from Kopparapu et al. (2017) as the inputs for our 1-D models here. These mean profiles are both time-averaged (over many orbits) and spatially averaged. The spatial averaging methodology factors the difference in grid box sizes between equator to pole, and the profiles are averaged equally amongst all terminator columns. The multi-earth year temporal means spanned 5 Earth years (i.e.  $\sim 90$  orbits), so temporal variability is small. Spatial variability at the model top is also generally small, generally less than a factor of 1.5 to 2. Orders of magnitude is what matters for our results in this study, and since this is small for both variabilities, neither are significant for our study. So, the averaged profiles suffice for our purpose.

We use the planetary terminator results of the 3300 K model star irradiating the synchronously rotating (orbital-rotational period: 19.6 days) Earth-like planet (see Table 4.1) at  $1650 \text{ W/m}^2$  ( $1.213S_0$ ). In Kopparapu et al. (2017), GCM simulations were conducted for HZ planets around six different M dwarf model stars ( $T_{\text{eff}} = 2600, 3000, 3300, 3700, 4000, 4500 \text{ K}$ ). The study focused on climate states near the inner edge of the HZ, the runaway greenhouse effect, and stratospheric  $H_2O$ . The model planets were subject to increasing stellar fluxes until a runaway greenhouse was triggered and the persistent substellar clouds dissipated, marking the terminal inner edge of the habitable zone. That is, the runaway greenhouse effect is characterized by

a collapse of the substellar cloud deck, and thus a sharp drop in the planet's albedo, due to reduction in the convection transporting moisture up. Temperatures rise rapidly as the planet's surface is then suddenly exposed to the higher incoming stellar irradiation. A large top of atmosphere (TOA) energy imbalance is maintained, and the increasingly strong water vapor greenhouse prevents the planet from radiatively cooling (please see Figures 6, 7 and 8 from Kopparapu et al. (2017)).

For planets orbiting M dwarf stars with  $T_{\text{eff}} \leq 3000$  K, atmospheres transitioned from mild climates with little stratospheric water vapor directly to a runaway greenhouse, with no stable moist greenhouse state existing between. (However, see Bin et al. (2018), where they have found a solution for an even smaller star, with an effective temperature of 2550 K, where the water vapor mixing ratio is  $2 \times 10^{-3}$  at 10hPa, which matches the water vapor value computed at 10hPa in our photochemical models for our planet-star pair). For stars with  $T_{\text{eff}} \geq 3300$  K, Kopparapu et al. (2017) found that the planets can maintain a stable moist greenhouse regime with their climate remaining stable against a runaway greenhouse. For our study here, we choose a stable moist greenhouse state around a 3300 K star. Detections around a 3300 K star will be easier than those around larger hosts because a smaller star means larger transit signals, and a shorter orbital period means that more transit observations can be stacked together in a shorter period of time, improving signal to noise. The 3300 K star was thereby the sole case for which spectra were shown and implications for MIRI observations discussed in Kopparapu et al. (2017). So, we are able to compare to those results directly in Section 4.4.

Our input  $P$ - $T$  profile (i.e. mean terminator thermal profile from the GCM) shows a temperature minimum at 2 mbar, which translates to a cold trap in the  $\text{H}_2\text{O}$  profile where cloud condensation would occur. Table 1 of Kopparapu et al. (2017) reports a GCM model top  $\text{H}_2\text{O}$  mixing ratio of  $5.55 \times 10^{-4}$ . While this is the global mean value across the stratosphere, the mean terminator value is similar due to the strong mixing. Since photolysis of water vapor increases with altitude due to the strengthening incoming stellar UV, we also want to explore the region above 1 mbar in this study. Thus, we extend the 1 mbar  $\text{H}_2\text{O}$  and  $T(P)$  values to a TOA pressure of  $8.1 \times 10^{-7}$  bar in our 1-D simulations by simply holding them constant at those values for the atmosphere above 1 mbar in the input profile; photochemical kinetics drives the ultimate steady-state abundances.

#### 4.2.2 Stellar Parameters: Variable UV Activity

We extract high-resolution stellar data of a 3300K UV-quiet star from 1000 to 8500 Å, from the BT-Settl grid of models (Allard et al. 2003, 2007). This model spectrum was used in the Kopparapu et al. (2017) work; it is our starting scenario—the lowest activity boundary exemplifying a no stellar activity end-member case, with stellar UV levels from blackbody emission only (red spectrum in Figure 4.2). However, real stars are not perfect blackbodies at UV wavelengths like these BT-Settl model stars. All stars, even the oldest ones, show some level of chromospheric emission that adds to the net UV spectra. This is especially significant over the FUV region, where the photolysis cross-section values for many key species tend to be the highest.

We incorporate the full spectra (1216-8450 Å) into Atmos. The UV region is

primarily driving the photochemistry. In addition to the BT-Settl model, we use high-resolution spectra of the M dwarf stars from the MUSCLES database. We choose the two stars with the most divergent wavelength-dependent UV (GJ581 and Proxima Centauri)—from the seven M dwarfs in this database—to generate two of the four other UV scenarios. For the remaining two cases, we use AD Leo and GJ876 data from the existing Atmos spectral database. Both spectra have prominent Ly- $\alpha$  features.

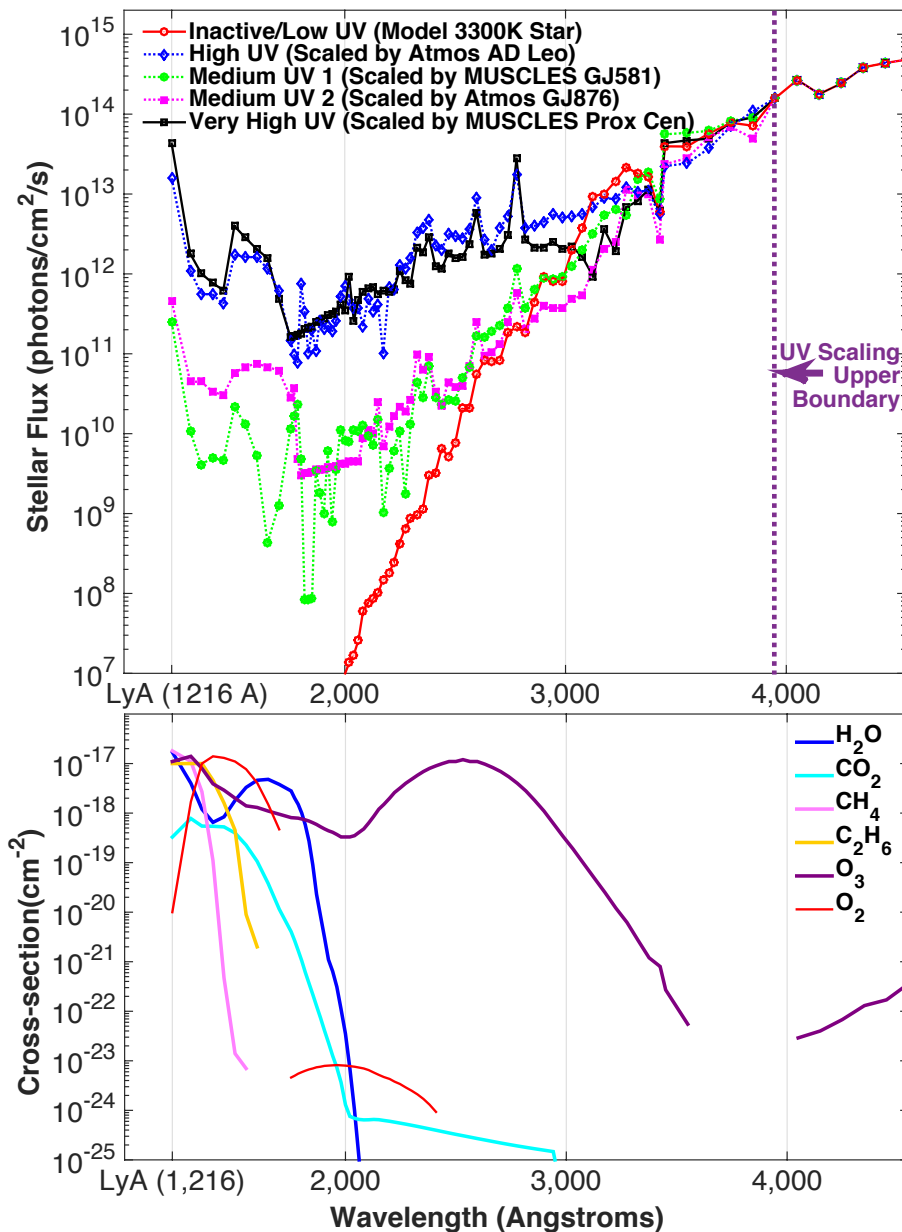


**Figure 4.2:** *Top Panel:* Earth-equivalent spectral energy distribution is shown for the inactive model star, with the four synthetically constructed  $< 3950 \text{ \AA}$  profiles overlaid. The spectra result from binning the original high-resolution data over the Atmos wavelength grid for the UV cross-section data, after converting the flux density units from  $\text{ergs cm}^{-2} \text{ s}^{-1} \text{ \AA}^{-1}$  to  $\text{photons cm}^{-2} \text{ s}^{-1} \text{ \AA}^{-1}$  as expected by Atmos. The UV scaling boundary is marked at  $3950 \text{ \AA}$  by the purple vertical line. Since we use real stellar UV data for the scaling, the difference amongst the profiles is not particularly dramatic after the binning. Earth-equivalent fluxes are obtained by taking the original stellar data and dividing by the solar constant. *Bottom Panel:* available UV cross-section data used by Atmos shown for the species relevant to our 1-D model results.

We create each synthetic UV spectrum by stitching the extracted data to our UV-quiet model flux data, after binning our stellar data to a predefined coarser wavelength grid used by default in Atmos (see Figure 4.2 grid). The "stitching together" is done by scaling the stellar data (up to  $3950 \text{ \AA}$ ), such that the value at  $3950 \text{ \AA}$  matches the model star value. In sum: shortward of  $3950 \text{ \AA}$ , we use the scaled extracted data; longward of  $3950 \text{ \AA}$ , we use the model star flux. Atmos' spectral database stores unscaled stellar flux data as Earth-equivalent incident flux values ( $S_0$ ) (red spectrum in Figure 4.2). This means that the overall incident flux at the top of the atmosphere is 1.213 times the fluxes shown in Figure 4.2.

The AD Leo (spectral type: M3.5V) and GJ876 (M4V) spectra (France et al. 2012, 2013) have been used in several recent 1-D simulation studies of planetary atmospheres using our photochemical model (Segura et al. 2005, 2010; Domagal-Goldman et al. 2014; Harman et al. 2015; Arney et al. 2017). Their scaled versions correspond to "High UV" and "Medium UV 2," respectively, in Figure 4.2. We assign the highest activity level ("Very High UV") to the scaled MUSCLES Proxima Centauri (M6V) data. The remaining case ("Medium UV1") corresponds to scaled GJ581 (M3V) MUSCLES UV spectra. The model star is regarded as the base inactive/low UV case.

### 4.2.3 Photochemistry in the Atmosphere via Atmos

VPL's Atmos has been used in 1-D photochemical and climate modeling of early Mars, and the Archean and modern Earth atmospheres. Atmos simulations of rocky exoplanets have helped define the HZ (Kopparapu et al. 2013a, b, 2014).

The photochemical model in Atmos (Arney et al. 2016, 2017) solves a set of nonlinear, coupled ordinary differential equations for the mixing ratios of all species at all heights using the reverse Euler method. The method is first order in time and uses second-order centered finite differences in space. The system of equations is explicitly formulated as time-dependent equations that are solved implicitly by a time-marching algorithm. The model is run to steady state to obtain the final mixing ratio profiles. In each step, the model measures the relative change of the concentration of each species in each layer of the atmosphere. When all species in all layers move their concentrations by less than 15% in the time step, the size of the time step grows. When this size is greater than  $10^{17}$  seconds ( $\sim 3$  billion years) the model is considered to have reached the steady state (i.e. convergence). This means that the steady-state solutions have stable chemical profiles on timescales of billions of years, assuming constant boundary conditions. These boundary conditions can include biological gas fluxes, volcanic outgassing, atmospheric escape, and parameterization for ocean chemistry (see Figure 4.1 from earlier in this section).

We use the species and reaction list of the existing "Modern Earth" template<sup>1</sup> in Atmos. Note that our use of this template does not imply that we are attempting to

---

<sup>1</sup> Public Atmos: <https://github.com/VirtualPlanetaryLaboratory/atmos/>

reproduce modern Earth's atmosphere. After all, we are modeling an abiotic anoxic planetary atmosphere here. Rather, this template is used for its representative mixture of gases for an N<sub>2</sub>-H<sub>2</sub>O dominated planet. The base model has 193 forward chemical reactions and 40 photolysis reactions for 40 chemical species made from H, C, O, N, and S, 23 of which participate in photolysis. While CO<sub>2</sub> is kept constant at 360 ppm in all five models, other species are allowed to vary. While a thick CO<sub>2</sub> atmosphere could radiatively cool the middle atmosphere, acting as a bottleneck for H<sub>2</sub>O loss to space, the Earth-like CO<sub>2</sub> amount we assume here should have a relatively minor effect on stratospheric temperatures (Wordsworth & Pierrehumbert 2013).

We modify the boundary conditions to simulate an abiotic planet after Harman et al. (2015). In all five runs, we fix the surface flux of CH<sub>4</sub> to a 1-Earth mass planet abiotic production rate of  $1 \times 10^8$  molecules cm<sup>-2</sup> s<sup>-1</sup> after Guzmán-Marmolejo et al. (2013). To determine the lower boundary conditions for the other varying species (see Table 4.2), we assume the surface environment (atmosphere and ocean) obeys redox balance (i.e. free electrons are conserved), using the methodology by Harman et al. (2015). While the atmospheric model ensures redox balance in the atmosphere, we must tune the boundary conditions to prevent a redox imbalance in the oceans or on the planet's surface. We do this in our model by changing the H<sub>2</sub> flux value into the atmosphere so that there is no net deposition of oxidizing or reducing power into the oceans or onto the surface. Thus, we tune the H<sub>2</sub> flux value across the five UV scenarios until atmosphere and ocean redox balance independently for each case. This ensures that the atmospheric concentrations we report here are sustainable over geological timescales with only geological (and not biological) fluxes.

It is worth pointing out here that while we do have the ability to model hydrocarbon hazes within the Atmos framework, we do not include them in our study. The  $\text{CH}_4/\text{CO}_2$  ratio determines haze formation. Hydrocarbon organic hazes only form for  $\text{CH}_4/\text{CO}_2$  ratios  $> 0.1$  (actually closer to 0.2). In our atmospheres, we have modeled  $\text{CO}_2$  abundance as a constant 360 ppm value, while  $\text{CH}_4$  is allowed to vary. The largest amount of atmospheric  $\text{CH}_4$  is calculated for the model star (red curve in Figure 4.3), where  $\text{CH}_4$  mixing ratio is  $\sim 2 \times 10^{-5}$ , i.e. the maximum value of  $(\text{CH}_4/\text{CO}_2)$  is  $(2 \times 10^{-5})/3.6 \times 10^{-4} < 0.1$ . Therefore, organic hazes are not expected to form in our modeled atmospheres. We do not need to include complex haze formation chemical pathways as a result, and thus can use the “Modern Earth” template—that excludes these hazes—instead of our “Archean Earth” template, which includes them.  $\text{H}_2\text{O}$  is the only non-background species with mixing ratios provided by the GCM. So, instead of defining surface conditions, we fix the  $\text{H}_2\text{O}$  abundance profile below the tropopause to the mixing ratios of those levels from the GCM.

We assume that the atmosphere is hydrostatic, and there is no atmospheric escape occurring for species besides H and  $\text{H}_2$ . H and  $\text{H}_2$  are both allowed to escape according to their diffusion-limited rate, computed within the model. This results in hydrogen having a positive outflow flux at the top of the atmosphere. The effects of this H escape have been included in our budgets for redox balance. It is worth noting here that photochemical reaction timescales are much shorter (seconds to hundreds of years) than the timescales of atmospheric escape (billions of years). The largest timestep of the model is long with respect to long-term climate evolution; the latter can be driven by hydrogen escape. Thus, we do not expect the effects of escape to have

much bearing on the steady state chemistry; escape should primarily impact the long-term evolution of the atmosphere and not its steady state composition.

**Table 4.2:** Some key species in our photochemical model template and their lower boundary conditions

Species	Lower bound type	Lower bound value
O	$\nu_{\text{dep}}$	1.
O <sub>2</sub>	$\nu_{\text{dep}}$	$1.5 \times 10^{-4}$
H <sub>2</sub> O	see table comment	from GCM result
H	$\nu_{\text{dep}}$	1.
OH	$\nu_{\text{dep}}$	1.
HO <sub>2</sub>	$\nu_{\text{dep}}$	1.
H <sub>2</sub> O <sub>2</sub>	$\nu_{\text{dep}}$	$2. \times 10^{-1}$
H <sub>2</sub>	$\nu_{\text{dep}}, \text{flux}, \text{dith}$	$2.4 \times 10^{-4}, 4. \times 10^5 - 2. \times 10^{10}, 1.$
CO	$\nu_{\text{dep}}$	$1. \times 10^{-8}$
CO <sub>2</sub>	$f\text{CO}_2$	$3.6 \times 10^{-4}$
HCO	$\nu_{\text{dep}}$	1.
H <sub>2</sub> CO	$\nu_{\text{dep}}$	$2. \times 10^{-1}$
CH <sub>4</sub>	<i>flux</i>	$1. \times 10^8$
CH <sub>3</sub>	$\nu_{\text{dep}}$	1.
C <sub>2</sub> H <sub>6</sub>	$\nu_{\text{dep}}$	0.
NO	$\nu_{\text{dep}}$	$3. \times 10^{-4}$
NO <sub>2</sub>	$\nu_{\text{dep}}$	$3. \times 10^{-3}$
HNO	$\nu_{\text{dep}}$	1.
O <sub>3</sub>	$\nu_{\text{dep}}$	$7. \times 10^{-2}$
HNO <sub>3</sub>	$\nu_{\text{dep}}$	$2. \times 10^{-1}$
N	$\nu_{\text{dep}}$	0.
NO <sub>3</sub>	$\nu_{\text{dep}}$	0.
N <sub>2</sub> O	$\nu_{\text{dep}}$	0.
HO <sub>2</sub> NO <sub>2</sub>	$\nu_{\text{dep}}$	$2. \times 10^{-1}$
N <sub>2</sub> O <sub>5</sub>	$\nu_{\text{dep}}$	0.
N <sub>2</sub>	<i>fixedN<sub>2</sub></i>	0.9956

**Note:** Starting boundary conditions are fixed surface deposition efficiency (" $v_{\text{dep}}$ "), constant mixing ratio (" $fCO_2$ "), fixed mixing ratio at the surface (" $fixedN_2$ "), or constant upward flux (" $flux$ "); the first three quantities are dimensionless, fluxes are in molecules  $\text{cm}^{-2} \text{s}^{-1}$ .  $\text{H}_2\text{O}$  concentration below the tropopause is held at the input  $\text{H}_2\text{O}$  values from the GCM.  $\text{H}_2$  is defined by both  $v_{\text{dep}}$  and a vertically distributed upward  $flux$  value over a height of  $disth$  (in km). A range is given for  $\text{H}_2 flux$  value as it is the only condition allowed to vary across the five cases to ensure redox balance in the oceans (Harman et al. 2015). S-based species ( $\text{H}_2\text{S}$ ,  $\text{HS}$ ,  $\text{S}$ ,  $\text{SO}$ ,  $\text{SO}_2$ ,  $\text{H}_2\text{SO}_4$ ,  $\text{HSO}$ ,  $\text{S}_2$ ,  $\text{S}_4$ ,  $\text{S}_8$ ,  $\text{SO}_3$ ,  $\text{OCS}$ ,  $\text{S}_3$ ,  $\text{SO}_4$  and  $\text{S}_8$  aerosols) are not shown in this list. While they are retained from the validated Modern Earth template's list to assure convergence, extremely low arbitrary boundary values are given to keep their presence negligible (mixing ratio  $< 10^{-30}$ ).

The vertical grid is distributed evenly over 200 levels and extends to a TOA altitude of 91 km. The lower boundary pressure is set at 1 bar and the upper boundary at  $8.1 \times 10^{-7}$  bar. Both chemistry and vertical transport are considered for the 40 long-lived species. Transport is neglected for the 9 additional short-lived species such as  $\text{O}(^1\text{D})$ . For the long-lived species, vertical transport is approximated with a profile of eddy diffusion coefficients. Typically, these coefficients are patterned after eddy diffusivities that best reproduce modern-day Earth (Kasting 1979, 1990). However, the vertical mixing has been shown to be stronger for Earth-like planets with slow rotation rates, owing to the aforementioned strong substellar convection. We need to tune the eddy diffusivity to mimic this strong upwelling circulation. The original "Modern Earth" template's eddy profile is for our rapidly rotating home planet, and thus underestimates stratospheric  $\text{H}_2\text{O}$ , because the assumed upwelling is then too weak, relative to the general circulation of the atmosphere for these slow rotators. Thus, for our runs, we adopt a constant eddy profile by iteratively determining a single large eddy coefficient value ( $K_{zz} = 8.95 \times 10^6 \text{ cm}^2 \text{ s}^{-1}$ ) that allows us to maintain the original GCM  $\text{H}_2\text{O}$  mixing ratio at 1 mbar, while letting the atmosphere column above vary.

Above 1 mbar, we expect photochemistry to dominate over the vertical mixing.

Lastly, we hold the zenith angle at  $50^\circ$  (see Table 4.1) within the photochemical model, even though we are simulating the planetary terminator. The point of 1-D photochemical modeling is to best approximate the global atmospheric chemistry of a planet. Zenith angles are typically chosen in order to reproduce the globally averaged properties of the planet. For modern Earth, the angle that reproduces the global average chemistry has been determined to be  $50^\circ$ . To our knowledge, no systematic study has demonstrated what the proper zenith angle is for a tidally-locked, synchronously rotating world. Furthermore, it is unclear how to account for the impact of dynamics at the terminator of such planets through the use of a single zenith angle. In these close-in planets, much of the chemistry will be driven by photolysis at the substellar point to create species that are then pushed to the night side of the planet by strong zonal winds (for example, see Figure 11 in Haqq-Misra et al. 2018 and Figure 1 in Chen et al. 2018). While a study to determine the proper zenith angle to account for all this is warranted, it is beyond the scope of this work. That being said, we do, after all, “tether” the 1 mbar water vapor concentration in our photochemical model to the 1 mbar value from the GCM model grid (GCM TOA) at the planet’s terminator. This means that we have incorporated the impact of dynamics to the extent possible without the utilization of GCM with fully interactive chemistry.

#### 4.2.4 Radiative Transfer Spectra via Exo-Transmit

Exo-Transmit is an open-source software package to calculate exoplanet transmission spectra. Here we use Exo-Transmit to generate spectra from the computed

steady-state mixing ratios of species for which spectral contribution has been established in IR, including trace species for which opacity data is available in the package.

Exo-Transmit is designed to generate spectra of planets with a wide range of atmospheric composition, temperature, surface gravity, size, and host star. There is also an option to include an optically thick gray "cloud" deck at a user-specified pressure above the surface. As this cloud deck is not modeled from actual particles, wavelength-dependent cloud properties are not involved. This simply serves as a reasonable method for incorporating the effects of optical thick cloud layers in simulated transmission calculations. When this feature is employed, the transit base is raised to the user-specified cloud-top pressure, meaning data pertaining to the atmosphere column below this pressure level is not read. Our purpose is to quantify spectral differences stemming from varying the UV alone; we keep the transit radius at the model base of 1 bar in our simulations, thus calculating the maximum signal that we would obtain for these atmospheres. We do, however, utilize the cloud truncation feature to compare our spectra to the spectrum shown in Kopparapu et al. (2017), which did include clouds (see Section 4.4). Exo-Transmit is available publicly on Github with open-source licensing at [https://github.com/elizakempton/Exo\\_Transmit](https://github.com/elizakempton/Exo_Transmit).

Exo-Transmit comes with predefined  $P$ - $T$  and mixing ratio profiles binned to the resolution of its opacity data, where the pressure grid spans  $10^{-6}$  –  $10^3$  bars in logarithmic steps of one dex (i.e.  $P = 10^n$ , where  $n$  is an integer). For our study, we replace these input files with our own ones containing the newly computed mixing ratios and the mean terminator  $P$ - $T$  profile. Our  $P$ - $T$  profile is much more finely sampled than Exo-Transmit's opacity/chemistry grid. During each run of Exo-

Transmit, the opacity is first interpolated onto each point of our  $P$ - $T$  grid, then the radiative transfer calculation is run to compute the net spectrum.

## 4.3 Results

### 4.3.1 Atmospheric Constituent Mixing Ratio Profiles

Although the two Medium UV spectra have much higher UV levels than the inactive model spectra at wavelengths  $< 3950\text{\AA}$ , with  $\sim 10$  orders of magnitude difference at  $1216\text{\AA}$  (Figure 4.2), we find neither of them to be high enough to cause appreciable  $\text{H}_2\text{O}$  loss (see the top of the  $\text{H}_2\text{O}$  mixing ratio panel in Figure 4.3).

In the inactive model star case—where no photolytic loss is noted for any of the species shown—we see high constant values for the  $\text{CH}_4$  and  $\text{C}_2\text{H}_6$  mixing ratios being maintained over the entire atmosphere. The  $\text{CH}_4$  source in this abiotic atmosphere is dominated by the lower boundary constant upward flux ( $flux = 1 \times 10^8$  molecules  $\text{cm}^{-2} \text{s}^{-1}$  in Table 4.2). So, we can expect total  $\text{CH}_4$  production to be similar across all five cases. For the four UV-active cases, higher UV would translate to higher total loss of  $\text{CH}_4$  due to photolysis.  $\text{CH}_3$  is a highly reactive product of  $\text{CH}_4$  photolysis and combines with itself to produce  $\text{C}_2\text{H}_6$ , which also photodissociates and cycles back into  $\text{CH}_4$ ; the three hydrocarbons cycle amongst themselves. The dominant exit pathway from this cycle—reaction of  $\text{CH}_3$  with oxidants—is limited by the rate of  $\text{CH}_4 + \text{OH} \rightarrow \text{CH}_3 + \text{H}_2\text{O}$ . Thus,  $\text{CH}_4$  chemistry is dominated by the abundance of  $\text{OH}$  in the atmosphere, as evidenced by a negative correlation between the  $\text{OH}$  and  $\text{CH}_4$  profiles. The higher the  $\text{OH}$  abundance, the higher the  $\text{CH}_4$  loss via combination with  $\text{OH}$ . This is also demonstrated by our examination of the sinks for  $\text{CH}_4$ ; for UV-active stars, des-

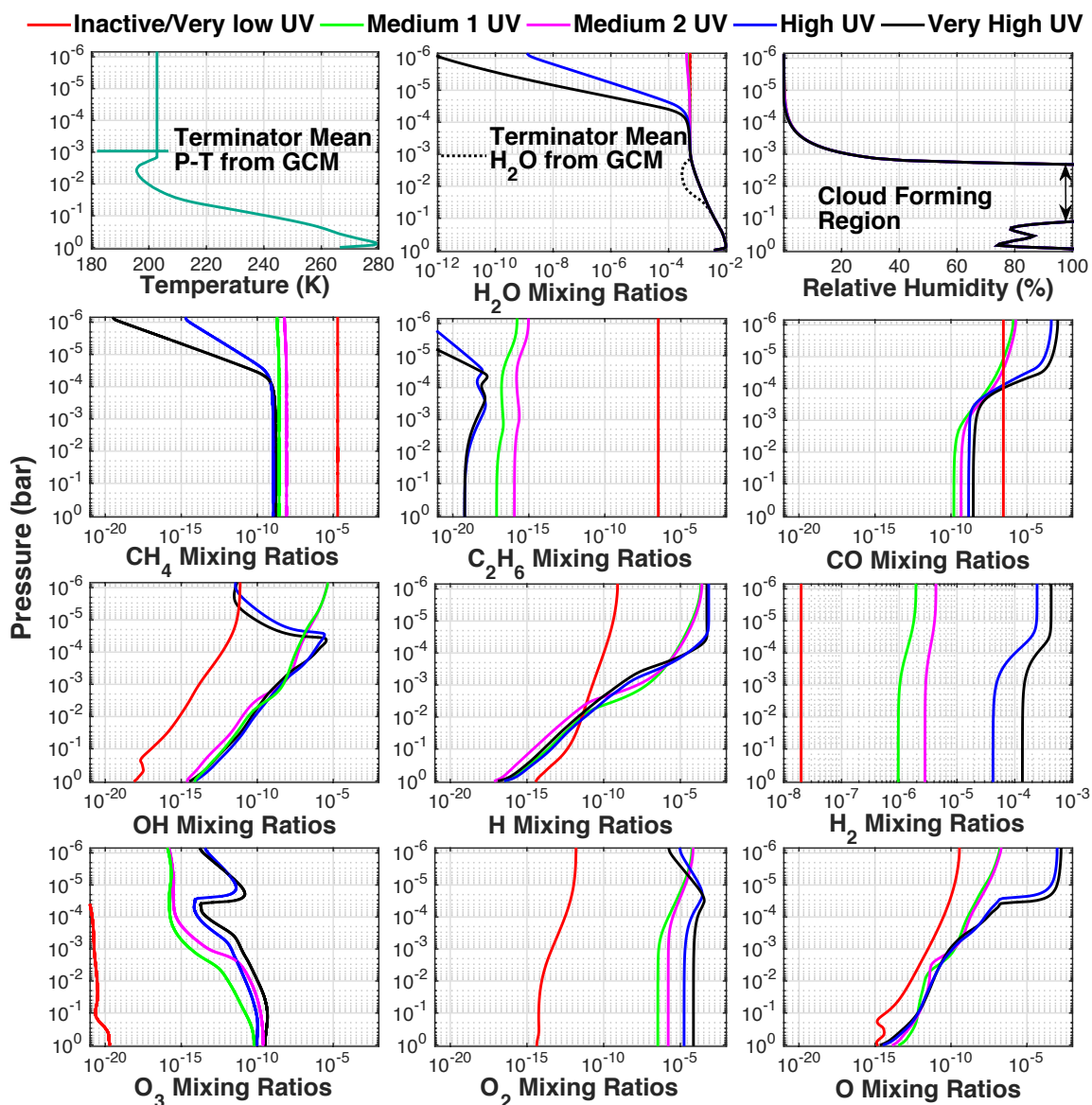


**Figure 4.3:** Steady-state mixing ratio profiles computed by the photochemical model are shown for all varying nontrace species of interest. 1-D model input for the terminator mean  $\text{H}_2\text{O}$  (dotted black line in the  $\text{H}_2\text{O}$  panel), and  $P$ - $T$  (plotted in the first panel) profiles from the GCM simulation are shown next to each other for interpretation. With the exception of the  $\text{H}_2$  and  $\text{H}_2\text{O}$  panels, all other species are shown on the same wide mixing ratio scale for easy visual comparison. Relative humidity profiles from the 1-D model for the resulting atmospheres are also shown next to the  $\text{H}_2\text{O}$  panel, with the cloud condensation pressure range indicated.

truction of CH<sub>4</sub> is dominated by reaction with OH, and this rate even outpaces our abiotic surface CH<sub>4</sub> flux. The net impact of this chemistry is much lower abundances for CH<sub>4</sub> and C<sub>2</sub>H<sub>6</sub> for the UV-active stars compared to the inactive model star.

OH is primarily produced in the atmosphere via H<sub>2</sub>O photolysis. Our Medium UV stars show similar Ly- $\alpha$  strengths, so the resultant H<sub>2</sub>O photolysis rates are also similar. For the High UV and Very High UV stars—both with synthetic UV  $\sim$ 2 orders of magnitude higher than the Medium UV stars—we see significant H<sub>2</sub>O loss: The High UV star depletes TOA H<sub>2</sub>O by  $\sim$ 6 orders of magnitude; while the Very High UV star depletes the TOA H<sub>2</sub>O by  $\sim$ 3 further orders (i.e. total of  $\sim$ 9 orders) of magnitude. Ly- $\alpha$  strength is slightly higher in the Very High UV spectra (black profile in Figure 4.2).

Like most species in our model, atomic O, O<sub>2</sub>, and O<sub>3</sub>, have only been defined by lower boundary deposition efficiency values. Without a surface source of O<sub>2</sub> and O<sub>3</sub>, atmospheric chemistry is their only source. Thus, their concentrations are minor for the inactive star (red profiles in Figure 4.3). As UV increases, we see higher abundances in all three species, especially O<sub>2</sub> and O<sub>3</sub>, although their presence remains below detectable levels. At high altitudes, both O and O<sub>2</sub> generally increase in concentration, consistent with having a photolytic source. O<sub>2</sub> maintains a high abundance (for an anoxic atmosphere) throughout the column for the highest UV cases as the stellar UV flux is relatively high between 1300 and 1500 Å. The O<sub>2</sub> photolysis cross-section curve peaks here, while O<sub>3</sub> photolysis cross-section values remain large. Although far UV activity is important for O<sub>3</sub> production, O<sub>3</sub> remains somewhat minor throughout the atmosphere even for the highest UV case. O<sub>3</sub> is produced in the model by the three-body reaction  $O + O_2 \rightarrow O_3$  and this is the only

mechanism that produces it in this atmosphere.  $O_3$  is destroyed via photolysis reactions  $O_3 + h\nu \rightarrow O_2 + O(^1D)$  and  $O_3 + h\nu \rightarrow O_2 + O$ , along with 10 other chemical reactions. When  $O_3$  is destroyed via these pathways,  $O_2$  is always produced.

### 4.3.2 Transmission Spectra

For all cases considered, with no cloud cover, we obtain large  $H_2O$  features—around 50 ppm in strength—between 2.5-3.8 and 4.5-9  $\mu m$  (see top panel of Figure 4.4). The locations where these  $H_2O$  features peak are consistent with Figure 11 of Kopparapu et al. (2017; Figure 4.5). The 2.5-3.8  $\mu m$  feature peaks within the *JWST* NIRCam grism with the F322W2 filter, as well as the NIRSPEC G235M/H and NIRISS SOSS (Single Object Slitless Spectroscopy) bandpasses. The 4.5-9  $\mu m$  feature is well within the *JWST* MIRI LRS (Low Resolution Spectroscopy) bandpass. For the model star case, we also see additional absorption at 2.2, 3.3, and 7.4-8.4  $\mu m$  (i.e. the red profile minus the black profile in the top panel of Figure 4.4), caused by the high  $CH_4$  ( $>10^{-5}$ ) predicted by the model for our choice of  $CH_4$  lower boundary condition.

$CO_2$  produces the tallest feature in our spectra (Figure 4.4). This narrow feature at 4.3  $\mu m$  ( $\sim 0.4 \mu m$  wide when measured along the brown dotted spectrum) is  $\sim 20$  ppm larger than the  $H_2O$  features, and 40 ppm larger than the  $N_2-N_2$  collision induced absorption (CIA) feature it overlaps. This region falls within the bandpasses of the NIRCAM F444W filter (3.8-4.8  $\mu m$ ) and the NIRSPEC G333/H grating (2.9-5  $\mu m$ ). The  $N_2-N_2$  CIA feature spans the 3.8-5  $\mu m$  wavelength range (cyan colored bumps in Figure 4.4). This opacity source stems from the deep atmosphere (right panel of Figure 4.5) and is strong due to the high  $N_2$  (Schwieterman et al. 2015) content of the

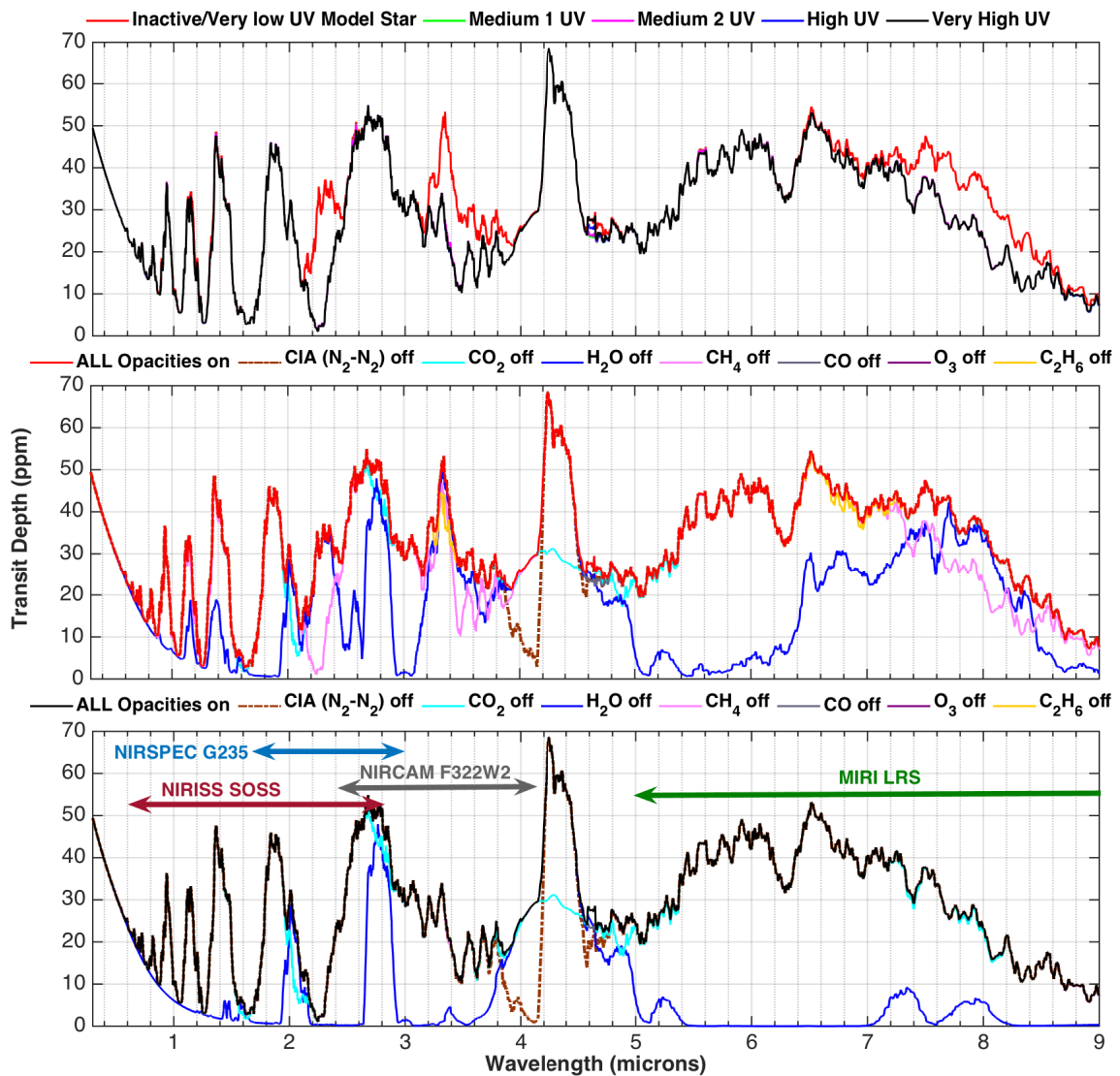


**Figure 4.4:** *Top panel:* full spectra from Exo-Transmit shown for all five UV scenarios. Spectra assume there are no clouds. The four synthetic UV active cases completely overlap, with a slight mismatch at 4.3 μm due to CO differences. *Middle panel:* full spectra from the inactive model star shown (red, per Figure 4.3’s convention), along with individual contributions removed. *Bottom panel:* full spectra for the Very High UV case (black, also same convention) shown this time, along with the same individual species removed. *JWST* instrument bandpasses with prominent H<sub>2</sub>O features have also been indicated here. We do not show the equivalent plots corresponding to the three other UV-active cases here as the spectra are almost identical to each other (the biggest discrepancy is at 4.6 μm due to CO variations), as evidenced by their near complete overlap in the top panel.

atmosphere. This implies we may be able to quantify atmospheric  $N_2$  from this feature's strength in a cloudless atmosphere. As evident from the two spectra shown with CIA removed (brown dotted plots in Figure 4.4), the base of the  $4.3 \mu\text{m}$   $\text{CO}_2$  feature is broadened by the overlapping CIA band but the height is unaffected; the CIA bump is the only other absorption signature found between  $4 \mu\text{m}$  and the  $\text{CO}_2$  feature.

While  $\text{O}_2$  is significantly enhanced with increasing UV, it is spectrally insignificant. The few features from  $\text{O}_2$  molecular and collision induced opacities occur  $< 1.0 \mu\text{m}$  and are completely masked by the Rayleigh tail. Atomic O is enhanced at high altitudes, but there is no atomic opacity from non-metal atoms.  $\text{O}_3$  can be spectrally important in IR as it produces molecular and collision induced features at wavelengths longer than  $1.1 \mu\text{m}$ .  $\text{O}_3$  acts as a UV shield for atmospheres where it is present (e.g. Earth) and thus has important consequences for habitability (Rugheimer et al. 2015b, a).  $\text{O}_3$  appears to have no impact on any of the spectra we have presented here.

Most importantly, Figure 4.4 (top panel) shows that spectra from the UV active runs overlap almost completely. However, in the inactive model star's case, additional absorptions longward of the peak  $\text{H}_2\text{O}$  features stem primarily from the high  $\text{CH}_4$  and some from  $\text{C}_2\text{H}_6$ . The  $\text{C}_2\text{H}_6$  contribution is most noteworthy at  $3.3 \mu\text{m}$ , where it also overlaps with major contribution from  $\text{CH}_4$  and  $\text{H}_2\text{O}$ , and then from  $6.5$  to  $7.4 \mu\text{m}$ , where most of the contribution is still from  $\text{H}_2\text{O}$ . These demonstrate the impact of M dwarf UV activity on the planet's transit observations. We find that for any realistic levels of UV radiation from an M dwarf host star, the atmospheric response to the amount of radiation is undetectable.

From our 1-D modeling results, we infer that  $\text{H}_2\text{O}$  photodissociation from high

levels of UV instellation does not impact transmission spectra, and thus should not affect our ability to detect H<sub>2</sub>O absorption features from a habitable synchronously rotating Earth-like planet around a nearby M dwarf. This is expected as transmission features should primarily originate from lower regions of the atmosphere  $\geq 1$  mbar (left panel of Figure 4.5). In the upper atmosphere above the substellar cloud altitudes, there is no reason for the planet-wide vertical mixing driven by strong convection to continue dominating. Thus, photochemistry can dominate here, meaning we cannot expect the water vapor to stay enriched this high into the atmosphere. Accordingly, we only highlight the visible impact from photochemistry above the stratosphere (and cloud decks) for all species involved in photolysis, in the modeled atmospheres (Figure 4.3).

#### 4.4 Discussion

Figure 4.3 shows that the water vapor concentration is highest between 0.1 and 1 bar, close to the surface as expected. The cold trap minimum is also found between two other Exo-Transmit pressure grid points. To ensure accuracy of our interpolations onto this coarse pressure grid, we have experimented with shifting the cold trap altitude. Of course, the transit depths shown in Figure 4.4 should still not be taken at face value; moist atmospheres have water clouds that are not accounted for here. Since Exo-Transmit does not presently have the capability to include specific cloud properties, we do not include the liquid and ice data from the GCM run outputs as part of our spectral analysis. We see the impact of such water clouds in the transmission spectra provided in Kopparapu et al. (2017), computed by VPL's

Spectral Mapping Atmospheric Radiative Transfer (SMART) tool for the planet-star configuration we have studied here. Data from the GCM simulation results were used directly in SMART to calculate the spectrum for the synchronously rotating planet.

We are able to compare our spectra with the SMART spectrum by raising the base altitude and thus sampling a lower pressure range (i.e. a shallower column) of the atmosphere in Exo-Transmit. For comparison, we compute a single spectrum for the original pure N<sub>2</sub>-H<sub>2</sub>O GCM atmosphere, with no photochemical alteration. We do this for a few cases with Exo-Transmit: a default case with the original 1 bar base, and some additional computations to simulate the effects of clouds by raising the spectral model base to successively lower pressures. In the left panel of Figure 4.5, we show the spectrum of the default case with no clouds, and the spectrum for a cloud-top pressure of 0.05 bar—the location of the water clouds in the SMART-computed version of the GCM results. For comparison, we overplot the spectrum from SMART. We see that by artificially truncating our spectra at this cloud-top pressure, we are able to capture the most important effects of the clouds on the spectrum.

We validate the consistency of our Exo-Transmit calculations with the SMART spectrum by noting a reasonable overlap between the two cloudy spectra (in both panels of Figure 4.5). We see that the spectra diverge in the near-IR, for wavelengths shortward of 4  $\mu\text{m}$ . The transit depths are consistently larger in the cloudy spectrum computed by Exo-Transmit for wavelengths shorter than 4  $\mu\text{m}$ ; Exo-Transmit computes a larger apparent size for these planets than SMART in the near-IR. Differences in the treatment of clouds (properties such as particle size, optical constants, etc.) between the two spectral models would be responsible for this kind

of discrepancy, as differences in interpolation should affect the spectrum globally, and not just over this specific wavelength range. As we mentioned earlier in Section 4.2.4, Exo-Transmit treats its clouds as a fully gray optically thick deck, so cloud properties do not vary with wavelength. However, SMART has wavelength-dependent water cloud properties incorporated in the spectral modeling scheme. We believe the discrepancies we are seeing between the two spectral models is explained by this.

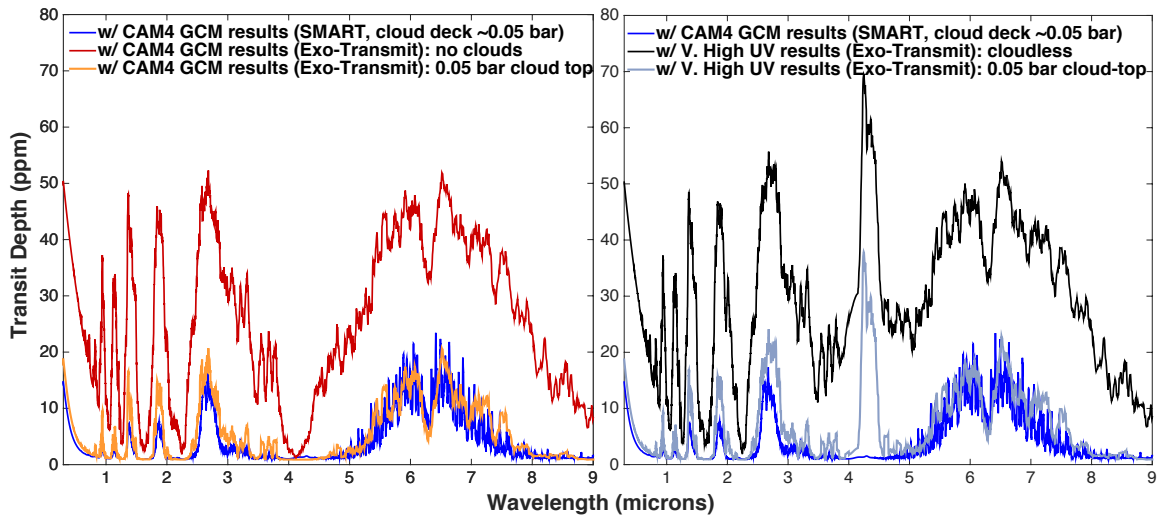


**Figure 4.5:** *Left panel:* Exo-Transmit spectra computed using terminator mean mixing ratios from the pure  $N_2$ - $H_2O$  atmosphere (GCM results) shown alongside the Kopparapu et al. (2017) SMART version of it (blue). As the water clouds occur  $\sim 0.05$  bar in the SMART computations, we also include the spectrum that results from placing an opaque cloud at 0.05 bar within Exo-Transmit. Exo-Transmit spectra shown here have CIA turned off for direct comparison; the SMART spectrum does not include CIA. The CIA opacity has a minimal effect on these spectra so their inclusion or non-inclusion is not a dominant factor in the modeling outcomes. *Right panel:* Very High UV Exo-Transmit spectra shown for cloudless (same black spectrum from Figure 4.4) and 0.05 bar cloud-top (gray) cases, in comparison to the SMART spectrum of the GCM results. Note that the difference in the 4-5  $\mu m$  range between the GCM + SMART simulation (in blue) and the GCM + PHOTOCHEM + Exo-transmit simulations (gray/black spectrum) is due to the inclusion of  $CO_2$  in the photochemical models, but not in the GCM, which assumed a pure  $N_2$ - $H_2O$  atmosphere.

The right panel of Figure 4.5 also shows that the CO<sub>2</sub> 4.3 μm feature remains prominent in the cloudy spectrum of the photochemical model results. The atmospheric column above 0.05 bar is still being transmitted and contributes to the spectrum. At 0.05 bar, the H<sub>2</sub>O mixing ratio is  $\sim 2 \times 10^{-3}$ . Transit spectroscopy typically sample the planet at  $\sim 1$  mbar atmospheric pressure, which is also the GCM TOA. The GCM TOA H<sub>2</sub>O mixing ratio is  $\sim 5.55 \times 10^{-4}$  (Figure 4.3, also see Table 1 of Kopparapu et al. (2017)). Since our CO<sub>2</sub> abundance is slightly less than that and also less than  $\sim 1/5$ th of the 0.05 bar H<sub>2</sub>O abundance, the much higher CO<sub>2</sub> transit depth signal is noteworthy for future observing efforts.

Greene et al. (2016) has suggested systematic noise floors of  $\sim 20$  ppm for NIRISS/NIRSpec and  $\sim 30$  ppm for the NIRCам grism, which is not only well below the  $\sim 70$  ppm CO<sub>2</sub> 4.3 μm signal strength for the cloudless case for the 360 ppm of atmospheric CO<sub>2</sub>, but is also comparable to the difference in magnitude between this feature and the largest H<sub>2</sub>O features. These observational advantages still hold for the 0.05 bar cloud-top spectra. So, in a similarly cloudy atmosphere but with modern Earth-like amounts of CO<sub>2</sub>, the CO<sub>2</sub> may be more readily detected. Of course, the true performance of the instruments will only be known once *JWST* actually flies.

During the manuscript revision process, our reviewer suggested checking the spectral impact of other levels of CO<sub>2</sub>, even though our study is not a climate study (and thus *P-T* and CO<sub>2</sub>—which affect each other for high CO<sub>2</sub> concentrations—are kept constant). While we did not include the results of this mini side project in our ApJ paper to keep it focused on its non-climatic goals, we share it here. For the atmospheres presented here, if the constant CO<sub>2</sub> level is changed from 360 ppm to 10 ppm

on its own (i.e. CO<sub>2</sub> abundance is lowered from 360 ppm to 10 ppm in the abundance files we use in calculating the spectrum, but not within the actual photochemical model itself...), the corresponding CO<sub>2</sub> feature has the same strength as the two peak H<sub>2</sub>O features. Thus, mixing ratios below that (e.g. 1 ppm) produce 4.3 um features weaker than the 50 ppm *JWST*/MIRI instrument's noise threshold (from Green et al. 2016). For constant CO<sub>2</sub> volume mixing ratios  $\leq 10^{-6}$ , the feature mostly blends into the N<sub>2</sub>-N<sub>2</sub> CIA bump, and completely blends in for mixing ratios  $\leq 10^{-9}$ .

One issue that can impact our quantitative predictions of O<sub>2</sub> and O<sub>3</sub> is how Atmos treats the CO<sub>2</sub>. Atmos presently accepts CO<sub>2</sub> as a user-specified constant mixing ratio for terrestrial planets, though it allows for CO<sub>2</sub> production and destruction reactions, including photolysis ( $\text{CO}_2 + h\nu \rightarrow \text{CO} + \text{O}$  and  $\text{CO}_2 + h\nu \rightarrow \text{CO} + \text{O}(^1\text{D})$ ). So, a caveat here is that the model produces excess CO<sub>2</sub> in order to maintain the constant 360 ppm CO<sub>2</sub> abundance throughout the defined atmospheric column. This overestimates both the upper atmosphere CO<sub>2</sub> abundance and the total O budget. This could be important for the computed O<sub>2</sub> and O<sub>3</sub> mixing ratios (and possibly other species). However, because we note photochemical effects only above the column of the atmosphere sampled by transits, a major impact on transit observations is unlikely and this impact is mostly just quantitative. For now, we save discussion of O<sub>3</sub> absorption features for a subsequent manuscript focused more on O chemistry (see Chapter 5).

H<sub>2</sub> and CH<sub>4</sub> are the only nonnegligible species in our model defined by lower boundary *flux* values (see Table 4.2) that also dominate their source functions. The higher the stellar UV flux, the higher the H<sub>2</sub> *flux* value needs to be to achieve global redox balance for a given CH<sub>4</sub> flux. H and OH trends across the models are thus

affected by the varying H<sub>2</sub> source. We keep the CH<sub>4</sub> flux fixed in this study as small changes to this flux do not have an impact on the concentrations of gases for which we note detectable spectral features in Figures 4.4 and 4.5. Further investigation of the effects of the choice of CH<sub>4</sub> flux on the abundances and detectability of relatively trace species is being explored for a future paper. Our study on the impact of changing methane flux on ozone abundance is presented in the following chapter (Chapter 5).

## 4.5 Conclusions

We have taken a synchronously orbiting aquaplanet-star pair result from Kopparapu et al. (2017) within the stable moist habitable regime, and have conducted a case study on its future detectability via *JWST*. We have investigated the impact of stellar activity on the detection of terrestrial planets with water-rich stratospheres, as photolysis from high levels of UV activity would continuously destroy the water lofted into the high atmosphere. We have run five photochemical models, each with different wavelength-dependent UV activity, ranging from the inactive model (BT-Settl) star data used in Kopparapu et al. (2017) to Proxima Centauri-like levels. We have used stellar fluxes from the VPL spectral database in Atmos and the MUSCLES Treasury Survey to vary the UV levels.

We find that as long as the atmosphere is well-mixed up to 1 mbar, H<sub>2</sub>O strengths observed in transit spectra should remain unaffected by UV activity. However, for the inactive model star, transit depths are larger due to contributions from the high CH<sub>4</sub> in the atmosphere for our specified CH<sub>4</sub> surface flux, which assumes Earth-like abiotic sources of CH<sub>4</sub>. Detectable CH<sub>4</sub> is absent in the UV active cases.

CO<sub>2</sub> produces a narrow but large detectable feature at 4.3 μm. For our assumed atmospheric CO<sub>2</sub> level of 360 ppm, this feature is about 20 ppm larger than the tallest H<sub>2</sub>O features. At the wavelengths where CO<sub>2</sub> does overlap H<sub>2</sub>O features, the maximum contribution is also 20 ppm over a very narrow (<1 μm broad) region at 2 μm (i.e. before the prominent H<sub>2</sub>O features appear) for a cloudless case. We also see broadening of the base of the 4.3 μm CO<sub>2</sub> feature due to opacity from N<sub>2</sub>-N<sub>2</sub> collisional pairs. However, upon comparing the two "Very High UV" spectra in the right panel of Figure 4.5, we see that the N<sub>2</sub>-N<sub>2</sub> CIA feature is a high-pressure feature originating from well below cloud decks. Thus, due to the presence of clouds in real atmospheres, the CIA feature should not contribute to the observed signal from CO<sub>2</sub> in practice.

While UV activity may not impact transit depths at the ppm level, water clouds do. Upon comparing the cloud-containing SMART spectrum from Kopparapu et al. (2017) for the synchronously rotating planet modeled by the GCM, with a cloud-free version of it from Exo-Transmit, we find that the 0.05 bar cloud weakens the strongest H<sub>2</sub>O feature at 6 μm from 50 ppm—comparable to the postulated MIRI systematic noise floor—to only 15 ppm. This means should the terminator cloud deck occur lower in the atmosphere, at pressures > 0.05 bar, we should require less observing time to make a positive detection. Overall, we see few detectable impacts of photochemistry on the spectra of these worlds.

## Acknowledgements

We thank contributors and fellow developers of the Atmos software and the open-source Exo-Transmit tool used in this study. This work was carried out at the NASA Goddard Space Flight Center (GSFC) under the Center for Research and Exploration in Space Science and Technology (CRESST) II cooperative agreement between the lead author's institution, University of Maryland College Park, and GSFC (Task 699.05). Goddard affiliates are thankful for support from GSFC Sellers Exoplanet Environments Collaboration (SEEC), which is funded by the NASA Planetary Science Division's Internal Scientist Funding Model. This work was performed as part of the NASA Astrobiology Institute's Virtual Planetary Laboratory, supported by NASA under cooperative agreement NNH05ZDA001C. R.K.K. and E.T.W. gratefully acknowledge funding from NASA Habitable Worlds grant NNX16AB61G. The 3D simulation results used in this study were facilitated through the use of advanced computational, storage, and networking infrastructure provided by the Hyak supercomputer system, supported in part by the University of Washington eScience Institute. This work also utilized the Janus supercomputer, which is supported by the National Science Foundation (award number CNS-0821794) and the University of Colorado at Boulder. E.T.W. thanks NASA Astrobiology Institute CAN7 award NNH13DA017C through participation in the Nexus for Exoplanet System Science (NExSS). S.D.D.G. and R.K.K. also acknowledge financial support from the NASA Astrobiology Program via NExSS. Any opinions, findings, and conclusions or recommendations expressed in this material are those of the author(s) and do not necessarily reflect the views of NASA or the National Science Foundation.

## Chapter 5: Robust Quantification of Abiotic CH<sub>4</sub> and O<sub>3</sub> in Moist Habitable Anoxic Terrestrial Atmospheres Orbiting a 3300 K M Dwarf Host

### Abstract

The search for life involves assessing false positives and negatives in potentially habitable atmospheres via future missions. In Chapter 4 and paper I, Afrin Badhan et al. (2019b), we determined that ultra-violet (UV) stellar activity should not impact the detection of water vapor in moist habitable atmosphere of a synchronously rotating 1-Earth mass terrestrial aquaplanet orbiting an M dwarf host star. We also established that for an abiotic methane production rate of  $10^8$  molecules  $\text{cm}^{-2} \text{s}^{-1}$ , while CH<sub>4</sub> should be spectrally detectable for a hypothetically inactive 3300K M dwarf star, detectable CH<sub>4</sub> is absent for realistic levels of UV activity. Abiotically sourced oxygen allotropes (O, O<sub>2</sub>, O<sub>3</sub>) and CH<sub>4</sub> prevalent in an Earth-like planet's atmosphere is important for gauging its habitability. However, while O<sub>2</sub> is barely spectrally detectable in IR due to the Rayleigh scattering tail, we find that enhanced O<sub>3</sub> from high stellar UV may be potentially detectable in the mid-infrared (MIR) with the future *Origin Space Telescope (OST)*. Past work has shown that O<sub>3</sub> accumulation in these atmospheres is determined by the ratio of far-ultraviolet (FUV) to near- and mid- ultraviolet (NUV and MUV) radiation from the host star. In this paper, we robustly investigate this behavior as a function of slight instellation variations on the synthetic UV-active stellar fluxes from Chapter 4, as well as variable methane production rates, for a range of water vapor content within the habitable zone of our 3300K star from Chapter 4. We employ our 1-D photochemical model from Chapter 4 with varied stellar UV, to assess

how  $O_3$  accumulation varies with  $CH_4$  production rates in these atmospheres. We find  $O_3$  accumulation in these atmospheres to be sensitive to the three factors: UV activity, the instellation level, as well as the chosen methane production rate. Temperature and  $H_2O$  profiles are consistent with Chapter 4 for our base instellation level of  $1650 \text{ W/m}^2$ ; we use the GCM results for lower instellation levels reported in Wolf et al. (2019). We deduce that simultaneous detection of  $O_3$  and  $CH_4$  in synchronously rotating Earth-like planets around M dwarfs is possible for a purely abiotic atmosphere.

## 5.1 Introduction

The simultaneous detection of few key possibly biogenic gases in the atmosphere of a habitable zone terrestrial planet around a main sequence stellar host is a first order indicator of its potential for habitability. Such gases are known as biosignatures and include  $CH_4$ ,  $O_2/O_3$ ,  $N_2O$ , beside  $H_2O$ . However,  $CH_4$  and  $H_2O$  have large sources of abiotic production in the atmosphere, even within our own planet. Large amounts of  $O_2/O_3$  and  $N_2O$ , on the other hand are associated with oxidized atmospheres, similar to modern-day Earth.  $O_3$  is often a proxy for  $O_2$  as  $O_3$  can only be produced in atmospheres containing some level of  $O_2$ .  $O_3$  is also easier to quantify via transit detections in the MIR, whereas  $O_2$  features are common over UV and NIR wavelengths and often masked by other overlapping features. Furthermore,  $O_2$  is known to have limited abiotic sources but many abiotic sinks, while disequilibrium from  $O_3$  is primarily abiotic and sourced by photochemistry. In either case, as per convention in the field, it is crucial that we extend the range of false positive and negative scenarios for  $O_2/O_3$  and the combination of ( $O_3 + CH_4$ ) together.

In Chapter 4, we simulated a potentially habitable N<sub>2</sub>-dominated moist atmosphere (i.e. 100-1000x as moist as our own Earth is at the stratosphere—the region of the atmosphere probed by IR transit techniques), with allowance for 360 ppm of CO<sub>2</sub> (“modern Earth” amount) and other CHNO species. Since our modeled planet was entirely covered by water ocean, we can assume some of the C-containing species are sequestered into the water. C-based gases in our own atmosphere also vary largely as a function of surface outgassing, although CO<sub>2</sub>, being present in large quantities, remains fairly constant large scales while methane can vary temporally. For simplicity, we assumed a constant abiotic methane influx of 10<sup>8</sup> molecules cm<sup>-2</sup> s<sup>-1</sup>, a lower boundary of abiotic flux for a 1-Earth-Mass planet, and obtained steady state mixing ratios with redox balance determined by surface H<sub>2</sub> flux. While we talk about most of our findings in the previous Chapter, we have reserved the discussion of ozone for this chapter as the focus of the previous chapter was detectability of abundant species via the *James Webb Space Telescope (JWST)*, which is not sensitive to the ozone quantities we are able to produce in these kinds of atmospheres. Detecting such trace but key biosignatures, however, is a primary goal of the *Origin Space Telescope* mission.

### 5.1.1 Future Biosignature Study with the Origin Space Telescope

The *Origins Space Telescope (OST)* is a concept study for mid- to far- infra-red surveyor space telescope mission for the mid-2030s (Meixner et al. 2018; Leisawitz et al. 2018). *OST*'s transit spectrometer is being designed to tackle a basic question: How common are life bearing planets around M dwarf stars (Fortney et al. 2018)? If *OST* is selected and successfully launches, it will provide the exoplanet community

with 3-D spectroscopic surveys for characterizing biosignatures in exoplanets around M dwarfs by obtaining primary transits, secondary eclipses and thermal phase curves of volatile-rich rocky atmospheres in the mid- and far- infra-red wavelengths. *OST* will have higher sensitivity in the MIR and FIR than its predecessors and thus will be able to detect even trace quantities of key species.

*OST* will also be building on prior work by current and upcoming missions. The planetary system sample for *OST* follow-up will be known: *TESS*, *MEARTH*, *SPECULOOS* and other surveys will have yielded dozens of temperate planets around mid/late M dwarfs within a 15-parsec distance, and these candidates will have been further studied and vetted by *JWST* observations in the coming decade.

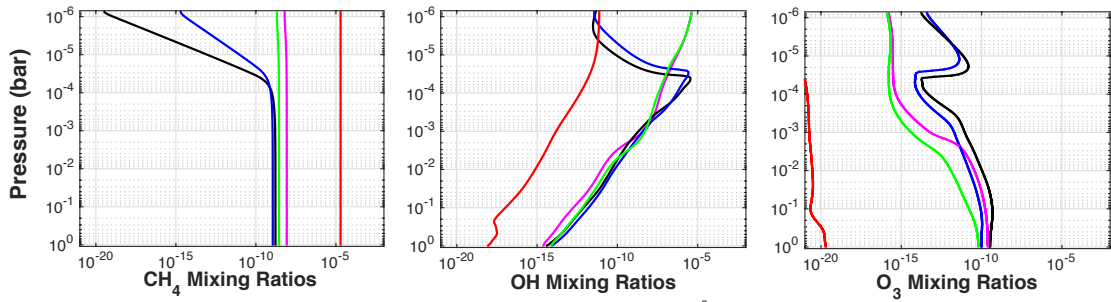
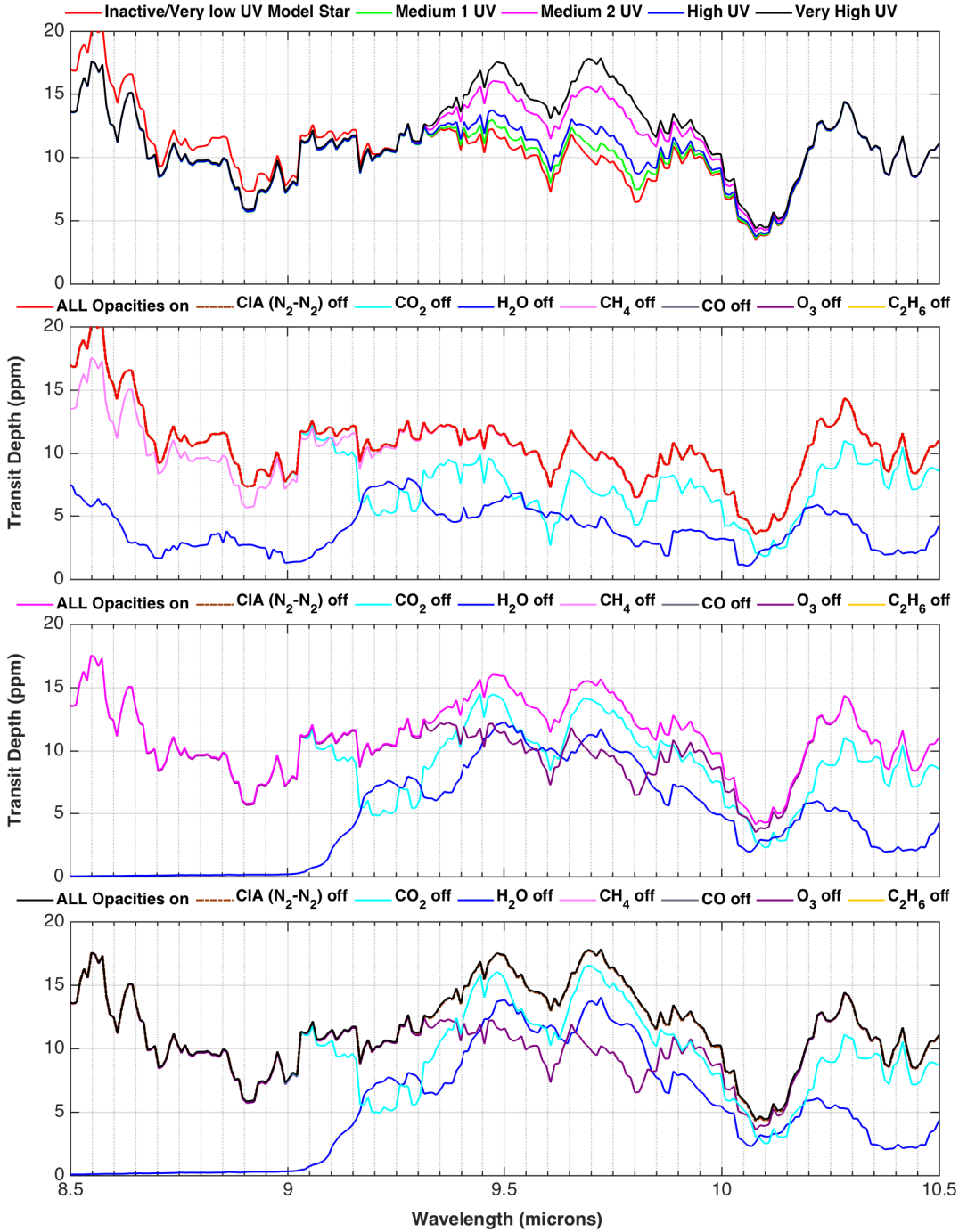
*OST*'s MIR Transit Spectrometer Module (MISC TRA) will obtain molecular transitions of CH<sub>4</sub>, O<sub>3</sub>, H<sub>2</sub>O, CO<sub>2</sub> and N<sub>2</sub>O from these atmospheres. These biosignatures have strong absorption features in the MIR for HZ planets; contrast between the blackbody emission from an Earth-like planet and that of the host star is maximized between 5–30 μm. Detecting biosignatures in habitable worlds in both primary and secondary transit requires spectroscopy in 5–18 μm at R ~100 and in 17–25 μm at R ~300, with very high spectrophotometric stability—better than 10 ppm on timescales of hours to days. The MISC TRA module is able to achieve this through employing a densified pupil spectroscopic design. MISC TRA covers 5–26 μm with R=100–300, with a spectrophotometric stability of 3–5 ppm on timescales of hours to days, excluding any fluctuation of detector gain (Matsuo et al. [2016](#); Battersby et al. [2018](#)).

## 5.1.2 This Study: Motivation and Structure

In our previous results, we found that for our chosen production rate of methane,  $flux(\text{CH}_4)$ , ozone distinctly contributed to the spectrum of the atmospheres for some of the active UV cases (see Figure 5.1), for an instellation of  $1650 \text{ W/m}^2$  (i.e.  $S = 1.213S_0$ , where  $S_0$  is the earth-equivalent instellation of  $1360 \text{ W/m}^2$ ). For the Medium UV 2 and Very High UV stellar profiles, we found more than 5 ppm level of ozone at  $9.6 \mu\text{m}$ —on par with noise floor of the MISC TRA reported above (Matsuo et al. 2016).

For the other two UV activity cases—Medium UV 1 and High UV—we found small ozone contributions below noise floor. As this suggests the possibility of detectable ozone with MISC TRA even from a clearly abiotic planetary atmosphere, we are motivated to extend the range of our modeled atmospheric states to include higher  $flux(\text{CH}_4)$ —starting with the purely abiotic flux range (Chapter 4) value as the lower boundary to a likely lower biotic/upper abiotic range of  $10^{10} \text{ molecules cm}^{-2} \text{ s}^{-1}$  (Krisanssen-Totton et al. 2018; Arney et al. 2017). Simultaneously detectable methane and ozone is particularly interesting to us as it is postulated that a planet is highly likely to have a biosphere if both biosignatures are found together in its atmosphere. We conduct this study as the results we just shared here indicate otherwise.

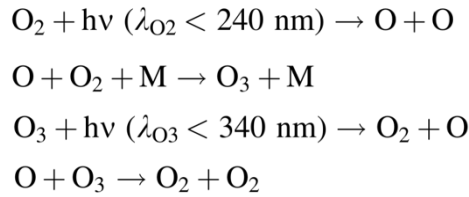
**Figure 5.1: Spectra panels:** Spectra shown over  $8.5\text{-}10.5 \mu\text{m}$  for our results from Chapter 4. The wavelength range longer than what we showed in Chapter 4 and includes the  $9.6 \mu\text{m}$  ozone feature. We maintain the same color convention as Chapter 4. The top panel shows the ozone spectral contribution at  $9.6 \mu\text{m}$  for all five different UV cases. The panel immediately below (with individual species removed) show that we do not find any ozone for the inactive star as we expect. Panels below show that we can possibly get 5-10 ppm of ozone for Medium UV 2 (third panel) and Very High UV (fourth panel) cases. These cases have the most  $\text{O}_3$  in the lower atmosphere according to the mixing ratio plots. *Bottom/Mixing ratio panel:* Extracted from the mixing ratio figure in Chapter 4, these show the  $\text{CH}_4$ ,  $\text{O}_3$  and  $\text{OH}$  profiles for the methane abiotic production rate of  $10^8 \text{ molecules cm}^{-2} \text{ s}^{-1}$ , as they affect each other's abundance.



We already have a water-vapor rich atmosphere at our chosen instellation level, so we do not have to place this planet any closer to the star. At closer distances, the planet would not be able to hold onto the water vapor anyway due to runaway loss over time (Wolf et al. 2017, 2019; Kopparapu et al. 2017; Bin et al. 2018). Furthermore,  $\text{N}_2\text{O}$  concentrations are low for this configuration for our modeled atmospheres, so we can think of our starting point as a purely abiotic atmosphere governed by transport and chemical processes. So, we can choose to focus on  $\text{O}_3$  and  $\text{CH}_4$  only.

In addition to varying the surface  $flux(\text{CH}_4)$  into the atmosphere, we also test the impact of slight variations in instellations,  $S$ , to lower values, using results of discrete increments of instellations from Wolf et al. (2019). We note the lack of high-altitude ozone shielding for the Medium UV stars for our selected  $S$  and  $flux(\text{CH}_4)$ , but their clear presence for the two higher UV cases (see Figure 5.1). At different instellation levels around the same star varying from 0.80 to 1.213 times Earth-level, the GCM simulations from Kopparapu et al. (2017) and Wolf et al. (2019) found different water vapor level concentrations, with a much drier climate for lower instellations as expected, where the ocean would be frozen solid for the majority of the surface area. We want to know if two planets that are otherwise identical in size and composition, but differ in orbit slightly, can have widely different amounts of methane and ozone in their atmospheres. Past studies have told us that the  $\text{FUV}/(\text{NUV and MUV})$  ratio controls the relative  $\text{O}_3$  production and destruction rates in a planet with  $\text{H}_2\text{O}$  (Rugheimer et al. 2015 b,a; Segura et al. 2003; Grenfell et al. 2007; 2014; Harman et al. 2015; also reviewed in Meadows et al. 2016 and Schwieterman et al. 2018). This is due to the varying availability of the OH radical—sourced from the dissociation of

H<sub>2</sub>O—to provide catalytic cycle feedback for the destruction of O<sub>3</sub>, and its production via CO<sub>2</sub> photolysis. Current literature also tells us that significant quantities of O<sub>3</sub> can be produced through abiotic photochemical means, a process that is particularly favored for planets orbiting M dwarf and F dwarf hosts (Domagal-Goldman et al. 2014; Harman et al. 2015). O<sub>3</sub> is produced in Earth’s stratosphere via reactions that split O<sub>2</sub> and is dictated by the availability of free oxygen atoms as well. Reviewed briefly in Chapter 4, O<sub>3</sub> is produced and destroyed in the atmosphere via a chain of reactions involving the oxygen allotropes, known as the Chapman scheme (Chapman 1930a,b):



While O<sub>2</sub> only has strong bands in the VIS/NIR region (Hermans et al. 1999; Richard et al. 2012; Schwieterman et al. 2018), O<sub>3</sub> shows strong absorption over the wavelength regions necessary for detection via transit spectroscopy (i.e. UV and MIR). Thus, O<sub>3</sub> acts as a good proxy for the presence of O<sub>2</sub> in an atmosphere. However, it has not been established if, by changing the total amount of flux from a realistic star, we are able to vary the UV enough to cause meaningful changes in ozone quantities with abiotic presence of methane. Here we attempt this very task.

The rest of this chapter is laid out as follows: In Section 5.2, we begin our methodology description by repeating key details of the original method from Chapter 4 as we use the same base method in this study. We then talk about our justification for varying methane the way we do. We conclude this section with a description of our new installation levels, and also list the inputs we change in our photochemical model

template for these instellations. We begin Section 5.3 by sharing our findings for the different methane fluxes at our original instellation level of 1.213 $S_0$  for a total of 22 different atmospheric states at this instellation (Case I), carefully explaining the reasons behind the different trends from one activity level to another. We then share our ozone and methane spectral predictions for our lower instellation levels (Case II), also for the same range of methane fluxes. In Section 5.4, we discuss the implications of the results on molecular detection of ozone and methane via future observations with *OST*, and also summarize our study.

## 5.2 Methods

### 5.2.1 Summary of the Methods Section from Chapter 4

We use the 3-D global climate model (GCM) result of a particular planet-star pair at a specific instellation from Kopparapu et al. (2017) our input. Specifically, we use terminator mean vertical profiles of P, T, N<sub>2</sub> and H<sub>2</sub>O from the 3-D model as inputs to a 1-D photochemistry model. The GCM is the Community Atmosphere Model v.4. CAM was created by the National Center for Atmospheric Research (NCAR) to simulate the climate of Earth (Neale et al. 2010). To model the 1-D chemical evolution, we use the Atmos photochemical modeling tool, developed by our group at GSFC.

We augment our 1-D modeled atmospheres with other species and let the atmosphere evolve for five different UV activity profiles, including the original UV-quiet model star used in Kopparapu et al. (2017). The other four are synthetic "active" UV scenarios, created with UV profiles from the MUSCLES Treasury Survey (Youngblood et al. 2016) and Atmos' own spectral database (Domagal-Goldman et al. 2014),

generated via the process we describe in Section 4.2.2 in the previous chapter. We run a single 1-D model per UV case; we determine steady state abundances for all modeled species for a total of five simulated atmospheres. We use the Exo-Transmit spectral calculation tool (Kempton et al. 2017) for the transmission spectra.

The Virtual Planetary Laboratory's Atmos is a coupled 1-D photochemical (PHOTOCHEM) & radiative transfer/convection modeling (CLIMA) (Arney et al. 2017) tool. Atmos has been used in 1-D photochemical and climate modeling of early Mars, the Archean and modern Earth atmospheres, and the templates for these validated simulations are part of our public version. The two modules can be used stand-alone; since we do not vary the 1-D  $P$ - $T$  profile in our calculations, we only employ the PHOTOCHEM module for this study. The input mixing ratio file is merely a placeholder; the steady state mixing ratio profiles are computed from boundary conditions, diffusion parameters, and 2-body and 3-body chemical reactions specified.

The constant boundary conditions can include biological gas fluxes, volcanic outgassing, atmospheric escape, deep atmosphere abundances (from equilibrium chemistry), and parametrization for ocean chemistry. Lower boundary conditions to the model can be supplied in the following forms for each diffusing species: a) fixed surface deposition efficiency ("*vdep*"), b) constant mixing ratio throughout the atmospheric column (e.g. CO<sub>2</sub> in this study), c) fixed mixing ratio at the surface (e.g. N<sub>2</sub> here), or d) constant upward flux ("*flux*"); the first three quantities are dimensionless, fluxes are in molecules cm<sup>-2</sup> s<sup>-1</sup>. We define H<sub>2</sub> by both *vdep* and a vertically distributed upward flux over a 1 km range from the surface (see Table 4.2 in Chapter 4 for more).

We use the reactions and species list of the "Modern Earth" template in Atmos for these runs as that template excludes species that will only be formed for a high CH<sub>4</sub>/CO<sub>2</sub> atmosphere. We have 193 forward chemical reactions and 40 photolysis reactions for 40 long-lived and 9 short-lived species made from H, C, O, N, and S, 23 of which participate in photolysis. All other species apart from CO<sub>2</sub> and N<sub>2</sub> are allowed to vary. CO<sub>2</sub> is held at a conservative modern Earth value of 360 ppm, and for these high N<sub>2</sub> atmospheres, the photochemical model also enforces our user-defined fixed lower boundary N<sub>2</sub> mixing ratio, *fixedN<sub>2</sub>* (from the GCM), over the entire atmosphere.

We modify the boundary conditions to simulate an abiotic planet after Harman et al. (2015). We fixed the surface methane production to a 1-Earth mass planet abiotic rate of 10<sup>8</sup> molecules/cm<sup>2</sup>/s (Guzmán-Marmolejo et al. 2013) in Chapter 4, but vary *flux*(CH<sub>4</sub>) in this follow-up study. To determine the lower boundary conditions for other varying species, we assume both the atmosphere and ocean obey redox balance, using the methodology in Harman et al. (2015). The amount of reducing material flowing out of the ocean into the atmosphere can be controlled by using a H<sub>2</sub> flux value that balances the quantity of oxidants. Thus, we vary the H<sub>2</sub> flux across each of the five scenarios until global redox balance is achieved for each case. H<sub>2</sub>O is the only non-background species with mixing ratios provided by the GCM. So, instead of defining surface conditions, we fix the H<sub>2</sub>O abundance profile in the lower atmosphere to the mixing ratios of those levels from the GCM. We continue to assume a hydrostatic atmosphere with diffusion-limited TOA escape (see Chapter 2) for H and H<sub>2</sub>.

Chemistry and vertical transport are both considered for long-lived species. Transport is not factored for short-lived species (e.g. O1D). Vertical transport within

the atmosphere is approximated with  $K_{zz}(P)$  coefficients. Vertical mixing has been shown to be much stronger (than Earth) for Earth-sized slow rotators, owing to the strong convection at the substellar point. Thus, for our runs for our starting instellation level of  $S = 1.213S_0$ , we adopted a constant eddy profile by iteratively determining a single eddy coefficient that allows the input H<sub>2</sub>O value at 1 mbar (GCM model's TOA) to be maintained, while letting the atmospheric column above vary. For this instellation and for all instellation levels above  $S = S_0$ , the tropopause occurs close to the GCM TOA of 1 mbar (see  $P$ - $T$  profile in Chapter 4 and Figure 5.2 below), so the substellar clouds (and the H<sub>2</sub>O enhancement effects) would extend to the GCM TOA.

### 5.2.2 Varying the Methane Surface Boundary Condition $flux(\text{CH}_4)$

As previously discussed, both the upper and lower boundary conditions for every species present in the model, with the exception of background gases, can be changed via specifying a fixed mixing ratio, a velocity for effusion/diffusion, or a flux at the respective boundaries. For our model runs, we have found that different fluxes of incoming H<sub>2</sub> need to be specified to redox balance a template with a given methane flux for varying stellar activity, as well as varying methane for a given stellar activity profile. For each of the five UV cases, we pump the lower boundary methane flux value in successive runs, redox balancing in each change, from the lower clearly abiotic value of  $10^8$  through to  $10^{10}$  molecules  $\text{cm}^{-2} \text{s}^{-1}$  in increments of half dex flux increase (for context, the modern Earth biotic flux is  $30 \text{ Tmol yr}^{-1}$ , which equates to just over  $10^{11}$  molecules  $\text{cm}^{-2} \text{s}^{-1}$ ), for a total of four distinct new methane fluxes. So, with four models per each of the five UV-activity case, we run at least 20 modified cases for this

phase of the study. While we run 25 base models in total (when Chapter 4 runs are included in the count), if we suspect that an intermediate value of methane flux in the range may maximize the ( $\text{CH}_4 + \text{O}_3$ ) quantity simultaneously close to a 5-ppm level, we also run that. Conversely, if our runs indicate that continuing to increase the methane flux to above  $10^{10}$  molecules  $\text{cm}^{-2} \text{s}^{-1}$  may allow for simultaneous signals of  $\text{CH}_4$  and  $\text{O}_3$  at the 5-ppm level for any configuration, we run that too. Demonstrative results for these have also been included in the Results section later in this chapter.

Previous studies have suggested an abiotic production upper limit of  $\sim 1$  Tmol (teramoles)  $\text{yr}^{-1}$  for methane, which is  $\sim 3.7 \times 10^9$  molecules  $\text{cm}^{-2} \text{s}^{-1}$  for a 1-Earth-sized planetary surface. The study in Krissansen-Totton et al. (2018), which provides a probability distribution for the likelihood of the methane production rate in an Earth-like atmosphere to be abiotically sourced (via serpentinization), allows this limit to go up to 15 Tmol  $\text{yr}^{-1}$  ( $5.6 \times 10^{10}$  molecules  $\text{cm}^{-2} \text{s}^{-1}$ ), with increasing likelihood of biogenic origin especially past 7 Tmol  $\text{yr}^{-1}$  ( $\sim 2.5 \times 10^{10}$  molecules  $\text{cm}^{-2} \text{s}^{-1}$ ). Henceforth, we can think of  $\text{flux}(\text{CH}_4)$  exceeding  $10^{10}$  molecules  $\text{cm}^{-2} \text{s}^{-1}$  as an ambiguous abiotic/biotic grey area zone, where fluxes get increasingly likely to be biogenically sourced, but can still be abiotic. However, since present modern Earth atmospheric templates—including our template in Atmos—use a methane source of just over  $10^{11}$  molecules  $\text{cm}^{-2} \text{s}^{-1}$  (also specified in Krissansen-Totton et al. 2018, which also specifies 20-40 Tmol  $\text{yr}^{-1}$  as the range for Archean Earth), and based our work on that template, we will treat  $10^{11}$  molecules  $\text{cm}^{-2} \text{s}^{-1}$  ( $\sim 27$  Tmol  $\text{yr}^{-1}$ ) as our absolute upper boundary for abiotic fluxes. Otherwise, given that we are trying to push the limits of abiotically-sourced methane to see if we are able to obtain ozone features with those

fluxes, using an upper limit of  $10^{10}$  molecules  $\text{cm}^{-2} \text{s}^{-1}$  for  $flux(\text{CH}_4)$  is justified.

For a given UV activity profile, the  $flux(\text{H}_2)$  needed to redox balance different  $flux(\text{CH}_4)$  is different as  $\text{CH}_4$  is a highly reducing species. The balancing  $flux(\text{H}_2)$  also changes from one instellation to another for a given  $flux(\text{CH}_4)$ , as a given methane production rate results in a different methane abundance from one atmosphere to another (Table 5.2).  $flux(\text{H}_2)$  value required to balance the redox in the combined ocean and atmosphere system varies with UV activity profile we use, the methane production rate we prescribed, as well as the profiles and parameters that have changed as a result of changing the planet's orbital distance. Since this study involves finding this  $\text{H}_2$  flux value for over 120 different atmospheric states, whereas Chapter 4 involved static boundary conditions for the other species and thus only five atmospheric states in total, we automated our balancing methodology slightly for this study. We used a fast Euler's method approach; assuming a linear response of redox value to the  $flux(\text{H}_2)$ , we computed the intercept of the line  $y = mx + c$  where  $y$  = total redox value and  $x = flux(\text{H}_2)$ , setting the absolute intercept value as our starting  $flux(\text{H}_2)$ , and kept iterating  $x$  in smaller increments until we obtained the smallest magnitude of  $y$  we could obtain for  $x$  specified to four decimal places. We discuss the trends and patterns for the relationship between  $\text{H}_2$  and these other factors varied in this study at the end of next section, before delving into the results in the following section.

### 5.2.3 Lowering Instellation from 1.213 $S_o$ to 0.8, 1.029, 1.103 & 1.176 $S_o$

We are able to take the stellar flux data we used in Chapter 4, but scale the entire flux to mimic different orbital placements for our planet within the HZ boundaries

established in Kopparapu et al. (2017). For our studies thus far based on their GCM computations for the 3300 K star, we have used the planet terminator average GCM simulation result corresponding to  $S = 1.213S_o$  ( $a \sim 0.085\text{-}0.088$  AU, from albedo range 0 to 0.12). We chose this from the set of runs for the 3300K star (i.e. the smallest M dwarf in the sample with computed moist regime atmospheric states), as this configuration not only had the lowest mean surface temperature that was still higher than the freezing point of water, but also had the highest atmospheric water vapor abundance of all the runs with stable stratospheric moisture content. After all, our focus was habitability determination based on water vapor content and maximizing detectability of this water vapor via *JWST*. While using the GCM results for instellation levels higher than  $1650 \text{ W/m}^2$  would have allowed for the planet to be closer and warmer, meaning both an enhancement in the planet-star radii contrast—a likely observational advantage—and surface temperatures closer to Earth’s temperate values, the GCM runs put these results in the unstable water loss to eventual runaway regime.

However, we are able to move the planet *farther* out, i.e. to instellations closer to Earth-equivalent levels or even below that. While the terminator average surface—which is already below freezing at  $S = 1.213S_o$  (but with substellar temperature still above freezing)—become colder and the planet-to-star size ratio decreases, this allows us to robustly quantify ozone as a function of incremental changes in instellation. By utilizing some  $S/S_o < 1650 \text{ W/m}^2$  GCM results from Kopparapu et al. (2017) and Wolf et al. (2019), we chose to explore the instellation range 1088 (i.e.  $S = 0.8S_o$ ) to  $1600 \text{ W/m}^2$  for the 3300 K star. In Wolf et al. (2019),  $S < S_o$  instellation levels of 688 and  $1088 \text{ W/m}^2$  were also investigated via the GCM, as well as  $S > S_o$  in-

stellation ranges 1400 through 1800 W/m<sup>2</sup> (in 50 W/m<sup>2</sup> increments) for each  $T_{eff}$ , as the original Kopparapu et al. (2017) study.

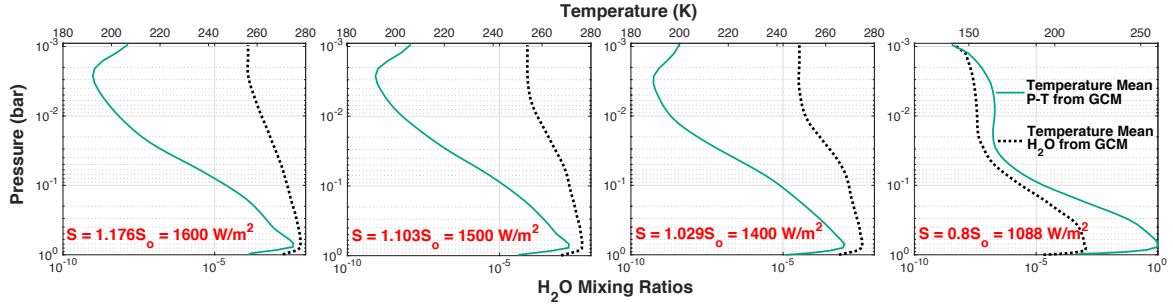


**Figure 5.2:** Plots of mean terminator vertical profiles of H<sub>2</sub>O and temperature from GCM.

To contain the scope of our follow-up study, we choose to work with the mean terminator GCM results for these four instellation cases only (see Figure 5.2): 1088 W/m<sup>2</sup> (i.e.  $S = 0.8S_0$ ,  $a \sim 0.126$  AU), 1400 W/m<sup>2</sup> ( $S = 1.029S_0$ ,  $a \sim 0.099$  AU); 1500 W/m<sup>2</sup> ( $S = 1.103S_0$ ,  $a \sim 0.094$  AU) and 1600 W/m<sup>2</sup> ( $S = 1.176S_0$ ,  $a \sim 0.090$  AU). The planet’s equilibrium temperature at instellation,  $S$ , can henceforth be calculated by substituting relevant parameter values listed here, into the equation that relates planetary surface temperatures to the stellar temperature for tidally-locked planets (e.g. Mendez et al. 2017). We can assume a total global-mean greenhouse effect temperature contribution of only 8-10K for a tidally-locked planet orbiting an M dwarf star from Figure 2 of Yang et al. (2013), as well as unit emissivity, which is a particularly valid assumption for an ocean-covered surface (Lewis et al. 2018).

For the lowest instellation case, the entire planet is below freezing temperatures (see Table 5.1). However, Wolf et al. (2019) shows that the simulated cold planets (the cases subjected to only 1088 and 688 W/m<sup>2</sup> instellation fluxes) maintain a small zone of liquid water at the substellar point even at these extremely cold

temperatures. Since they compute drastically lower H<sub>2</sub>O mixing ratios regardless (as evident from Figure 5.2 and Table 5.1), this could be particularly interesting for ozone detection. Table 5.1 lists the planet parameters for these four lower instellation cases, that we have acquired from the GCM result files; as before, these supply stationery inputs to our photochemical model. We report in Table 5.2 our boundary conditions for species that need to be modified for these low instellation templates to a) maintain the N<sub>2</sub> background from the GCM, b) match the TOA H<sub>2</sub>O mixing ratio just as our original case, c) achieve minimization of the combined redox balance value of the ocean and atmosphere (via tweaking H<sub>2</sub> surface flux as before).

While mixing is enhanced within the lower atmosphere below the cloud decks due to the slowing rotation with increasing instellation within the tidally-locked regime, water abundance decreases as the surface gets cooler. Our aim is to see how the lesser availability of OH radical due to both lower UV stellar and a dryer stratosphere (combined with increasingly frozen ocean surface), translates to changes in the build-up of atmospheric O<sub>3</sub>. This allows us to get a more thorough picture of cases where methane and ozone can be simultaneously detectable at the 5-ppm level for an abiotic atmosphere, and as a function of total stellar flux to TOA as well as varying UV profile.

Since the H<sub>2</sub>O profiles from the GCM have decreasing abundance of water (surface through GCM TOA) with decreasing instellation, we need to use a weaker  $K_{zz}$  profile below 1 mbar to continue to match the GCM TOA 1 mbar water vapor mixing ratio value for these lower instellation cases. To minimize the impact of the lowered  $K_{zz}$  value for the atmosphere above the GCM TOA, where we are still assuming an isothermal temperature profile held constant at the  $T(P = \text{GCM TOA})$  value, we hold

**Table 5.1** Summary of planetary parameters from the GCM simulations for the four lower instellation cases we use as input in the photochemical model...

Parameter	Value			
Instellation at Planet	1600 W/m <sup>2</sup> ( $S=1.176S_o$ )	1500 W/m <sup>2</sup> ( $S=1.103S_o$ )	1400 W/m <sup>2</sup> ( $S=1.029S_o$ )	1088 W/m <sup>2</sup> ( $S=0.8S_o$ )
Surface Pressure <sup>1</sup>	1.007 bar	1.006 bar	1.006 bar	1.006 bar
Surface Temperature <sup>1,2</sup>	257 K	250 K	243 K	213 K
Surface Albedo <sup>1</sup>	0.17	0.21	0.24	0.32
Period	20.03 days	21.02 days	22.14 days	26.75 days
1 mbar $f(\text{H}_2\text{O})^1$	$1.25 \times 10^{-4}$	$8.14 \times 10^{-5}$	$3.41 \times 10^{-5}$	$4.44 \times 10^{-9}$
Tropopause Location <sup>3</sup>	2.67 mbar (40.3 km)	2.67 mbar (41.5 km)	3.40 mbar (39.3 km)	16.3 mbar (25.8 km)

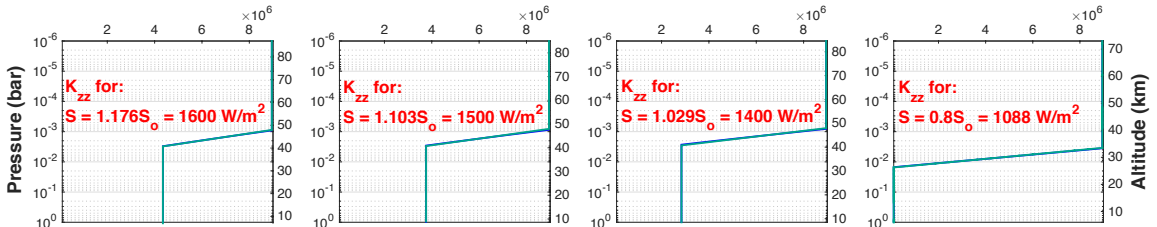
<sup>1</sup>These are planetary terminator mean values, not global mean of substellar point values.

<sup>2</sup>For reference, substellar surface temperatures are 279K, 275K, 272K and 258K, respectively.

<sup>3</sup>For our original  $S = 1.213S_o = 1650 \text{ W/m}^2$  case, the tropopause is at 2.08 mbar (44 km).

**Table 5.2** Species boundary conditions and  $K_{zz}$  profiles in photochemical model

Parameter	Value			
Instellation at Planet	1600 W/m <sup>2</sup> ( $S=1.176S_o$ )	1500 W/m <sup>2</sup> ( $S=1.103S_o$ )	1400 W/m <sup>2</sup> ( $S=1.029S_o$ )	1088 W/m <sup>2</sup> ( $S=0.8S_o$ )
N <sub>2</sub> ( <i>fixed</i> N <sub>2</sub> value) <sup>1</sup>	0.9928	0.9945	0.9956	0.9985
To balance $flux(\text{CH}_4)^2$	H <sub>2</sub> surface flux/ $flux(\text{H}_2)$ range (for UV-active cases only)			
$5 \times 10^8$ (0.13 Tmol yr <sup>-1</sup> )	$2.6 \times 10^9$ - $4.4 \times 10^9$	$1.2 \times 10^9$ - $3.7 \times 10^9$	$5.9 \times 10^8$ - $2.0 \times 10^9$	$5.2 \times 10^6$ - $2.1 \times 10^8$
$1 \times 10^9$ (0.27 Tmol yr <sup>-1</sup> )	$2.6 \times 10^9$ - $4.4 \times 10^9$	$1.2 \times 10^9$ - $3.7 \times 10^9$	$6.1 \times 10^8$ - $2.0 \times 10^9$	$9.8 \times 10^6$ - $2.2 \times 10^8$
$5 \times 10^9$ (1.33 Tmol yr <sup>-1</sup> )	$2.7 \times 10^9$ - $4.4 \times 10^9$	$1.3 \times 10^9$ - $3.7 \times 10^9$	$6.9 \times 10^8$ - $2.0 \times 10^9$	$5.9 \times 10^7$ - $2.4 \times 10^8$
$1 \times 10^{10}$ (2.7 Tmol yr <sup>-1</sup> )	$2.9 \times 10^9$ - $4.5 \times 10^9$	$1.4 \times 10^9$ - $3.8 \times 10^9$	$7.9 \times 10^8$ - $2.0 \times 10^9$	$9.8 \times 10^7$ - $2.8 \times 10^8$
Other species	Boundaries unchanged from Table 4.2 of Chapter 4			
$K_{zz}$ profile boundaries <sup>3</sup> [also see below]	$4.35 \times 10^6$ $8.95 \times 10^7$	$3.76 \times 10^6$ $8.95 \times 10^7$	$2.84 \times 10^6$ $8.95 \times 10^7$	$1.00 \times 10^5$ $8.95 \times 10^7$



<sup>1</sup>We fix the lower boundary mixing ratio to the maximum N<sub>2</sub> mixing ratio value from the GCM.

<sup>2</sup>This is the  $flux$  (in molecules cm<sup>-2</sup> s<sup>-1</sup>) of the species going into the atmosphere from the bottom.

<sup>3</sup>The top and bottom  $K_{zz}$  values (in cm<sup>2</sup> s<sup>-1</sup>) are constants we maintain at the top and bottom of the atmosphere, respectively. We connect the two with a linear slope as shown in the figure.

the  $K_{zz}$  value at our default instellation case value of  $8.95 \times 10^6 \text{ cm}^2 \text{ s}^{-1}$  over the atmosphere at altitudes above the TOA pressure of 1 mbar, but use an iteratively determined much lower single  $K_{zz}$  value around and below the tropopause of the atmosphere, connecting the two regions with a single linear slope (see bottom of Table 5.2). Thus, the cooler the atmosphere, the smaller the lower atmosphere value needs to be to allow us to match the decreasing 1 mbar water vapor value with decreasing instellation. Keeping the  $K_{zz}$  profile at the lower atmosphere constant is justified as  $K_{zz}$  profiles computed with equations for Earth-like planets (Gierasch & Conrath 1985, pp. 121), as well as what we have in the photochemical model for modern Earth and Archean templates, show constant  $K_{zz}$  values in the lowest part of the atmosphere.

In Table 5.2, we also list the range of  $\text{H}_2$  *flux* values (accurate to 1 decimal place) needed to balance the four different methane production rates in our nominated range for the four different instellations. The range given in each entry spans all four active UV profiles for the indicated *flux*( $\text{CH}_4$ ) at the indicated value of  $S$ . The total *flux*( $\text{H}_2$ ) range spans from  $5.2 \times 10^6$  to  $4.5 \times 10^9$  molecules  $\text{cm}^{-2} \text{ s}^{-1}$  (0.0013 to 1.2  $\text{Tmol yr}^{-1}$ ). This range is realistic as it is well below  $3.7 \text{ Tmol yr}^{-1}$ , which is the maximum value of *flux*( $\text{H}_2$ ) occurring on Earth from volcanic sources (from Table 2 of Catling 2013). We can also deduce the following from these summarized entries of the required  $\text{H}_2$  fluxes for redox balance: a) a higher flux of  $\text{H}_2$  is generally needed to balance a higher methane production rate at a given instellation, and this is true for all variants of UV-activity, b) as instellation goes down, the *flux*( $\text{H}_2$ ) values needed to balance methane also go down, but the range for a given instellation does not vary widely as methane production rate increases. Furthermore, for instellation values

where  $S > S_0$ , the higher the UV activity level, the higher the balancing  $H_2$  flux value needs to be. This means the required  $H_2$  flux value is largely determined by the instellation level, followed by the UV activity level, with the  $flux(CH_4)$  value itself being the least important determinant here of the three factors. It should be noted the trend between UV activity and required  $flux(H_2)$  for redox balance does not remain linear for the lowest instellation, where the relationship flips between the Medium UV cases. This likely has to do with the computed OH and  $CH_4$  mixing ratios, and trends resulting differing for the one  $S < S_0$  instellation case. All mixing ratio profiles for  $H_2$  and  $CH_4$ , corresponding to the new instellations, are given in upcoming Section 5.3.2.

## 5.3 Results

### 5.3.1 Case I: Instellation Unchanged, Methane Production Increased

We present the individual residual contributions to the transmission spectrum from the two species—methane and ozone—in Figures 5.3 through 5.7, computed for the four higher methane fluxes from  $5 \times 10^8$  through  $10^{10}$  molecules  $cm^{-2} s^{-1}$  in half order increments of increase. The two spectra are obtained by first computing the spectrum for the case shown with opacities from every contributing species included, followed by another spectrum with  $CH_4$  opacity off, and then a third one separately with  $O_3$  opacity off. Each of these two spectra is then subtracted from the first full spectrum separately, resulting in the two residual spectra per row. We focus on specific  $2 \mu m$  wide wavelength range increments of interest, and keep the y-axis limited to 6 ppm large, even if some features exceed that strength for methane (e.g. the inactive star case), as we primarily care about broad signals close to 5 ppm in strength

over the mid IR wavelengths, and our O<sub>3</sub> feature sizes never exceed 6 ppm for these methane fluxes and at this instellation anyway. In each row, the two right panels show MIR wavelengths over which CH<sub>4</sub> and O<sub>3</sub> transmission signals are maximized. Some contribution from the tail-end of water and carbon dioxide features would also be present over the two adjacent ranges, but have comparatively small contributions when there is a noteworthy ozone feature. The leftmost panel is given as a reference and covers the wavelength range over which CH<sub>4</sub> contributions to the net spectra would be maximized in NIR for a given CH<sub>4</sub> abundance, which we also noted in the first spectra plot in Chapter 4. While the 3.4 μm region also has overlapping ethane and water vapor features as we saw in Figure 4.4, the 2.3 μm region is interesting as methane is the sole broad contributing species to the spectrum at that wavelength.

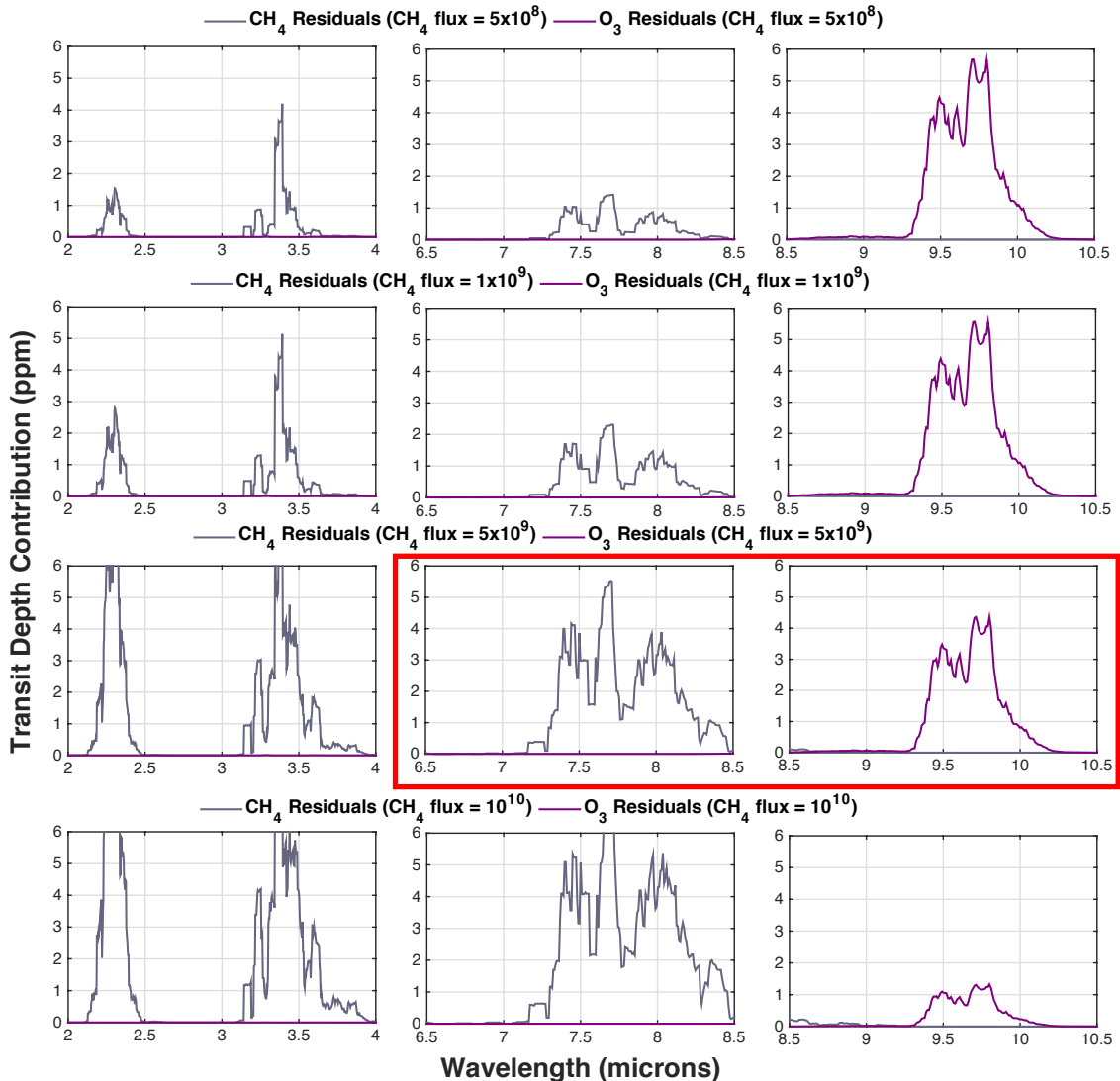
Each of the five figures in this subsection cover each different UV activity profile, but we start with the UV case that imply the highest simultaneous abundance of CH<sub>4</sub> and O<sub>3</sub> from Figure 5.1, namely Medium UV 2, as this is the most promising case and served as the motivation for this study, and work our way to the other UV activity cases. For the last figure—the Very High UV case—we include simulations for  $5 \times 10^{10}$  and  $10^{11}$  molecules cm<sup>-2</sup> s<sup>-1</sup> as well, even though those fluxes may not be entirely explained by an abiotic source alone as continuing to increase the methane flux just this much allows us to obtain comparable strength signals for both for the most active UV profile, similar to what we see for the Medium UV 2 figure. We also do not show the contributions for our default initial methane production rate of  $10^8$  molecules cm<sup>-2</sup> s<sup>-1</sup> as it should be apparent from looking at the five figures here that we are unable

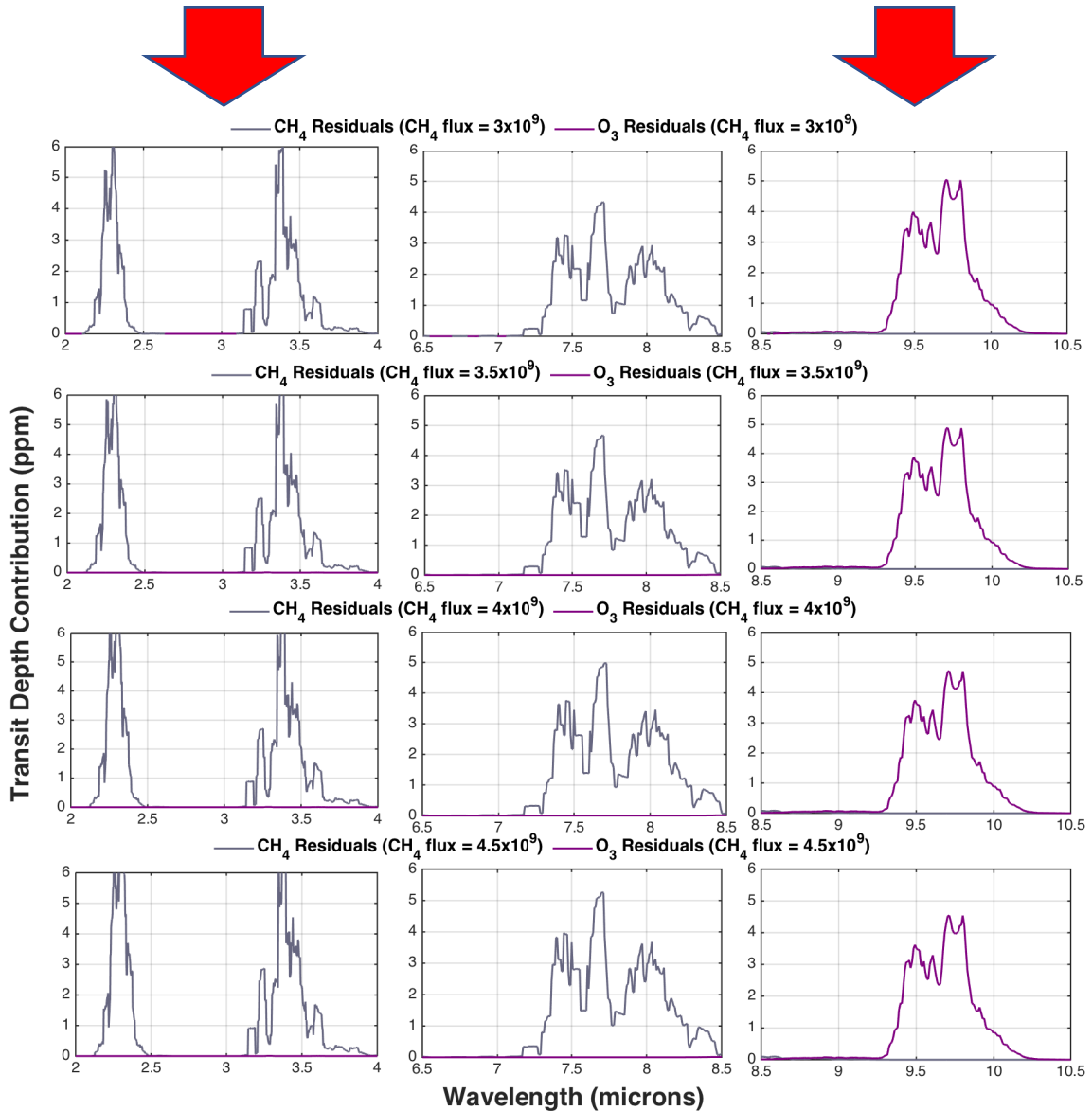
to obtain simultaneous  $\sim 5$ -ppm level contributions for both species for such a low flux of methane for any of the five cases.

We also do not show plots of the mixing ratios for the default instellation case, as the analysis from the second part of this study indicates that trends found within each mixing ratio panel and from one mixing ratio panel to another does not vary substantially as we increase the methane flux, with the most noteworthy trend variation being between the OH and CH<sub>4</sub> panels in the lower atmosphere, which we address later in this section.

The results for our most interesting starting case—Medium UV 2 star—is shown in Figure 5.3. When the methane flux is increased to about  $5 \times 10^9$  molecules cm<sup>-2</sup> s<sup>-1</sup>, we see simultaneous contributions from both CH<sub>4</sub> and O<sub>3</sub> around the 5-ppm level. In the second part of Figure 5.3, we show finer increments of the CH<sub>4</sub> flux and find both contributions to be just about 5 ppm when  $flux(\text{CH}_4)$  is about  $5 \times 10^9$  molecules cm<sup>-2</sup> s<sup>-1</sup> (just over 1 Tmol yr<sup>-1</sup>), which can be thought of as a conservative upper limit for purely abiotic methane fluxes (abiotic/biotic makeup is ambiguous between 10-15 Tmol yr<sup>-1</sup> or  $\sim 3.7$  to  $5.6 \times 10^{10}$  molecules cm<sup>-2</sup> s<sup>-1</sup>, according to the plots in Krisansen-Totton et al. 2018). This means for the Medium UV 2 star irradiating the planet at 1650 W/m<sup>2</sup>, we should be able to detect both ozone and methane assuming a spectrophotometric stability of at least 5 ppm in *OST*'s MISC transit spectrometer (MISC TRA) module with abiotic quantities of methane only. For methane fluxes higher than that, we only see increasing methane features, but ozone strength drops significantly with even a half dex increase in methane flux. For lower fluxes of methane, methane becomes undetectable but ozone features are stronger.

**Figure 5.3:** *Top Panels:* Spectral features residuals for the Medium UV 2 star, to show signal from methane and ozone separately over IR wavelengths where they are maximized (gray is for methane and purple is for ozone). The O<sub>3</sub> residuals are shown in the rightmost column, while the other two columns show CH<sub>4</sub> residuals. As per Chapter 4 convention, the data has been smoothed over 15 points (R~65) from the native Exo-Transmit resolution of ~1000 to show the essential features in the spectrum. The middle and right columns show MIR features (i.e. over *OST*'s bandpass). The NIR wavelength range provided on the left column is the range containing the largest methane features. Methane flux increases from top to bottom in increments of half order magnitude from 10<sup>8</sup> through 10<sup>10</sup> molecules cm<sup>-2</sup> s<sup>-1</sup>. The red rectangular border marks the *flux*(CH<sub>4</sub>) case for which simultaneous detection appears possible. *Bottom panels (next page):* Same type of information has been presented here as the preceding figure for the same star, but for a selected narrower range of *flux*(CH<sub>4</sub>) values corresponding to where the signals from both CH<sub>4</sub> and O<sub>3</sub> are maximized. We can conclude that the signals are largest together for ~ 4 × 10<sup>9</sup> molecules cm<sup>-2</sup> s<sup>-1</sup> from this.





The version of Figure 5.2 for our inactive case is shown below. As expected, we simply see increasingly strength of CH<sub>4</sub> contribution to the spectrum with increasing  $flux(CH_4)$  and in all cases and over all three wavelength ranges shown, the strength from CH<sub>4</sub> is well above the 6 ppm cutoff we selected. The methane features are so large here that the contribution from the longer wavelength tail extends well into the rightmost panel in all four cases, which remain devoid of ozone features completely.

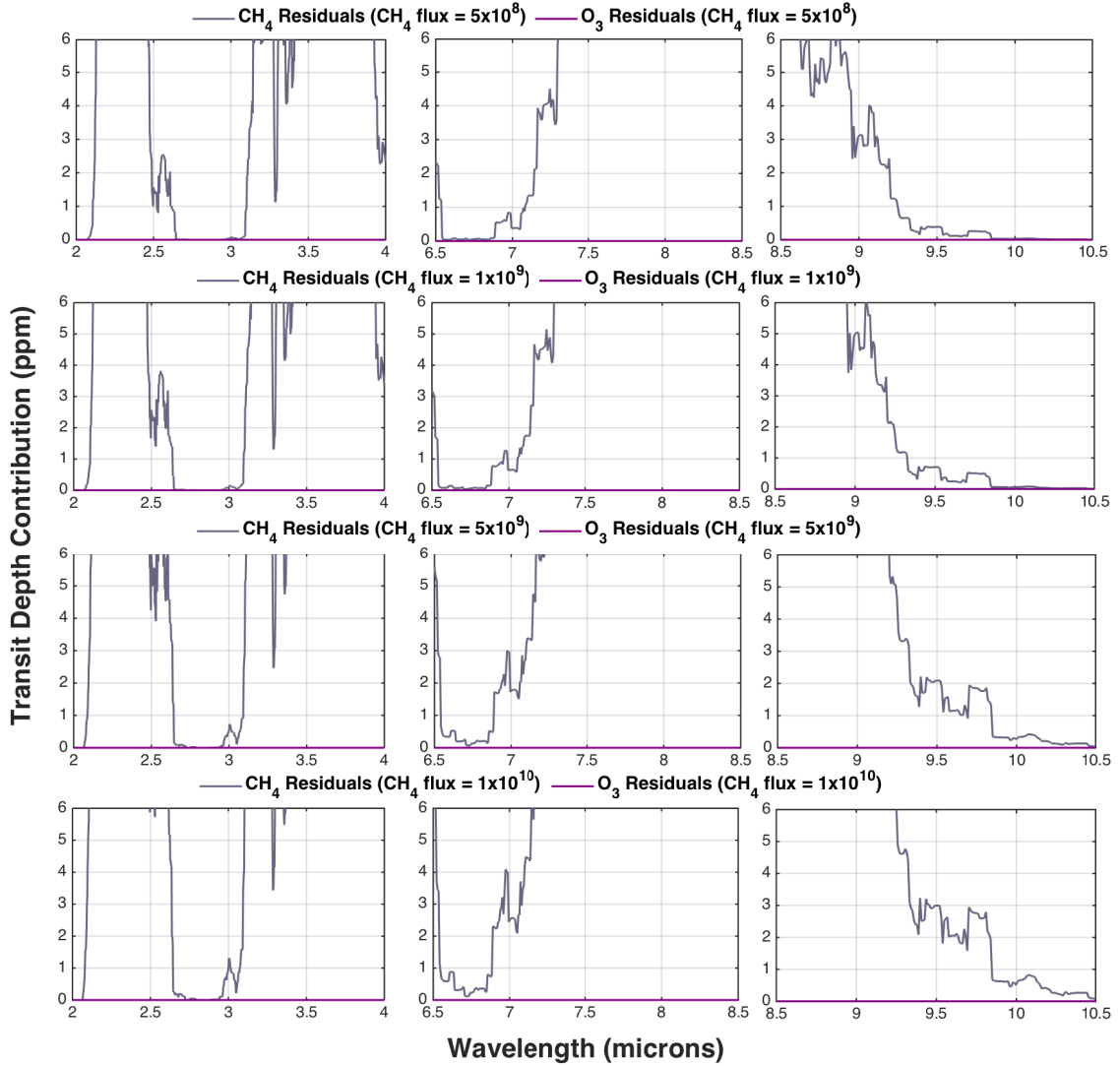


**Figure 5.4:** Spectral feature contribution residuals for the inactive/low UV/model star case, resulting from blackbody-only UV levels. This is presented with same convention as previous (and forthcoming) plots. There is not much ozone, but there is a lot of methane as expected.

The results corresponding to lowest realistic activity level—Medium UV 1 star—is shown in Figure 5.5.  $\text{CH}_4$  increases to detectable levels, and quite noticeably for higher  $flux(\text{CH}_4)$ , where the tail again extends to the rightmost panel. We do not find quantifiable  $\text{O}_3$  for any of the cases as this star has the lowest FUV flux strength, even noticeably lower than the Medium UV 2 star even (please refer back to Figure 4.2). With so little photolysis going on,  $\text{O}_3$  production and loss rates stay small and

comparable. As  $flux(\text{CH}_4)$  increases, a higher  $flux(\text{H}_2)$  is needed for redox balance as we mentioned in the previous section, and the lower OH that results in the lower atmosphere allows for less consumption of  $\text{CH}_4$ , and thus leads to a more rapid increase.

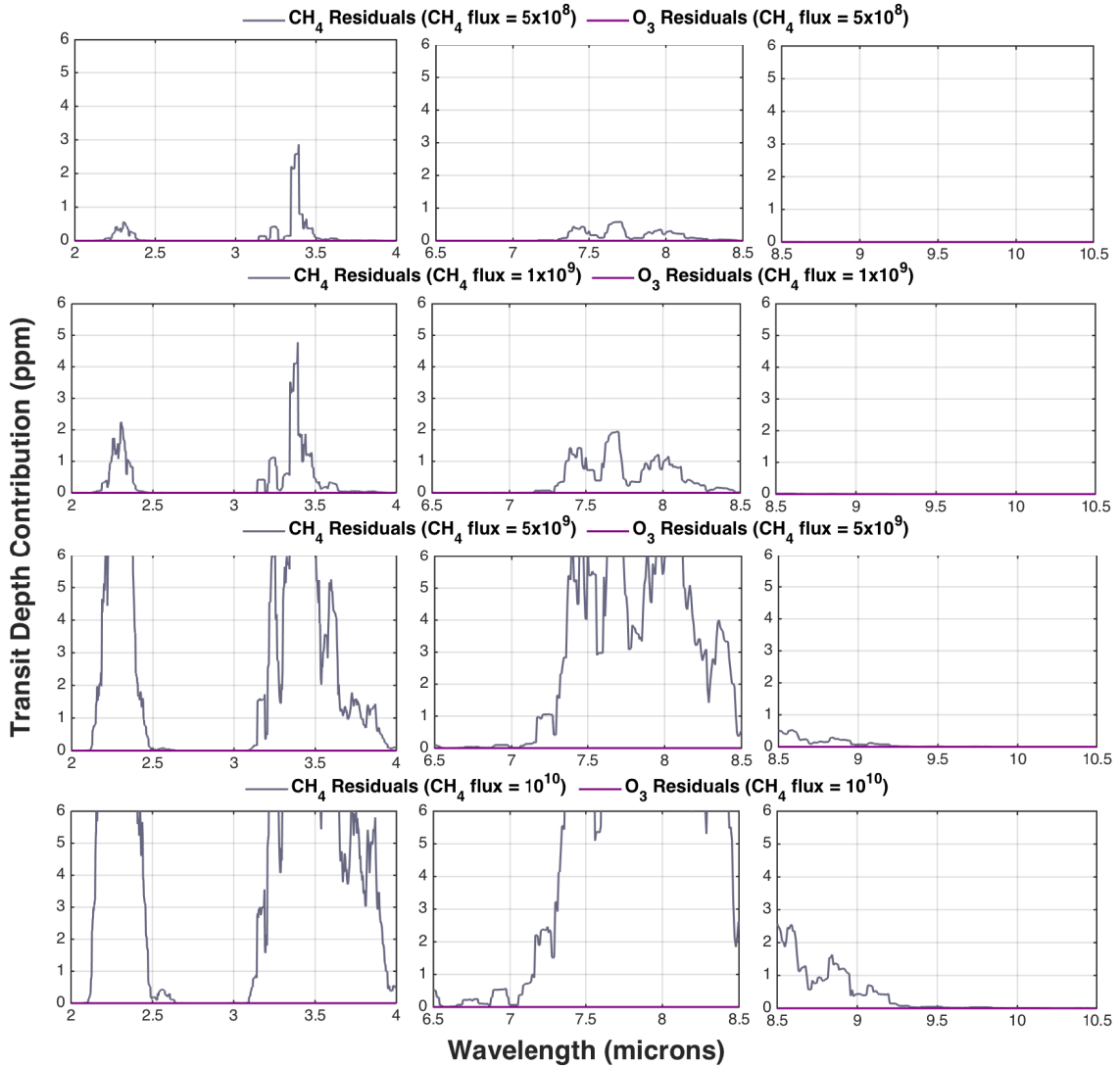


**Figure 5.5:** Spectral feature contribution residuals for the Medium UV 1 star presented with same convention as previous plot. We do not find quantifiable ozone, just the usual methane.

The results corresponding to our second highest UV case—High UV star—is shown in Figure 5.6. For all methane fluxes, both methane and ozone remain below what we could consider to be detectable levels, the methane abundance is actually

pretty low over the NIR range as well. Amongst all five UV activity profiles, this case shows the least dramatic scaling of methane (and ozone, where applicable) with increasing methane flux, and thus is also the case with the least amount of atmospheric methane produced for a given methane flux. As this star has the highest UV activity profile of all the stars discussed before, we see a case of overall stellar UV activity being higher than another star (e.g. Medium UV 2 in this case)—this does not necessarily result in higher quantities of a photochemically introduced species. This particular shift in trend shows the role of the relative strength of FUV to NUV and MUV in determining the steady state abundance of biosignatures that are depleted (e.g. CH<sub>4</sub>) or enhanced (e.g. O<sub>2</sub> and thus O<sub>3</sub>) via photochemistry in the atmosphere.

CH<sub>4</sub>, CO<sub>2</sub> and H<sub>2</sub>O only have cross-section data in the FUV (please refer back to bottom panel of Figure 4.2) and they are all responsible for breaking down into atomic O and OH, the former combines with O<sub>2</sub>—which has cross-section data in the NUV—to create O<sub>3</sub>, while the latter destroys O<sub>3</sub> through a catalytic cycle. O<sub>3</sub> has cross-section values from FUV through NUV (also Figure 4.2). Since the FUV flux increases with increasing UV activity, there is more atomic O available from photolysis of key species and OH from water —meaning both the production and loss of O<sub>3</sub> increases with increasing FUV, but the production mainly happens from products O made available from FUV reactions. And increasing FUV also increases photochemical depletion of CH<sub>4</sub>. However, NUV to MUV region is responsible for breaking down O<sub>2</sub> and O<sub>3</sub> only, and thus primarily drive the breakdown of O<sub>3</sub> to atomic O. The integrated flux ratio  $FUV(1216A-2000A)/[NUV+MUV(2000-4000 A)]$  is much higher for the Medium UV 2

star than Medium UV 1 star (please refer to top panel of Figure 4.2), as numerator is larger but denominator is smaller for Medium UV 2 compared to Medium UV 1, implying a greater production of  $O_3$  for Medium UV 2 than breakdown.

Of course, this does not factor other reactions that are happening that also affect the total O budget in the atmosphere, so the relationship does not stay as straightforward. For example, the High UV case has a slightly higher  $FUV(1216A-2000A) / [NUV+MUV(2000-4000 A)]$  ratio than Medium UV 2, but at those high FUV fluxes, we lose a lot of  $CH_4$  but also gain a lot of OH from significantly increased photolysis. As we discussed in Chapter 4, OH combines with  $CH_4$  and further decreases available  $CH_4$  for the High UV case compared to the Medium UV 2 case, but the higher abundance of OH in the upper atmosphere for the Medium UV cases (compared to High UV) means there is more  $O_3$  destruction as well in the upper atmospheres of the Medium UV stars, whereas for the highest two UV cases, the ozone shield is formed, meaning there is more OH and less  $O_3$  destruction in the upper atmosphere. However, the Medium UV 2 star also has a higher net production of  $O_3$  in the lower atmosphere than High UV; when all  $O_3$  production and loss reactions are integrated over the lower half of the atmosphere, while significantly more  $O_3$  is produced over this region from recombination of O and  $O_2$  for High UV, there is more O produced for the Medium UV stars in the lower atmosphere as well as the rates as some of the reactions that breakdown  $O_3$  to  $O_2$  and O have a higher rates in the lower atmosphere Medium UV 2 star. The high lower atmosphere reservoir of O and  $O_2$  for the Medium UV 2 star, combined with the lower availability of OH means a higher net abundance of  $O_3$  in the lower

atmosphere for Medium UV 2 star, and this is the region that contributes most significantly to our assumed cloudless spectrum. Putting this together explains the small spectral features of CH<sub>4</sub> and O<sub>3</sub> for this High UV case.

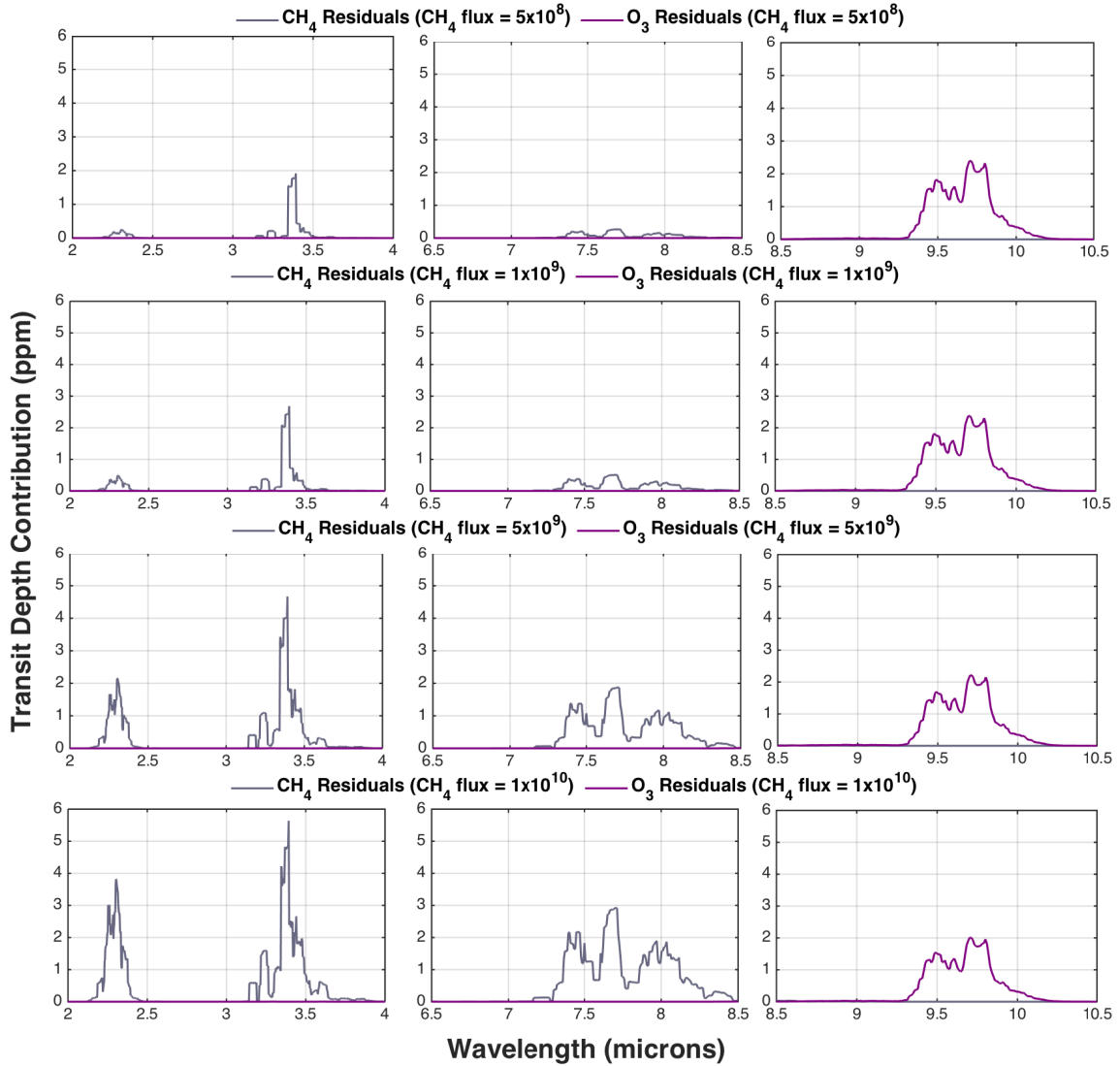


**Figure 5.6:** Spectral feature contribution residuals for the High UV star—our second highest UV case—presented with same convention as previous plots. Both methane and ozone remain below minimum detection threshold despite increasing methane flux. This is also the case with the least amount of atmospheric methane for higher methane fluxes. This particular result demonstrates that overall stellar UV (FUV-NUV-MUV) activity can be higher than a less active star like Medium UV 2, but still produce less of a photochemically sourced species.

Lastly, we show our results for our highest UV activity case—the Very High UV star, below in Figure 5.7. This activity profile not only has the highest stellar flux values at a given instellation, but also has the highest FUV/(NUV+MUV) ratio of all the cases. Thus, while the H<sub>2</sub> fluxes required for redox balance do not vary much as we increase methane in the abiotic range, this star is the most efficient at photochemistry and both depletes and enhances photochemically altered species the most. Thus, the lower atmosphere OH mixing ratios are the highest of all UV cases as we saw in Chapter 4, and does not vary much as methane increases, thereby not consuming methane further, so the rate at which the methane mixing ratio increases with increasing flux is just slightly higher than the High UV case, but at a much lower rate than Medium UV 2. This profile produces the most O<sub>3</sub> for a given methane flux amongst all stars, and appears to maintain this high abundance for all four fluxes.

For this case, we further keep increasing the  $flux(\text{CH}_4)$  beyond our nominated abiotic range to two more half orders (as mentioned in the last part of the Methods section), and CH<sub>4</sub> appears to increase dramatically. We find simultaneously detectable quantities of both species for this active-UV case at  $flux(\text{CH}_4)$  of roughly 10 times the flux at which we found simultaneous features for the Medium UV 2 star—the only other case for which simultaneous ~ 5-ppm level of CH<sub>4</sub> and O<sub>3</sub> spectral contribution is also computed. This case gives the largest simultaneous signals of methane and ozone, but for a methane flux that is somewhat ambiguous in its likelihood of abiotic/biotic makeup. That is, while large quantities of ozone appear to build up for very low abiotic methane fluxes, buildup of detectable quantities of both species are only possible for methane fluxes that may be too high to be entirely abiotic sourced.

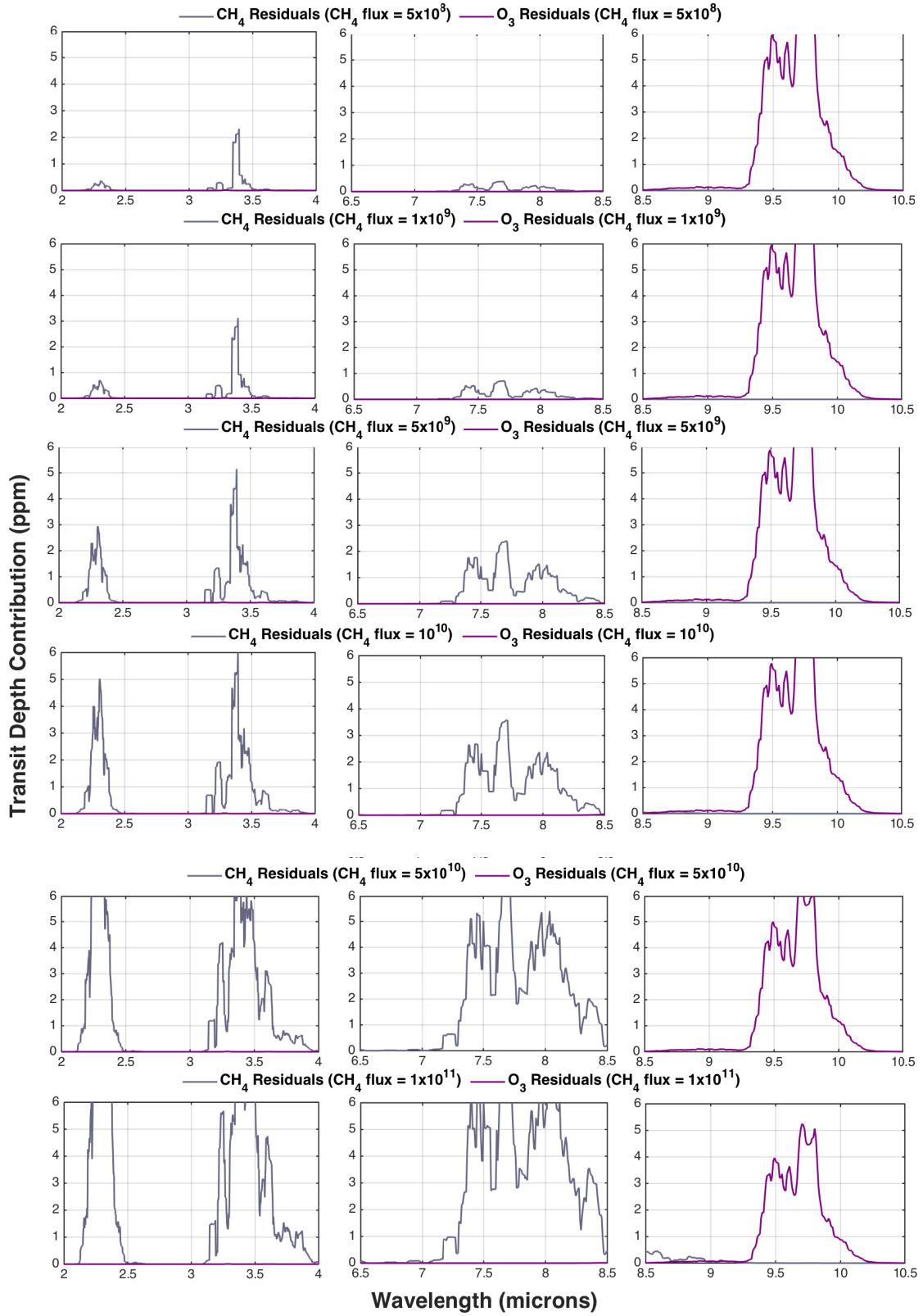


**Figure 5.7:** Spectral feature residuals we compute for the highest activity star from Chapter 4/Paper I (Very High UV). Even for our usual uppermost methane flux of  $10^{10}$  molecules  $\text{cm}^{-2}$   $\text{s}^{-1}$ , methane remains below 4 ppm. This stellar profile produces the most ozone, as we saw in Figure 5.1, and the ozone abundance does not appear to decrease with increasing methane flux as dramatically within our selected nominal methane flux variation range, but is primarily dictated by the high level of photochemical activity. For this Very High UV case only—our highest UV case—we allow the methane flux to continue increasing to  $10^{11}$  molecules  $\text{cm}^{-2}$   $\text{s}^{-1}$  in the last two panels and find simultaneously large (i.e. above 5 ppm) signals for both species.

### 5.3.2 Case II: Instellation Varied with updated H<sub>2</sub>O, Methane Also Varied

In this section, we present the spectral contributions from the two species—methane and ozone—separately computed just as they are in the five figures in the previous section, but for decreasing instellation. We present a comprehensive set spectra plot and the accompanying mixing ratio plots for each instellation below, starting with the highest lower instellation value of  $1600 \text{ W/m}^2$  and working our way down to our final instellation case with  $S < S_0 = 0.8S_0 = 1088 \text{ W/m}^2$ .

The two figures per instellation summarize all the essential spectral and mixing ratio information we conveyed to explain our results in the preceding discussion. In the spectra figure for a given instellation, we show only the MIR range and as a single panel this time, and show four bordered boxes (for the four different active UV profile cases), each containing a column of four panels with spectra results for increasing methane fluxes as above. We have plotted all 20 profiles (from 5 UV activity cases with 4 methane fluxes for each case) computed for each of the species included (H<sub>2</sub>, H<sub>2</sub>O, OH, CH<sub>4</sub>, O<sub>3</sub>). Each panel in a given row attempts to show the results for all five UV profiles for that species, for a given  $flux(\text{CH}_4)$ , within the x-axis range we chose for the panel. In other words, the mixing ratio figures follow the same convention as

our mixing ratio figure from Chapter 4 (Figure 4.3) and should be compared with it, as these serve as the best 1-D visual representation of the atmospheric states. To allow for direct comparison from species to species within a single row (i.e. a single CH<sub>4</sub> flux) we let the mixing ratio range span exactly 12 orders of magnitude for all panels, adjusting the exact range for a given panel to what best suits the data shown in the panel. For a given species at a given instellation, the range remains unchanged as methane increases. As we go down the mixing ratio figure for a given instellation, we can see how methane and the other shown species evolve with increasing methane flux across the entire atmospheric column.

In addition, the description we provide above for our default instellation case of  $S = 1.213S_0$  should also hold for these three additional  $S > S_0$  cases, as the atmospheres are still moist and the profiles thus behave in a similar manner; the description of Section 5.3.1 is informed by these mixing ratio plots. The troposphere is also close to 1 mbar level for all three cases and the atmosphere remains moist up to that level, even if the H<sub>2</sub>O column below 1 mbar is getting drier with decreasing instellation. As such, the qualitative spectral trends from our default instellation case above still hold for these. However, as these stars are all further away (meaning smaller scale heights), and have different H<sub>2</sub>O,  $P$ - $T$  and  $K_{zz}$  profile shapes from one instellation to another, the differences in the inputs also result in minor differences in the output.

### 5.3.2.1 Instellation Cases with $S > S_0$

As before, for all three instellations, we find large quantities of detectable methane only and no ozone for the Medium UV 1 star, simultaneously detectable

methane and ozone for the Medium UV 2 star, small amounts of both (not large enough to be simultaneously detectable) for High UV star, and also find contributions from both species for the Very High UV star. Note that we are assuming contributions of 3-4 ppm to have met the 5 ppm threshold required for detection via OST MISC TRA as we do not present our spectra at either the native resolution of Exo-Transmit ( $R \sim 1000$ ; Kempton et al. 2017) here, or even at the  $R \sim 100-300$  (TRA-S, TRA-M) spectral resolution that is required of *OST* to do primary and secondary transits spectroscopy of habitable planets for biosignature studies over 5-25  $\mu\text{m}$ . In order to maintain consistency with our first paper (i.e. with Chapter 4), we have continued to use a much coarser resolution of  $R \sim 65$  for our spectra plots, where we smooth the data over 15 adjacent points in each spectrum via a moving low pass filter. If the data is plotted at *OST* MISC TRA's minimum required spectral resolution of  $R \sim 100$ , the features are sharper; 4 ppm  $\text{O}_3$  signals at  $R \sim 65$  surpass the 5-ppm mark at  $R \sim 100$ . For the  $\text{CH}_4$  feature, which has a central peak at 7.7  $\mu\text{m}$ , this value is 3 ppm. We thus consider a spectrum at which the  $\text{CH}_4$  contribution is at least 3 ppm and/or ozone is at least 4 ppm to have detectable contributions of those species.

Given this assumption, we find that while it may be possible to find detectable quantities of both species for the two lowest instellation cases (1500 and 1400  $\text{W}/\text{m}^2$ ) for Very High UV profile, the quantities of ozone are far too low at 1600  $\text{W}/\text{m}^2$  to be detectable—this is our only instellation case where simultaneous detections are not being predicted for the Very High UV profile. As instellation decreases from 1650 to 1400  $\text{W}/\text{m}^2$ , we generally find detectable levels of simultaneous  $\text{CH}_4$  and  $\text{O}_3$  at lower methane fluxes, while finding lower quantities of  $\text{O}_3$  at a given methane flux, but a

higher quantity of methane at that same methane flux, which is why the computed methane for two lowest instellation cases in this range predict detectable spectral contributions from CH<sub>4</sub> for the High UV case as well. Note that compared to our default instellation case, there is less ozone produced for all of these new cases of lower instellation with  $S > S_0$  (see Figures 5.8 through Figure 5.13). Furthermore, while the ozone signal decreases for a given methane flux as the instellation goes down for Medium UV 2, the ozone signals in the High and Very High UV cases do not follow that pattern – the ozone strength for a given  $flux(CH_4)$  is low for 1600 W/m<sup>2</sup> compared to our starting 1650 W/m<sup>2</sup> instellation case (bottom two boxes in Figure 5.8 & blue and black curves in Figure 5.9). It increases again for 1500 W/m<sup>2</sup> (Figure 5.11 & 5.12), and finally decreases again for 1400 W/m<sup>2</sup>, just not as much. In sum, 1600 W/m<sup>2</sup> case has the highest ozone signals amongst these three instellation for Medium UV 2, but the lowest ozone signals amongst the three for High and Very High UV cases, and this trend is maintained for all methane fluxes. We suspect this trend is the result of water loss being the highest in the 1600 W/m<sup>2</sup> star of all the  $S > S_0$  instellation cases, especially for these highly photolyzing stellar profiles (blue and black curves in the H<sub>2</sub>O panels in Figures 5.9, 5.11 & 5.13 and also compare to Figure 4.3 in Chapter 4, for the 1650 W/m<sup>2</sup> case) resulting in this instellation having the largest reservoir of OH available to destroy O<sub>3</sub>. Comparing the H<sub>2</sub>O panels in Figure 5.13 ( $S = 1400$  W/m<sup>2</sup> case) to 5.11 (1500 W/m<sup>2</sup>) shows that the 1400 W/m<sup>2</sup> instellation has the second highest water loss, and 1500 W/m<sup>2</sup> has the least water loss following our default case. It is worth remembering here that with all our efforts, none of new cases produce more ozone than our original 1650 W/m<sup>2</sup> instellation results from Case I (Section 5.3.1).

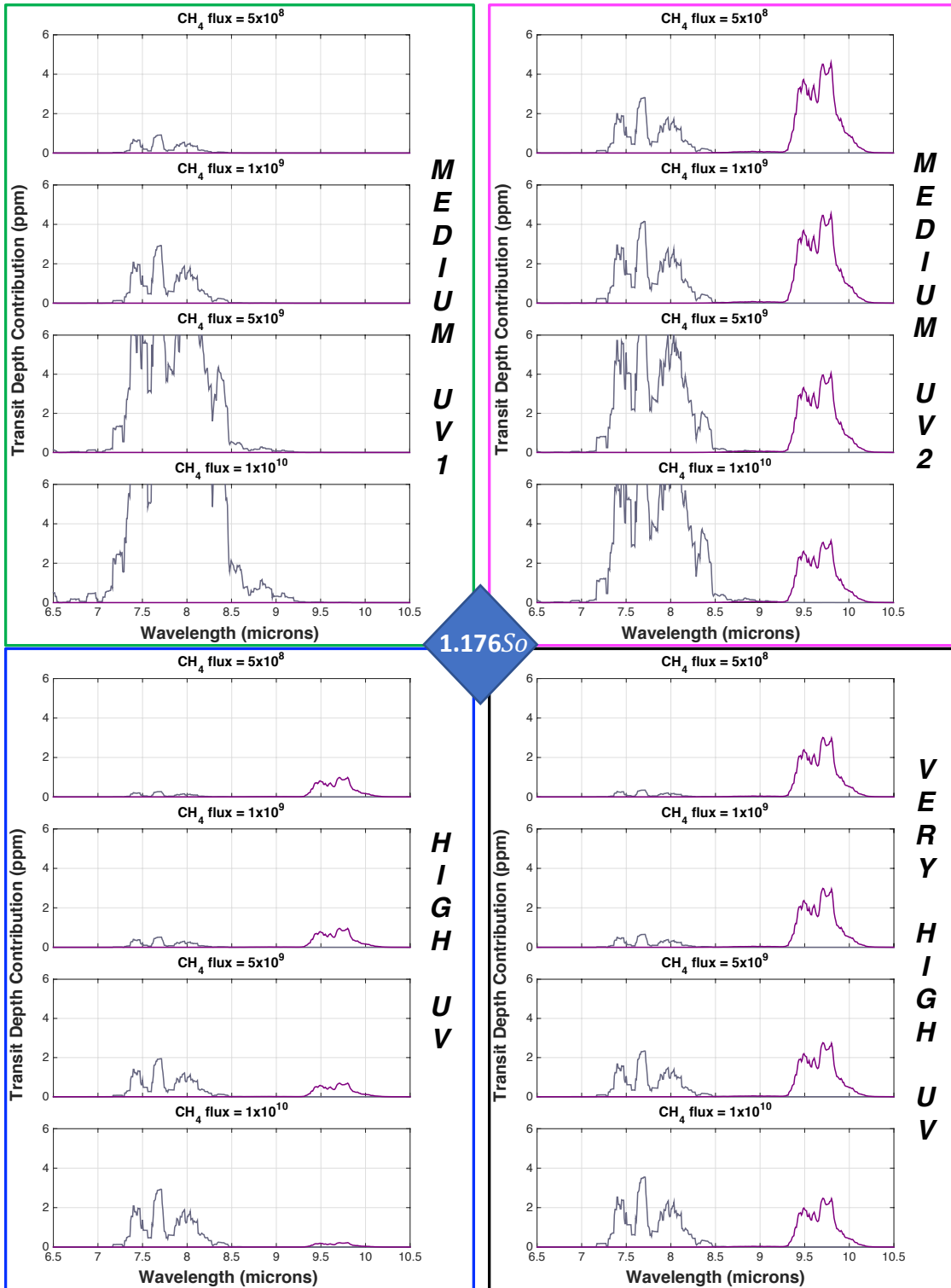


**Figure 5.8:** Spectral contribution of  $O_3$  and  $CH_4$  generated using the Atmos-computed mixing ratios shown for the GCM instellation case of  $S/S_0 = 1.176 = 1600 \text{ W/m}^2$  as input. Going from top left to bottom right, we show our computed transmission feature strength for  $O_3$  and  $CH_4$

for the Medium UV I (green border), Medium UV 2 (magenta border), High UV (blue border), and Very High UV (black border) stars, respectively. We do not show plots for the inactive case; as per our results from the default instellation case of  $S/S_0 = 1.213 = 1650 \text{ W/m}^2$ , covered in preceding plots and in Chapter 4, the inactive star causes negligible accumulation of photochemically generated species. This continues to be true for other instillations as predicted.

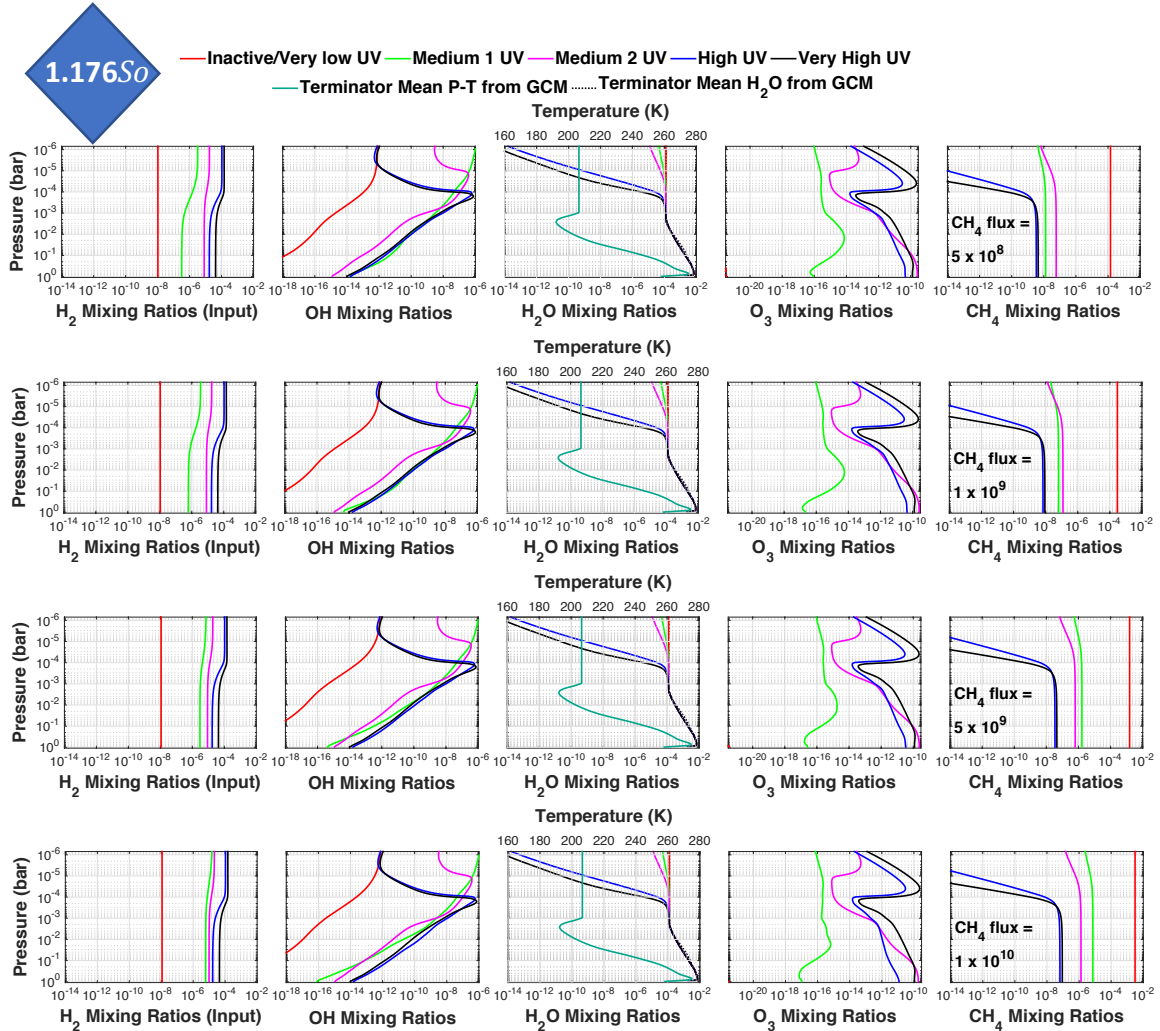


**Figure 5.9:** The mixing ratio profiles, from the photochemical model, responsible for the preceding spectra figure for instellation  $S/S_0 = 1.176 = 1600 \text{ W/m}^2$ . Other species most relevant to the O<sub>3</sub> and CH<sub>4</sub> abundances (last two columns) in the atmosphere have also been included for comparison. For the mixing ratio axis, we have chosen a scale spanning 12 orders of magnitude for each species to facilitate direct visual comparison, but we let the range differ from one species to another (e.g. H<sub>2</sub>O vs its photolytic byproduct OH). We also show H<sub>2</sub> mixing ratio panel to show the mixing ratios that result from the H<sub>2</sub> flux value that was required to fulfill redox balance in both atmosphere and ocean (see Table 5.2 for the values). In O<sub>3</sub> panels where the red curve—i.e. the profile that corresponds to the inactive/low UV star case—is missing, it indicates that the profile values are all  $< 5 \times 10^{-20}$ .

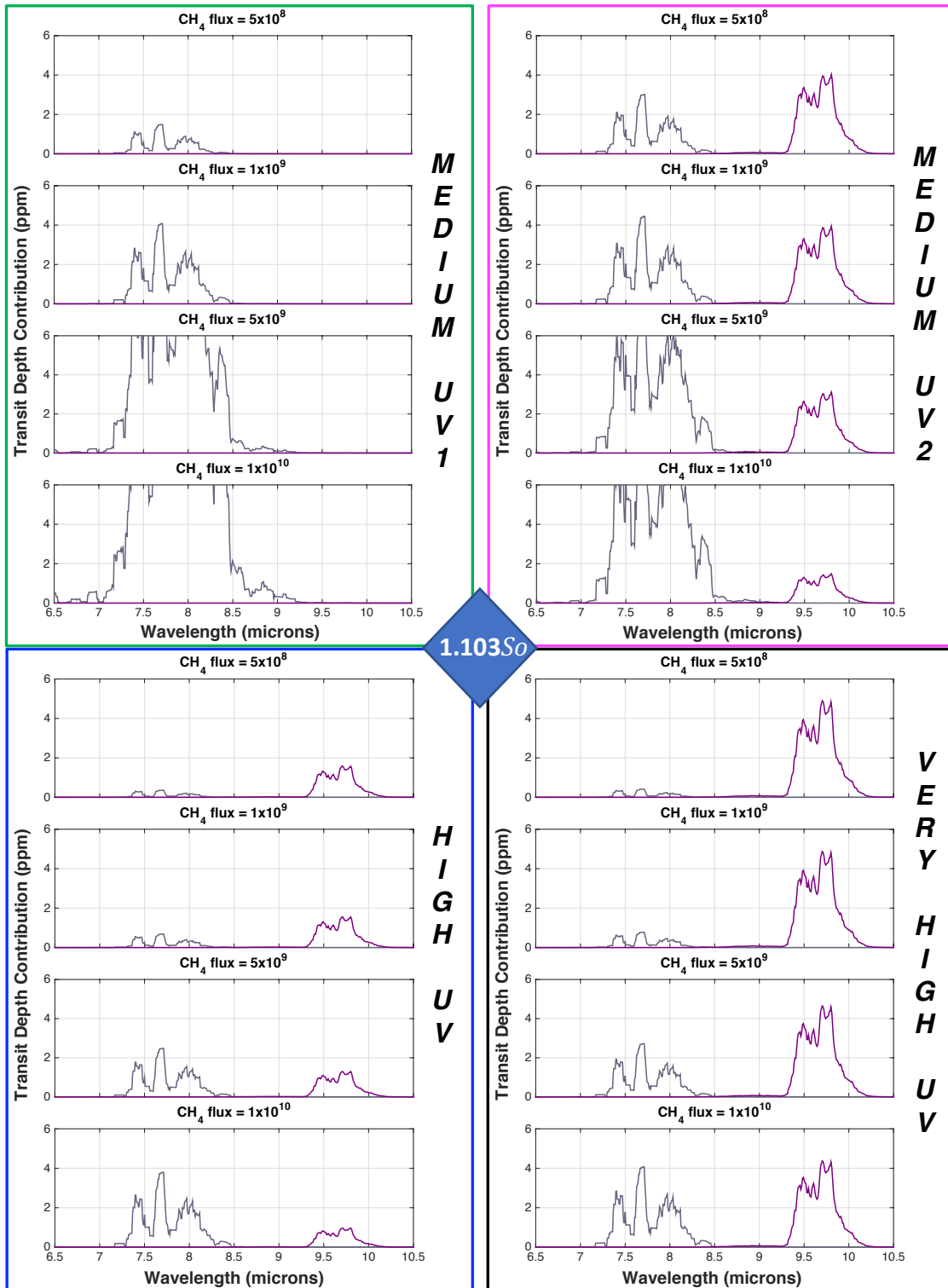


**Figure 5.10:** Spectral contribution of O<sub>3</sub> and CH<sub>4</sub> corresponding to the instellation case of S/So = 1.103 = 1500 W/m<sup>2</sup> shown. Our layout here (and our reasoning for exclusion of inactive star result data) remain the same as the preceding figure.

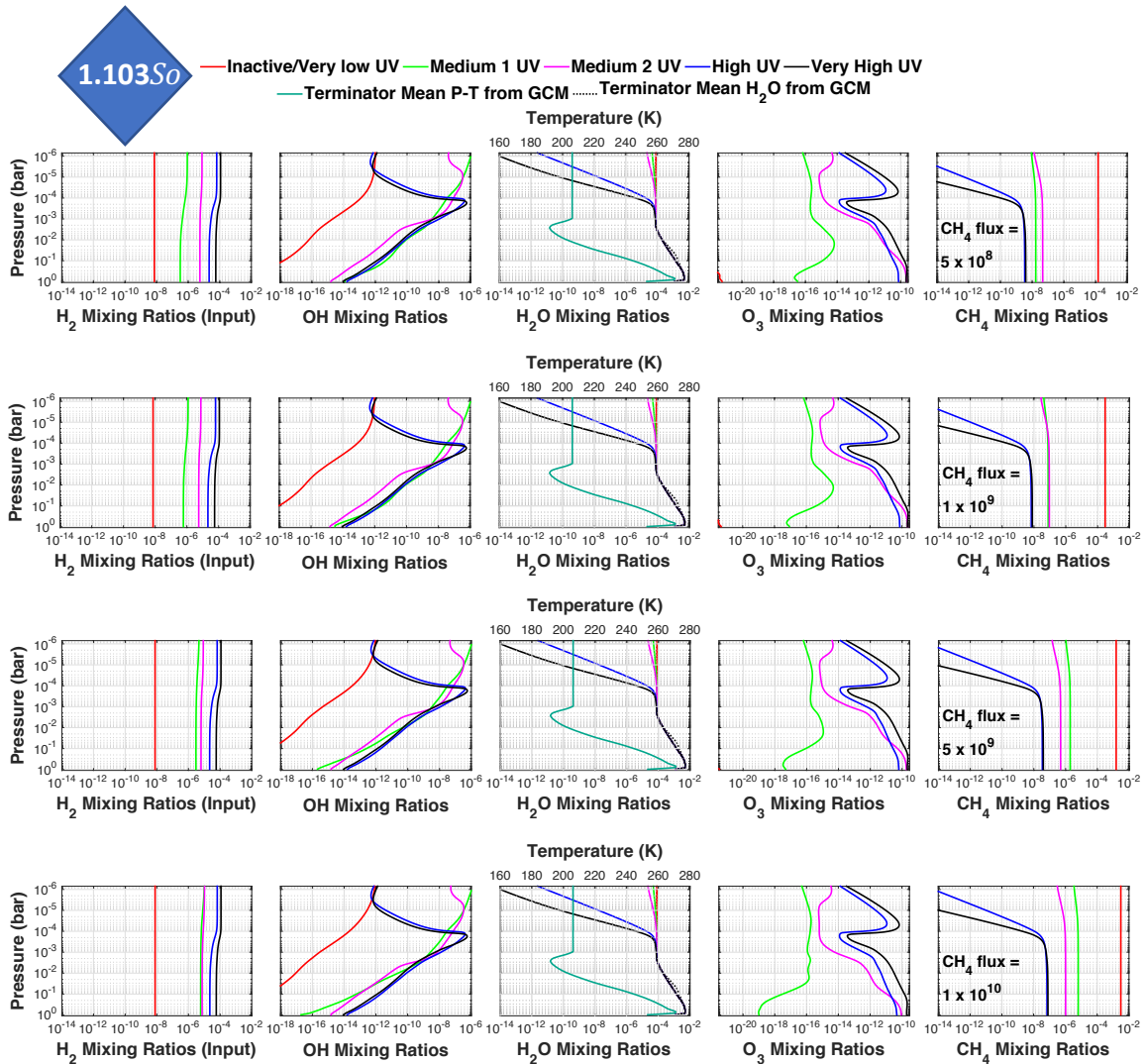


**Figure 5.11:** The mixing ratio profiles, from the photochemical model, responsible for the preceding spectra figure for instellation  $S/S_0 = 1.103 = 1500 \text{ W/m}^2$ . Other species most relevant to the O<sub>3</sub> and CH<sub>4</sub> abundances (last two columns) in the atmosphere have also been included for comparison. Just as the previous mixing ratio figure, we have chosen mixing ratio scales spanning 12 orders of magnitude for each species, but let the range differ from one species to another (e.g. H<sub>2</sub>O vs its photolytic byproduct OH) as different species span different ranges.

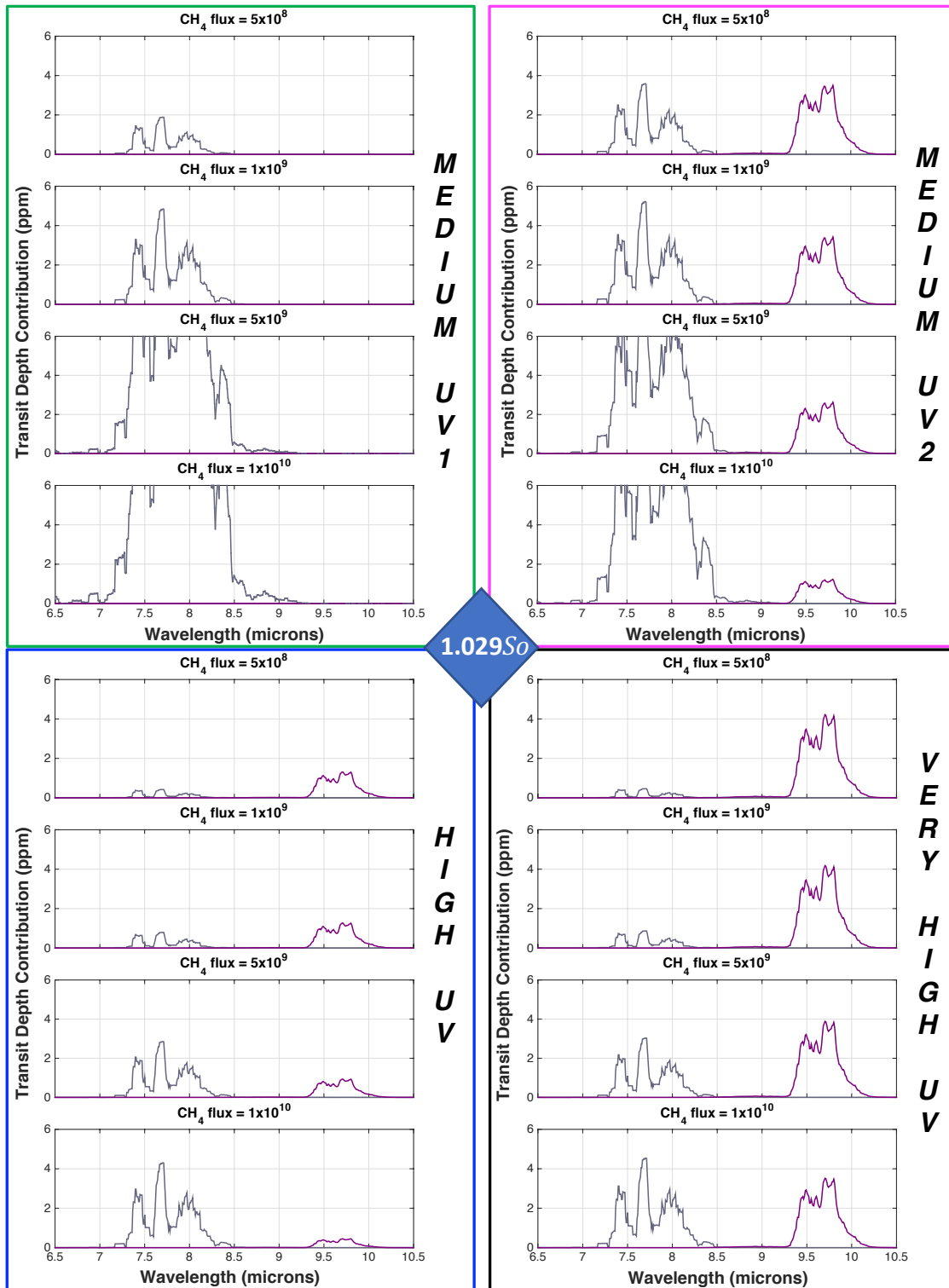
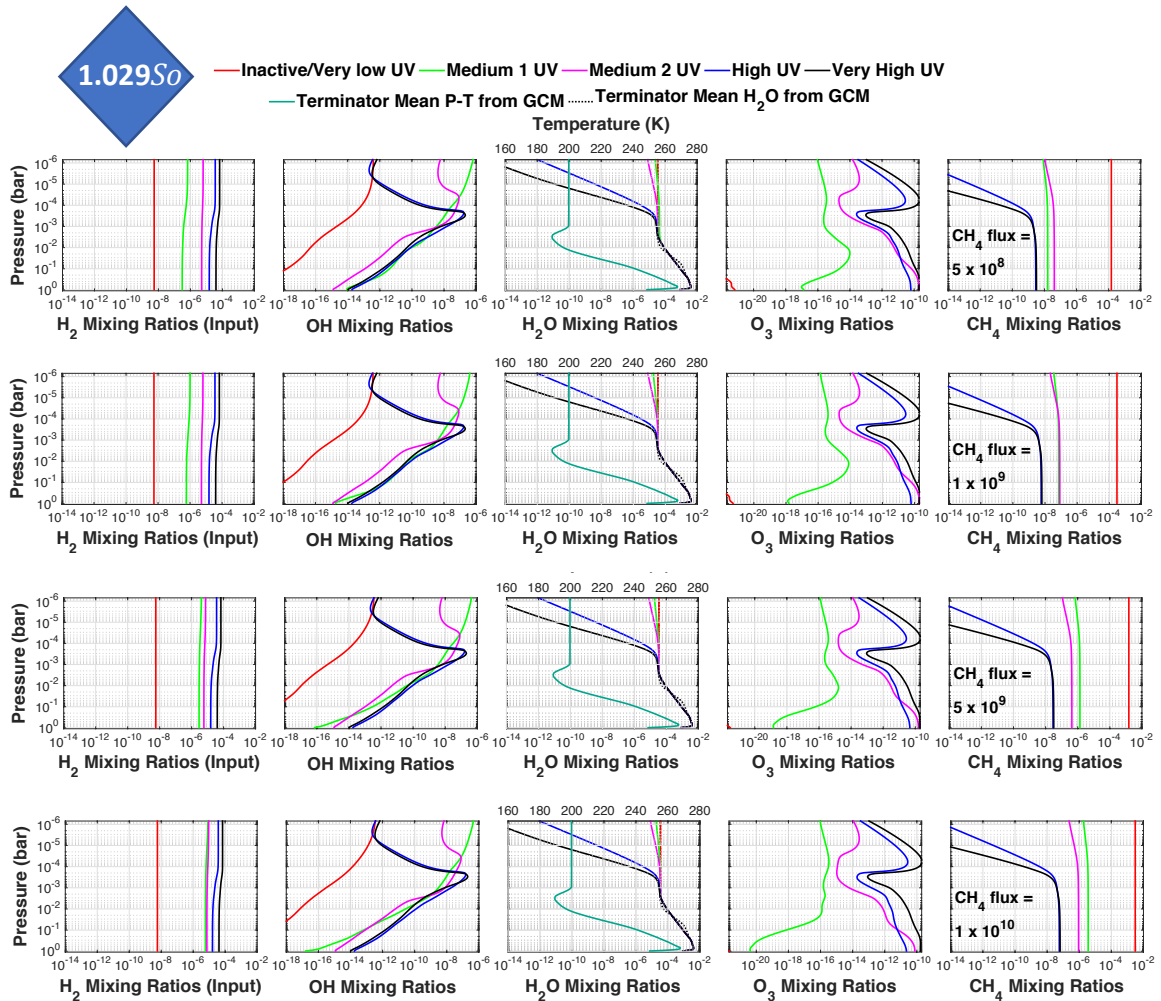


Figure 5.12: Spectral contribution of O<sub>3</sub> and CH<sub>4</sub> for  $S/S_0 = 1.029 = 1400 \text{ W/m}^2$  case shown.



**Figure 5.13:** The mixing ratio profiles, from the photochemical model, responsible for the preceding spectra figure for installation  $S/S_0 = 1.029 = 1400 \text{ W/m}^2$ . Other species most relevant to the O<sub>3</sub> and CH<sub>4</sub> abundances (last two columns) in the atmosphere have also been included for comparison. Other conventions are identical to the preceding Figures 5.9 and 5.11.

### 5.3.2.2 Instellation Case with $S < S_0$

The lowest instellation case we use in our study,  $S = 0.8S_0 = 1088 \text{ W/m}^2$ , is also our one instellation case where the stratosphere is truly dry, despite being tidally locked, due to freezing conditions of the planet. The water mixing ratios are 4-5 orders of magnitude lower at 1 mbar, and because the stratosphere also starts lower due to a smaller scale height and tropopause, the enhanced vertical mixing is constrained below 25 km in altitude, as opposed to 40 km or higher. These conditions combine to create an atmosphere where photolysis effects are felt at a lower altitude in the atmosphere, so the ozone shield can also form at lower altitudes, just above 25 km. This means that at the much lower altitude at 1 mbar, there is already quite a bit of water vapor, methane, and carbon dioxide lost to photolytic loss. However, while these atmospheres lose a lot of these key species, the OH released into the atmosphere from  $\text{H}_2\text{O}$  photolysis (and mediated by other reactions) is limited by much smaller initial reservoir of water vapor throughout the atmosphere.

The  $flux(\text{H}_2)$  value needed to balance the two High UV cases are almost identical for the higher methane fluxes and they are identical for all methane fluxes for the Medium UV cases. Thus, the OH profiles for the Medium UV stars almost overlap for this instellation, meaning difference in  $\text{O}_3$  profiles between the two are largely dictated by methane – for a given methane flux, Medium UV 1 has the highest methane mixing ratio consistently, and thus the lower ozone, similar to other cases. The High UV case has the most OH in the atmosphere (but still less OH than all other instellation cases), so the most OH available for destroying  $\text{O}_3$ , however there is an increased abundance of O and  $\text{O}_2$  produced, in addition to the generally less available OH, as a

result of increased photolysis. Since photolysis effects are still the most impactful for the Very High UV case, and it also has less OH available for O<sub>3</sub> destruction, we see the highest abundance of O<sub>3</sub> for the Very High UV case. In general, due to the abundance of O<sub>3</sub> makers being present in higher quantities from a lower altitude in this atmosphere in all five UV cases, but OH reservoir being low in general, these atmospheres are able to build comparable amounts of ozone in the upper atmosphere, especially, in the stratosphere, similar to rapidly rotating earth where we can use ozone abundances to distinguish the troposphere from the stratosphere—where it is enhanced.

However, O<sub>3</sub> is not particularly enhanced in the lower atmosphere. As a result, we get large narrow O<sub>3</sub> features from the upper atmosphere only, where the ozone is not only higher in abundance for all methane cases but also has the highest abundance of all cases studied thus far. The two broad bumps we typically see at the base for O<sub>3</sub> (e.g. Figure 5.1) are absent because of low mixing ratios in the deep region of the atmosphere, the region subjected to pressure broadening. Since mixing ratios are only high enough to produce features at the upper region, the entire O<sub>3</sub> contribution consists of a few narrow lines, with the two long spikes centered at the region where we typically see the bump. This is actually promising for observations as the cloud decks are lower for this cold atmosphere, meaning the large spikes are almost entirely coming from the upper atmosphere. Thus, it is safe to deduce that in practice, O<sub>3</sub> features should be the most easily and readily detected in these kinds of dry and cold atmospheres, if the planets are further away from the star, as O<sub>3</sub> is enhanced in the upper atmosphere, where the atmosphere is thinner and unshrouded by thick water clouds. This is also the region typically sampled by space-borne IR spectrometers.

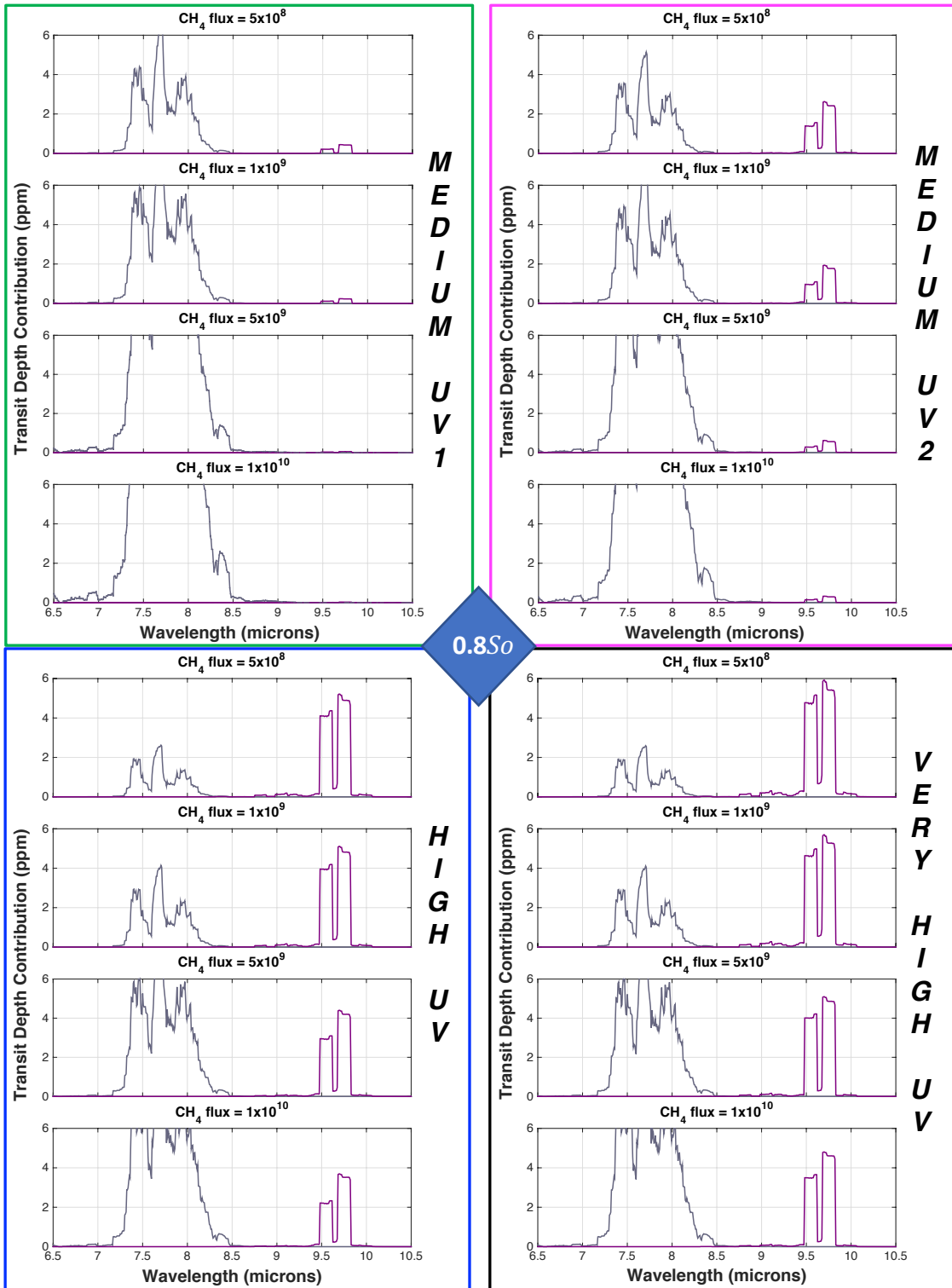


**Figure 5.14:** Spectral contribution of  $O_3$  and  $CH_4$  resulting from the mixing ratios for the low-est installation case, with  $S/S_o = 0.8 = 1088 \text{ W/m}^2$  case shown. This is the highest installation case we have from the GCM data for  $S < S_o$ , and with very low abundances of water compared to our own Earth as well as the  $S > S_o$  installation cases presented above.

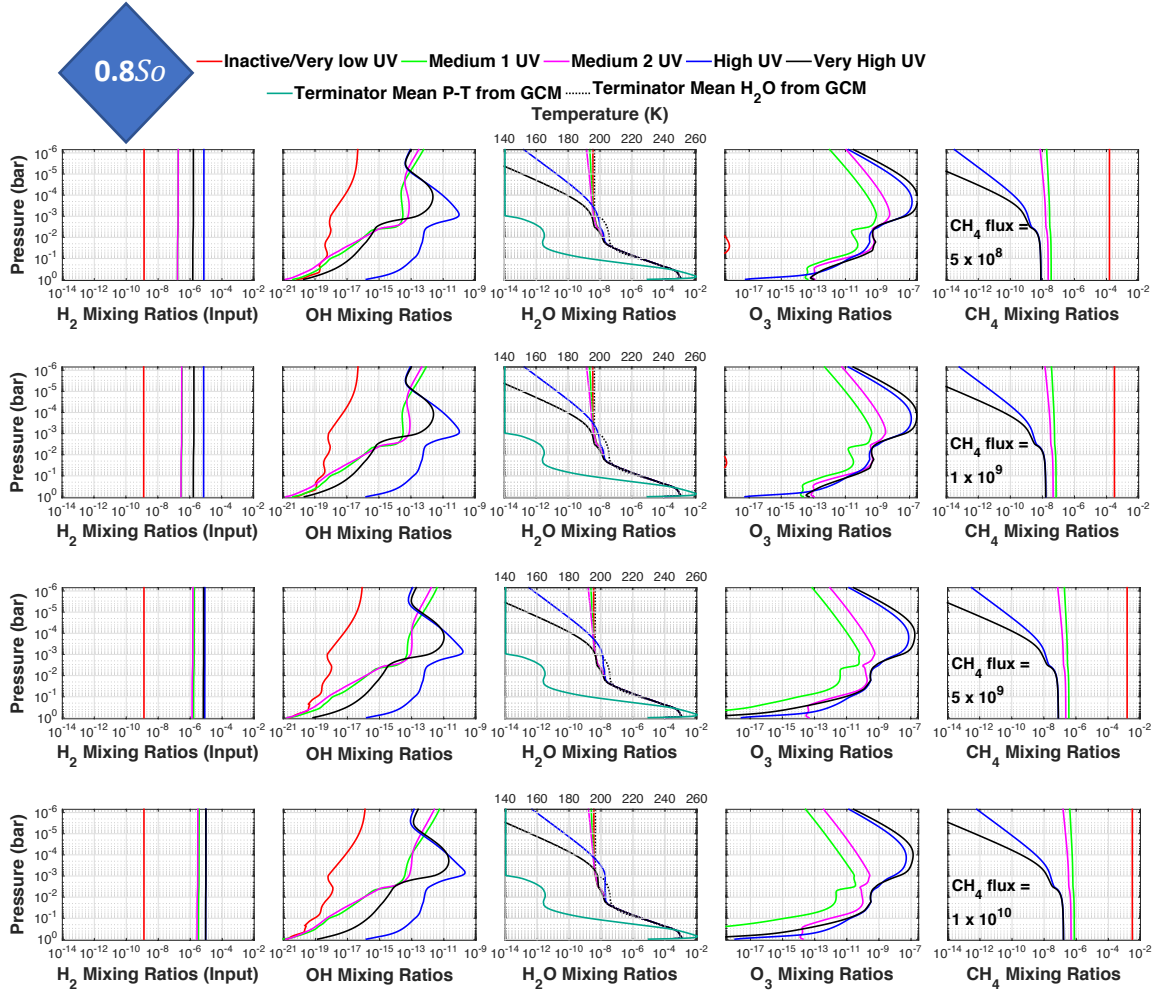


**Figure 5.15:** The mixing ratio profiles, from the photochemical model, responsible for the preceding spectra figure for instellation  $S/S_o = 0.8 = 1088 \text{ W/m}^2$ . In  $\text{O}_3$  panels where the red curve—i.e. the profile that corresponds to the inactive/low UV star case—is missing, it indicates that the profile values are all  $< 1 \times 10^{-19}$ . Other conventions are identical to the preceding mixing ratio panel figures.

## 5.4 Discussion and Summary

We have applied the methodology of our work detailed in Chapter 4 (Afrin Badhan et al. 2019) to do a follow-up study on those atmospheric states (i.e. an Earth-like aquaplanet irradiated at  $S = 1.213S_o$  from a 3300K M dwarf star), with increasing

methane fluxes from  $5 \times 10^8$  through  $10^{10}$  (up to  $10^{11}$  for one case) molecules  $\text{cm}^{-2} \text{s}^{-1}$ . We did this to simulate the photochemical impact on the abundance of a relatively trace species in these atmospheres—ozone under the varying UV-activity scenarios prescribed in Chapter 4. Furthermore, in order to investigate this further as a function of instellation level (and thus water vapor reservoir in the atmosphere), we subsequently ran photochemical models with new related GCM simulations as inputs. We choose four lower instellation cases for the 3300K star ( $S = 0.8S_0, 1.029S_0, 1.103S_0, 1.176S_0$ ) from the GCM datasets presented in Kopparapu et al. (2017) and Wolf et al. (2019). We ran a total of 125 ( $5 \times 5 \times 5$ ) base models spanning five different instellation levels, five discrete methane fluxes and for our five different UV UV-activity scenarios from Chapter 4. For our default  $S = 1.213S_0$  case only—which motivated this follow-up study—we also ran six additional cases (i.e. four intermediate methane fluxes for the Medium UV 2 star and two higher methane fluxes for the Very High UV star).

Our results for the methane and ozone abundances for all of these are provided in Figures 5.3 through 5.15. The MIR methane feature is found at  $7.6 \mu\text{m}$  and the ozone feature at  $9.6 \mu\text{m}$ . In Table 5.3, we have summarized our top-level findings. For each instellation level, we find at least two likely configurations that show simultaneous presence of ( $\text{CH}_4 + \text{O}_3$ ) at the 5 ppm-level spectral contribution level over *OST's* MIR wavelengths for abiotic methane fluxes  $\sim 1 \text{ Tmol yr}^{-1}$ . 5 ppm has been suggested to be the sensitivity threshold for the transit spectrometer being planned for the *Origin Space Telescope* mission. While we see this largely for the Medium UV 2 and Very High UV profiles, explained by the observation that these two UV profiles have the highest integrated  $\text{FUV} \times (\text{O}_3 \text{ photolysis cross-section}) / \text{MUV} \times (\text{O}_3 \text{ photolysis cross-}$

section) values, this trend is maintained for the  $S > S_0$  cases only. For the really cold  $S = 0.8S_0$  case, where the water vapor reservoir is low, affecting the availability of the OH radical for  $O_3$  destruction, we find a highly enhanced  $O_3$  mixing ratio profile, with higher quantity of  $O_3$  in both the lower and upper atmosphere for all UV-active profiles. The upper atmosphere shows a higher abundance of  $O_3$  than the lower atmosphere and is unique to this instellation level. Furthermore, an ozone shield is computed for all of the UV-active profiles for this instellation, whereas for the other higher instellation cases, only the two highest UV activity levels create a shield. Because the upper atmosphere is 100 times as enhanced in ozone and the tropopause is almost 15 km lower for this cold planet, cloud decks would be located at lower altitudes. This further implies that there is a greater chance of detection in a real atmosphere, despite being the furthest away from host star out of all the cases studied.

However, within our investigated range, the largest simultaneous ( $CH_4 + O_3$ ) signal occurs for the Very High UV star at our default instellation level (i.e.  $S = 1.213S_0$ , the atmosphere with the moistest stratosphere from the GCM runs) with methane production rate outside our nominal range ( $> 10 \text{ Tmol yr}^{-1}$ ), and may be indicative of a simultaneous detection for abiotic methane flux. For a given UV-activity scenario and methane flux for our investigated narrow range of  $S > S_0$  instellation values, we find no noteworthy trend—such as an increase or decrease of ozone quantities—with decreasing instellation. That is, we find no such scaling trend for the simultaneous detection of the two species either. We do, however, find some evidence of  $f(CH_4)$  getting higher, and thus feature getting stronger, for a given  $flux(CH_4)$ , with decreasing instellation (see  $CH_4$  panels, this is also implied going down Table 5.3).

Detectables →	~5 ppm CH <sub>4</sub> ?	~5 ppm O <sub>3</sub> ?	Simultaneous (O <sub>3</sub> + CH <sub>4</sub> )?
$S = 1650 \text{ W/m}^2 = 1.213S_0$ (GCM simulation case in Paper I/Chapter 4)			
Medium UV 1	✓	✗	✗
Medium UV 2	✓	✓	✓
High UV	✗	✗	✗
Very High UV	✓*	✓	✓*
$S = 1600 \text{ W/m}^2 = 1.176S_0$			
Medium UV 1	✓	✗	✗
Medium UV 2	✓	✓	✓
High UV	✗	✗	✗
Very High UV	✓*	✗	✗
$S = 1500 \text{ W/m}^2 = 1.103S_0$			
Medium UV 1	✓	✗	✗
Medium UV 2	✓	✓	✓
High UV	✗	✗	✗
Very High UV	✓	✓	✓
$S = 1400 \text{ W/m}^2 = 1.029S_0$ (i.e. closest to earth-equivalent instellation)			
Medium UV 1	✓	✗	✗
Medium UV 2	✓	✓	✓
High UV	✓	✗	✗
Very High UV	✓	✓	✓
$S = 1088 \text{ W/m}^2 = 0.8S_0$ (i.e. surface temperatures are below 0)			
Medium UV 1	✓	✗	✗
Medium UV 2	✓	✗	✗
High UV	✓	✓**	✓**
Very High UV	✓	✓**	✓**

\*Detectable for methane surface fluxes in likely biotic range. \*\*Possibly, as low cloud decks.

**Table 5.3:** Table summarizing the findings we have reported in this study in the previous section regarding whether we can expect to detect methane and ozone individually and simultaneously over the MIR bandpass of the *OST* instrument, given a detection threshold of ~ 5 ppm and assuming a planetary limb not enshrouded by clouds. Green ticks indicate possible detection as predicted by our model, and red crosses indicate otherwise. Where detection is only possible for methane influx clearly in a biogenic range, the box is marked in grey.

The trends we have seen here are both due to the decreasing water vapor in the atmosphere as well as changing temperature structure (Grenfell et al. 2007). A caveat here is that the methane and ozone abundance are also a function of other input variables affecting stellar UV photons, as well as chemical evolution, that we have held fixed for each instellation. These include, but are not limited to, the zenith angle—which we have held fixed at 50 degrees for the reasons we describe in Chapter 4—and the exact  $K_{zz}$  structure. Zenith angle should not impact the results much as we increase the orbital separations (via instellation changes) so little that the planets are still all tidally-locked. Photochemistry is still being driven by stellar flux over the dayside of the planet, closest to the substellar point the photons are the most numerous and the photolysis rates the fastest, and the efficient transport to the night side via a single large circulation cell should still be in effect. However, we have continued to make certain assumptions for the  $K_{zz}$  profile we use for each instellation (Table 5.2), though we do keep our assumptions uniform over all four of these new cases. We do not have an upper boundary for  $f(\text{H}_2\text{O})$  to help us constrain  $K_{zz}$  beyond the tropopause, but the  $K_{zz}$  values above that region do visibly affect the middle and upper atmosphere water vapor abundance, and thus could impact the amount of ozone produced. Investigating the impact of different  $K_{zz}$  in the future could be insightful.

Regardless of such caveats, our study provides modeled evidence for atmospheric states where 5ppm-level detectable levels of simultaneous ozone and methane is possible in abiotic anoxic atmospheres on Earth-like planets orbiting the habitable zones of M dwarfs. Furthermore, we see that for our  $S < S_0$  case, when the atmosphere is no longer moist and temperatures too frigid to allow for a comfortable biosphere,

there would be more cases of simultaneous presence of both species. The ozone column depth is higher as the ozone concentrations are actually higher in the upper atmosphere than the lower atmosphere, a region that also transmits to us readily due to being above clouds. This suggests we may not only be able to detect the species simultaneously, but that they would be more readily detected from the coldest planets within the habitable zone, where even dayside temperature is below freezing.

While the *OST* mission is still in its concept study phase for a potential launch in the 2030s, studies like the one we have described in this chapter are necessary to establish a parameter space for cases where the simultaneous detection of methane and ozone can still be considered a false positive biosignature detection. Going into the future, our study should serve as a caution to the exoplanet community looking to find biosignatures via *OST* data from nearby potentially habitable planets.

## Chapter 6: Outlook

### 6.1 Future Work: Mapping 3.3 $\mu\text{m}$ non-LTE Emissions from Methane ( $\text{CH}_4$ ) from Exoplanets for a Range of Temperatures and Host Stars

Recently, I became involved in a study at NASA GSFC that will combine my hot Jupiter modeling work from both the NEMESIS and the Atmos software packages. In this project, we are looking for signatures of non-equilibrated or (non-LTE) emissions from the upper atmospheres of several exoplanet populations, spanning a broad temperature range, host stars and signature molecules. Local thermodynamic equilibrium is an idealized state of an atmosphere where the source function is the Planck function, and atomic and molecular level populations are in Boltzmann ratios at the local temperature. At high spectral resolutions, strong and narrow molecular emissions are observable in giant planets from non-equilibrium radiative (non-LTE) regimes. In the upper atmospheres of planets in general (i.e. above optically thick layers), and in inflated atmospheres of close-in giant exoplanets, many regions are in non-LTE. Non-LTE emission has been observed from other planetary objects as well, including comets and rocky planets, e.g. it dominates the Venusian flux at 4.3  $\mu\text{m}$  (Roldan et al. 2000). Chemical reactions also lead molecules into highly excited non-equilibrium states, from which diagnostic photons are released, for example, the dayglow  $\text{O}_2$  (1D) emission tracks the photo-destruction of  $\text{O}_3$  in terrestrial atmospheres (Novak et al. 2002). In some cases, the non-LTE emission can be much greater than the intrinsic planetary emission due to stellar flux amplification via cascades (Figure 6.1). Accurate interpretation of future observations of a large range of planetary objects

(by space missions and ELTs) will require us knowing the location of these emissions and their detectability. Since assessing this process requires complicated tracking of the photon paths, past investigations of non-LTE regimes have been limited.

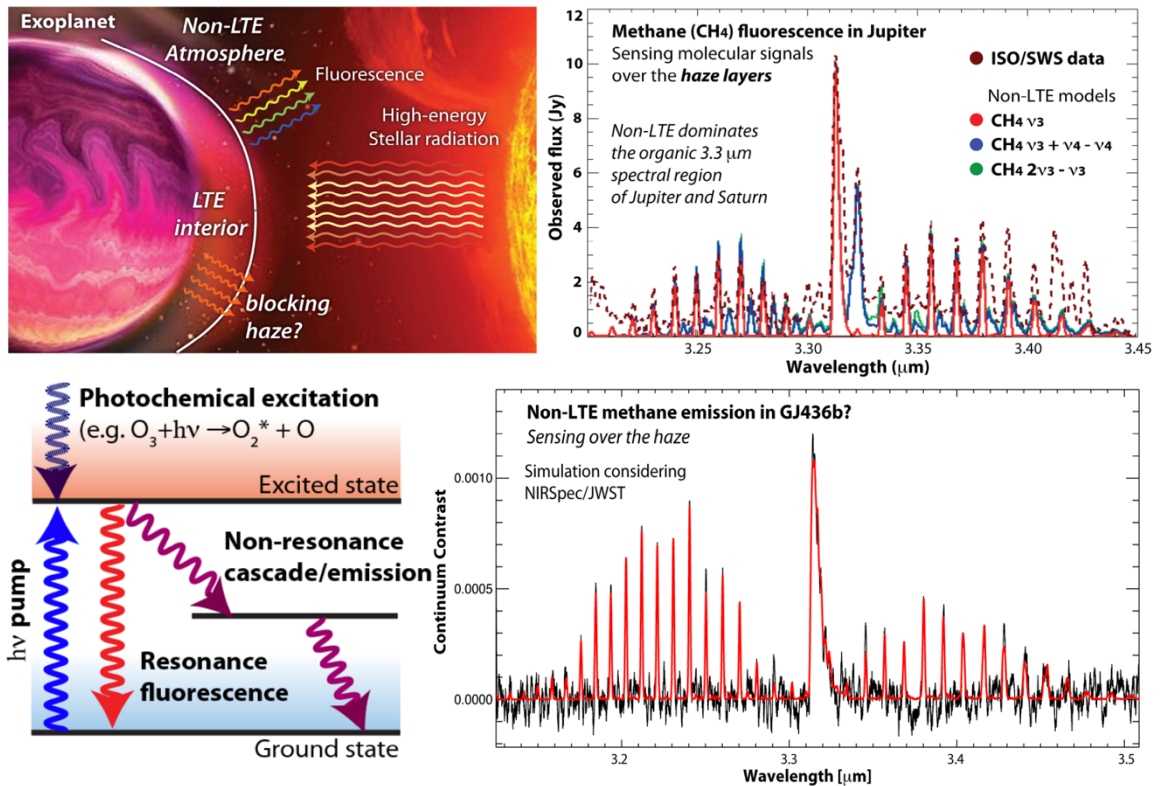


**Figure 6.1:** (All four figures taken directly from the motivation section of PI Villanueva’s 2015 proposal) *Top-left panel:* An adaption of an artist’s impression showing the way the upper atmosphere is affected by high-energy stellar irradiation; when bombarded via these highly energetic photons, the upper atmosphere emits efficiently via non-LTE fluorescence. *Top-right panel:* the 3.3  $\mu\text{m}$  methane non-LTE emission feature on Jupiter (Encrenaz et al. 1996; Drossart et al. 1999). *Bottom-left panel:* Example of a photochemical reaction with excitation (and subsequent emission) processes in a non-equilibrated environment. The photons pump the molecule to an excited state, from which multiple photons are then emitted. *Bottom-right panel:* The 3.3  $\mu\text{m}$  methane non-LTE emission feature predicted for GJ436b with simulated *JWST*/NIR-SPEC noise assumed. This plot used  $P$ - $T$  from the Line et al. analytical thermal structure I discussed in Chapter 2 (and incorporated in the hot Jupiter work in Chapter 3), methane mixing ratio profile from Moses et al. (2013), and haze locations inferred from Knutson et al. (2014).

At NASA GSFC, we have developed some novel community-oriented tools do these non-LTE flux computations (PI: Geronimo Villanueva), given high-energy databases, realistic climate models, and advanced radiative transfer models (Figure 6.2). The now-completed Planetary Spectrum Generator (PSG) at GSFC (Villanueva et al. 2018) is able to add non-LTE contributions to LTE transit spectra. We have different people working on these various requirements. I am solely responsible for the first independent task of our project—which is to a) establish the grid of model parameters to use for our representative atmospheres, and then b) model the atmospheres corresponding to these individual cases with Atmos' PHOTOCHEM module. I am compiling a set of density, mixing ratio and temperature profiles for the hot Jupiter grid-end initially. We will compute fluorescence spectra for these atmospheres to see what type of emission spectra can be produced for hot Jupiters, and for which molecules.

This will be the focus of the first paper I plan to submit from this work. We have plans to extend the validity of PHOTOCHEM to the warm-Neptune regime by adding a GJ1214b template (for sample spectra of this planet, see Figure 6.4). While the chart in Figure 6.2 summarizes the complete list of data desired for the whole project, I am presently only focusing on methane non-LTE emission calculation and not looking at any of the other molecules. We do not have ammonia in our PHOTOCHEM-computed model templates at the moment, and thus also lack Rayleigh scattering coefficients for it. This will be fixed as part of future upgrades. But for now, the remaining species of interest from the list ( $\text{CH}_4$ ,  $\text{H}_2\text{O}$ ,  $\text{CO}_2$ ,  $\text{CO}$ ,  $\text{HCN}$ ) are present in our models and since we will be publishing their profiles as part of our photochemical

study for at least the Hot Jupiter templates, those profiles may be used for non-LTE computations of the other molecules in the future.

This is a large collaboration with several exciting goals for a population of exoplanets, especially now that PSG is being widely publicized by the GSFC community. My responsibilities are limited to developing the chemistry portion; the radiative transfer portion is being handled by PI Villanueva and other core PSG team members. Other modeling and database development tasks are advancing independently. As such, we anticipate a stream of papers to come out as we accomplish the various tasks.

Our grid of model parameters can leverage the list of established boundaries for different classes of planets from the Kopparapu et al. (2018) paper. The paper classifies exoplanets based on physical property boundaries and estimates yields. Temperature-based boundaries (i.e. “hot”, “warm”, “cool”) are marked based on the order in which certain volatiles condense in the atmospheres (see Figure 6.3). Within each such boundary, the occurrence rates for terrestrial, Neptune-type and Jupiter-type planets are given, along with their direct imaging yields for different *LUVOIR* concept mirror sizes. It would be worthwhile to study each type as a population for future observations of the representative population. Non-LTE signatures should differ to some extent from population to population, so there is a dire need to complete a grid of representative models for each population. A completed database of modeled non-LTE emission quantifications can be used as a diagnostic tool for distinguishing between the populations anticipated to have the highest yields for the conservative 8-meter case (now known as the *LUVOIR-B* concept).

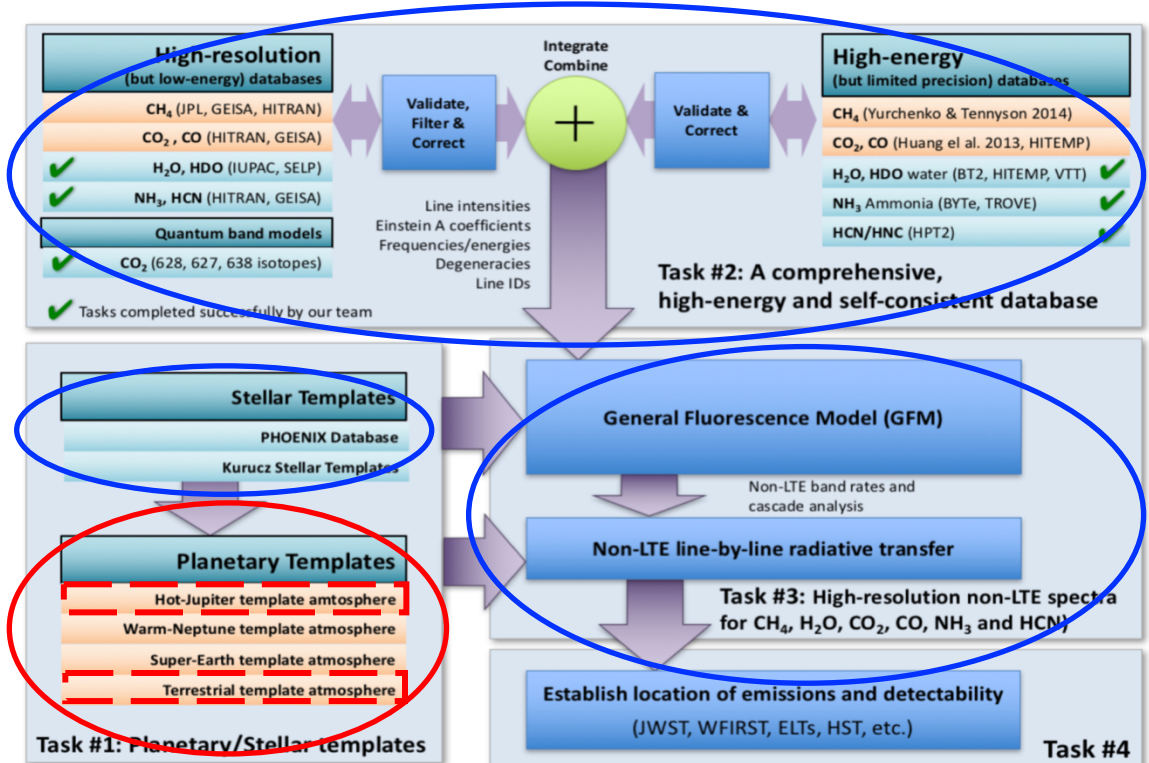
Of-course, since non-LTE signatures are observable with other high-resolution instruments, the non-LTE models we develop would also benefit the retrieval studies of directly-imaged planets from other UV/vis/IR instruments. The *LUVOIR* case I presented above is an example of a direction that interests my immediate research group. We can do a similar statistical study for *HabEX* as well, for Sun-like stars, by predicting equivalent estimates of the largest sample sizes of different types of planets. Besides finding and characterizing rocky worlds, the observations enabled by both observatories will include other (sometimes easier to observe) worlds residing between the inner and outer working angles of the starlight suppression.

### 6.1.1 Spectral Modeling and Addition of non-LTE fluorescence effects

Data for molecular and atomic linelists are available for 1259 species in the PSG database. The equilibrium chemistry models from Kempton et al. (2017), used in generating the EOS files that come packaged with the Exo-Transmit distribution, is also part of the PSG packages. The present HITRAN database (Gordon et al. 2017) is reasonably comprehensive (for IR, optical and UV at low temperatures) for the typical planetary atmosphere. It has become the main repository of line information for many spectral modeling software geared towards the modeling of planets over a broad temperature range. At radio wavelengths, the JPL Molecular Spectroscopy and Cologne Database of Molecular Spectroscopy (CDMS) is generally more complete and with a better description of the rotational spectrum of complex molecules (Pickett et al. 1998). GSFC currently holds the main repository for non-LTE fluorescence linelists, suitable when synthesizing cometary spectra in the UV/optical/IR range. The

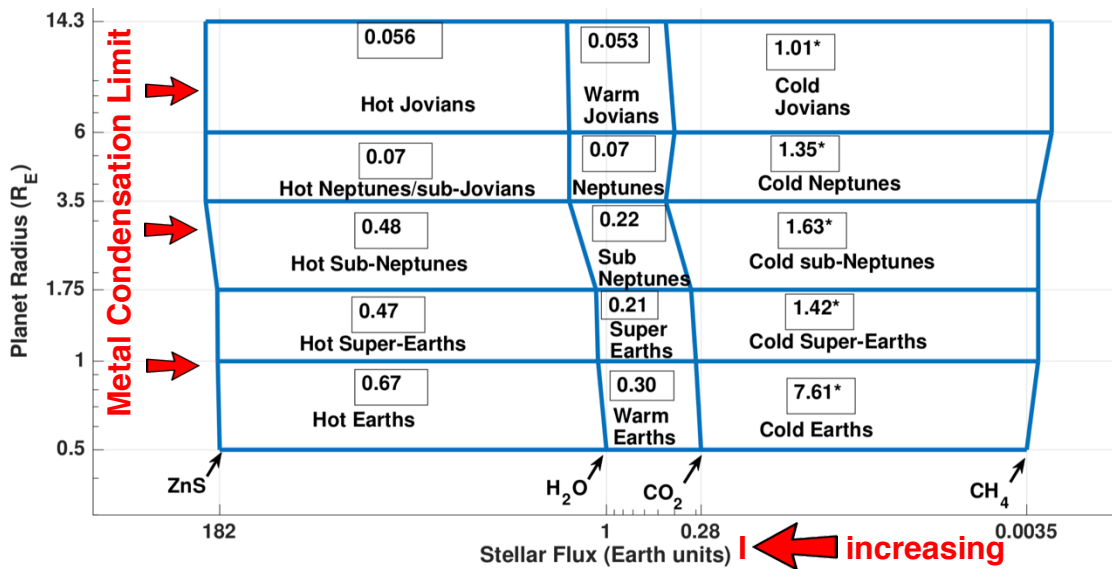
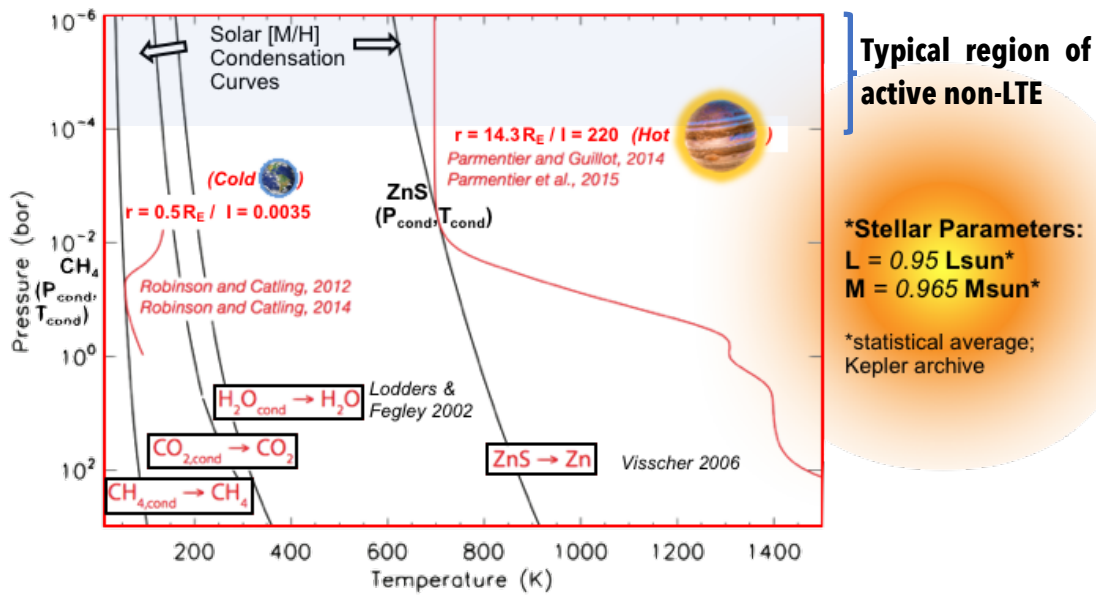
fluorescence database (Villanueva et al. 2011) covers wavelengths shortward of 10  $\mu\text{m}$  for 24 species, has 530,281 lines based on 2 billion non-LTE lines. For daughter species, rotational populations are heavily affected by photodissociation. Thus, a database of photochemically modeled species abundance is the missing part of an otherwise comprehensive network of the necessary tools and databases.

<b>The four key parameters required to compute realistic non-LTE fluxes from excitation:</b>
<b>High-energy (for stellar radiative pumping) and comprehensive (UV-submm) spectral databases <math>\rightarrow</math> track possible cascades and emission frequencies.</b>
<b>Non-LTE radiative transfer models.</b>
<b>Collision cross-sections (even best estimates) <math>\rightarrow</math> establish where LTE breaks down.</b>
<b>Photochemistry atmospheric models of exoplanets <math>\rightarrow</math> densities, P-T and mixing ratios</b>



**Figure 6.2:** A table and a flow chart (modified from a figure summarizing tasks in PI Villanueva’s 2015 proposal) showing how the work I am doing fits into the grand scheme of GSFC’s non-LTE spectra computation tool set. The deliverables expected from my end are marked with a red oval. The red boxes within the oval marks template types that are already part of the PHOTOCHEM suite, but over broad planet categories (more specific categories can be found in Figure 6.4 below). Key tools that are readily available now (collection of model stellar templates, the GFM, non-LTE radiative transfer model, high-resolution and high-energy compilations for H<sub>2</sub>O, CH<sub>4</sub>, HCN, etc.)—done as part of independent sub-tasks—have been marked by blue oval boxes.

**Figure 6.3:** *Top Panel:* The top plot below (modified from Kopparapu et al. 2018) shows where the gaseous species ZnS, H<sub>2</sub>O, CO<sub>2</sub> and CH<sub>4</sub> condense in *pressure-temperature (P-T)* space, and how their dependence matters for representative temperature profiles for different classes of planets (based on temperature). The *P-T* profiles for two different sizes of planets, 0.5 R<sub>⊕</sub> and 14.3 R<sub>⊕</sub> and two different instellations, 0.004 I<sub>⊕</sub> and 220 I<sub>⊕</sub>, respectively, are shown. The intersections of the condensation curves indicate that CH<sub>4</sub> and ZnS are condensing out in the cold and hot planetary atmospheres, respectively. The former marks a transition point for cooler hot Jupiters and the latter serves as a lower boundary for cold planets. The high-*T* *P-T* profiles were computed with the Parmentier model, which are also part of the PSG database, and planned for use in our photochemical model computations. *Bottom panel:* (also modified from Kopparapu et al. 2018) Exoplanet classification bins (type by temperature and density) shown based on current observables – incident stellar flux I and radius R<sub>E</sub> boundaries – at which ZnS, H<sub>2</sub>O, CO<sub>2</sub>, CH<sub>4</sub> would successively condense in the planetary atmospheric sphere. We can use these bins as the grid.



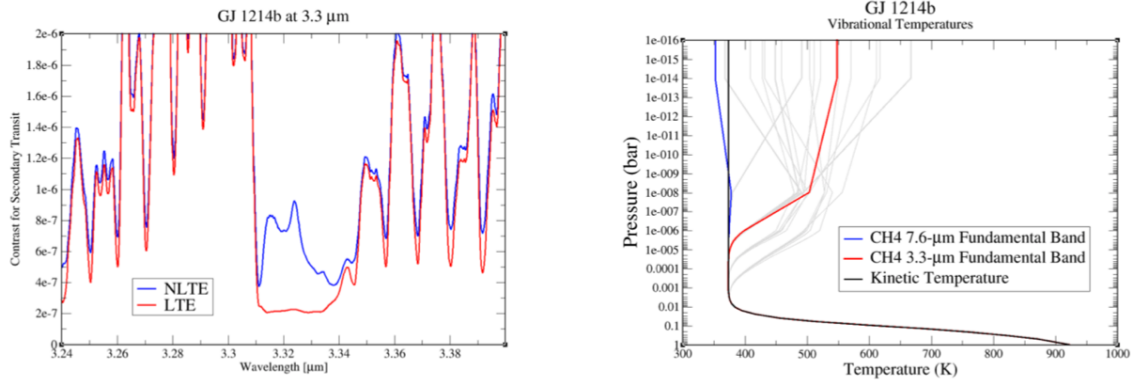


**Figure 6.4:** (From private communication with G. Villanueva, note that this will not be their final spectra due to the confusion introduced by the labeling of the first figure.) *Left panel:* High-resolution simulated limb absorption + non-LTE emission spectra (i.e. limb + nadir), centered at 3.3  $\mu\text{m}$ , shown for GJ1214b. Both LTE (red) and non-LTE (blue) contribution from methane shown. *Right panel:* The kinetic temperature profile shown (black) along with the vibrational temperatures at the two methane fundamental bands. The kinetic temperature profile was also computed via the Line et al. formalism from earlier. Vibrational temperatures are computed via level population determinations using the Einstein's equations. There is a factor of 4 difference, highlighting the importance of the 3.3  $\mu\text{m}$  band non-LTE emission strength. Note that as the labeling indicates, the red/blue color scheme represents different things in the two different figures and thus are not meant to correlate.

## 6.2 Dissertation Takeaway

We can conclude the following from the discussion I have presented in this dissertation and the works I have cited in the process:

- Factoring photochemical effects in assessing the abundance of atmospheric constituents will be more important for interpreting future exoplanet observations.
- A 1-D photochemical model can be used to map the composition of altitudes above the range mapped by 3-D models by coupling the two (using 3-D as input).
- Core science results from the 3-D to 1-D model pseudo-coupling studies for inner habitable zone planets around M dwarfs affecting future observations:

1. *JWST* relevant (i.e. relevant in next decade of potentially habitable planet observations): Observed water vapor absorption signals from H<sub>2</sub>O-rich planets should not diminish due to high stellar UV activity. Carbon dioxide is more detectable than water vapor if present in Earth-like quantities ( $f(\text{CO}_2) = 360$  ppm) in these planets. Methane may be detectable even from highly irradiated atmospheres if present in high abiotic quantities (i.e. close to the biotic limit).
  2. *OST* relevant (prospects in 2030s if selected and successfully launched): It may be possible to simultaneously detect both methane and ozone (also proxy for molecular oxygen) from abiotic anoxic nitrogen-rich IHZ rocky planets.
- I have extended the validity of the VPL photochemical and thermochemical model tool, Atmos, created for (and previously valid only for) temperate rocky planets to high temperature giant planets. The new generalized routines now in Atmos resulting from this effort are being used towards developing other templates (e.g. Titan, Mars, other exoplanets, Venus).
  - New planet type templates can be used towards other targeted future observation prediction and studies and interpretation of existing data: e.g. in the computation of non-LTE emission from certain relevant molecules in template (see previous section).

## Bibliography

- Afrin Badhan, M., Wolf, E. T., Kopparapu, R. K., et al. 2019a, in ASP Conf. Ser., Vol. 523, ADASS XXVIII, ed. P.J. Teuben, M.W. Pound, B.A. Thomas, & E.M. Warner (San Francisco: ASP), pp 467
- Afrin Badhan, M., Wolf, E. T., Kopparapu, R. K., et al. 2019b, arXiv e-prints, ADS, 1902.04086, *in press*
- Allard, F., Allard, N. F., Homeier, D., et al. 2007, A&A, 474, L21, ADS, 0709.1192
- Allard, F., Guillot, T., Ludwig, H.-G., et al. 2003, in IAU Symposium, Vol. 211, Brown Dwarfs, ed. E. Martín, 325
- Allen, M., Yung, Y. L., & Pinto, J. P. 1980, ApJL, 242, L125
- Anderson, D. R., Collier Cameron, A., Hellier, C., et al. 2015, 575, A61
- Anglada-Escudé, G. et al. 2016, Nature, 536, 437, ADS, 1609.03449
- Arney, G., Domagal-Goldman, S., & Meadows, V. 2014, in Search for Life Beyond the Solar System. Exoplanets, Biosig. Instruments, ed. D. Apai & P. Gabor, P2.11
- Arney, G., Domagal-Goldman, S. D., Meadows, V. S., et al. 2016, Astrobiology, 16, 873, ADS, 1610.04515
- Arney, G. N., Meadows, V. S., Domagal-Goldman, S. D., et al. 2017, ApJ, 836, 49, ADS, 1702.02994
- Agundez, M., Parmentier, V., Venot, O., et al., 2014, A&A, 564, A73
- Atreya, S. K., Crida, A., Guillot, T., et al. 2016, arXiv e-prints, arXiv:1606.04510, ADS, 1606.04510
- Barber R. J., Tennyson J., Harris G. J., Tolchenov R. N., 2006, MNRAS, 368, 1087
- Baudino, J.-L., Bonnefoy, M., Vigan, A., & Irwin, P. J. 2017a, in SF2A-2017: Proceedings of the Annual meeting of the French Society of Astronomy and Astrophysics, ed. C.Reylé, P. Di Matteo, F. Herpin, E. Lagadec, A. Lan con, Z. Meliani, 343–346
- Baudino, J.-L., Irwin, P., & Garland, R. 2018, in Diversis Mundi: The Solar System in an Exoplanetary Context, 3
- Baudino, J.-L., Mollière, P., Venot, O., et al. 2017b, ApJ, 850, 150, ADS, 1710.08235
- Banks, P.M. and Kockarts G., Academic Press, New York (1973)
- Barnes, R. et al. 2016, arXiv e-prints, arXiv:1608.06919, ADS, 1608.06919
- Barnes, R., Meadows, V. S., & Evans, N. 2015, ApJ, 814, 91, ADS, 1509.08922

- Barstow, J. K., Aigrain, S., Irwin, P. G. J., et al. 2012, ArXiv e-prints, 1212.5020
- Barstow, J. K., Aigrain, S., Irwin, P. G. J., et al. 2013, 434, 2616
- Barstow, J. K., Aigrain, S., Irwin, P. G. J., et al. 2017, ApJ, 834, 50
- Baranne, A., Queloz, D., Mayor, M., et al. 1996, A&AS, 119, 373
- Barstow, J. K., Aigrain, S., Irwin, P. G. J., et al. 2014, 786, 154
- Barstow, J. K., Aigrain, S., Irwin, P. G. J., et al. 2015a, 448, 2546
- Barstow, J. K., Bowles, N. E., Aigrain, S., et al. 2015b, Experi. Astronomy, 40, 545
- Barstow, J. K., Irwin, P. G. J., Fletcher, L. N., et al. 2016, 271, 400
- Barstow, J. K., Aigrain, S., Irwin, P. G. J., & Sing, D. K. 2017, ApJ, 834, 50, ADS, 1610.01841
- Batalha, N., Kalirai, J., Lunine, J., et al. 2015, ArXiv e-prints, 1507.02655
- Batalha, N. E., Mandell, A., Pontoppidan, K., et al. 2017, PASP, 129, 064501
- Battersby, C., Armus, L., Bergin, E., et al. 2018, Nature Astronomy, 2, 596, ADS, 1809.07351
- Batygin, K., Bodenheimer, P. H., & Laughlin, G. P. 2015, ArXiv e-prints, 1511.09157
- Benneke, B., & Seager, S. 2013, ApJ, 778, 153, ADS, 1306.6325
- B  tr  mieux, Y., & Kaltenegger, L. 2014, The Astrophysical Journal, 791, 7
- Bilger, C., Rimmer, P., & Helling, C. 2013, MNRAS, 435, 1888, ADS, 1307.2565
- Bin, J., Tian, F., & Liu, L. 2018, EPSL, 492, 121
- Borucki, W., Koch, D., Batalha, N., et al. 2009, Transiting Planets, 253, 289
- Borucki, W. J., Koch, D. G., Basri, G., et al. 2011, ApJ, 736, 19
- Burrows, A., Hubeny, I., Budaj, J., et al., 2007, ApJ, 668, L171
- Burrows, A., Budaj, J., & Hubeny, I. 2008, ApJ, 678, 1436
- Burrows, A., Budaj, J., & Hubeny, I. 2008, ApJ, 678, 1436
- Catling, D. C., Claire, M. W., Zahnle, K. J., et al. 2010, JGRE (Planets), 115
- Catling, D. C., in The Atmosphere -- History, vol. 13, Treatise on Geochemistry (2nd Ed.) (Eds. D. Canfield, J. Farquhar, J. F. Kasting), Elsevier, 2012/3

- Catling, D. C., & Kasting, J. F. 2017, "Atmospheric Evolution on Inhabited and Lifeless Worlds"
- Chameides, W.L., D.H. Stedman, R.R. Dickerson, et al., 1977: NO<sub>x</sub> Production in Lightning. *J. Atmos. Sci.*, **34**, 143–149
- Chen, J., & Kipping, D. 2017, *ApJ*, 834, 17, ADS, 1603.08614
- Chamberlain, J. W., & Hunten, D. M. 1987, Theory of planetary atmospheres. An introduction to their physics and chemistry., ADS
- Chapman, S. 1930a, The London, Edinburgh, and Dublin Phil Mag and Journal of Sci, 10, 345, <https://doi.org/10.1080/14786443009461583>
- Chapman, S. 1930b, The London, Edinburgh, and Dublin Phil Magazine and Journal of Sci, 10, 369, <https://doi.org/10.1080/14786443009461588>
- Chapman, S. 1942, Reports on Progress in Physics, 9, 92
- Charbonneau, D., Brown, T. M., Latham, D. W., et al. 2000, *ApJL*, 529, L45, ADS, astro-ph/9911436
- Chen, H., Wolf, E. T., Kopparapu, R., et al. 2018, *ApJL*, 868, L6, ADS, 1810.12904
- Crisp, D. 1997, *Geophys. Res. Lett.*, 24, 571
- Dai, F., Winn, J. N., Arriagada, P., et al. 2015, 813, L9
- Dawson, R. I., & Johnson, J. A. 2018, *ARA&A*, 56, 175, ADS, 1801.06117
- Del Genio, A.D., Way, M.J., Amundsen, D.S., et al. 2019, *Astrobiology* 19(2), 127
- Diamond-Lowe, H., Stevenson, K. B., Bean, J. L., Line, M. R., & Fortney, J. J. 2014, 796, 66
- Dittman, J.A., Irwin, J.M., Charbonneau, D. et al. 2017, *Nature* 544, 333
- Domagal-Goldman, S. D., Segura, A., Claire, M. W., et al. 2014, *ApJ*, 792, 90, ADS, 1407.2622
- Drossart, P. *et al.*, 1999. Eds. P. Cox & M. F. Kessler. ESA-SP 427. 427, p. 169
- Encrenaz, T. *et al.*, 1996. *A&A* 315, pp. L397–L400.
- Eriksson, G. *Acta Chemica Scandinavica*, 1971, Vol 25, 2651
- Fegley, B. J. & Lodders, K. 1994, *Icarus*, 110, 117
- Feng, Y.K., Line, M. R., Fortney, J. J., et al. 2016, *ApJ*, 829, 52, ADS, 1607.03230
- Feng, Y. K., Robinson, T. D., Fortney, J. J., et al. 2018, *AJ*, 155, 200, ADS, 1803.06403

Fletcher, L. N., Irwin, P. G. J., Sinclair, J. A., et al. 2015, 250, 131

Fletcher, L. N., Sinclair, J. A., Irwin, P. G. J., et al. 2014, EPSC 2014 Abstracts 62, Vol. 9

Fleury, B., Gudipati, M. S., Henderson, B. L., & Swain, M. 2019, ApJ, 871, 158

Ford, E. B. 2005, 129, 1706

Fortney, J. J., Saumon, D., Marley, M. S., et al., 2006, ApJ, 642, 495

Fortney, J. J., Lodders, K., Marley, M. S., & Freedman, R. S. 2008, ApJ, 678, 1419

Fortney, J. J., Robinson, T. D., Domagal-Goldman, S., et al. 2016, arXiv e-prints, ADS, 1602.06305

Fortney, J., Kataria, T., Stevenson, K., et al. 2018, arXiv e-prints arXiv:1803.07730, ADS, 1803.07730

France, K., Froning, C. S., Linsky, J. L., et al. 2013, ApJ, 763, 149, ADS, 1212.4833

France, K., Linsky, J. L., Tian, F., et al. 2012, ApJL, 750, L32, ADS, 1204.1976

Fujii, Y., Angerhausen, D., Deitrick, R., et al. 2018, Astrobiology, 18, 739, ADS, 1705.07098

Fujii, Y., Del Genio, A.D., & Amundsen, D.S. 2017, ApJ, 848, 100, ADS, 1704.05878

Gierasch, P. J., & Conrath, B. J. 1985, “Energy conversion processes in the outer planets”, ed. G. E. Hunt, 121–146

Gao, P., Hu, R., Robinson, T. D., et al. 2015, ApJ, 806, 249, ADS, 1501.06876

Garland, R., & Irwin, P. G. J. 2019, arXiv e-prints, arXiv:1903.03997, ADS, 1903.03997

Gaudi, B. S. et al. 2018, arXiv e-prints, arXiv:1809.09674, ADS, 1809.09674

Garcia Munoz, A. 2007, Planet. Space Sci., 55, 1426

Gillon, M. et al. 2017, Nature, 542, 456, ADS, 1703.01424

Gordon, I. E. et al. 2017, *J. Quant. Spectrosc. Radiat. Transf.* **203**, 3–69

Greene, T. P., Line, M. R., Montero, C., et al. 2016, ApJ, 817, 17, ADS, 1511.05528

Grenfell, J.L., Gebauer, S., Paris, P.V., et al. 2014, Planet Space Sci 98:66–76.

Grenfell, J.L., Stracke, B., von Paris, P., et al. 2007, Planet Space Sci 55:661–671.

Guillot, T. 2010, A&A, 520, A27, ADS, 1006.4702

- Guzmán-Marmolejo, A., Segura, A., & Escobar-Briones, E. 2013, *Astrobio.*, 13, 550
- Haqq-Misra, J., Wolf, E. T., Joshi, M., et al. 2018, *ApJ*, 852, 67, ADS, 1710.00435
- Hansen, B. M. S. 2008, 179, 484
- Harman, C. E., Schwieterman, E. W., Schottelkotte, J. C., et al. 2015, *ApJ*, 812, 137, ADS, 1509.07863
- Harrington, J., Luszcz, S., Seager, S., et al., 2007, *Nature*, 447, 691
- Heiter, U., Barklem, P., Fossati, L., et al. 2008, *JPhCS*, 130, 012011
- Heng, K. 2012, 761, L1
- Heng, K., & Demory, B.-O. 2013, *ApJ*, 777, 100, ADS, 1309.5956
- Hermans, C., Vandaele, A. C., Carleer, M., et al. 1999, *Env. Sci Pollut Res* 6:151–158.
- Hesman, B. E., Bjoraker, G. L., Sada, P. V., et al. 2012, 760, 24
- Hippler, S. 2019, *JAI*, 8, 1950001, ADS, 1808.02693
- Holton, J., & Hakim, G. 2017, “An Introduction to Dynamic Meteorology”, Academic Press
- Hu, R., Seager, S., & Bains, W. 2012, *ApJ*, 761, 166, ADS, 1210.6885
- Hu, Y. and Yang, J. 2014, *PNAS* 111(2), 629634
- Huang, C. X., Hartman, J. D., Bakos, G. G., et al. 2015, 150, 85
- Hubeny, I., Burrows, A., & Sudarsky, D. 2003, *ApJ*, 594, 1011
- Irwin, P. G. J., Fletcher, L. N., Read, P. L., et al. 2016, 264, 72
- Irwin, P. G. J., Teanby, N. A., de Kok, R., et al. 2008, 109, 1136
- Joshi, M. 2003, *Astrobiology* 3(2), 415
- Kasting, J. F. 1979, PhD thesis, Michigan Univ., Ann Arbor
- Kasting, J. F. 1990, *Origins of life and evolution of the biosphere*, 20, 199
- Kasting, J. F., Whitmire, D. P., & Reynolds, R. T. 1993, *Icarus*, 101, 108
- Kempton, E. M.-R., Zahnle, K., & Fortney, J.J. 2012, *ApJ*, 745, 3, ADS, 1104.5477
- Kempton, E. M.-R., Lupu, R., Owusu-Asare, A., et al. 2017, *PASP*, 129, 044402, ADS, 1611.03871

- Knutson, H. A., Charbonneau, D., Allen, et al. 2007, *Nature*, 447, 183
- Knutson, H. A., Charbonneau, D., Allen, et al. 2008, *ApJ*, 673, 526
- Knutson, H. A., Charbonneau, D., Burrows, A., et al., 2009, *ApJ*, 691, 866
- Knutson, H. A., Benneke, B., Deming, D., et al. 2014, *Nature*, 505, 66, ADS, 1401.3350
- Kopparapu, R. k., Kasting, J. F., & Zahnle, K. J. 2012, *ApJ*, 745, 77, ADS, 1110.2793
- Kopparapu, R. K., Ramirez, R., Kasting, J. F., et al. 2013a, *ApJ*, 765, 131, ADS, 1301.6674
- Kopparapu, R. K., et al. 2013b, *ApJL*, 767, L8, ADS, 1303.2649
- Kopparapu, R. K., Ramirez, R. M., SchottelKotte, J., et al. 2014, *ApJL*, 787, L29, ADS, 1404.5292
- Kopparapu, R. K., Wolf, E. T., Haqq-Misra, J., et al. 2016, *ApJ*, 819, 84, ADS, 1602.05176
- Kopparapu, R. K., Wolf, E. T., Arney, G., et al. 2017, *ApJ*, 845, 5, ADS, 1705.10362
- Kopparapu, R. K., Hébrard, E., Belikov, R., et al. 2018, *ApJ*, 856, 122, ADS, 1802.09602
- Krasnopolsky, V. A., & Pollack, J. B. 1994, *Icarus*, 109, 58
- Kreidberg, L., Bean, J. L., Désert, J.-M., et al. 2014, *Nature*, 505, 69, ADS, 1401.0022
- Kreidberg, L. et al. 2015, *ApJ*, 814, 66, ADS, 1504.05586
- Kreidberg, L., Line, M. R., Thorngren, D., et al. 2018, *ApJL*, 858, L6, ADS, 1709.08635
- Krissansen-Totton, J., Garland, R., Irwin, P.G.J., et al. 2018, *AJ*, 156, 114, ADS, 1808.08377
- Lacis, A. A., & Oinas, V. 1991, 96, 9027
- Lavvas, P., & Koskinen, T. 2017, *ApJ*, 847, 0
- Lee, J.-M., Fletcher, L. N., & Irwin, P. J. 2012, *MNRAS*, 420, pp170-182
- Lee, J.-M., Irwin, P. G. J., Fletcher, L. N., et al. 2014, *ApJ* 789, 14
- Leconte, J., Wu, H., Menou, K., et al. 2015, *Science*, 347, 632, ADS, 1502.01952
- Leisawitz, D., Amatucci, E., Carter, R., DiPirro, M., et al. 2018, in *Society of Photo-Optical Instru. Eng. (SPIE) Conference Series*, Vol. 10698, Proc. SPIE, 1069815

Lewis, N.T., Lambert, F.H., Boule, I.A., et al. 2018, ApJ, 854, 171, ADS, 1802.00378

Liang, M.-C., Parkinson, C. D., Lee, A. Y.-T., et al. 2003, ApJL, 596, L247

Liang, M.-C., Seager, S., Parkinson, C. D., et al. 2004, ApJL, 605, L61, ADS, astro-ph/0402601

Lin DNC, Bodenheimer P, Richardson DC. 1996. Nature 380:606–607

Lincowski, A. P., Lustig-Yaeger, J., & Meadows, V. S. 2019, AJ, 158, 26, ADS, 1905.12821

Line, M. R., Zhang, X., Vasisht, G., et al. 2012, 749, 93

Line, M. R., & Yung, Y. L. 2013, ApJ, 779, 3, ADS, 1309.6679

Line, M. R., & Fortney, J. J. 2014, 796, 66

Line, M. R., & Parmentier, V. 2016, 820, 78

Line, M. R., Stevenson, K. B., Bean, J., et al. 2016, AJ, 152, 203, ADS, 1605.08810

Lodders, K. and Fegley B. 1999 The Planetary Scientist's Companion. Oxford.

Lodders, K. 1999, ApJ, 519, 793. 2002, ApJ, 577, 974

Lodders, K. and Fegley, B.J. 2002. Icarus 155, 393-424.

Lodders K., 2003, ApJ, 591, 1220

Lustig-Yaeger, J., Meadows, V., Line, M., & Crisp, D. 2015, in AAS/DPS Meeting Abstracts, Vol. 47, 416.10

Lustig-Yaeger, J., Meadows, V. S., & Lincowski, A. P. 2019, AJ, 158, 27, ADS, 1905.07070

MacDonald R. J., Madhusudhan N., 2017b, ApJ , 850, L15

Machalek P., McCullough P., Burke C.J., et al., 2008 Astrophys. J. 684,1427-1432.

Madhusudhan, N., Harrington, J., Stevenson, K. B., et al. 2011, Nature, 469, 64

Madhusudhan, N., Mousis, O., Johnson, T.V., et al., 2012, ApJ, 743, 191

Madhusudhan, N., Agúndez, M., Moses, et al. 2016, ArXiv e-prints, 1604.06092

Madhusudhan, N., Amin, M. A., & Kennedy, G. M. 2014, 794, L12

Matsuo, T., Itoh, S., Shibai, H., et al. 2016, ApJ, 823, 139, ADS, 1511.00508

Manabe, S., & Wetherald, R. T. 1967, Journal of Atmospheric Sciences, 24, 241

- Marley, M. S., Ackerman, A. S., Cuzzi, J. N., et al 2013, in *Comparative Climatology of Terrestrial Planets*, S. J. Mackwell, A. A. Simon-Miller, J. W. Harder, and M. A. Bullock (eds.), University of Arizona Press, Tucson, pp. 367-391
- Mayor, M., & Queloz, D. 1995, *Nature*, 378, 355
- Mbarek, R., & Kempton, E. M.-R. 2016, *ApJ*, 827, 121, ADS, 1602.02759
- Meadows, V. S., & Crisp, D. 1996, *J. Geophys. Res.*, 101, 4595, ADS Merlis, T. M., & Schneider, T. 2010, *JAMES*, 2, 13, ADS, 1001.5117
- Meadows, V. S. 2017, *Astrobiology*, 17, 1022; <http://doi.org/10.1089/ast.2016.1578>
- Meadows, V. S., Arney, G. N., Schwieterman, E. W., et al. 2018a, *Astrobiology*, 18, 133, ADS, 1608.08620
- Meadows, V. S., Reinhard, C. T., Arney, G. N., et al. 2018b, *Astrobiology*, 18, 630, ADS, 1705.07560
- Meixner, M., Cooray, A., Leisawitz, D., et al. 2018, in *The Cosmic Wheel and the Legacy of the AKARI Archive: From Galaxies and Stars to Planets and Life*, 59–65
- Mello, A. J. T. S., Bouchez, A. H., Szentgyorgyi, A., van Dam, M. A., & Lupinari, H. 2018, *MNRAS*, 481, 3804, ADS, 1810.01020
- Méndez, A., & Rivera-Valentín, E. G. 2017, *ApJL*, 837, L1, ADS, 1702.07314
- Merlis, T.M. & Schneider, T. 2010, *JAMES* 2(13), 17 pp
- Miguel, Y., Kaltenegger, L., & Linsky, J. L. o. 2014, *MNRAS*, 446, 345
- Misra, A., Meadows, V., & Crisp, D. 2014, *ApJ*, 792, 61, ADS, 1407.3265
- Misra, A., Meadows, V., Claire, M., et al. 2014a, *Astrobio.*, 14, 67, ADS, 1312.2025
- Misra, A., Meadows, V., & Crisp, D. 2014b, *ApJ*, 792, 61, ADS, 1407.3265
- Misra, A. K., & Meadows, V. S. 2014, *ApJL*, 795, L14, ADS, 1409.7072
- Morley, C. V. 2016, PhD thesis, UC Santa Cruz
- Morley, C. V., Knutson, H., Line, M. et al. 2017, *AJ*, 153, 86, ADS, 1610.07632
- Moses, J. I., Visscher, C., Fortney, J. J., et al. 2011, *ApJ*, 737, 15, ADS, 1102.0063
- Moses, J. I., Line, M. R., Visscher, C., et al. 2013, *ApJ*, 777, 34, ADS, 1306.5178
- Neale, R. B., Chen, C. C., Gettelman, A., et al. 2010, *Description of the NCAR Community Atmosphere Model (CAM 5.0)*, NCAR/TN-486+STR NCAR Technical Note
- Neveu et al. (2015) *GRL*, 42, 10197-10206

- Neveu-VanMalle, M., Queloz, D., Anderson, D. R., et al. 2015, ArXiv e-prints, 1509.07750
- Nixon, C. 2014, in *Habitable Worlds Across Time & Space*, proceedings of a conference held April 28-May 1 2014 at STScI.
- Nixon, C. A., Achterberg, R. K., Čedámkovics, M., et al. 2016, 128, 018007
- Nixon, C. A., Jennings, D. E., Bezar, B., et al. 2014, AGU Fall Meeting Abstracts
- Nixon, C. A., Jennings, D. E., Bézard, B., et al. 2013, 776, L14
- Nixon, C. A., Temelso, B., Vinatier, S., et al. 2012, 749, 159
- Noda, S. et al. 2017, *Icarus*, 282, 1
- Novak, R.E., Mumma, M.J., Disanti, et al, 2002, *Icarus* 158(1), pp. 14–23.
- Öberg, K. I., Murray-Clay, R., & Bergin, E. A. 2011, 743, L16
- Parmentier, V., Showman, A.P., & Lian, Y. 2013, *A&A*, 558, A91, ADS, 1301.4522
- Parmentier, V., & Guillot, T. 2014, 562, A133
- Parmentier, V. 2014, PhD thesis, Université Nice Sophia Antipolis (UNS); Observatoire de la Côte d’Azur CNRS
- Parmentier, V., Guillot, T., Fortney, J. J., & Marley, M. S. 2015a, 574, A35
- Parmentier, V., Jonathan, F., Showman, A. P., et al. 2015b, in *AAS/DESS Meeting Abstracts*, Vol. 3, 111.03
- Pickett HM, Poynter RL, Cohen EA, et al., 1998, Sub-millimeter, millimeter, and microwave spectral line catalog. *JQSRT* 60:883–890.
- Pontoppidan, K. M., Pickering, T. E., Laidler, V. J., et al. 2016, *Proc. SPIE*, 9910, 991016
- Rackham B. V., Apai D., Giampapa M. S., 2018, *ApJ*, 853, 122
- Richard, C., Gordon, I.E., Rothman, L.S., et al. 2012, *JQSRT* 113:1276–1285.
- Richardson, L. J., Deming, D., Horning, K., et al., 2007, *Nature*, 445, 892
- Rocchetto, M., Waldmann, I. P., Venot, O., et al. 2016, *ApJ*, 833, 120
- Rocchetto, M. 2017, PhD thesis, University College London
- Robinson, T. D., & Catling, D. C. 2012, 757, 104

- Rodler, F., & López-Morales, M. 2014, *ApJ*, 781, 54, ADS, 1312.1585
- Roldan, C., López-Valverde, M.A., Lopez-Puertas, M. & Edwards, D.P., 2000. *Icarus* 147(1), pp. 11–25
- Rothman, L. S., & Gordon, I. E. 2014, in 13th International HITRAN Conference
- Rothman, L. S., Gordon, I. E., Barber, R. J., et al. 2010, *JQSRT*, 111, 2139
- Rothman, L. S., Wattson, R. B., Gamache, R., et al. 1995, in *Proc. SPIE*, 2471, 105
- Rugheimer, S., Kaltenecker, L., Segura, A., et al. 2015a, *ApJ*, 809, 57, ADS, 1506.07202
- Rugheimer, S., Segura, A., Kaltenecker, L., et al. 2015b, *ApJ*, 806, 137, ADS, 1506.07200
- Schwieterman, E. W., Robinson, T. D., Meadows, V. S., et al. 2015, *ApJ*, 810, 57, ADS, 1507.07945
- Schwieterman, E. W., Kiang, N. Y., Parenteau, M. N., Harman, C. E., et al. 2018, *Astrobiology*, 18, 663, ADS, 1705.05791
- Sing, D. K., Fortney, J. J., Nikolov, N., et al. 2016, *Nature*, 529, 59, ADS, 1512.04341
- Segura, A., Krelow, K., Kasting, J.F., et al. 2003, *Astrobiology* 3:689–708.
- Segura, A., Kasting, J. F., Meadows, V. S., et al. 2005, *Astrobiology*, 5, 706, ADS, astro-ph/0510224
- Segura, A., Walkowicz, L. M., Meadows, V., et al. 2010, *Astrobiology*, 10, 751, ADS, 1006.0022k
- Shields, A. L., Meadows, V. S., Bitz, C. M., et al. 2013, *Astrobiology*, 13, 715, ADS, 1305.6926
- Smith, E. Virgo, N., and Kleidon, A. 2014, *Earth Syst Dynam* 4:317– 331.
- Soummer, R., Pueyo, L., Ferrari, A., et al., 2009, *ApJ*, 695, 695, ADS
- Stevenson, K. B., Lewis, N. K., Bean, J. L., et al. 2016, *ArXiv e-prints*, 1602.08389
- Swain, M. R., Vasisht, G., & Tinetti, G. 2008, *Nature*, 452, 329
- Swain, M. R., Vasisht, G., Tinetti, G., et al. 2009, 690, L114
- Swain, M. R., Deroo, P., Griffith, C. A., et al. 2010, *Nature*, 463, 637
- Tashkun, S. A., Perevalov, V. I., Teffo, et al. 2003, *JQSRT*, 82, 165
- Tashkun, S. A., & Perevalov, V. I. 2011, 112, 1403

- Tian, F., Yang, J., et al. 2016, *ApJL*, 823, L20
- Tilley, M. A., Segura, A., Meadows, V., et al. 2017, arXiv e-prints, 1711.08484
- Tilley, M. A., Segura, A., Meadows, V., et al. 2019, *Astrobiology*, 19, 64
- Tinetti, G., Meadows, V. S., Crisp, D., et al. 2005, ArXiv Astrophysics e-prints, astro-ph/0502238
- Tinetti, G. et al. 2012, *Experimental Astronomy*, 34, 311, ADS, 1112.2728
- Tinetti, G., Encrenaz, T., & Coustenis, A. 2013, 21, 63
- Tovar, G., Arney, G., & Meadows, V. 2015, Vol. 225, AAS Meeting Abstracts, 239.03
- Toon, O. B., McKay, C. P., Ackerman, T. P., et al, 1989, *J. Geophys. Res.*, 94, 16287
- Torres, G., Winn, J. N., & Holman, M. J. 2008, *ApJ*, 677, 1324
- Venot, O., Hébrard, E., Agundez, M., et al. 2012, *A&A*, 546, A43
- Villanueva, G.L., Mumma, M.J. & Magee-Sauer, K., 2011. *JGR* 116(E08012), pp. 1–23.
- Visscher, C., Lodders, K., & Fegley, Jr., B. 2006, *ApJ*, 648, 1181
- Visscher, C., & Moses, J. I. 2011, *ApJ*, 738, 72, ADS, 1106.3525
- Vogt, S. S., et al. 1994, *Proc. SPIE*, 2198, 362
- von Paris, P., Selsis, F., Kitzmann, D., & Rauer, H. 2013, *Astrobiology*, 13, 899
- Wakeford, H. R., Visscher, C., Lewis, N. K., et al. 2017, *MNRAS*, 464, 4247, ADS, 1610.03325
- Wakeford, H. R., et al. 2015, *A&A*, 573, A122, ADS, 1409.7594
- Wang, Y., Liu, Y. Wenger, C., & Champion, J. P. 1998, *JQSRT*, 59, 471
- Way, M.J., Del Genio, A.D., Aleinov, I. et al. 2018, *ApJ Supp. Series* 239, 24
- White, W. B., Johnson, S. M., & Dantzig, G. B. *The J. of Chem. Phys.*, 1958, Vol 28, Number 5
- The LUVOIR Team. 2018, arXiv e-prints, arXiv:1809.09668, ADS, 1809.09668
- Wang, Y., Tian, F., & Hu, Y. 2014, *ApJL*, 791, L12
- Way, M. J., Del Genio, A. D., Kiang, N. Y., et al. 2016, *Geophys. Res. Lett.*, 43, 8376, ADS, 1608.00706
- Wolf, E. T. 2017, *ApJL*, 839, L1, ADS, 1703.05815

- Wolf, E. T., & Toon, O. B. 2013, *Astrobiology*, 13, 656, ADS
- Wolf, E. T., & Toon, O. B. 2014, *Geophys. Res. Lett.*, 41, 167, ADS
- Wolf, E. T., & Toon, O. B. 2015, *JGRD*, 120, 5775, ADS
- Wolf, E. T., Kopparapu, R. K., & Haqq-Misra, J. 2019, *ApJ*, 877, 35, ADS, 1906.02697
- Wolszczan, A., & Frail, D. A. 1992, *Nature*, 355, 145
- Wolszczan, A. 1994, *Science*, 264, 538
- Wordsworth, R. D., & Pierrehumbert, R. T. 2013, *ApJ*, 778, 154, ADS, 1306.3266
- Yang, J., Boué, G., Fabrycky, D. C., et al. 2014a, *ApJL*, 787, L2, ADS, 1404.4992
- Yang, J., Cowan, N. B., & Abbot, D. S. 2013, *ApJL*, 771, L45, ADS, 1307.0515
- Yang, J., Leconte, J., Wolf, E. T., et al. 2016, *ApJ*, 826, 222, ADS
- Yang, J., Liu, Y., Hu, Y., et al. 2014b, *ApJL*, 796, L22, ADS, 1411.0540
- Yang, J., Abbot, D.S., Koll, D.D.B., et al. 2019, *ApJ* 871, 26 (17pp)
- Yelle, R. V. 2004, *Icarus*, 170, 167
- Youngblood, A., France, K., Loyd, R. O. P., et al. 2016, *ApJ*, 824, 101, ADS, 1604.01032
- Yung, Y. L. 1976, *JQSRT*, 16, 755, ADS
- Yung, Y. L., Allen, M., & Pinto, J. P. 1984, *ApJS*, 55, 465
- Yung, Y. L., & Demore, W. B. 1982, *Icarus*, 51, 199
- Yurchenko S. N., Tennyson J., 2014, *MNRAS*, 440, 1649
- Yurchenko S. N., Barber R. J., Tennyson J., 2011, *MNRAS*, 413, 1828
- Zahnle, K., Haberle, R.M., Catling, D.C. et al. 2008, *J Geophys Res* 113:E11004.
- Zahnle, K., Marley, M. S., & Fortney, J. J. 2009a, *ArXiv e-prints*, ADS, 0911.0728
- Zahnle, K., Marley, M. S., Freedman, R. S., et al. 2009b, *ApJL*, 701, L20, ADS, 0903.1663
- Zahnle K., Freedman R. S., and Catling D. C. 2011, *Icarus*, 212: 493-503.
- Zhang, X., & Showman, A. P. 2018a, *ApJ*, 866, 1, ADS, 1803.09149
- Zhang, X., & Showman, A. P. 2018b, *ApJ*, 866, 2, ADS, 1808.05365